COMPUTATIONAL MODELING OF CARDIAC MECHANICS: MICROSTRUCTUAL MODELING & PULMONARY ARTERIAL HYPERTENSION

By

Ce Xi

A DISSERTATION

Submitted to
Michigan State University
in partial fulfillment of the requirements
for the degree of

Mechanical Engineering – Doctor of Philosophy

2019

ABSTRACT

COMPUTATIONAL MODELING OF CARDIAC MECHANICS: MICROSTRUCTUAL MODELING & PULMONARY ARTERIAL HYPERTENSION

By

Ce Xi

Heart diseases, which approximately account for 31% of all human mortality every year, are the leading cause of death worldwide. Computational cardiac models have gained increasing popularity and become an indispensable and powerful tool in elucidating the pathological process of different heart diseases. They can be used to estimate important physiological and clinically relevant quantities that are difficult to directly measure in experiments. The broad goals of this thesis were to develop 1) a microstructure-based constitutive model of the heart and 2) patient-specific computational models that would ultimately help medical scientists to diagnose and treat heart diseases.

Heart diseases such as heart failure with preserved ejection fraction (HFpEF) are characterized by abnormalities of ventricular function that can be attributed to, changes in geometry, impaired myocyte (LV) relaxation, cardiac fibrosis and myocyte passive stiffening. Understanding how LV filling is affected by each of the many microstructural pathological features in heart diseases is very important and may help in the development of appropriate treatments. To address this need, we have developed and validated a microstructure-based computational model of the myocardium to investigate the role of tissue constituents and their ultrastructure in affecting the heart function. The model predicted that the LV filling function is sensitive to the collagen ultrastructure and the load taken up by the tissue constituents varies depending on the LV transmural location. This

finding may have implications in the development of new pharmaceutical treatments targeting individual cardiac tissue constituents to normalize LV filling function in HFpEF.

Pulmonary arterial hypertension (PAH) is a life-threatening disease characterized by elevated pulmonary artery pressure (PAP) and pulmonary artery vascular resistance, with limited survival rate and can affect patients of all ages. The increased pressure or afterload in the right ventricle (RV) can result in pathological changes in RV mechanics, which are currently not well-understood. To fill this void, we have developed patient-specific computational models to investigate effects of PAH on ventricular mechanics. Specifically, we have quantified regional ventricular myofiber stress, myofiber strain, contractility, and passive tissue stiffness in PAH patients, and compare them to those found in age- and gender-matched normal controls. Our results showed that RV longitudinal, circumferential and radial strain were depressed in PAH patients compared with controls; RV passive stiffness increased progressively with the degree of remodeling as indexed by the RV and LV end-diastolic volume ratio (RVEDV/LVEDV); Peak contractility of the RV was found to be strongly correlated, and had an inverse relationship with RVEDV/LVEDV. These results provide the mechanical basis of using RVEDV/LVEDV as a clinical index for delineating disease severity and estimating RVFW contractility in PAH patients.

ACKNOWLEDGEMENTS

First of all, I would like to thank my advisor, Dr. Lik Chuan Lee, who gave me tremendous support and guidance during my entire Ph.D. research study. During those hard times when I was stuck in my research and couldn't make progress, he didn't give me up and instead encouraged me and helped me to discover my potentials to overcome various difficult challenges. Also, I would like to thank my committee members, Dr. Seungik Baek, Dr. Sara Roccabianca, Dr. Tamara Reid Bush and Dr. Mohsen Zayernouri for providing valuable advice and insights for this research.

Second, I would like to thank my collaborators in National Heart Center Singapore (Hua Zou, Xiaodan Zhao and Liang Zhong), École Polytechnique (Martin Genet) and Simula Research Laboratory (Henrik Finsberg and Samuel Wall) for their extraordinary contributions and continuous support in this research.

Third, I would like to thank all my families who always believe in me and care about me. Especially, I would like to thank my grandpa who cultivate and educate me since my childhood. Although he passed away during my first year in Michigan State University, I will never forget his goodness to me and will continue to move forward to make him feel proud of me.

Last but not least, I would like to thank my lifetime friend Ziguang Lee and my girlfriend Mengqi Tu for their companion and warmhearted help during those lonely and dark times.

TABLE OF CONTENTS

LIST OF TABLES

LIST OF FIGURES

CHAPTER 1

OVERVIEW

1.1 Background

Heart diseases, which approximately account for 31% of all human mortality every year, are the leading cause of death worldwide. With the recent advancement in both experimental and imaging techniques, patient-specific computational cardiac modeling using the finite element (FE) method has gained increasing popularity and has become an indispensable and powerful tool in elucidating the effects of various heart diseases and clinical interventions such as passive left ventricular (LV) constraint [5], [6] and cardiac support device (CSD) [7]. Cardiac computational model can be used to estimate important physiological and clinically relevant quantities that are difficult, if not impossible, to directly measure in experiments. For example, myocardial stress distributions, which are important determinants of myocardial oxygen consumption [8], [9] and ventricular hypertrophy [10], are not clinically or experimentally measurable. Computational heart models can also provide deformation map, stress and strain fields that supplement clinical data. They also enable one to quantify the relative contribution of underlying mechanisms in the human heart towards some phenomenon without incurring the typical high costs associated with conducting new experiments [11]. In spite of significant advancements associated with computational cardiac models, there remains unresolved issues and aspects that need to be addressed and improved. Here, we list 3 issues and limitations as described below:

A. Lack of microstructure-based computational model to quantify the contribution of individual tissue constituent to LV function

Construction of a constitutive law for the myocardium is of fundamental importance for accurate computational simulation and analysis of the mechanical behavior of

ventricular myocardium. Two traditionally employed approaches for modeling the mechanical behavior of soft tissues at the continuum level are, namely, the phenomenological or structure-based approaches. The phenomenological approach in soft tissue mechanics was pioneered by Fung [12], who found that the elasticity of living soft tissue is highly nonlinear, and that the elastic stress of the rabbits' mesentery in simple elongation test is approximately an exponential function of the stretch ratio. This result lays the foundation for many future phenomenological constitutive models in soft tissues, including those of the myocardium [13]–[16], arteries [17], skin [18]. Although phenomenological models can represent the bulk cardiac tissue mechanical behavior, their model parameters lack physical interpretation and cannot elucidate the underlying mechanisms of tissue behavior.

Microstructural constitutive models attempt to integrate information on tissue composition and microstructure to avoid ambiguities in material characterization. This class of models can potentially offer insights into the mechanical effects due to changes in function, structure, and mechanics of individual tissue components [19]. Structural constitutive models have been developed for a variety of intact tissues and tissue components including lung [20], collagen [21], [22], cartilage [23], heart valves [24], and maturing skin [25]. Lanir developed the first comprehensive, multidimensional structural constitutive model formulation [26]. With some modifications made to the original formulation, Horowitz et al. proposed a three-dimensional constitutive law for the passive myocardium [27] and implemented it in a two-dimensional finite element framework for the simulation of the passive-state mechanics of a thin myocardial strip [28], together with three-dimensional formulation for a thick ventricular wall segment [29]. Microstructural

approach, however, requires a detailed description of the complex microstructure, thereby rendering it mathematically involved and significantly more difficult to employ than the phenomenological approach. It remains to be implemented for the realistic 3D LV geometry with detailed measured structure information to enhance understanding of how changes in the tissue ultrastructure and micromechanical behaviors (e.g., collagen distribution and waviness, myofiber orientation) affect LV functions.

B. Difficulty in quantifying RV strain

Quantification of RV function is important for the clinical management of PAH patients. Recent studies have demonstrated that the RV strain is strongly associated with RV function and is a potentially useful prognostic marker of PAH patients [30], [31]. Compared to quantifying strain in the LV, *in vivo* quantitative assessment of the strain in the right ventricle is challenging because of complexity of ventricular shape, the thinness of the RV free wall. Tissue Doppler Echocardiography (TDE) is a relatively new real-time ultrasound technique that offer an objective means to quantify global and regional left and right ventricular function. Although it can improve the accuracy and reproducibility of conventional echocardiography, significant limitations of TDE include angle dependency [32]. Speckle-Tracking Echocardiography (STE) is the most widely available imaging modality for quantification of myocardial deformation and is angle-independent. Its image quality of the RV is also often poor [33]. Meanwhile, cardiac magnetic resonance (CMR) imaging has emerged as the gold standard for quantification of LV and RV strains [34]–[36], it can provide tomographic images of the right ventricle with superior spatial resolution. In addition, CMR was demonstrated to have superior reproducibility over two-dimensional (2D) echocardiography [37].

Hyperelastic warping is a deformable image registration technique that has been used to obtain strain measurements from medical images such as magnetic resonance imaging (MRI), positron emission tomography (PET) and computed tomography (CT) [38]–[40]. It integrates nonlinear continuum mechanics with image-based data to find a compatible deformation map between a target image and a template image. Application of hyperelastic warping approach in cardiac motion has been primarily confined to quantifying the LV strains [40], which has been verified by tagged MRI [41] and 3D CSPAMM MR images [42]. Little has been done, however, to further this efficient and robust image registration technique to estimate regional myocardial strains in both the LV and RV, which may help serve as a potential prognostic marker for the severity of heart diseases such as PAH as well as a reference for validating computational heart models.

C. Lack of patient-specific computational model that investigates right ventricular mechanics

Computational models have primarily been used to analyze LV mechanics in heart diseases (e.g. myocardial infarction [43], left branch bundle block [44], and mitral valve regurgitation [45], [46]) as well as heart failure treatments [47]. In comparison, the role of the right ventricular (RV) function has been overlooked for many years. Restricted in its role to pumping blood through a single organ (the lung) that is in close proximity, and less frequently involved compared to the left ventricle in epidemic heart diseases, the RV is less muscular and has generally been considered as a mere passive chamber [48]. Emerging data have, however, shown that RV function is the major determinant of functional state and prognosis in many heart diseases such as pulmonary arterial hypertension (PAH) [49]–[52].

Affecting the RV function, PAH is a disease associated with vasoconstriction of the pulmonary arterial vessels that results in an elevated pulmonary arterial pressure. The clinical diagnosis for PAH is an elevated mean pulmonary artery (PA) pressure greater than 25 mmHg with normal wedge pressure [53]. Without treatment, PAH can quickly lead to decompensated right heart failure and death. The current prognosis of PAH remains poor, with about 15% mortality within 1 year on modern therapy [54] and a low 3-year survival rate of 67% [55].

High afterload in the right ventricle caused by PAH can lead to changes in ventricular mechanics [56]. For example, an elevated RV pressure can lead to abnormal ventricular deformation in the form of a “left ventricular septal bow” (LVSB), which is a leftward motion of the septum into the left ventricle (LV) cavity. Moreover, PAH is also associated with long-term functional, structural, and geometrical changes in the RV [57]. These changes and their impacts on ventricular mechanics are currently not well-understood [58]. Although animal models have been used to understand ventricular mechanics associated with RV remodeling in PAH [59], [60], similar studies in humans are lacking and most clinical investigations have been confined to quantifying global ventricular mechanics through pressure–volume (PV) loop measurements [61], [62].

On the other hand, the increased size and pressure overload in RV caused by PAH can also impair LV filling and systolic performance through ventricular interdependence [63], [64], as well as through direct mechanical interactions via the interventricular septum and myofibers that encircle both chambers. Thus, it is of increasing importance to develop a biventricular computational model to understand and quantify biventricular mechanics in PAH.

1.2 Objectives of this dissertation

In this dissertation, we seek to overcome the issues and limitations discussed earlier, namely:

1. Implement a microstructure-based computational modeling framework to quantify the roles and contributions of each myocardial tissue constituent to LV passive mechanics.
2. Implement and extend an effective and robust image registration technique based on hyperelastic warping to quantify both LV and RV strains in PAH.
3. Develop patient-specific computational models to investigate biventricular mechanics in PAH. Specifically, we seek to quantify regional ventricular myofiber stress, myofiber strain, contractility, and passive tissue stiffness as well as the effects of trans-septal pressure gradients on the septum curvature based on patient data.

CHAPTER 2

LITERATURE REVIEW

2.1 Heart anatomy and microstructure

2.1.1 Organ structure

In humans and other mammals, the heart is a hollow muscular organ that pumps blood through vascular vessels to provide the whole body with oxygen and nutrients and to remove metabolic wastes. The heart can be divided into four chambers. The upper receiving chambers are called the left and right atria, which collect blood that returns to the heart and facilitate filling of the ventricles. The lower discharging chambers are called the left and right ventricles (**Figure 2.1**), which serve as a pump for the systemic circulation and pulmonary circulation, respectively. The left ventricle is much thicker and more muscular than the right ventricle as a consequence of the need to support a higher pressure in the systemic circulation. The cavity of the left ventricle is conical in shape during diastole and characterized by a more spherical shape as interventricular pressure rises at the end of isovolumic contraction [65], whereas the right ventricle possesses a more irregular crescent shape when viewed from its cross-section. The left and right sides of the heart are separated by a wall of muscle called the septum. The heart has four valves. The mitral valve connects the left ventricle and the left atrium, which prevents backflow of blood into the left atrium when the left ventricle contracts and ejects blood to the aorta through the aortic valve. Correspondingly, the tricuspid valve connects the right atrium and the right ventricle, which prevents backflow of blood into the right atrium when the right ventricle contracts and ejects blood to the pulmonary artery through the pulmonary valve.

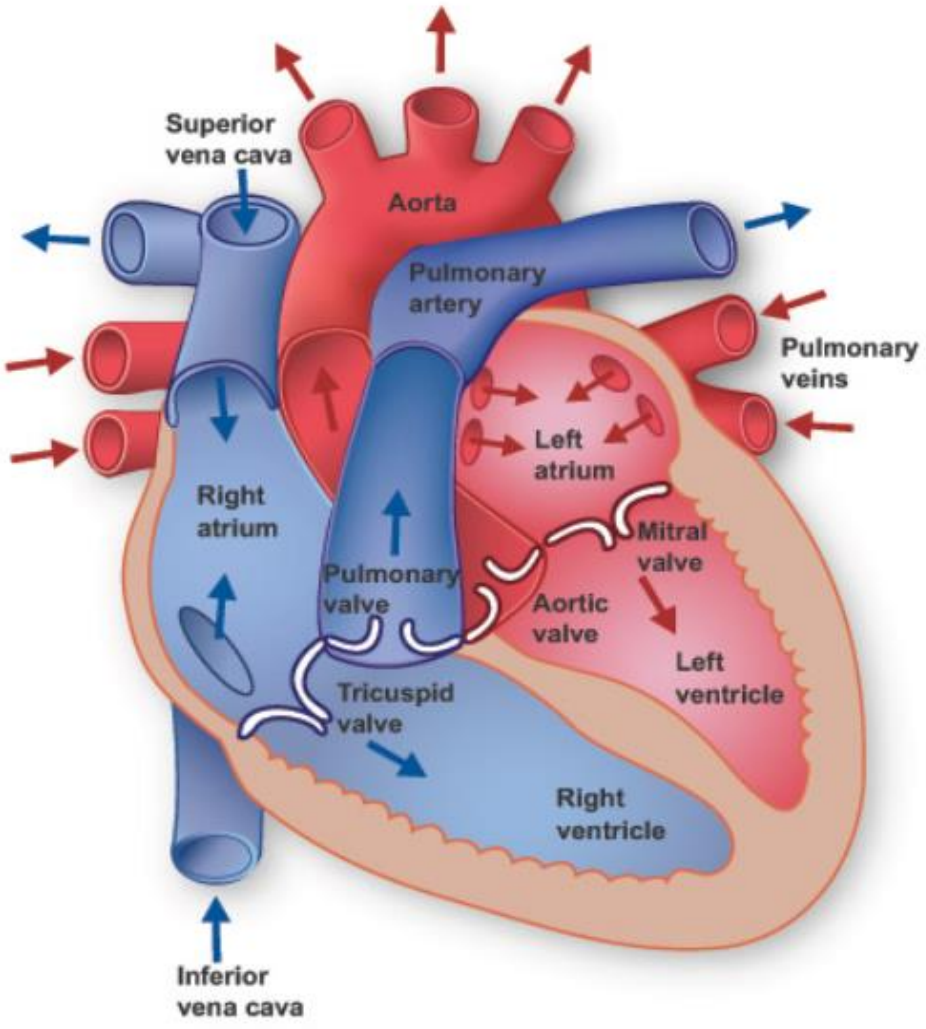

Figure 2.1. Cross-section of the heart, showing atria, ventricles and valves. Adapted from (https://www.texasheart.org)

2.1.2 Histology

The heart, together with a small amount of fluid, is surrounded by a noncompliant fibrous sac called the pericardium, whose outer surface is called the parietal pericardium. The heart wall comprises of three distinct layers: an inner layer (the endocardium), a middle layer (the myocardium) and an outer layer (the epicardium) (**Figure 2.2**).

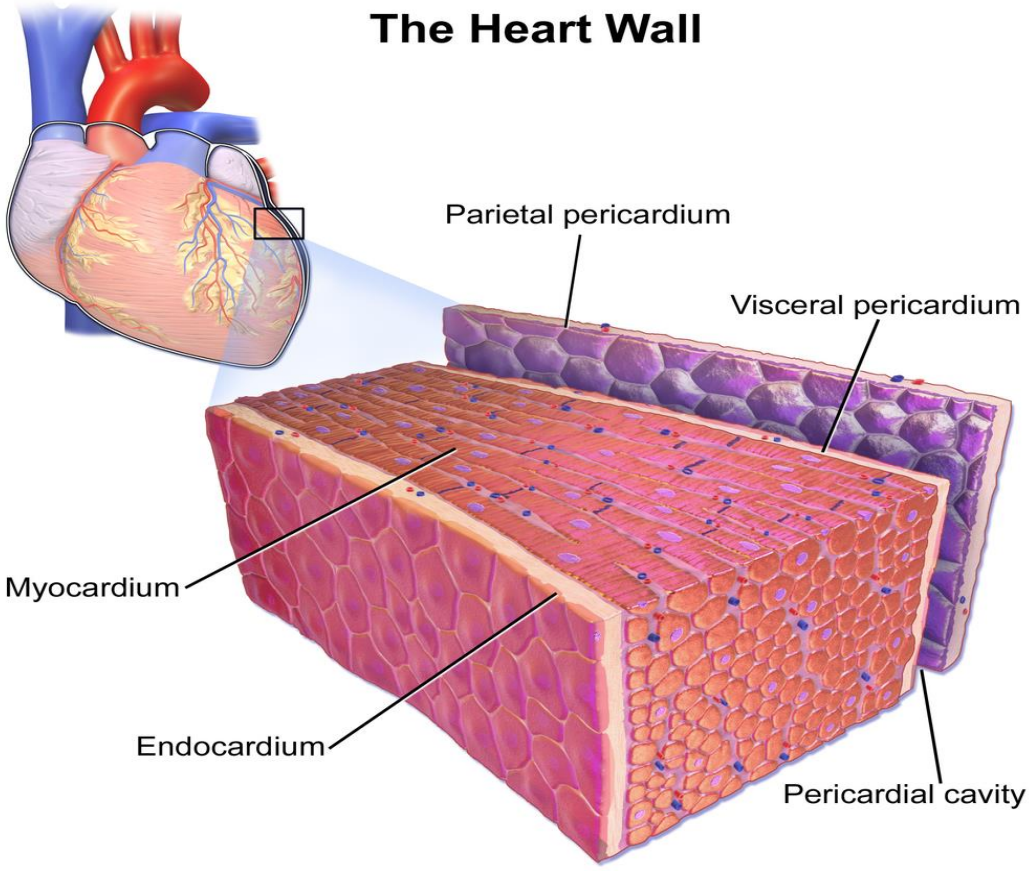

Figure 2.2. Illustration showing the comprising layers of the heart wall [66]

The epicardium (also called visceral pericardium) is a layer of squamous cells that overlies a network of fibrillar connective tissue. The endocardium lines with the inside of the four chambers and consists mainly of epimysial collagen, elastin and a layer of endothelial cells. The myocardium is the thickest layer of the heart wall, which is a composite material consisting of myocytes that are tethered and supported by an extensive fibrillar connective tissue network composed largely of collagen. The myocytes are the most prominent type of fibers, which occupy about 70 percent of the myocardium in volume. The remaining 30 percent consists of various interstitial components [67], and 2-5 percent of the interstitial volume is occupied by the collagen fibers [68]. The collagen

fiber network is arranged in several levels of organization: epimysium, the sheath of connective tissue that surrounds muscles; perimysium, tendon-like extensions of the epimysium that aggregate myocytes into bundles; endomysium, collagen fibrils that connect adjacent myocytes to one another (**Figure 2.3**) [69].

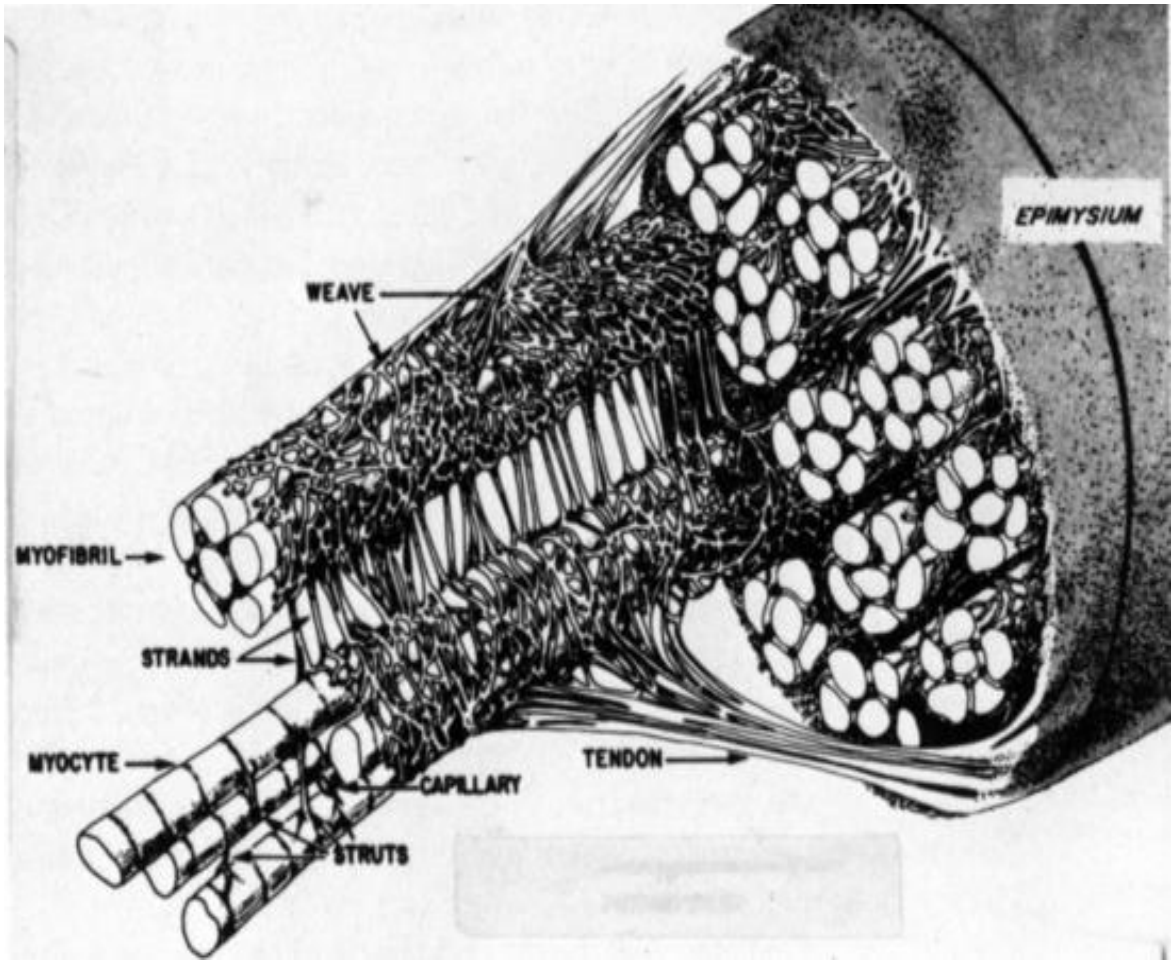

Figure 2.3. Schematic representation of the fibrillar collagen matrix of the myocardium (Adapted from Weber et al. [1])

Because of its spatial configuration and strong tensile strength relative to the myocytes, the collagen matrix is a major determinant of diastolic and systolic myocardial stiffness, structure integrity and mechanical properties of the myocardium. Also, the remodeling of fibrillar collagen matrix of the myocardium plays an active role in the hypertrophy that

accompanies various forms of chronic pressure overload, in which an accumulation and enhanced dimension of the collagen fibers and their realignment relative to muscle fibers, have been observed [1].

2.2 Cardiovascular diseases

Cardiovascular disease (CVD) is a class of diseases that affect the structure and function of the heart and/or blood vessels, and is the leading cause of death worldwide [70]. About 17.1 million people die each year from CVDs, which account for 31% of all death globally and impose a heavy financial burden on the human society [71]. Various CVDs include myocardial infarction (i.e., heart attack), stroke, cardiomyopathy, valvular heart disease and etc. Here we focus on two types of heart diseases: (1) pulmonary arterial hypertension (PAH) that causes right heart failure, and (2) heart failure with preserved ejection fraction that is also previously referred to as diastolic heart failure.

2.2.1 Pulmonary arterial hypertension

Pulmonary arterial hypertension (PAH) is a disease resulting from the constriction of pulmonary arteries that produces an elevated pulmonary vascular resistance, which ultimately leads to right heart failure [53]. The clinical diagnosis for PAH is sustained elevation of pulmonary arterial pressure at more than 25 mmHg at rest or 30 mmHg with exercise and with normal mean pulmonary-capillary wedge pressure and left ventricular end-diastolic pressure of less than 15 mmHg [72]. While previously considered a rare disease, the most recent evidence suggests the prevalence of PAH is about 15 per million in France [73] . This disease also affects more females than males [74].

Pulmonary arterial hypertension can be idiopathic in which its exact cause is unknown, or familial, or associated with several conditions or diseases, such as congenital heart disease, HIV infection, exposure to toxins and drugs [73]. Common symptoms of PAH include shortness of breath during exertion, dizziness, swelling of ankles and legs, chest pain as well as a fast heartbeat. As the condition worsens, its symptoms may limit all physical activity. There is no known cure for this disease and supportive measures such as oxygen therapy, diuretics and blood-thinning medicines are used to manage this disease [75]. The current prognosis of PAH remains poor, with about 15% mortality within 1-year on modern therapy [54] and a low 3-year survival rate of 67% [76].

Image-based computational models are increasingly used to analyze ventricular mechanics in heart diseases (e.g., myocardial infarction [43] , left branch bundle block [44], and mitral valve regurgitation [45], [77]) as well as heart failure treatments [78]. The focus of these computational analyses is, however, on the LV that has historically received more attention than the RV. The RV, whose function is a major determinant of prognosis in PAH [79], has largely been overlooked.

To fill the void in the current research of PAH, our goal is to develop an image-based computational model to investigate effects of PAH on ventricular mechanics. Specifically, we seek to quantify regional ventricular myofiber stress, myofiber strain, contractility, and passive tissue stiffness in a PAH patient, and compare them to those found in an age- and gender-matched normal subject. We also want to investigate and quantify the effects of transseptal pressure gradients on the septum curvature.

2.2.2 Heart failure with preserved ejection fraction

It is well established that approximately half of patients with heart failure (HF) have preserved systolic function (LV ejection fraction ≥ 45-50%) (i.e., heart failure with preserved ejection fraction, HFpEF), while the rest have a reduction in ejection fraction, (i.e., heart failure with reduced ejection fraction, HFrEF) [80]. The prevalence of HFpEF is increasing at an alarming rate at about 1% per year, with mortality rates comparable to HFrEF [81]. Taken together with the aging world population, HFpEF is expected to become the predominant form of HF, where 65% of patients hospitalized with HF by the year 2020 are projected to have EF > 40 % [82]. Besides, in contrast to improved prognosis of HFrEF through proof of effective medications, the prognosis of HFpEF have remained poor and unchanged over the past 20 years [80]. These trends underscore the importance of this growing public health problem.

Compared to HFrEF, epidemiological studies have shown that HFpEF patients are typically older, consist of more women and has hypertension as the most common etiology [83]. Other risk factors for HFpEF include hyperlipidemia, diabetes, renal dysfunction, obesity and the presence of ischemic heart disease [84]. Clinical manifestations of HFpEF include shortness of breath, exercise intolerance, fatigue [85].

Historically, HFpEF was termed “diastolic heart failure”, which is characterized by abnormalities of ventricular diastolic function such as impaired LV relaxation and increased LV diastolic stiffness. This increased LV stiffness has been associated with many micro-level remodeling features found in HFpEF patients such as interstitial fibrosis (e.g. progressive collagen accumulation, enhanced collagen cross-linking and collagen phenotype shift) [86], myocyte stiffening [87] and increased myocyte diameter [88] that

leads to increased LV mass and thickened LV wall, which is referred as concentric hypertrophy.

On the other hand, HFpEF patients typically also have subtle abnormalities in systolic performance, which become more exacerbated during exercise. Very recent studies [33], [89]–[91] have discovered that global longitudinal and circumferential strains are reduced in HFpEF patients. These results suggest that systolic function may also be impaired. Moreover, ongoing investigations suggest that, although diastolic abnormalities may be present in HFpEF patients, other aspects of pathophysiology are likely to be responsible for the symptoms, such as chronotropic incompetence, atrial dysfunction, pulmonary hypertension and RV dysfunction, impaired vasodilation, endothelial dysfunction [92].

Clinical trials have yet to identify an effective treatment for HFpEF [93]. This issue is largely because of the pathophysiological heterogeneity that exists within the broad spectrum of HFpEF. Large randomized trials in broad populations of patients with HFpEF have generally shown neutral results [94]. Recently, substantial attention has been paid to the cardiac interstitium as a promising therapeutic target in HFpEF, since studies have shown a correlation between cardiac collagen and diastolic dysfunction in this syndrome [95].

Our current understanding of the impact of LV microstructural remodeling on its function in HFpEF patients is largely based on inference drawn by correlating simplified indices such as LV relaxation time and stiffness constant with microstructural features such as extracellular matrix volume fraction [96], [97] and force measurements in single cardiomyocytes [87]. While useful, the lack of a physics-based connection between these

data makes it very difficult to quantify the role and contribution of microstructural changes in tissue constituents and their mechanical behavior to changes in LV diastolic function in HFpEF.

Thus, our second goal is to develop a microstructural computational model by taking into account mechanics and microstructural features of individual tissue constituents (e.g. collagen waviness, spatial orientation) in order to i) isolate roles and contributions of each tissue constituent to ventricular dysfunction ii) enhance our understanding in pathophysiology of HFpEF so that targeted therapies can be developed based on a sound scientific foundation.

2.3 Cardiac imaging techniques

Cardiac imaging techniques play a significant role in diagnosis and management of heart failure, quantitative analysis of heart function and myocardial deformation, and development of better treatment strategies [98]. Various imaging modalities are increasingly used in the diagnostic evaluation of cardiovascular diseases, among which echocardiography and cardiac magnetic resonance (CMR) imaging represent two of the most commonly performed imaging examinations in routine clinical practice.

2.3.1 Echocardiography

With the merits of availability, safety and low cost, echocardiography is the first and most widely used exam for the diagnosis, prognosis and reassessment of heart failure patients [98] . Over the past 50 years, this imaging technique has evolved from a simple M-code tracing to a family of modalities including two-dimensional (2D) imaging, spectral Doppler, color flow Doppler and tissue Doppler imaging [99]. They can measure

multiple clinically important parameters of cardiac function, including LV ejection fraction, cavity volumes and mass.

In most studies, ventricular strain is measured using tissue Doppler imaging, which can provide an objective means to quantify global and regional ventricular function and improve the accuracy and reproducibility of conventional echocardiography [32]. However, tissue Doppler-based assessment of ventricular function is angle-dependent and typically assess only mitral annular motion [33]. More recently, B-mode speckle tracking has allowed for quantitative assessment of ventricular deformation and is angle-independent. However, the image quality of RV is often poor, thus limiting its accuracy and reproducibility in evaluation of RV strain, which is a useful prognostic marker for PAH patients [31].

2.3.2 Cardiac magnetic resonance imaging

Cardiac magnetic resonance (CMR) imaging, also known as cardiac MRI, is a key imaging technique for noninvasive assessment of myocardial structure and function [100]. It has emerged as the gold standard for quantification of myocardial deformation [35], [101], which can provide tomographic images of both ventricles with superior spatial resolution. In addition, CMR was demonstrated to have superior reproducibility over echocardiography [37].

Hyperelastic warping is a deformable image registration technique that has been used to obtain strain measurements from medical images such as magnetic resonance imaging (MRI), positron emission tomography (PET) and computed tomography (CT) [38]–[40]. It integrates nonlinear continuum mechanics with image-based data to find a compatible deformation map between a target image and a template image. Application

of the hyperelastic warping approach in cardiac motion has been primarily confined to quantifying the LV strains [40], which has been verified by tagged MRI [41] and 3D CSPAMM MR images [42]. Little has been done, however, to further this efficient and robust image registration technique to estimate regional myocardial strains in both LV and RV, which may help serve as a potential prognostic marker for the severity of heart diseases such as PAH and provide clinical reference for validating computational heart models.

Therefore, our third goal is to implement this image registration technique to quantify biventricular strains associated with PAH patients for quantitative evaluation of cardiac function.

2.4 Cardiac computational modeling

The combination of cardiac computational models and biophysical simulations can help interpret experimental data and promote understanding, diagnosis and treatment of heart failure [102]. For this reason, cardiac computational modeling has become a rising field of research. With the recent advancement in both experimental and imaging techniques, cardiac computational modeling has become an indispensable and powerful tool in elucidating effects of various heart diseases and clinical interventions such as passive left ventricular (LV) constraint [5], [6] and cardiac support device (CSD) [7].

Cardiac computational models can be used to estimate important physiological and clinically relevant quantities that are difficult, if not impossible, to directly measure in experiments. Of crucial importance is the ventricular wall stress [9], [103], which is an important determinant of myocardial oxygen consumption and key driver for pathological

ventricular remodeling and hypertrophy [104]. Thin-walled [105] or thick-walled [106] simplified ellipsoidal formulas generalized from the Laplace's Law have been widely used to estimate stress in idealized geometries, however, these methods severely underestimate myofiber stress in realistic patient-specific geometries and cannot accurately estimate regional stress [107]. In order to use cardiac computational models for accurately evaluation of ventricular stress, it is necessary to develop accurate constitutive models describing the mechanical behavior of the myocardium.

Two categories of constitutive models have been used traditionally to model the mechanical behavior of the cardiac tissues. The first category is phenomenological models, which are based on experimental measurements of the tissue mechanical behaviors. The second category is microstructural models, which directly model the inherent microstructure and composition of ventricular constituents.

2.4.1 Phenomenological models

The phenomenological approach in describing soft tissue mechanics was pioneered by Fung [12] , who found that the elasticity of living soft tissue is highly nonlinear, and that the elastic stress for the rabbits' mesentery in simple elongation test is approximately an exponential function of the stretch ratio. This result lays the foundation of many future phenomenological constitutive models for ventricular myocardium.

Most of the phenomenological models of myocardium were proposed based on the assumption material properties of myocardium are symmetric about the myofiber orientation. These models are typically known as transversely isotropic models, of which typical examples include models of Humphrey and Yin [13], Humphrey et al. [108],

Guccione et al. [14], Costa et al. [109] and Kerckhoffs at el. [110]. While transversely isotropic models are proposed based on biaxial tests of cardiac tissues, the results from shear experiments showed that the resistance of myocardial tissue to simple shear loading in different planes is noticeably different [111], which suggests that myocardial tissue is actually an orthotropic material with distinct material properties in orthonormal planes of symmetry.

More recently, orthotropic models of passive myocardium have been proposed including the pole-zero model of Hunter et al. [112], Holzapfel & Ogden[16] and Schmid et al. [113]. Although phenomenological models have been widely used to describe cardiac mechanics and can represent the bulk cardiac tissue mechanical behaviors, their model parameters typically lack physical interpretation and cannot elucidate the underlying mechanisms of tissue behavior.

2.4.2 Microstructural models

Microstructural constitutive models attempt to integrate information on tissue composition and microstructure to avoid ambiguities in material characterization. This class of models can potentially offer insights into the mechanical effects due to changes in function, structure, and mechanics of individual tissue components [114]. Structural constitutive models have been developed for a variety of intact tissues and tissue components including lung [20], collagen [21], [22], cartilage [23], heart valves [24], and maturing skin [25]. Lanir developed the first comprehensive, multidimensional structural constitutive model formulation [26]. With some modifications made to the original formulation, Horowitz et al. proposed a three-dimensional constitutive law for the passive myocardium [27] and implemented it in a two-dimensional finite element framework for

the simulation of the passive-state mechanics of a thin myocardial strip [28], together with three-dimensional formulation for a thick ventricular wall segment. Recently, M. S. Sacks implemented a structural constitutive model into a finite element framework for membrane tissues, However, finite element implementation of structural models that takes into account the realistic LV geometry and muscle fiber architecture is still lacking, which is an essential step to promote our understanding of how changes in the tissue ultrastructure and micromechanical behaviors (e.g., collagen distribution and waviness, myofiber orientation) affect LV functions.

CHAPTER 3

MICROSTRUCTURE-BASED FINITE ELEMENT MODEL OF LEFT VENTRICLE PASSIVE INFLATION

Abstract

Isolating the role(s) of microstructural pathological features in affecting diastolic filling is important in developing targeted treatments for heart diseases. We developed a microstructure-based constitutive model of the myocardium and implemented it in an efficient open-source finite element modeling framework to simulate passive inflation of the left ventricle (LV) in a representative 3D geometry based on experimentally measured muscle fiber architecture. The constitutive model was calibrated using previous tissue-level biaxial mechanical test data derived from the canine heart and validated with independent sets of measurements made at both the isolated constituent and organ level. Using the validated model, we investigated the load taken up by each tissue constituent and their effects on LV passive inflation. The model predicts that the LV compliance is sensitive to the collagen ultrastructure, specifically, the collagen fiber azimuthal angle with respect to the local muscle fiber direction and its waviness. The model also predicts that most of the load in the sub-epicardial and sub-endocardial regions is taken up, respectively, by the muscle fibers and collagen fiber network. This result suggests that normalizing LV passive stiffness by altering the collagen fiber network and myocyte stiffness is most effective when applied to the sub-endocardial and sub-epicardial regions, respectively. This finding may have implication for the development of new pharmaceutical treatments targeting individual cardiac tissue constituents to normalize LV filling function in heart diseases.

3.1 Introduction

Passive filling capacity of the left ventricle (LV) is a major determinant of the heart's pumping performance [115], [116]. Heart failure with preserved ejection fraction (HFpEF) (referred previously as diastolic heart failure) is associated with abnormalities in LV filling that can be detected from clinical imaging [117], [118]. Because HFpEF accounts for about one-half of all chronic HF patients [119], understanding how LV filling is affected by the many microstructural pathological features associated with this syndrome (e.g., cardiac fibrosis [120], myocyte passive stiffening [87], and collagen ultrastructure alterations [121] is very important. As such, the development of a 3D LV mechanics model that includes myocardial tissue constituents and their microstructure will enable one to isolate and quantify the impact of each constituent on LV filling.

Current constitutive models used to describe the mechanical behavior of the myocardium can be broadly categorized into two types: i.e., phenomenological and microstructural models. In phenomenological constitutive models, the tissue's mechanical behavior is usually described by a mathematical expression of its strain energy function (SEF) with the form of a polynomial [108], an exponential [14], [16] or a zero-pole function [122] of either the invariants or components of the strain tensor. While able to represent the bulk cardiac tissue mechanical behavior, these phenomenological models cannot distinguish between contributions of tissue constituents' intrinsic mechanical behavior and ultrastructure (e.g., collagen waviness) to the LV mechanics and function. Moreover, model parameters in the phenomenological models can only be obtained by fitting with experimental measurements of stress-strain relationships and have no direct physical meaning.

First developed by Lanir, microstructural constitutive models take into account the tissue constituents' morphology and structural arrangement in a stochastic manner as well as their intrinsic mechanical behavior [123]. One advantage of microstructural constitutive models is that their morphometric parameters, in addition of being physiologically meaningful, can be directly measured. With the significant advancement in microscopy imaging (e.g., multiphoton microscopy) techniques that enable the tissue constituent's (e.g., elastin, collagen, cells) morphology and structure to be accurately measured, these models can be exploited to directly isolate and quantify the effects of microstructural changes on the overall tissue mechanical behavior and organ function. Microstructural constitutive models have been applied to describe the mechanics of various tissues, such as skin [124], heart valves [125], arteries [126] as well as the passive myocardium [27]. The solution of the mechanical equilibrium boundary value problem using these models, however, were obtained semi-analytically and their applications were therefore confined to simple idealized geometries such as thick-walled cylinder [127]. Quantification of three-dimensional tissue mechanics in a realistic organ geometry requires an efficient finite element (FE) implementation of the microstructural constitutive model, which is, to the best of our knowledge, currently lacking and limited to tissue mechanics of a thin myocardial strip [28], a thick single-element myocardial wall segment [29], as well as a thin membrane [128].

To address this gap, we developed a microstructural FE model of the LV with a representative 3D geometry and muscle fiber architecture to describe the passive mechanics of myocardial tissue during inflation. The model was implemented using an open-source FE library FEniCS [129]. Additionally, we estimated the microstructural

constitutive model parameters using previous biaxial mechanical test measurements of the canine myocardial tissue. These model parameters were also validated using independent sets of measurements made on isolated cardiac tissue constituents and the intact LV during passive filling. Based on the calibrated parameters, we investigated the load taken up by each constituent during passive filling. The FE model shows that the global LV filling function is sensitive to the tissue microstructure.

3.2 Materials and methods

3.2.1 Microstructural constitutive model formulation

The myocardium has two major load-bearing elements: collagen fibers and muscle fibers. Arranged in a fibrous network, collagen fibers form a network of “struts” interconnecting adjacent myocytes and fibrous weaves surrounding groups of myocytes [130], [131]. Both types of fibers are embedded in an interstitial fluid matrix. The fibers carry tensile forces, while the fluid matrix sustains only hydrostatic pressure. On the other hand, the myocardium also contains a non-fibrous ground matrix consisting of non-load bearing substances such as fibroblasts, plasma cells, as well as a gel-like ground substance composing of glycosaminoglycans and glycoproteins.

Following Horowitz *et al*. [27], we developed a microstructure-based constitutive model to describe the passive mechanical behavior of the myocardium based on the following assumptions:

(a) The myocardium is treated as an incompressible pseudo-hyperelastic composite material [132], namely, there exists a strain energy function from which the stresses are derived. The viscoelastic aspect of the tissue is not considered in our

study due to the relatively short duration of the cardiac cycle compared with the characteristic relaxation time of the myocardium.

(b) The fibers are thin and perfectly flexible. They can only carry tensile loads and have no compressive strength and if contracted will buckle under zero load.

(c) Each fiber is subjected to a uniaxial strain that is the tensorial transformation of the overall strain in the fiber's direction (affine deformation). This is intuitively justified by the numerous interconnections between muscle and collagen fibers [27], [114], [133].

Correspondingly, the total strain-energy function W_{total} of the myocardium can be represented by the volume-weighted summation of the strain energy function of its constituents, i.e.:

$$W_{total} = \phi_{\boldsymbol{g}} W_g + \phi_{\boldsymbol{m}} W_m + \phi_c W_c - p(J-1) \tag{3.1}$$

where ϕ_g, ϕ_m and ϕ_c are the volume fraction of the ground matrix, muscle fibers and collagen fibers, respectively, with $\phi_g + \phi_m + \phi_c = 1$. On the other hand, W_g, W_m and W_c are the corresponding SEF of the ground matrix, muscle fibers and collagen fibers, respectively. In Eq. (3.1), J is the determinant of deformation gradient tensor $\boldsymbol{F}$, and p is the Lagrange multiplier to enforce incompressibility due to the negligible fluid flow within the tissue for the pertinent time intervals. Correspondingly, we assume that the last term $-p(J-1)$ in Eq. (1) represents the contribution to W_{total} by the interstitial fluid matrix. The deformation gradient tensor is defined by $\boldsymbol{F} = \boldsymbol{I} + \nabla \boldsymbol{u}$, where $\boldsymbol{u}$ is the displacement field and $\boldsymbol{I}$ is the identity tensor**.** In the following, we describe the mechanical behavior of each constituent.

3.2.1.1 Non-fibrous ground matrix

Following a previous study [134], we modeled the non-fibrous ground matrix as an isotropic hyperelastic Neo-Hookean material with the SEF defined as:

$$W_g = \frac{C_1}{2}(I_1 - 3) \tag{3.2}$$

where $I_1 = \mathrm{tr}(\boldsymbol{C})$ is the first invariant of the right Cauchy-Green deformation tensor $\boldsymbol{C} = \boldsymbol{F^T F}$, and C_1 is a material constant. The resulting second Piola-Kirchhoff (PK2) stress tensor associated with the non-fibrous ground matrix is then given by:

$$\boldsymbol{S}_g = \phi_g \frac{\partial W_g}{\partial \boldsymbol{E}} = \phi_g C_1 \boldsymbol{I} \tag{3.3}$$

where $\boldsymbol{E} = \frac{1}{2}(\boldsymbol{C} - \boldsymbol{I})$ is the right Cauchy-Green strain tensor.

3.2.1.2 Muscle fibers.

Because the isolated myocyte exhibits a non-linear stress-strain relationship of an exponential form [135], we used an SEF [13] that is given as:

$$W_m = \begin{cases} C_2\left[e^{C_3(\alpha-1)^2} - 1\right] & \text{if } \alpha > 1 \\ 0 & \text{if } \alpha \leq 1 \end{cases} \tag{3.4}$$

to describe the muscle fiber's passive mechanical behavior. In Eq. (4), $\alpha = \sqrt{\boldsymbol{e}_f \cdot \boldsymbol{C} \cdot \boldsymbol{e}_f}$ is the uniaxial stretch of the muscle fiber, $\boldsymbol{e_f}$ is a unit vector describing the local muscle fiber direction in the undeformed configuration, whereas C_2 and C_3 are the material constants. The corresponding PK2 stress tensor associated with the muscle fibers is given by:

$$\boldsymbol{S}_m = \phi_m \frac{\partial W_m}{\partial \boldsymbol{E}} = \begin{cases} 2\phi_m C_2 C_3 (\alpha - 1) e^{C_3(\alpha-1)^2} \frac{\partial \alpha}{\partial \boldsymbol{E}} & \text{if } \alpha > 1 \\ \boldsymbol{0} & \text{if } \alpha \leq 1 \end{cases} \tag{3.5}$$

3.2.1.3 Collagen fiber network

For simplicity, different hierarchies of collagen fibers (perimysial, epimysial and endomysial or struts) are lumped into one inclusive system in the model. Because straightened individual collagen fiber exhibits a linear stress-strain relation [136], uniaxial stress S_c of a single straightened collagen fiber is prescribed to be a linear function of its strain taken with respect from its initial straightened configuration with a slope or elastic modulus C_4. Collagen fibers, however, are observed to be undulated and slack in the unstressed state in the myocardium [130]. Because of their crimped structural feature, the individual wavy collagen's true fiber strain ϵ_t taken with respect from its initial straightened configuration is given by:

$$\epsilon_t = \frac{\epsilon_c - \epsilon_s}{1+2\epsilon_s} \tag{3.6}$$

where ϵ_c is the total strain of the collagen fiber taken with respect from its initial wavy configuration and ϵ_s is the strain at which the collagen fiber first straightens; i.e., straightening strain. Assuming that the collagen fiber doesn't show any resistance to stretch before becoming straightened (or reaching their straightening strain ϵ_s), the resulting SEF for a single wavy collagen fiber is given by:

$$w_c = \int_{\epsilon_s}^{\epsilon_c} C_4 \epsilon_t d\epsilon_c = \frac{C_4}{2} \frac{(\epsilon_c - \epsilon_s)^2}{1+2\epsilon_s}. \tag{3.7}$$

The extent of collagen fiber undulation can vary, however, across collagen fibers in the myocardium [114]. To stochastically account for the gradual recruitment of wavy collagen fibers, we assume a truncated normal distribution with the density function:

$$D(x) = \frac{1}{K} \frac{1}{\sqrt{2\pi}\sigma_c} e^{-\frac{(m_c - x)^2}{2{\sigma_c}^2}} \tag{3.8}$$

where $K = 1 - \Phi(\frac{-m_c}{\sigma_c})$ is a truncated parameter with Φ denoting the cumulative normal distribution function, whereas, m_c and σ_c denote the mean and variance of the collagen fiber straightening strain, respectively. Thus, the resulting SEF for a uniaxial ensemble of collagen fibers over all possible waviness (weighted by the waviness distribution) is given by:

$$w_c = \frac{C_4}{2}\int_0^{\epsilon_c} D(x)\frac{(\epsilon_c - x)^2}{1+2x}\,dx \tag{3.9}$$

The mechanical behavior of the overall collagen fiber ensemble is the sum of the contributions from all uniaxial ensembles over all collagen fiber orientations. Following Horowitz *et al*.[27], we assume that the collagen fibers are symmetrically distributed around the muscle fiber to which they are attached, with the muscle fiber serving as an axis of symmetry (**Figure 3.1**). Following this assumption, the collagen fibers are ascribed a uniform distribution $R(\theta)$ in the circumferential $\theta-$ direction $(0 \le \theta \le 2\pi)$, and a bimodal normal distribution $R(\phi)$ in the azimuthal $\phi-$ direction$(0 \le \phi \le \pi)$. Thus, the overall spatial distribution function is given by:

$$R(\theta,\phi) = R(\theta) * R(\phi) = \frac{1}{2\pi}\left(\frac{1}{2\sqrt{2\pi}\sigma_\phi}\exp\left(-\frac{(m_\phi-\phi)^2}{2{\sigma_\phi}^2}\right) + \frac{1}{2\sqrt{2\pi}\sigma_\phi}\exp\left(-\frac{(\pi-m_\phi-\phi)^2}{2{\sigma_\phi}^2}\right)\right) \tag{3.10}$$

where $(m_\phi, \pi - m_\phi)$ are the means and $(\sigma_\phi, \sigma_\phi)$ are the standard deviations of the bimodal distribution of the azimuthal angle ϕ. Since the arrangement of the collagen fibers is referred to the muscle fibers to which they are attached, the uniaxial strain of a local collagen fiber oriented with respect to the local muscle fiber that it is attached to can be related to the local muscle fiber strains by a tensorial transformation as:

$$\epsilon_c(\theta,\phi) = \boldsymbol{N}_c \cdot \boldsymbol{E}_m \cdot \boldsymbol{N}_c \tag{3.11}$$

where $\boldsymbol{N}_c = \{\cos\phi,\ \cos\theta sin\phi,\ \sin\theta sin\phi\}$ and $\boldsymbol{E}_m$ is the Green-Lagrange strain tensor in the local material coordinate system. The components of $\boldsymbol{E}_m$ are related to the Green-Lagrange strain tensor $\boldsymbol{E}$ in the global coordinate system by:

$$E_{m_{ij}} = \boldsymbol{e}_i \cdot \boldsymbol{E} \cdot \boldsymbol{e}_j \tag{3.12}$$

with the subscript $(i,j) \in (f,s,n)$ denoting the muscle fiber $\boldsymbol{e}_f$, cross muscle fiber $\boldsymbol{e}_s$, tissue sheet normal $\boldsymbol{e}_n$ directions.

If the waviness density distribution function $D(x)$ is assumed to be homogeneous over all spatial orientations, the total collagen fiber SEF is given by:

$$\mathrm{W_c} = \begin{cases} \frac{\mathrm{C_4}}{2}\int_0^{2\pi}\int_0^{\pi}[\int_0^{\epsilon_c(\theta,\phi)} \mathrm{D(x)}\frac{(\epsilon_c(\theta,\phi)-\mathrm{x})^{\,2}}{1+2\mathrm{x}}\mathrm{dx}]\mathrm{R}(\theta,\phi)\mathrm{d}\phi\mathrm{d}\theta & \text{if } \epsilon_c > 0 \\ 0 & \text{if } \epsilon_c \le 0 \end{cases} \tag{3.13}$$

Correspondingly, the PK2 stress tensor associated with the collagen network is given by:

$$\mathbf{S_c} = \phi_c \frac{\partial W_c}{\partial \boldsymbol{E}} = \begin{cases} \phi_c \mathrm{C_4}\int_0^{2\pi}\int_0^{\pi}[\int_0^{\epsilon_c} \mathrm{D(x)}\frac{(\epsilon_c(\theta,\phi)-\mathrm{x})^{\,2}}{1+2\mathrm{x}}\mathrm{dx}]\mathrm{R}(\theta,\phi)\frac{\partial \epsilon_c}{\partial \mathbf{E}}\mathrm{d}\phi\mathrm{d}\theta & \text{if } \epsilon_c > 0 \\ \mathbf{0} & \text{if } \epsilon_c \le 0 \end{cases} \tag{3.14}$$

We note that the approach here to describe the collagen network stress tensor in Eq. (3.14) differs from the generalized structure tensor (GST) approach [137], which assumes that the dispersion of fiber orientation (as described by a structure tensor) is separable from the dispersion of tortuosity. No such assumption is made in this approach, which is also referred as the “angular integration” (AI) approach [137]. For a detail comparison of the GST and AI approaches, refer to Holzapfel and Odgen [138]. From Eq. (3.1), the total PK2 stress tensor of the myocardium is given as:

$$\boldsymbol{S}_{total} = \frac{\partial W_{total}}{\partial \boldsymbol{E}} = \boldsymbol{S}_g + \boldsymbol{S}_m + \boldsymbol{S}_c - p\boldsymbol{C}^{-1} \tag{3.15}$$

with the components defined in Eqs. (3.3), (3.5) and (3.14).

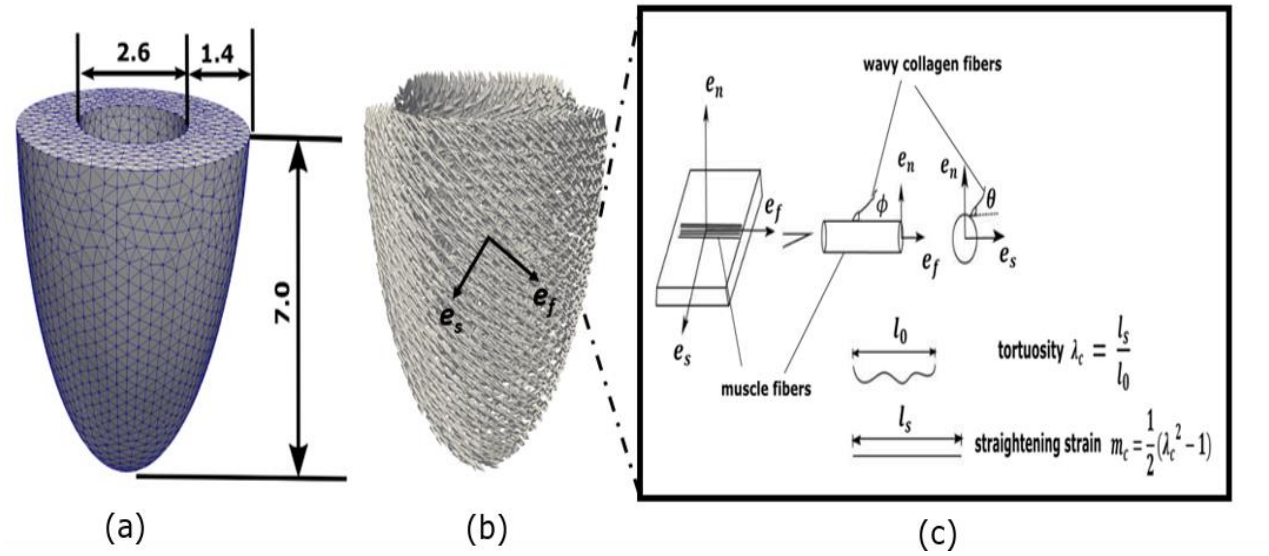

Figure 3.1. (a) Unloaded canine LV FE geometry (all dimensions are in cm). (b) Muscle fiber orientation with a linear transmural variation from $70°$ at the endocardium to $-40°$ at the epicardium. (c) Schematic representation of the local arrangement of muscle fiber and collagen fiber network. The muscle fiber defines an axis of symmetry for the spatial arrangement of collagen fiber that attached to it. Collagen fiber dispersion is prescribed by a continuous function with the angle θ and ϕ. An azimuthal angle $\phi = 0$ corresponds to the axial fiber family whereas a circumferential angle $\phi \neq 0$ corresponds to the radial fiber family.

3.2.2 Parameter estimation

We used the biaxial mechanical test data obtained from 6 canine mid-wall myocardium in a previous experimental study [139] to estimate the model's parameters. In that study, equi-biaxial stretching and constant α tests, where cross-fiber stretch was varied at a constant muscle fiber stretch of α, were performed on thin slab of tissues taken from the mid ventricular wall. We fixed the volume fraction of the tissue constituents to be $\phi_m = 0.7, \phi_c = 0.026, \phi_g = 0.274$ based on previous experimental measurements [67], [140]. The collagen spatial distribution variance σ_ϕ was also fixed at 0.1 rad (or

equivalently 6°) based on a quantitative analysis of the collagen orientation in the canine LV [121]. This leaves the remaining 7 unknown model parameters to be estimated, namely, material constants of the constituents C_1, C_2, C_3, C_4, mean value of the collagen spatial distribution function m_ϕ, and the mean m_c and variance σ_c of the collagen waviness distribution. These model parameters were fitted to the experimental data with an objective function defined as the sum of squared residuals (SSEs) between the model predictions and experimental measurements, i.e.,

$$SSE = \sum_{k=1}^{N}[\left({\sigma_{11}}^k - {\hat{\sigma}_{11}}^k\right)^2 + \left({\sigma_{22}}^k - {\hat{\sigma}_{22}}^k\right)^2] \quad (3.16)$$

In Eq. (16), N is the total number of data points and ${\hat{\sigma}_{ii}}^k$ are the measured values of the Cauchy stresses. We also imposed constraints to our model parameters, especially those related to the microstructural features, to vary within physiological ranges based on previous studies (**Table 3.1**). A nonlinear programming solver "fmincon" in MATLAB (The Mathworks, Inc., Natick, MA, USA) was used to find parameters that lie between the imposed physiological lower and upper bounds, and minimize the objective function. An optimal solution was obtained when the change in parameters or the objective function was less than 10^{-9}. Different sets of initial guesses were randomly generated between the lower bounds and upper bounds in order to eliminate parameter dependence on the initial guess values. Details of the plane stress formulation for fitting the biaxial test data is given in the **APPENDIX A**.

Table 3.1. List of model parameters with the corresponding lower/upper bounds according to literature references

Type	Parameter	Lower Bound	Upper Bound	References
Ground matrix	C_1 (kPa)	0.01	10	[141], [142]
Muscle fibers	C_2 (kPa)	0.1	1.0	[143]
	C_3	1	50	
Collagen fibers	C_4 (MPa)	0.1	100	[124]
	m_c	>0	0.3	[27], [127]
	σ_c	>0	0.1	
	m_ϕ (rad)	>0	$\frac{\pi}{2}$	

To investigate the identifiability and correlation of the fitted model's parameters, we estimated the asymptotic correlation matrix **R** associated with these parameters using the scaled inverse of the hessian matrix **H** evaluated at the optimal solution [142]. Specifically, components of the estimated correlation matrix **R** was defined as:

$$R_{ij} = \frac{(H^{-1})_{ij}}{\sqrt{(H^{-1})_{ii}}\sqrt{(H^{-1})_{ii}}} \quad (i,j \text{ not summed}). \tag{3.17}$$

The closer the absolute value of the off-diagonal terms R_{ij} to 1, the stronger the correlation between the ith and jth parameters.

3.2.3 Finite element simulation of left ventricular passive filling

3.2.3.1 Unloaded geometry and microstructure

The unloaded LV geometry was modeled as a half prolate ellipsoid with geometric dimensions that are based on measurements of isolated arrested canine hearts (**Figure 3.1**) [2]. Specifically, the unloaded LV cavity volume is about 20 ml. The geometry is meshed with 17600 quadratic tetrahedral elements and 83799 nodes. The local muscle fiber orientation in the LV is prescribed based on the mean values reported in an

experiment [2], which shows that the helical angle varied linearly in the transmural direction from about $70°$ at the endocardium to $-40°$ at the epicardium.

3.2.3.2 Finite element formulation

Passive filling of the LV was simulated by incrementally increasing the pressure at endocardium as a Neumann boundary condition. The weak form of the mechanical equilibrium equation is given by:

$$\mathcal{L}\big((\boldsymbol{u};\boldsymbol{v}),(p;q)\big) = \int_{\Omega_0} \boldsymbol{P}(\boldsymbol{u},p):\nabla\boldsymbol{v}\, dV + \int_{\partial\Omega_{endo}} P_{endo}\cdot J\boldsymbol{F}^{-\boldsymbol{T}}\boldsymbol{N}\cdot\boldsymbol{v}dA \; - \int_{\Omega_0} q(J-1)\, dV \quad (3.18)$$

where $\boldsymbol{P} = \boldsymbol{F}\boldsymbol{S}_{total} = \boldsymbol{F}(\boldsymbol{S}_g + \boldsymbol{S}_m + \boldsymbol{S}_c) - pJ\boldsymbol{F}^{-\boldsymbol{T}}$ is the first Piola-Kirchhoff stress tensor, P_{endo} is the prescribed LV cavity pressure at the endocardial surface $\partial\Omega_{endo}$ with unit outward normal of $\boldsymbol{N}$, whereas $\boldsymbol{v}$ and q are the variation of the displacement field $\boldsymbol{u}$ and the Lagrange multiplier p, respectively, Thus, the Euler-Lagrange problem becomes one of finding $\boldsymbol{u} \in H^1(\Omega_0), p \in L^2(\Omega_0)$ that satisfies $\mathcal{L}\big((\boldsymbol{u};\boldsymbol{v}),(p;q)\big) = 0 \;\; \forall\, \boldsymbol{v} \in H^1(\Omega_0), q \in L^2(\Omega_0)$. The basal deformation is constrained to be in-plane (i.e., $\boldsymbol{u}\cdot\boldsymbol{n}|_{base} = 0$) and the endocardial basal nodes are fixed in all directions to account for the relative stiff valve annuli [144]. The nonlinear FE problem was solved using Newton-Raphson method and implemented based on the parallel open-source FE library FEniCS. The code is freely available at https://cexi@bitbucket.org/cexi/microstructure_lv.git. Convergence of the numerical solution for the nonlinear FE problem was accepted when the normalized two-norm of the residual vector is smaller than 10^{-9}. Analyses of the mesh sensitivity and computational efficiency were also performed.

3.2.3.3 Post-processing of myocardial strains and stresses

To compare with strain measurements and estimate myocardial stress, we computed strains and stress components in the circumferential $\boldsymbol{e}_c$, longitudinal $\boldsymbol{e}_l$ and radial $\boldsymbol{e}_r$ directions, as well as fiber $\boldsymbol{e}_f$ and cross-fiber $\boldsymbol{e}_s$ directions (**Figure 3.2**). We also divided the LV FE mesh into 7 layers with equal thickness. The strain and stress components were averaged over the volume of each layer to determine their transmural variations (**Figure 3.2**).

3.2.3.4 Post-processing of collagen fiber tortuosity

Volume-averaged 2D tortuosity λ_c (fiber arc length/midline length) of the collagen fiber network was computed at a given ventricular pressure P as:

$$\lambda_c(P) = \begin{cases} \frac{1}{\Omega_0}\int_{\Omega_0}\int_0^{2\pi}\int_0^{\pi}\int_0^{\infty}\frac{\sqrt{2x+1}}{\sqrt{2\varepsilon_c(\theta,\phi,P)+1}}D(x)dx\,R(\theta,\phi)\,d\phi\,\mathrm{d}\theta\,dV & if\ 0<\varepsilon_c<x \\ \frac{1}{\Omega_0}\int_{\Omega_0}\int_0^{2\pi}\int_0^{\pi}\int_0^{\infty}D(x)dx\,R(\theta,\phi)\,d\phi\,\mathrm{d}\theta\,dV & if\ \varepsilon_c\geq x \\ \frac{1}{\Omega_0}\int_{\Omega_0}\int_0^{2\pi}\int_0^{\pi}\int_0^{\infty}\sqrt{2x+1}\,D(x)dx\,R(\theta,\phi)\,d\phi\,\mathrm{d}\theta\,dV & if\ \varepsilon_c<0 \end{cases} \quad (3.19)$$

where $\sqrt{2x+1}$ is the initial tortuosity for a collagen fiber with an initial straightening strain x, $\sqrt{2\varepsilon_c(\theta,\phi,P)+1}$ is the tortuosity of deformed local collagen fiber with spatial orientation (θ,ϕ) at ventricular pressure P and Ω_0 is the whole material volume at the reference configuration.

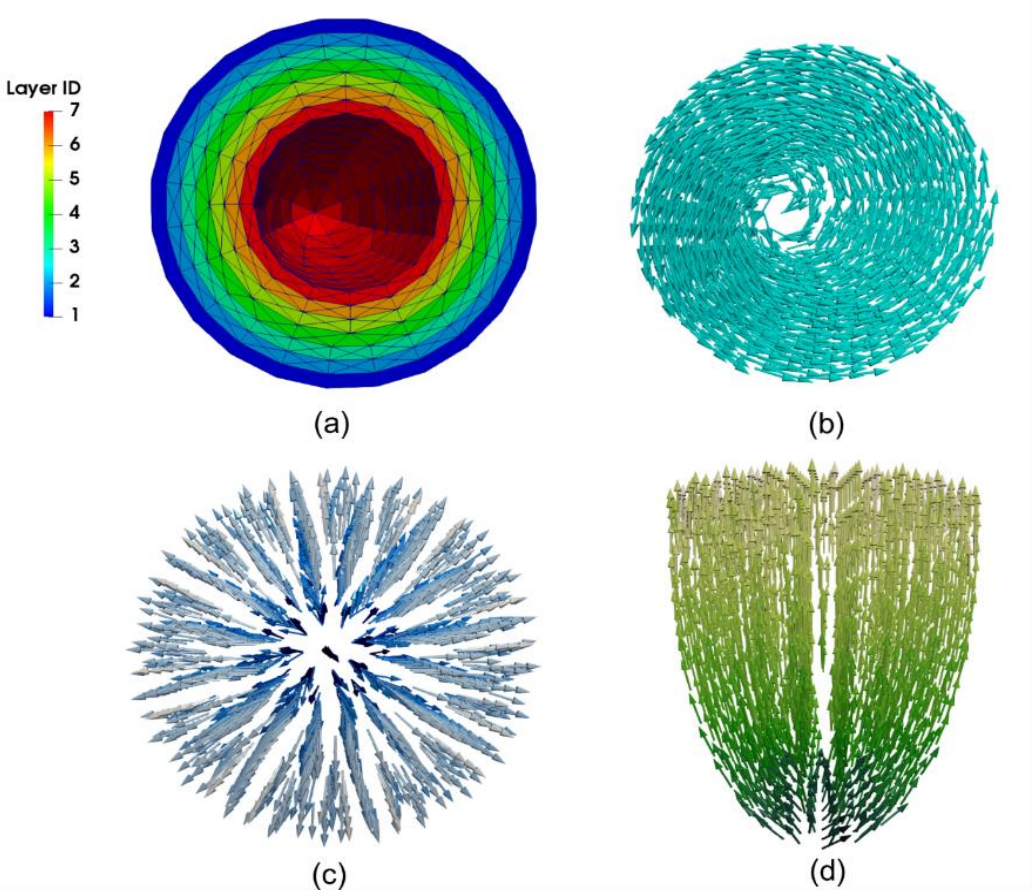

Figure 3.2. (a) Transmural division of mesh into 7 layers with the same wall thickness. (b) Circumferential direction. (c) Radial direction. (d) Longitudinal direction.

3.2.4 Statistical analysis

Categorical variables are expressed as number and percentage, and continuous variables as mean ± standard deviation (SD). Nonlinear regression analysis was performed to correlate model-predicted biaxial stresses with corresponding stress-strain measurements in canine LV midwall myocardium (n = 6).

3.3 Results

3.3.1 Biaxial tests

Table 3.2 lists the best fitted model parameters for 6 specimens with corresponding mean square errors. About eighty iterations were required to obtain the optimized model parameters for each specimen. In general, our microstructural model shows very good fit to the measurements. Except for C_1 , the spreads of all other parameter values are relatively small across the specimens. The large SD of C_1 may be related to the fact that the stiffness modulus and volume fraction for the ground matrix are much smaller than other the myocardial constituents[141]. The average correlation coefficient of the fit between the measurements and model-predicted stresses in the muscle fiber and cross-fiber directions are 0.980 and 0.999, respectively. The maximum root mean square error is 0.152 kPa, which is less than 2% of the range of stress reached in the biaxial tests. We also note that increasing the lower and upper bounds of the mean collagen waviness to $0.22 \leq m_c \leq 0.78$, which corresponds to the collagen tortuosity range of 1.2 – 1.6 as found in the skin [124], led to a larger mean square error and increased both the mean value of m_c and C_4 by about 2 times. A comparison between the measurements and model predictions of the equi-biaxial and constant α test using the best-fit material parameters for a representative specimen is shown in **Figure 3a**. Corresponding stresses in the muscle fiber and cross-fiber directions associated with each constituent in the equibiaxial test of specimen 0118 is shown in **Figure 3b**.

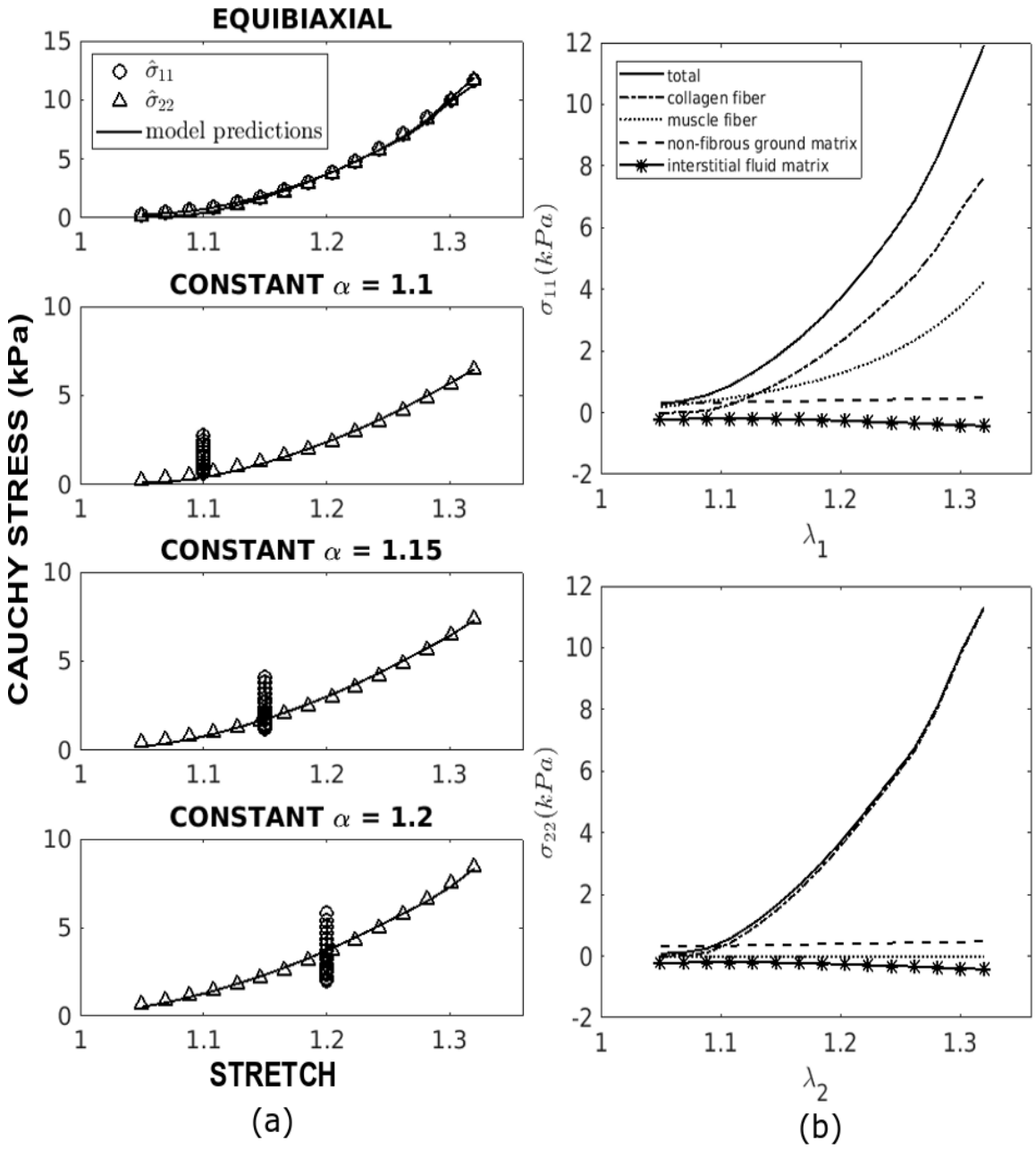

Figure 3.3. (a) Comparison of the fitted and experimental Cauchy stress-stretch data for equibiaxial and constant **α** = 1.1, 1.15 and 1.2 tests of specimen 0118. (b) Contribution of the collagen fiber network, muscle fibers, non-fibrous ground matrix and interstitial fluid matrix to the total stress in the fiber direction (top) and the cross-fiber (bottom) directions in the equi-biaxial test of specimen 0118.

Taking all the specimens into account, we found that the collagen fiber network accounts, on average, for 57% and 99.4% of the total stress in the muscle fiber and cross-fiber

directions, respectively, at a stretch of 1.32. The muscle fiber, on the other hand, accounts on average for about 43% of the total stress in the fiber direction at that stretch value. At stretch lower than 1.1, however, the collagen fiber network contributes very little to the total stress. For the results of all other specimens, refer to the **APPENDIX B**.

Table 3.2. Best-fit model parameters and root mean square errors (RMSE) for biaxial tests of six canine mid-wall LV myocardium

Specimen	C_1 (kPa)	C_2 (kPa)	C_3	C_4 (MPa)	m_c	σ_c	m_ϕ (rad)	RMSE (kPa)
0118	1.255	0.204	10.874	6.624	0.117	0.094	0.930	0.122
0119	0.1	0.261	10.911	3.818	0.117	0.052	0.901	0.152
0124	0.1	0.151	12.870	4.587	0.124	0.057	0.919	0.152
0217	0.438	0.596	6.579	4.287	0.116	0.084	0.915	0.084
0303	1.786	0.717	5.196	3.426	0.140	0.100	0.938	0.055
0330	0.1	0.392	8.451	7.816	0.123	0.075	0.959	0.134
Mean	0.630	0.387	9.147	5.093	0.123	0.077	0.927	0.122
SD	0.722	0.227	2.921	1.736	0.009	0.019	0.020	0.089

Table 3.3 compares the microstructural model parameters that are directly related to the constituents' structure and mechanical behaviors with measurements from experiments conducted on the isolated constituents. Specifically the average fitted values of the collagen fiber elastic modulus C_4, mean collagen fiber straightening strain m_c, and the stiffness and uniaxial stress computed from the material constants of the muscle fiber C_2, C_3 are within the range of reported values [135], [145]–[147]. We computed the uniaxial stress and the resulting stiffness modulus (see **APPENDIX C** for details) at an engineering strain $\epsilon \approx 0.158$, which is associated with the stretch imposed on the muscle fibers in the experiments. Measurements of the mean inclination angle of the collagen

fibers with respect to the muscle fibers m_{ϕ} are not available, however, for comparison with the fitted value of 53.1°.

Table 3.3. Comparison of fitted parameters with measurements of isolated myocytes and collagen fibers.

Description	Fitted model parameters	Reported Values
Cardiac muscle stiffness modulus	13.49 ± 1.92kPa*	Guinea pig:16.4 ± 11.0 kpa [145]; Hamster: 7.48 ± 1.73 kpa [135];
Cardiac muscle uniaxial stress	1.36 ± 0.28 kPa*	Guinea pig: 2.1 ± 1.4 kpa [145]; Hamster: 0.88 ± 0.48 kpa [135];
Collagen fiber stiffness C_4	5.1 ± 1.7MPa	Skin: 0 ~ 50 MPa [146]
Collagen fiber mean tortuosity	1.116**	Canine: 1.01~1.2 [147]

*Cardiac muscle stiffness and uniaxial stress were computed at 2.2 μm sarcomere length. Based on a resting sarcomere length of 1.9 μm, this translates at an engineering strain $\epsilon \approx 0.158$

** The collagen fiber mean tortuosity was computed from the collagen fiber straightening strain m_c by $\sqrt{2m_c + 1}$ where $m_c = 0.12$

Table 3.4 shows the estimated average correlation matrix **R** of the model parameters from all the specimens. Parameters C_2 and C_3 describing the muscle fiber mechanical behavior has the greatest interaction and are inversely related with correlation coefficient ≈ -0.93. Large positive correlation between the collagen elastic modulus C_4 and mean straightening strain m_c is also found (correlation coefficient ≈ 0.75). Interactions between the parameter pairs(C_1, C_2),(C_4, σ_c) and (m_c, σ_c) are moderate; their largest correlation coefficient is 0.55.

Table 3.4. Average correlation matrix of fitted model parameters

	C_1	C_2	C_3	C_4	m_c	σ_c	m_ϕ
C_1	1	-0.52	0.33	0.04	0.49	-0.09	-0.35
C_2		1	-0.93	0.27	-0.04	0.09	0.07
C_3			1	-0.37	-0.03	-0.07	0.23
C_4				1	0.75	0.54	-0.22
m_c					1	0.55	-0.04
σ_c						1	0.07
m_ϕ							1

3.3.2 Finite element simulation of passive filling

Differences of the transmural fiber stress distribution and pressure-volume relationship are found to be < 2% between FE meshes containing 17,600 and 38,985 elements in the mesh sensitivity analysis. (**APPENDIX E**). With 16 processors (Intel® Xeon (R) CPU E5-1660 v3@ 3.00GHz x 16), the computing time for simulating the inflation of an LV model with 17,600 elements is about 13 hours. The FE implementation (that utilizes the domain decomposition method in FEniCS) also exhibits an approximately linear scalability (**APPENDIX E**), which indicates that the computing time can be reduced substantially with more processors. An estimation of the simulation time for solving active mechanics over a cardiac cycle is also provided in **APPENDIX E**.

3.3.2.1 Inflation pressure-volume relations.

Figure 3.4 shows the relationships between the change in LV cavity volume ΔV with respect to the LV pressure using the fitted parameters in **Table 3.2** for all the 6 specimens. Compared to the measurements from the experiments on isolated canine hearts [2], [148], the pressure-volume curves derived from all 6 sets of parameter values fell largely within 1 SD of the mean measurements.

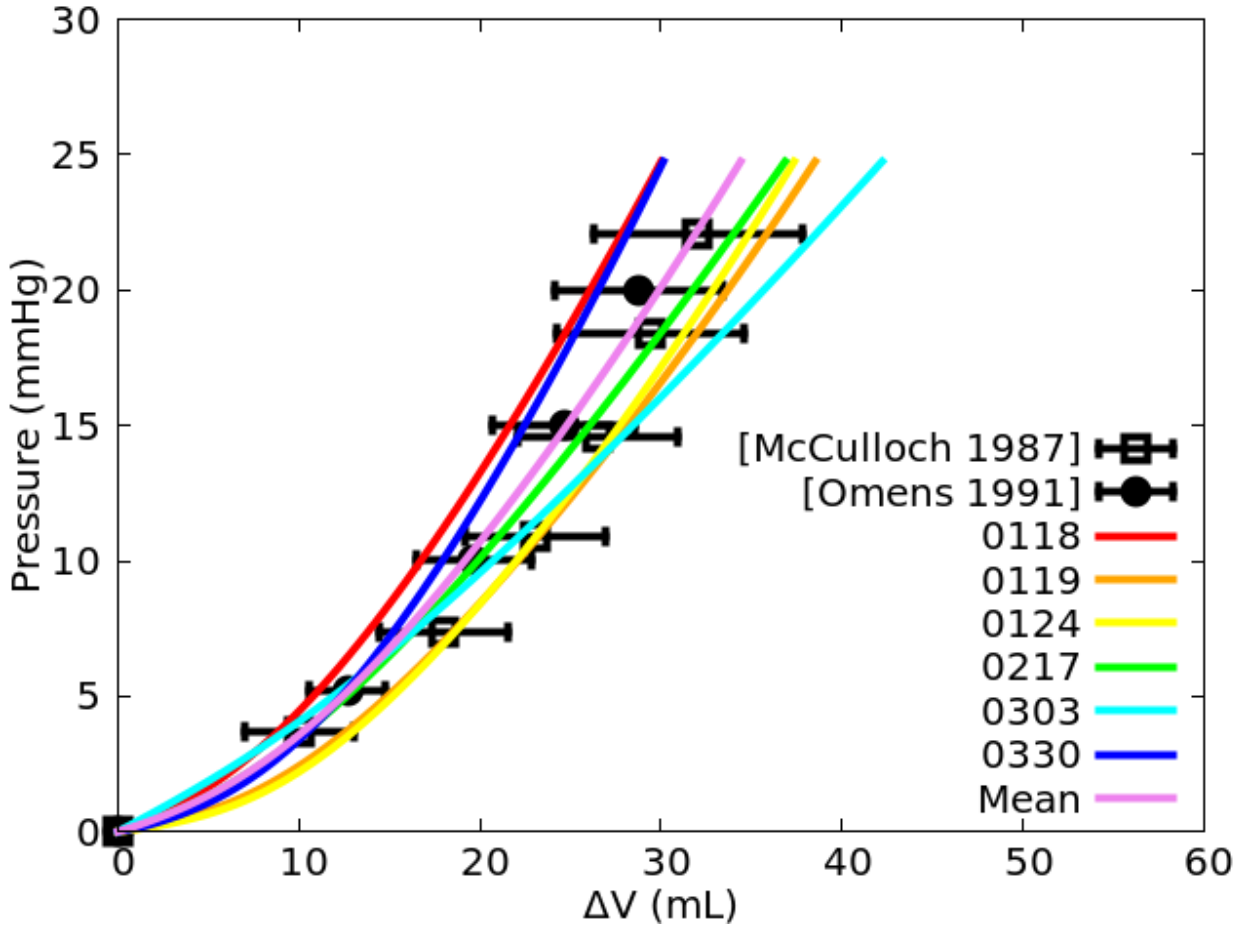

Figure 3.4. Comparison of the inflation pressure-volume curves derived from the 6 sets of fitted model parameter values (Table 3.2) and their mean values with measurements (plotted as mean ± SD).

3.3.2.2 Local ventricular wall strains

Figure 3.5 shows the comparison of transmural distribution of normal strains at a LV pressure of 8 mmHg with measurements [2]. Consistent with the experiments, the model predicted both circumferential strain E_{cc} and longitudinal strain E_{ll} to increase from the epicardium to endocardium, and the radial strain E_{rr} to be negative and decrease from epicardium to endocardium (**Figure 3.5a**). Model prediction of the E_{ll} transmural distribution is closest to the experiments, whereas the predicted transmural distribution of E_{rr} has an offset of ~ 0.08 with respect to the measured mean values. Both muscle fiber strain E_{ff} and cross fiber strain E_{ss} are predicted to increase from the epicardium to the endocardium, and both are largely within 1 SD of the measurements (**Figure 3.5b**). In-plane shear E_{cl} is negative and its magnitude increases from the epicardium to the endocardium. Compared to the normal strains, the magnitude and transmural gradient of shear strains are small (**Figure 3.5c**). We also compared model predictions of the normal and shear strains as a function of the change in LV cavity volume ΔV with measurements at the sub-epicardial, midwall, and sub-endocardial [2] (**APPENDIX D**). Overall, model predictions of the relationship between strains and ΔV are comparable to the measurements. Of all the normal strains, the relationship between E_{ll} and ΔV is closest to the measurements at all 3 transmural locations, whereas E_{cc} at ΔV = 20 ml in the sub-endocardial region has the largest discrepancy with the measurements (measured: 0.126; model: 0.257). The predicted relationship between the shear strains and ΔV are largely within the 1 SD of the measurements.

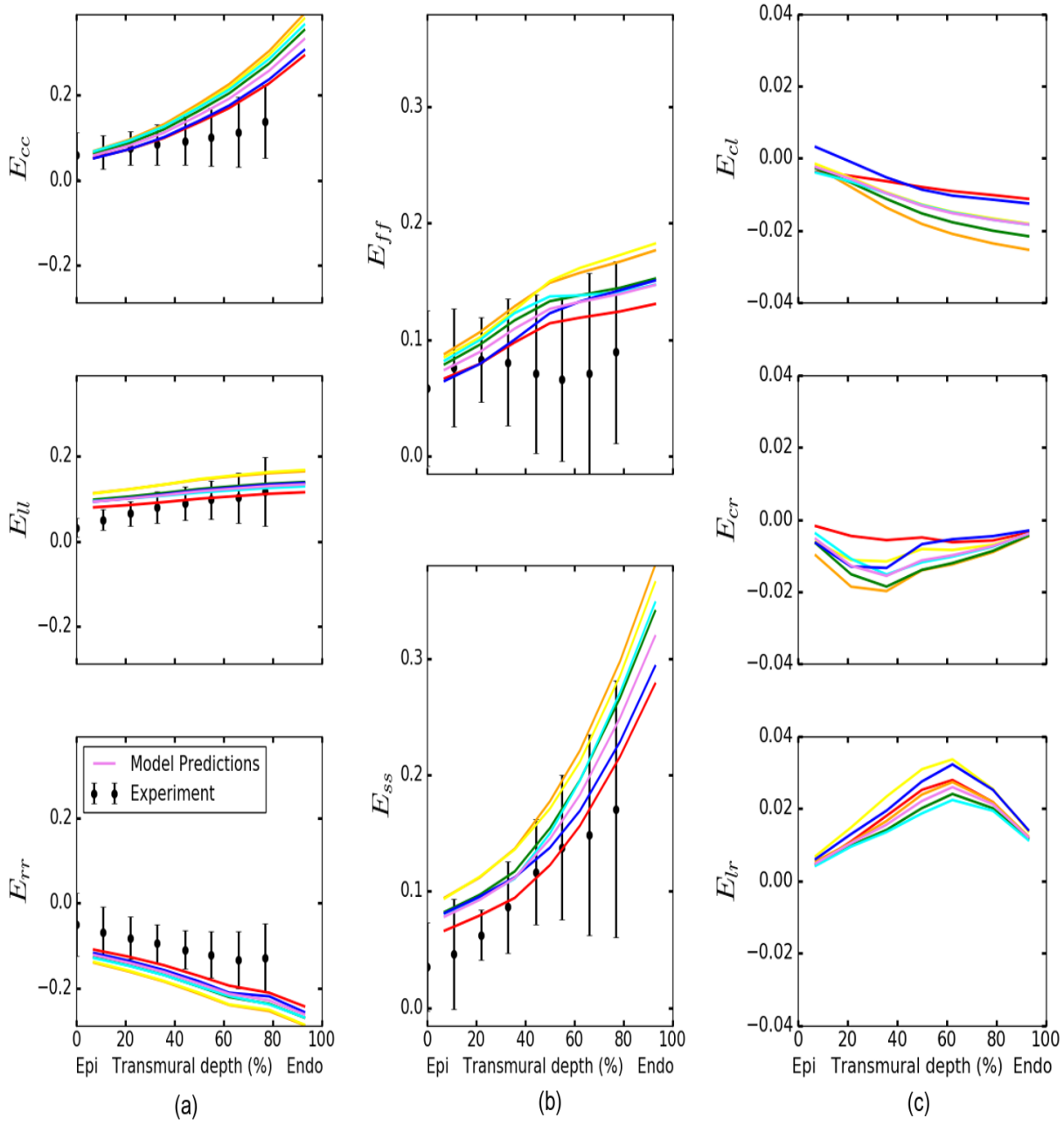

Figure 3.5. Transmural distributions of the strain components at a LV pressure of 8 mmHg. Colored solid lines: model predictions using best-fit and mean parameters in Table 2. Measurements of strains at LV pressure of 8 ± 4 mmHg [2] are plotted as means ± SD. Note: shear strain results from experimental data are not shown as the measured values are small and difficult to digitize.

3.3.2.3 Local ventricular wall stresses

Figure 3.6 shows the transmural distribution of stresses corresponding to a LV pressure of 8 mmHg. The results show that both circumferential stress σ_{cc} and longitudinal stress σ_{ll} increase from the epicardium to the endocardium (**Figure 3.6a**).

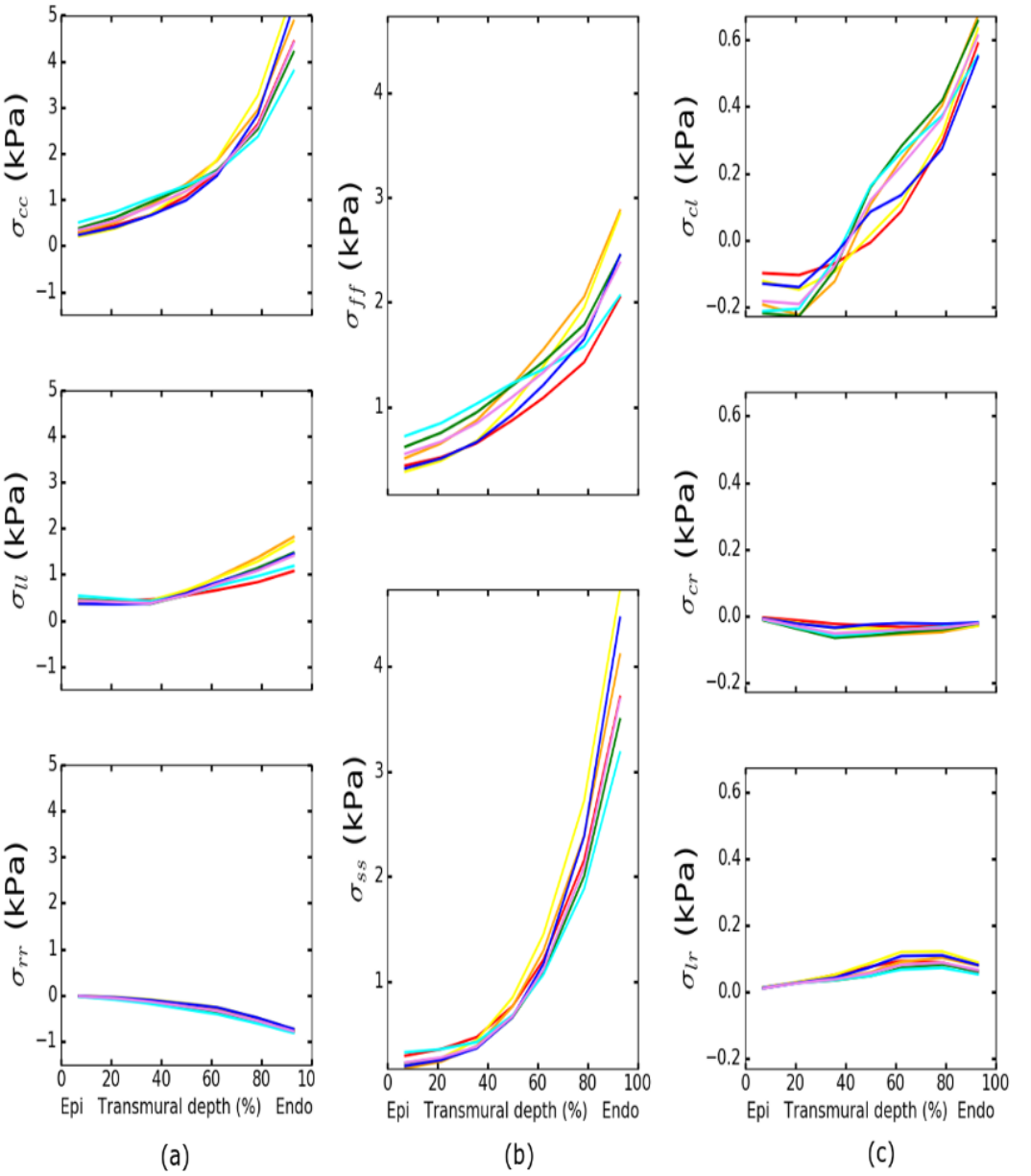

Figure 3.6. Transmural distributions of the stresses at a ventricular pressure of 8 mmHg. Colored solid lines: model predictions using best-fit and mean parameters in Table 3.2.

The magnitude of σ_{cc} is larger than σ_{ll} at all transmural depth. Radial stress is negative and increases in magnitude towards the endocardium. Both fiber stress σ_{ff} and cross-fiber stress σ_{ss} increase from the epicardium to the endocardium (**Figure 3.6b**). Magnitude of the shear stress components are small compared to the normal stresses. In-plane shear stress σ_{cl} has a larger transmural gradient than the other transverse shear stress (**Figure 3.6c**).

3.3.2.4 Contribution of the tissue constituents to the wall stress

Figure 3.7 shows the transmural variation of the contribution of each tissue constituent to the total normal stress in the mean muscle fiber direction σ_{ff} at an LV pressure of 8 mmHg as predicted by the model using the mean value of the fitted parameters in **Table 3.2**. The contribution of the interstitial fluid matrix to σ_{ff} is simply $-p$ based on Eq. (15). The results show that the contribution of muscle fiber is substantial at all transmural locations, accounting between 40 – 70% of the total stress. The contribution of collagen fibers to the total stress increases from 22% at the epicardium to 96% at the endocardium. Interestingly, the results also show that at 60% transmural depth, where $E_{ff} \approx 0.13$ or fiber stretch ≈ 1.12, the contribution of collagen fibers starts to exceed that of the muscle fibers; i.e., the collagen fibers become the dominant load-bearing constituent at a transmural depth > 60%. We also note that the contribution to σ_{ff} by each constituent remains largely unchanged using model parameters fitted from the biaxial test data with larger lower and upper bounds of the mean collagen waviness at $0.22 \leq m_c \leq 0.78$.

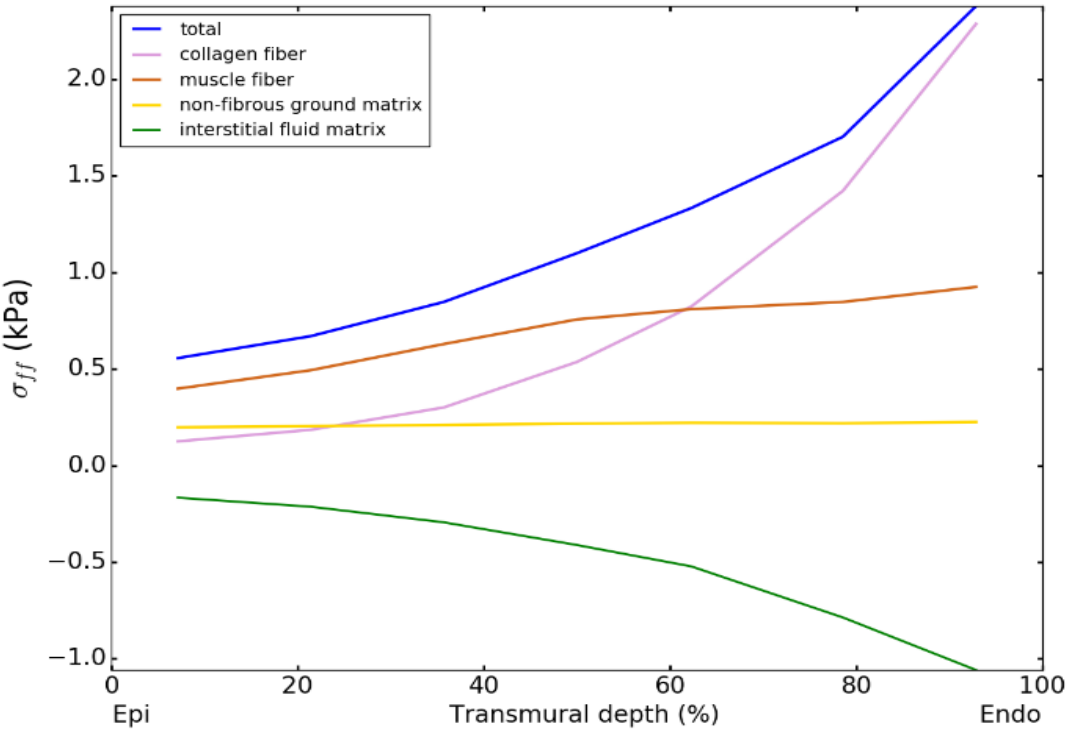

Figure 3.7. Transmural variation of the contribution of the collagen fiber network, muscle fibers, non-fibrous ground matrix and interstitial fluid matrix to the total normal stress in the local muscle fiber direction at an LV pressure of 8 mmHg using the mean fitted parameter values from Table 3.2.

3.3.2.5 Collagen fiber tortuosity

Figure 3.8 shows the comparison of the model predictions of the relationship between collagen fiber tortuosity and LV pressure with the measurements. Our model predicts that the collagen fiber tortuosity decreases from 1.123 ± 0.009 to 1.066 ± 0.01 when LV pressure is increased from 0 to 25 mmHg. The model predictions are mostly within the measured ranges when the LV pressure is less than 10 mmHg. Discrepancy between model prediction and measurement is generally larger at higher pressure.

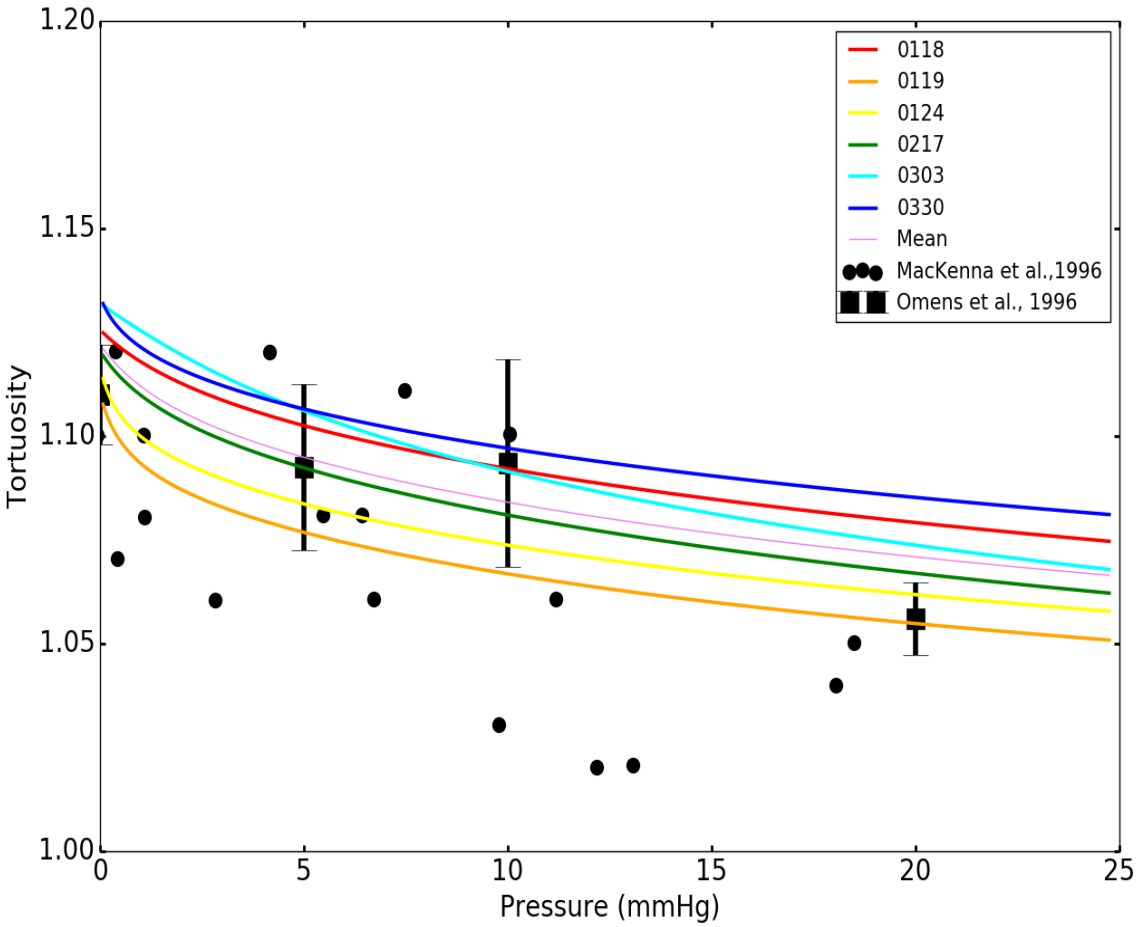

Figure 3.8. Collagen fiber tortuosity as a function of LV pressure. Colored solid lines: model predictions using the best-fit and mean parameters in Table 2. Black scattered dots: measurements of the perimysial collagen fiber tortuosity in rat hearts [149]. Black square marker with error bars (mean $\pm$ SD): measurements of collagen tortuosity in normal rat LV [150].

3.3.2.6 Parameter sensitivity analysis

Sensitivity analysis of the model's parameters revealed that the passive filling pressure-volume curve is very sensitive to the collagen volume fraction ϕ_c, collagen waviness m_c, collagen stiffness modulus C_4, collagen azimuthal angle m_ϕ and muscle fiber stiffness C_2 (Figure 3.9). The LV becomes less compliant as ϕ_c, C_4, C_2 are increased or as the collagen fiber waviness m_c is decreased. On the other hand, the relationship between the LV chamber stiffness and mean collagen azimuthal angle m_ϕ is non-monotonic for

the range $0° \leq m_\phi \leq 90°$. The effects on the pressure-volume curve are less for the other parameters.

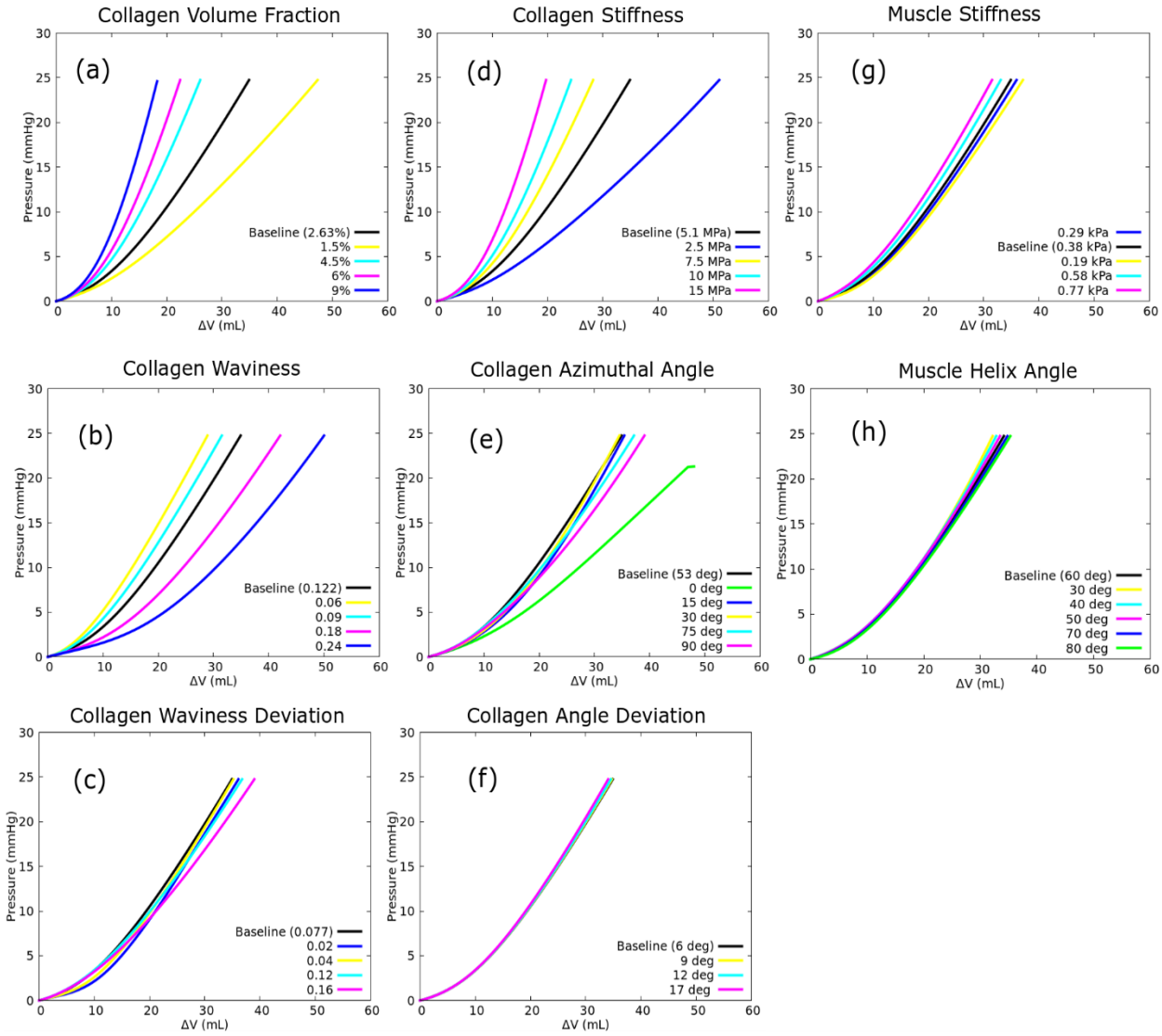

Figure 3.9. Sensitivity of (a) collagen volume fraction ϕ_c, (b) collagen waviness m_c, (c) collagen waviness deviation σ_c, (d) collagen stiffness modulus C_4, (e) collagen azimuthal angle m_ϕ, (f) collagen azimuthal angle deviation σ_ϕ, (g) muscle stiffness C_2 and (h) muscle fiber helix angle to the pressure-volume curve.

Table 3.5 shows the percentage of absolute change in ΔV at LV pressures of 20 and 30 mmHg when each model parameter is changed 100% with respect to the corresponding mean value (baseline). Our results show that the collagen ultrastructure (i.e., waviness and azimuthal angle) has a substantial impact on the ΔV. Collagen volume fraction and the stiffness of individual collagen fiber roughly have the same effects on ΔV. On the other hand, the muscle fiber stiffness and orientation have lesser influence on ΔV compared to the collagen network. The sensitivities of ΔV to the model parameters are relatively the same at both pressures.

Table 3.5. Percentage of absolute change in ΔV at a LV pressure of 20 and 30 mmHg with 100% change in each model parameter about its mean fitted value.

Model parameters	Percentage of absolute change in ΔV at 20 mmHg	Percentage of absolute change in ΔV at 30 mmHg
Collagen Azimuthal Angle	48.3	44.7
Collagen Waviness	46.7	39.9
Collagen Volume Fraction	29.5	31.5
Collagen Stiffness	29.6	31.6
Collagen Waviness Deviation	11.1	11.6
Muscle Stiffness	9.83	6.5
Muscle Helix Angle	4.4	7.5
Collagen Angle Deviation	0.84	1.1

*Sensitivity analysis of the muscle fiber helix angle was evaluated for a change between a symmetric transmural variation of helix angle of (30°/-30°) (baseline) to (60°/-60°).

3.4 Discussion

We have developed and validated a microstructure-based constitutive model of the passive myocardium in a three-dimensional FE modeling framework, and have shown that the LV filling function is sensitive to the collagen ultrastructure and the load taken up by the tissue constituents varies depending on the LV transmural location. To the best of our knowledge, this is the first FE implementation of a microstructural constitutive model to simulate passive filling of a LV in a representative 3D geometry with experimentally measured transmural muscle fiber orientation. Calibrated against the tissue-level biaxial test data derived from the mid-wall of the canine myocardium [139], we show that the fitted parameter values are consistent with microscale measurements made on individual cardiac tissue constituents and the FE model predictions using these values are largely in agreement with independent measurements from experiments on the intact canine LV. This study, therefore, provides a rigorous comparison of the microstructural constitutive model predictions with measurements made across multiple scales; i.e., at the constituent, tissue and organ levels.

At the constituent's level, the calibrated myocyte stiffness modulus and tension at a sarcomere length of 2.2 μm are comparable to the reported values of other species such guinea pig [145] and hamster [135] since we are not able to find any passive mechanical tests conducted on canine myocytes. For the collagen fiber network, the calibrated mean elastic modulus of a straightened collagen fiber C_4 is ~ 5 MPa, which is within the reported values of 0 – 50 MPa for collagen fibers in the skin tissue [146] and comparable to the mean fitted value of 3.76 MPa in the rat right ventricle [142]. Direct measurements of the collagen fiber elastic modulus are, to the best of our knowledge, not

available. In terms of the collagen fiber network microstructural features, the model's calibrated mean collagen fiber tortuosity of 1.116 is well within the histological measurements of 1.01 −1.2 [147]. While the calibrated mean inclination angle of 0.927 rad or 53.1° cannot be quantitatively compared with measurements, histological studies have reported qualitatively that the collagen fibers are inclined relative to the muscle fibers [131].

At the tissue level, the constitutive model is able to fit the measurements derived from all the biaxial testing protocols very well for each canine specimen (fiber direction: R=0.98; cross-fiber direction: R=0.999). An assessment of the relative contribution by each constituent to the total stress reveals that the collagen fiber network bears most of the load in the cardiac tissue, accounting for about 57% of the total load when cardiac tissue is stretched beyond 1.3. The cardiac muscle fibers, on the other hand, still accounts for a significant portion (~ 43%) of the total load. This finding is consistent with a recent study which shows that the mechanical contribution of muscle fibers is significant at all physiological ranges of stretch [142].

At the organ level, the FE implementation of the microstructural constitutive model in a representative 3D LV geometry enables comparison with measurements of the pressure-volume curves, strains and collagen tortuosity during inflation. The pressure vs. volume change curves predicted using the fitted model's parameters all fell within 1 SD of the measurements in canine hearts [2], [148]. Prediction of the relationship between collagen fiber tortuosity and LV pressure is also comparable with the measurements [149], [150], showing that the collagen fibers are not all fully stretched over the range of diastolic filling pressures (0 – 25 mmHg). Moreover, model predictions of the strains as a function

of LV cavity volume change and their transmural distribution across the LV wall are also largely in agreement with the measurements [2].

The generally good agreement between model predictions of tissue-level strain, collagen fiber tortuosity and pressure-volume relationship of the LV with measurements using the fitted parameters from biaxial mechanical data provide confidence of the model's ability to predict multiscale features associated with LV filling. More significantly, the consistency of the fitted parameters with microscale mechanical and structural measurements of isolated tissue constituents substantiate, to some level, the validity of the model prediction of the contribution of each constituent to the total stress during LV inflation. Specifically, the model predicts that the contribution of muscle fibers to the total stress is significant at low strain, but its contribution diminishes at higher strain. Conversely, the contribution of collagen fiber network to the total stress is small at low strain but its contribution increases due to the gradual recruitment of wavy collagen fibers at higher strain. As a result, the collagen fiber becomes the dominant load-bearing constituent at high strain, accounting for more than half of the normal stress in the local muscle fiber direction at a stretch of 1.32. This result supports the suggestion made in a previous study [151] that myocytes, where titin is the primary contributor to its passive stress response, may be the major component of the myocardial stiffness at low LV pressure.

Interestingly, this result is also reflected in the transmural variation of the constituent's contribution to the total fiber stress (**Fig. 3.7**). At a LV pressure of 8 mmHg, the simulations show that the cardiac muscle fiber accounts for most of the load in the local muscle fiber direction between the transmural depth of 0% (epicardium) – 60% of

the ventricular wall. The collagen fiber, on the other hand, is the dominant load-bearing constituent between the transmural depth of 60%-100% (endocardium) (i.e., the sub-endocardial region). This finding has implications on pharmaceutical therapies under investigation for treating HFpEF that targets specific tissue individual constituent; e.g., attenuating myocardial fibrosis [152] and reducing myocyte titin stiffness [153]. In particular, our finding suggests that reducing LV passive stiffness by altering the collagen fiber network may be most effective when applied to the sub-endocardial region. Conversely, altering the myocyte stiffness to reduce LV passive stiffness may be most effective when applied to the sub-epicardial region. Although we have demonstrated that the microstructural model can be applied to predict load sharing of the constituents that cannot be experimentally measured, caution must be exercised in directly applying these results for optimizing treatments as they were obtained based on **1)** normal LV geometry, **2)** assumptions that the LV has homogeneous material properties and collagen fiber waviness and **3)** omission of residual stresses. The model needs to be calibrated using more data, especially those from humans that consider gender-differences in the LV passive behavior [154], before predictions can be reliably applied in the clinics.

Through a parameter sensitivity study, we show that the LV passive stiffness is not only sensitive to the stiffness of the individual tissue constituents (particularly, muscle and collagen fiber), but it is also sensitive to the collagen fiber network ultrastructure; i.e., the mean waviness m_c, the mean azimuthal angle m_ϕ with respect to the muscle fibers. These findings underscore the importance of quantifying changes in the collagen fiber network ultrastructure during remodeling, particularly in diseases where fibrosis is a key feature such as HFpEF [155].

3.5 Limitations

The microstructural FE LV model is not without limitations. First, we adopt a linear transmural variation of the muscle fiber helix angle without any planar splay. This framework can be extended to include physiological distributions of muscle fiber splay in future. Second, the assumptions of homogeneous 1) axisymmetrical distribution of collagen fibers around local muscle fiber direction, 2) bimodal normal distribution to describe the collagen fiber spatial orientation and 3) truncated normal distribution to describe the collagen fiber waviness need to be validated against microscopy measurements of the myocardium, which to the best of our knowledge, is not available. Third, due to the lack of histological or microscopy measurements of the myocardial tissue ultrastructure, we had to fit most of the model's parameters using the biaxial test data, including morphometric parameters that should, in principle, be prescribed using values directly measured in experiments. This is not ideal as some of the parameters are highly correlated to each other (**Table 3.4**). Nevertheless, we have attempted to minimize this issue by imposing physiological bounds on the model's parameters in the fitting process and validating our fitted model parameters against independent measurements of the constituents and organ-scale LV inflation experiments. Fourth, we have, for simplicity, ignored the presence of residual strains and stresses in simulating passive filling of the intact LV that may produce a more uniform transmural distribution of stress [14]. The presence of residual stresses and residual strains in the LV may also be responsible for the transmural differences of collagen waviness as observed in some histological studies [149]. Finally, the microstructural model formulation ignores any direct mechanical or

physical interactions between the myocytes and collagen fibers, which a recent study suggests to be present in the LV [156].

In conclusion, we have developed a microstructural constitutive model in an efficient FE framework, and used it to investigate the contribution of individual tissue constituent to LV mechanics during passive inflation. This framework can be readily extended to increase the model's realism, such as by incorporating a more realistic biventricular geometry and an active contraction constitutive model of the myocyte to simulate active mechanics in the LV as well as by calibrating the model using human data.

CHAPTER 4

QUANTIFICATION OF THREE-DIMENSIONAL BIVENTRICULAR STRAINS IN PULMONARY ARTERIAL HYPERTENSION USING HYPERELASTIC WARPING

Abstract

Pulmonary arterial hypertension (PAH) is a life-threatening disease characterized by elevated pulmonary artery pressure (PAP) and pulmonary artery vascular resistance, with limited survival rate and can affect patients of all ages. Advanced imaging of multiple strain components may aid in the diagnosis and understanding of this disease. In this study, we use a model-to-image registration technique for rapid comprehensive assessment of biventricular circumferential, longitudinal and radial strains. 20 PAH patients and 20 age- and gender-comparable Controls underwent cardiac magnetic resonance (CMR) imaging. A three-dimensional (3D) heart model including the left ventricle (LV), right ventricle (RV) and septum was reconstructed from these CMR images. The hyperelastic warping method was used to reference the segmented model with the target images and biventricular circumferential, longitudinal and radial strains were obtained. Results show that RV longitudinal, circumferential and radial strain were significantly depressed compared with Controls (-11.00±3.65% vs. -14.79±2.18%, $p<0.001$; -7.56±2.83% vs. -9.47±1.88%, $p<0.05$; 18.48±9.56% vs. 24.81±7.02%, $p<0.05$); Septum circumferential and radial strain were significantly depressed compared with Controls (-4.35±1.77 vs. -5.89±1.74, $p<0.05$; -10.10±5.00 vs. 13.87±4.73, $p<0.05$); LV circumferential strain was depressed significantly compared with Control (-11.60±2.52 vs. -14.44±1.97, $p<0.001$). Our results show that not only RV, but also septum and LV impairment may exist in PAH patients although other CMR parameters in the LV show normal values. Our methodology holds the potential for characterizing 3D strains in PAH patients that may facilitate developing in-depth understanding of the interventricular influence in this disease.

4.1 Introduction

Pulmonary arterial hypertension (PAH) is a progressive disorder characterized by elevated pulmonary artery pressure (PAP) and pulmonary artery vascular resistance, which increase right ventricular (RV) afterload and lead to RV dysfunction and ultimately right-sided heart failure [157]–[159]. PAP measurement by right heart catheterization (RHC) is the current golden standard for PAH, but it is invasive [160]. Echocardiography is the modality of choice in evaluating PAH because of its availability and low cost, and three-dimensional echocardiography (3DE) is one technique that can be used to quantify RV volumes, image reconstructions and strains. 3DE overcomes the limitations of two-dimensional techniques, potentially allowing volume assessment without the use of any geometrical assumptions. However, the endocardial definition assessed by 3DE is sometime difficult to discern in the RV, owing to the abundance of aberrant papillary muscles. This poor lateral resolution in RV can result in underestimated RV cavity volumes using 3DE [161].

CMR has recently been considered as a potential one-stop-shop imaging modality in PH [162]–[164]. It is the gold standard for measuring ejection fraction, cavity volume and mass to non-invasively quantify global heart function [165]–[167]. It also provides superior resolution and reproducible results for quantifying ventricular curvedness, deformation, systolic and diastolic function in diverse heart diseases [168]–[170] as well as for quantifying *in vivo* myocardial properties through inverse finite element (FE) modeling [171], [172]. The most commonly used features in cine MRI are the endocardial and epicardial contours, or specific feature points on these contours. Due to its high resolution, motion tracking can be performed over the cardiac cycle. Most motion-tracking

methods aim to extract strains in the heart, as myocardial strain encapsulates the basic mechanical function of the myocardium and has the potential to become an important clinical index of regional ventricular function. Regional myocardial strains have direct and indirect relationships with cardiac diseases [173]. Normal strains are widely used in radial, circumferential and longitudinal directions, with circumferential strain the type reported most frequently [174]. Longitudinal strain is the main strain component in assessment of RV function. It has been found to be significantly associated with hemodynamic parameters of RV function [160], [175]–[177]. In addition, recent studies have shown that RV longitudinal strain may be a useful prognostic maker in patients with pulmonary hypertension [178], [179].

The hyperelastic warping approach is a deformable image registration technique used to obtain strain measurements from medical images such as magnetic resonance imaging (MRI) and computed tomography (CT). Veress *et al.*[39] proposed hyperelastic warping to determine left ventricular strain from mid-diastole to end diastole using multiple short-axis (SA) cone slices from MR images. In the hyperelastic warping method, a FE model of the region of interest is deformed by a body force that depends on the difference of image intensities between the template image and the target image. Hyperelastic strain energy based on continuum mechanics is applied to constrain and regularize the deformation [180], [181]. Other regularizers have also been proposed, such as incompressibility [182], or equilibrium gap [183], [184]. Application of the hyperelastic warping approach in cardiac motion and function has focused primarily on quantifying LV strains [38], [185] that has been verified by tagged MRI [186] and 3D CSPAMM MR

images [181]. This method has also been applied to quantify circumferential strain in individual patient with HFpEF [187] and pulmonary hypertension [188].

In this research, we aimed to quantify the 3D circumferential, longitudinal and radial strains in PH patients and normal controls using the hyperelastic warping method. The goals of the presented study were to introduce a novel framework to characterize 3D circumferential, longitudinal and radial strains simultaneously and to investigate the abnormalities in RV, LV and septum strains and interventricular interactions of PAH patients.

4.2 Materials and methods

4.2.1 Study population

Twenty paired sub-groups of subjects were enrolled and underwent CMR scans. For each sub-group, one Control, one PH patient were recruited. They were age-comparable and gender-matched. Normal controls had no known cardiovascular disease or other co-morbidities. Patients with a clinical history of PH were recruited as PH patients. All enrolled participants gave written informed consent. The demographics of the study groups are summarized in **Table 4.1**. The protocol was approved by the Local Institutional Review Board, and informed consents were obtained from all subjects.

Table 4.1. Baseline demographic and CMR characteristics of PAH patients and Controls. The control group did not undergo right heart catheterization

Variables	Control(n = 20)	PAH (n = 20)	P value [§]
Demographics			
Age, years old	48 ± 15	47 ± 15	0.824
Gender, Male/Female	5/15	5/15	N/A
Weight, kg	60 ± 14	58 ± 12	0.590
Height, cm	159 ± 10	160 ± 11	0.895
Cardiac magnetic resonance			
LV ejection fraction, %	65 ± 6	61 ± 9	0.177
LVEDV index, ml/m^2	71 ± 8	71 ± 24	0.991
LVESV index, ml/m^2	25 ± 6	28 ± 14	0.361
LVSV index, ml/m^2	45 ± 6	42 ± 12	0.334
LV mass index, g/m^2	39 ± 9	45 ± 14	0.180
RV ejection fraction, %	59 ± 6	43 ± 12	**<0.001**
RVEDV index, ml/m^2	75 ± 12	114 ± 44	**<0.001**
RVESV index, ml/m^2	31 ± 8	66 ± 31	**<0.001**
RVSV index, ml/m^2	44 ± 7	48 ± 21	0.498
Hemodynamics			
Heart rate, bpm	71 ± 13	83 ± 15	**0.012**
Diastolic blood pressure, mmHg	78 ± 13	77 ± 15	0.819
Systolic blood pressure, mmHg	131 ± 25	128 ± 23	0.615
Cardiac output, L/min	N/A	4.4 ± 2.2	N/A
Cardiac index, L/min/m2	N/A	2.7 ± 1.1	N/A
Right atrial pressure, mmHg	N/A	8.3 ± 7.5	N/A
Mean pulmonary artery pressure, mmHg	N/A	45.8 ± 15.2	N/A
Pulmonary capillary wedge pressure, mmHg	N/A	12.8 ± 6.5	N/A
Systemic vascular resistance, dynes/cm5	N/A	1774.9 ± 619.2	N/A
Pulmonary vascular resistance, dynes/cm5	N/A	745.9 ± 520.3	N/A
Pulmonary systemic flow ratio	N/A	1.24 ± 0.4	N/A
Pulmonary and systemic resistance ratio	N/A	0.4 ± 0.2	N/A

Data are mean ± SD. EDV: end-diastolic volume; ESV: end-systolic volume; SV: stroke volume;
[§] Independent Sample t Test.

4.2.2 CMR image acquisition

Cardiac MR scans were performed using steady-state free precession (SSFP) cine gradient echo sequences. All subjects were imaged in a 3.0T Philips scanner (Philips-Adrglam; Philips Healthcare, Netherlands) with a 12-element body matrix coil. SSFP end-expiratory breath-hold cine images were acquired in multi-planar short- and long-axis views. Typical imaging parameters were as follows: TR/TE 34/1 ms, flip angle 45^{o}, slice thickness 8 mm for both short and long-axis, echo time 1.404 ms, repetition time 2.808 ms, pixel bandwidth 1796 Hz, percent phase field of view 100 mm, temporal resolution ~35 ms, in-plane spatial resolution 1.6 × 1.6 - 1.8 × 1.8 mm, 40 frame /cardiac cycle for normal control and 30 for other enrolled subjects. Both short-axis images and long-axis images were acquired, showed in **Figure 4.1**.

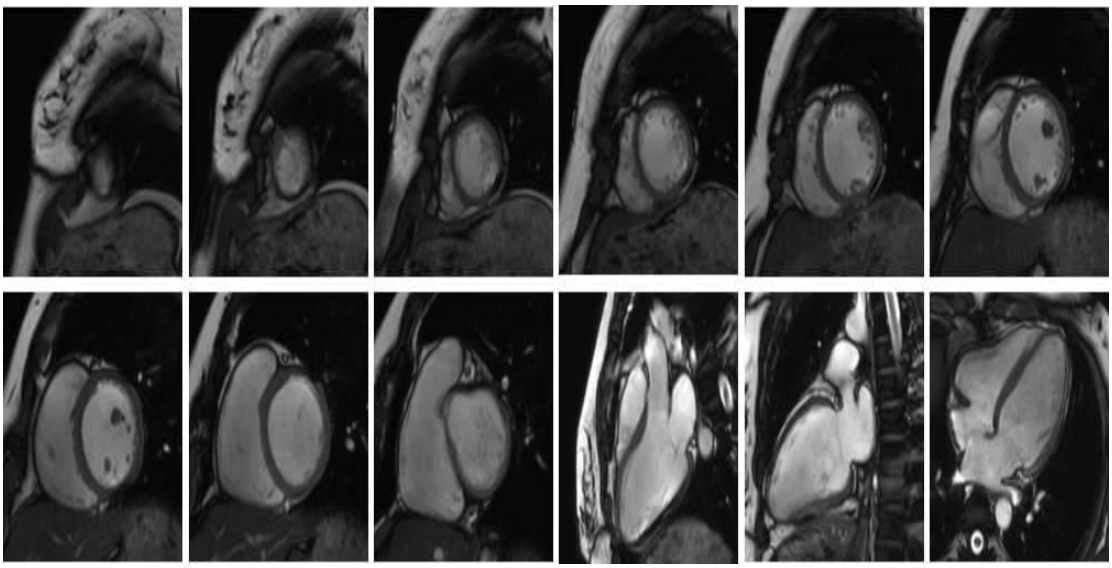

Figure 4.1. CMR images including short-axis image from apex to basal, and 2-chamber, 3 chamber and 4-chamber long-axis images.

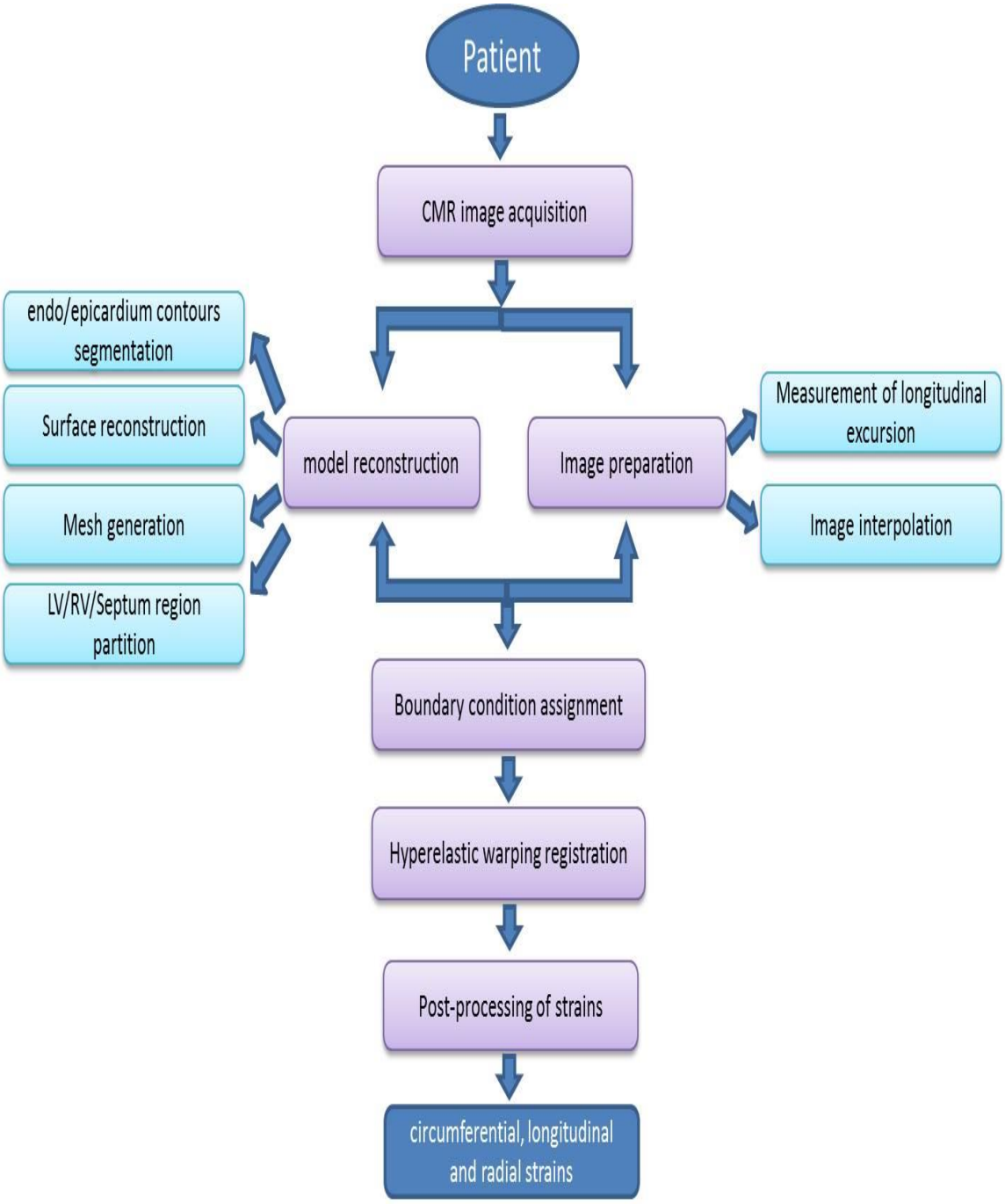

Figure 4.2. Overall framework of quantifying the biventricular circumferential, longitudinal and radial strains.

4.2.3 Right heart catheterization

Right heart catheterization (RHC) was performed at rest using standard techniques. PH was defined as having a mean pulmonary artery pressure (mPAP) of ≥25 mmHg. Invasive hemodynamic measurements were not available in the control group.

4.2.4 Overall framework of hyperelastic warping registration

The core of the method was based on the hyperelastic warping technique to register a meshed biventricular model reconstructed from the CMR images at end of systole (ES), along with the CMR images at other time point during a cardiac cycle, so as to track the motion of heart and obtain the strain-time curves. The short axis images were used as the target images. As there is an excursion in long-axis direction of the ventricle, we measured the displacement of septal manually, and assigned this displacement as a boundary condition in long-axis direction. The whole framework was illustrated in **Figure 4.2**, and it was implemented using a combination of open-source software: MeVisLab (MeVis Medical Solution AG, Bremen, Germany), Gmsh [189], FEniCS [129] and in-house code [181].

4.2.4.1 Model reconstruction

Figure 4.3 shows the reconstruction of the model. Contours of the LV, RV and Epicardium were manually segmented in both short-axis and long-axis images, as shown in **Figure 4.3 (A)**. The full image stack was evaluated and the frame with aortic valve closure had been identified as end-systole for all the short axis locations [190]. Papillary muscles were included as part of LV volume. Depending on the size of heart and quality of image, 4~9 short-axis images and 4-chamber long-axis images were used for each of the 40 subjects. These contours were then used to reconstruct the LV endo surface, RV

endo surface and epicardium surface, as shown in **Figure 4.3 (B)**. Using a plane to cut off the cover of the model, we obtained the biventricular mode **Figure 4.3 (C)**. Gmsh was used for generation of the meshes for each model, with a mesh size of 0.3, as shown in **Figure 4.3 (D)**. The points of these 40 models ranged from 2313~3298, and the finite elements ranges from 7527~11485. Each model was partitioned into three regions: LV, RV and Septum, as shown in **Figure 4.3 (E)**.

4.2.4.2 Image preparation and boundary condition assignment

Short–axis images were interpolated to double the number of short-axis slices for better registration, as the full short-axis image stack was sparse compared with the model. This step was implemented using a Lanczos filter in MeVisLab. Meanwhile, excursion of the ventricles in the long-axis direction was measured, as shown in **Figure 4.4**. A sinusoidal function of this displacement was imposed as a constraint in the biventricular model in the hyperelastic warping method.

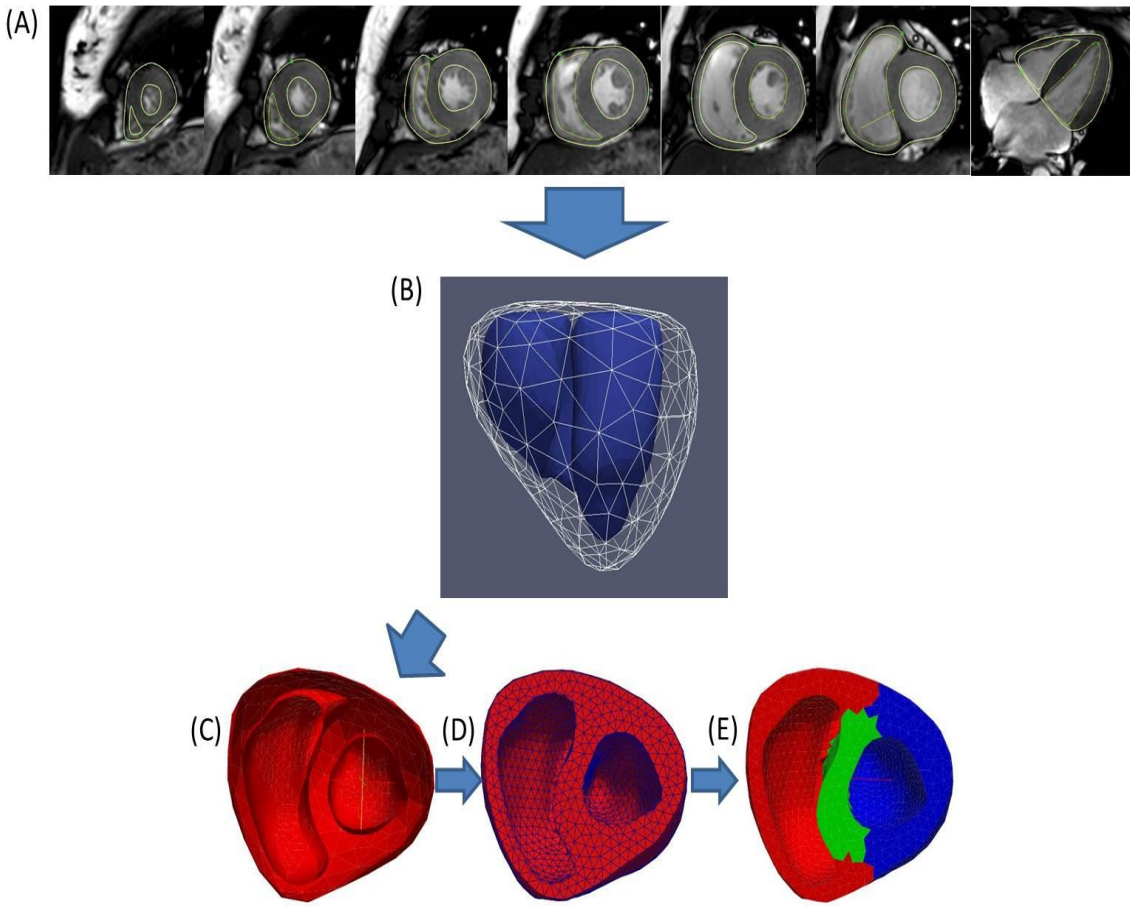

Figure 4.3. Reconstruction of biventricular mesh: (A) segmentation of contours of LV, RV and septum; (B) Surface reconstruction; (C) Bi-ventricular geometry (D) Biventricular mesh; (E) Partition of region (Red: RV free wall; Green: Septum; Blue: LV free wall).

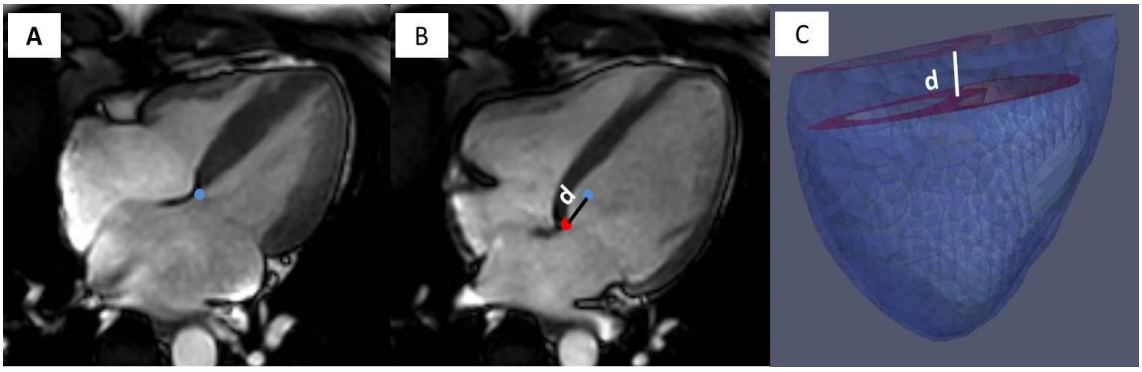

Figure 4.4. Measurement of the septal displacement in 4-chamber view as the boundary condition: (A) End of systole; (B) End of diastole; (C) Apply the displacement of septal on the model.

4.2.4.3 Hyperelastic warping registration

Hyperelastic warping is a deformable image registration technique that can be used to measure cardiac strain derived from analysis of medical images such as MRI, ultrasound and microPET imaging [38]. In hyperelastic warping, the meshed heart model is deformed to a target image (T) set during the registration process. Deformation of model is defined as $\boldsymbol{\varphi}(\boldsymbol{X}) = \boldsymbol{X} + \boldsymbol{u}(\boldsymbol{X})$, where *u* is the displacement field, $\boldsymbol{X}$ is the position, and the deformation gradient is defined as

$$\boldsymbol{F}(\boldsymbol{X}) = \frac{\partial \boldsymbol{\varphi}}{\partial \boldsymbol{X}} \tag{4.1}$$

The forces responsible for registration deformation are derived from the difference in image intensity of two volumetric image data sets by minimizing the energy expression

$$E(\varphi) = \int W(\boldsymbol{X}, \boldsymbol{C}) \frac{dv}{J} - \int U\big(R(\boldsymbol{X}) - T(\boldsymbol{\varphi})\big) \frac{dv}{J} \tag{4.2}$$

Here, *W* is the hyperelastic strain energy related to the material model of myocardium and $\boldsymbol{C} = \boldsymbol{F}^T \boldsymbol{F}$ is the Cauchy-Green deformation tensor. A Neo-Hookean strain energy function is used to define *W.* The other energy term U produces an image force field responsible for the local registration of the discretized reference image *R* to the target image *T*, and is given as

$$U(\boldsymbol{X}, \boldsymbol{\varphi}) = \frac{\gamma}{2} (R(\boldsymbol{X}) - T(\boldsymbol{\varphi}))^2 \tag{4.3}$$

where γ is the penalty parameter enforcing the alignment of the reference image to the target image. The hyperelastic warping registration was implemented by aligning the meshed model with all frames of short-axis images. Lagrange-Green strain component was obtained at different time frames during a cardiac cycle.

4.2.4.4 Post-processing of strains

Since the deformation gradient $\boldsymbol{F}$ was defined with ES as the reference configuration, the local Green-Lagrange strain tensor with end-diastole (ED) as the reference – a more commonly used metric – was defined as:

$$\boldsymbol{E} = \frac{\mathbf{1}}{\mathbf{2}} \left(\boldsymbol{F}^{\boldsymbol{T}} \boldsymbol{F}_{\boldsymbol{ED}}^{-\boldsymbol{T}} \boldsymbol{F} \boldsymbol{F}_{\boldsymbol{ED}}^{-\mathbf{1}} - \boldsymbol{I} \right) \tag{4.4}$$

where $\boldsymbol{I}$ is the identity tensor and $\boldsymbol{F}_{\boldsymbol{ED}}$ is the deformation gradient tensor at ED. Normal strains in the circumferential ε_{CC}, longitudinal ε_{LL}, and radial ε_{RR} directions were computed by projecting $\boldsymbol{E}$ onto these directions using $\varepsilon_{ii} = \boldsymbol{e_i} \cdot \boldsymbol{E} \boldsymbol{e_i}$ with $i \in (C, L, R)$. The circumferential $\boldsymbol{e_C}$, longitudinal $\boldsymbol{e_L}$ and radial $\boldsymbol{e_R}$ were prescribed using a Laplace-Dirichlet Rule-Based (LDRB) algorithm [3] with myofiber angle prescribed to be zero.

Figure 4.5 (A) shows the meshed model of three regions (LV, RV and septum) with the CMR images. **Figure 4.5 (B)** and **(C)** represents the circumferential strain direction and circumferential strain-time curve for LV, RV and septum respectively. **Figure 4.5 (D)** and **(E)** shows the longitudinal direction and the longitudinal strain-time curve, and **Figure 4.5 (F)** and **(G)** the radial direction and radial strain-time curve.

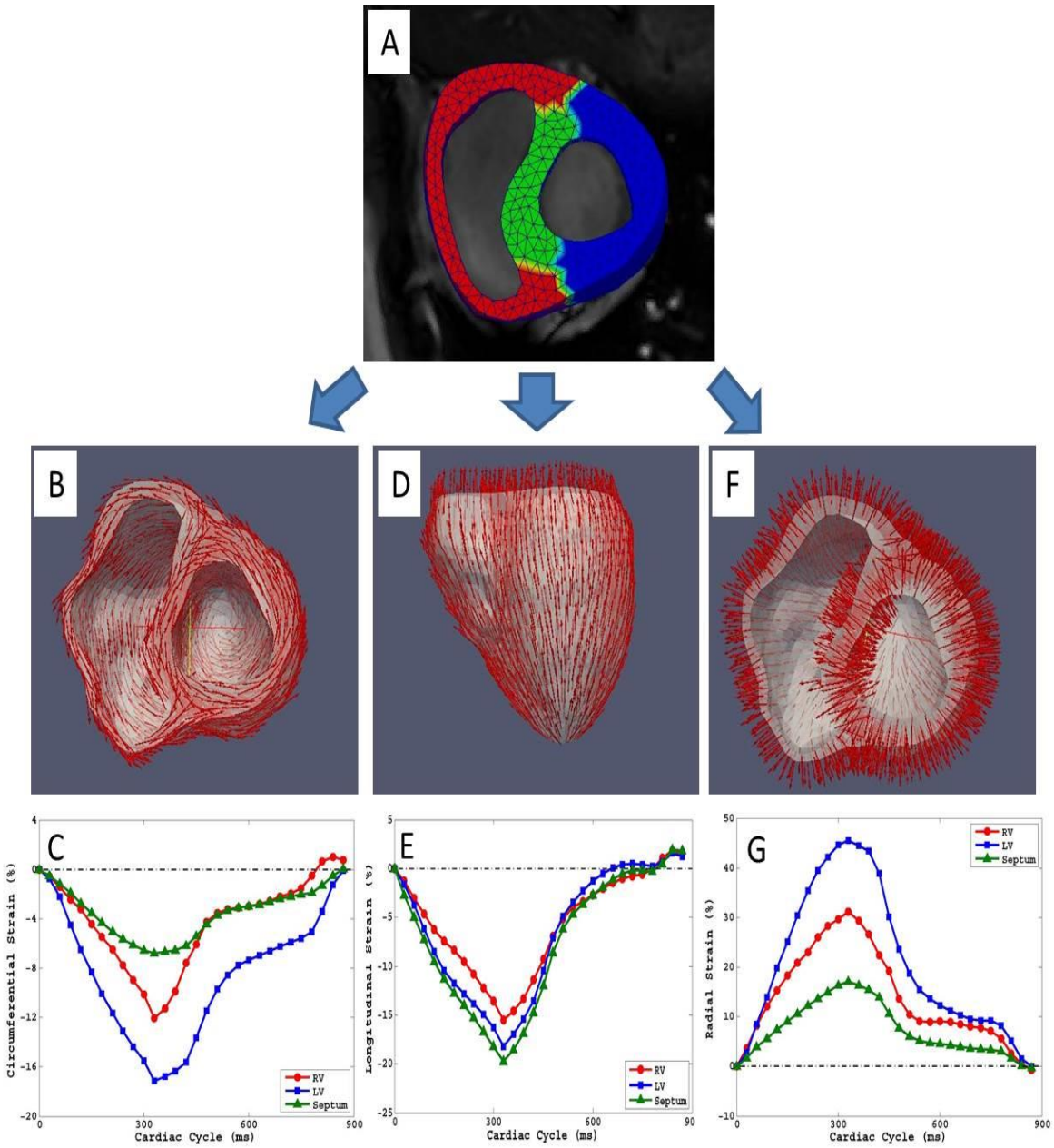

Figure 4.5. Registration the meshed model with images for strain-time curves (A) meshed model with CMR image; (B) circumferential strain orientation; (C) longitudinal strain orientation; (D) radial strain orientation; (E) circumferential strain-time curve; (F) longitudinal strain-time curve; (G) radial strain-time curve.

4.3 Results

4.3.1 Patient demographics

Study subjects consisted of 5 males and 15 females in each group, with a mean ± SD age of 48±15 and 47±15 years for Controls and PAH patients, respectively. Demographic and clinical characteristic of study subjects were given in **Table 4.1**. Compared with normal Controls, PAH patient had a comparable LV ejection fraction (EF), but RV EF was lower than the controls (43±12 vs. 59±6, p<0.001). RV end-diastolic volume (EDV) index and RV end-systolic volume (ESV) index were higher in PH patients than controls (114±44 vs. 75±12 and 66±31 vs. 31±8 respectively, p<0.001), but RV stroke volume (SV) was comparable. PH patients were comparable to Controls with respect to height, weight, body surface area (BSA), body mass index (BMI), systolic blood pressure (SBP), diastolic blood pressure (DBP), LV EDV, LV ESV, LV SV, LV mass index. Heart rate of PH patients was higher than Controls (83±15 vs. 71±13, p=0.012). Invasive hemodynamic parameters were reported in **Table 4.1** too. PAH patients had a mean pulmonary artery pressure (mPAP) of 45.8±15.2 mmHg, right atrial pressure (RAP) of 8.3±7.5 mmHg, pulmonary capillary wedge pressure of 12.8±6.5 mmHg, Cardiac output of 4.4±2.2 L/min, Cardiac index of 2.7±1.1 L/min/m2, pulmonary and systemic resistance ratio of 0.4±0.2, and pulmonary systemic flow ratio of 1.24±0.4. Systemic vascular resistance of PH patients was 1774.9±619.2 dyne s/cm5, and pulmonary vascular resistance of 745.9±520.3 dyne s/cm5.

4.3.2 Peak systolic circumferential, longitudinal and radial strains

Table 4.2 showed the peak circumferential, longitudinal and radial strains in different regions (RV, LV and septum) for Controls and PAH patients respectively. PH patients had significant depressed RV circumferential (-7.56 ± 2.83% vs. -9.47 ± 1.88%, p<0.05), longitudinal (-11.00 ± 3.65% vs. -14.79 ± 2.18%, p<0.001) and radial (18.48 ± 9.56% vs. 24.81 ± 7.02%, p<0.05) strains. LV strains were also lower in PAH patients, but only LV circumferential strain (-11.60 ± 2.52% vs. -14.44 ± 1.97%) had significant difference between patients and Controls (p<0.001). Septum strains in PAH patients were

lower in Controls, but only circumferential and radial strains had statistics significance (p<0.05).

Table 4.2. Average circumferential, longitudinal and radial strains in RV, LV and septum

Variables	Control (n = 20)	PH (n = 20)	P value [§]
$\varepsilon_{\mathrm{CC}}^{\mathrm{RV}}$ (%)	-9.47 ± 1.88	-7.56 ± 2.83	**0.016**
$\varepsilon_{\mathrm{LL}}^{\mathrm{RV}}$ (%)	-14.79 ± 2.18	-11.00 ± 3.65	**<0.001**
$\varepsilon_{\mathrm{RR}}^{\mathrm{RV}}$(%)	24.81 ± 7.02	18.48 ± 9.56	**0.022**
$\varepsilon_{\mathrm{CC}}^{\mathrm{LV}}$ (%)	-14.44 ± 1.97	-11.60 ± 2.52	**<0.001**
$\varepsilon_{\mathrm{LL}}^{\mathrm{LV}}$ (%)	-15.10 ± 2.14	-13.31 ± 3.68	0.068
$\varepsilon_{\mathrm{RR}}^{\mathrm{LV}}$ (%)	34.36 ± 9.25	27.84 ± 11.7	0.058
$\varepsilon_{\mathrm{CC}}^{\mathrm{Sep}}$ (%)	-5.89 ± 1.74	-4.35 ± 1.77	**0.008**
$\varepsilon_{\mathrm{LL}}^{\mathrm{Sep}}$ (%)	-16.42 ± 2.54	-14.05 ± 4.70	0.057
$\varepsilon_{\mathrm{RR}}^{\mathrm{Sep}}$ (%)	13.87 ± 4.73	10.10 ± 5.00	**0.019**

Values are mean ± SD. ε_{CC}^{RV}: Right ventricular peak circumferential strain; ε_{CC}^{LV}: left ventricular peak circumferential strain; ε_{CC}^{Sep}: Septum peak circumferential strain.ε_{LL}^{RV}: Right ventricular peak longitudinal strain; ε_{LL}^{LV}: Left ventricular peak longitudinal strain; ε_{LL}^{Sep}: Septum peak longitudinal strain; ε_{RR}^{RV} : Right ventricular peak radial strain; ε_{RR}^{LV}: Left ventricular peak radial strain; ε_{RR}^{Sep}: Septum peak radial strain. PAH: Pulmonary hypertension; [§] Independent Sample t Test.

4.4 Discussion

PAH is a serious disease often accompanied by RV dysfunction and failure. Survival in patients with PAH is strongly related to RV function [191]. In PAH, RV free wall strain emerged as an important predictor of outcome [192]. However, LV performance may be affected because both ventricles share the interventricular septum within the same pericardial sac, although PAH is defined by normal LV filling pressure. Keeping this concept of interventricular independence in mind, we performed this study to investigate

the 3D RV, LV and septum strains by treating the heart as a whole and to study the bi-ventricular motion simultaneously.

4.4.1 RV strains

Circumferential, longitudinal and radial strains in RV for PAH patients were significantly reduced compared with the controls, demonstrated the comprehensive impairment in RV motion for this type of heart disease. This is consistent with the reduced RVEF in PAH patients. Reduced RV longitudinal strain has been widely reported in PAH patients by MRI [193], [194], speckle-tracking on 2D echocardiography [175], [192] as well as 3D echocardiography [195]. Reduction in RV circumferential and radial strain may be due to circumferential stretch and subsequent reduction in contractility. Because the myocardium of RV free wall is oblique in the superficial submyocardium, this finding may signify the failure of outer layer to contract circumferentially [196]. MRI studies had highlighted the value of considering RV circumferential strain for some pathology such as arrhythmogenic RV cardiomyopathy or RV afterload changes [197].

4.4.2 Septum and LV strains

The finding that septal circumferential and radial strains are depressed in PAH patients is interesting and important. Under normal circumstances, the septum behaves much like a thick-walled cylinder subject to internal and external pressure, with the resulting stresses being circumferential tension and radial compression, just like the remainder of the left ventricle [198]. In PAH, however, this pressure gradient reduced or reversed. The septum withstanding this pressure load becomes more flatted, and is threatened by substantial compressive wall stress, which impedes septal blood flow and

affects septal performance [198]. In a study by Rico *et al*. [199], PAH was associated with impaired RV free wall longitudinal strain and septal circumferential strain.

Our study also revealed that the LV circumferential strain was reduced, but longitudinal and radial strain was preserved in PAH patients. Although no significant difference was observed in LV CMR parameters (**Table 4.1**), LV circumferential strain may reveal an early impairment of LV. This is consistent with the findings of Puwanant el al [200], who found both septum and LV circumferential strains were decreased in PAH patients, but the longitudinal strain in the LV was preserved. A potential explanation could be that a reverse septal curvature and more D-shaped LV in patients affect more than longitudinal myocardial fiber shortening. The finding that both circumferential and radial strains were reduced in septum and only the circumferential strain in LV was reduced supports the hypothesis that PAH influences the septum more than the LV free wall. Two studies on the finite element modelling can help us understand this physiology [201], [202].

4.5 Limitations

There are limitations in this study, including a small number of enrolled subjects. In order to increase the statistics power, a larger sample size should be included. Besides, longitudinal strain was calculated by imposing a basal longitudinal displacement that varies sinusoidally with time. Despite a reasonable peak longitudinal strain obtained, the longitudinal strain-time curve did not show exact dynamic function of the heart. A higher out-of-plane resolution (smaller slice thickness) may obviate the need to impose such an assumption.

CHAPTER 5

PATIENT-SPECIFIC COMPUTATIONAL ANALYSIS OF VENTRICULAR MECHANICS IN PULMONARY ARTERIAL HYPERTENSION

Abstract

Patient-specific biventricular computational models associated with a normal subject and pulmonary arterial hypertension (PAH) patient were developed to investigate the disease effects on ventricular mechanics. These models were developed using geometry reconstructed from magnetic resonance (MR) images, and constitutive descriptors of passive and active mechanics in cardiac tissues. Model parameter values associated with ventricular mechanical properties and myofiber architecture were obtained by fitting the models with measured pressure–volume loops and circumferential strain calculated from MR images using a hyperelastic warping method. Results show that the peak right ventricle (RV) pressure was substantially higher in the PAH patient (65 mmHg versus 20 mmHg), who also has a significantly reduced ejection fraction (EF) in both ventricles (left ventricle (LV): 39% vs. 66% and RV: 18% vs. 64%). Peak systolic circumferential strain was comparatively lower in both the left ventricle (LV) and RV free wall (RVFW) of the PAH patient (LV: 6.8% vs.13.2% and RVFW: 2.1% vs. 9.4%). Passive stiffness, contractility, and myofiber stress in the PAH patient were all found to be substantially increased in both ventricles, whereas septum wall in the PAH patient possessed a smaller curvature than that in the LV free wall. Simulations using the PAH model revealed an approximately linear relationship between the septum curvature and the transseptal pressure gradient at both early-diastole and end-systole. These findings suggest that PAH can induce LV remodeling, and septum curvature measurements may be useful in quantifying transseptal pressure gradient in PAH patients.

Nomenclature

C	Regional myofiber passive stiffness (kPa)
C_p	Pulmonary arterial compliance (mL/kPa)
C_s	Systemic arterial compliance (mL/kPa)
E_{cc}	Regional circumferential strain (%)
EDP	End-diastolic pressure
EDV	End-diastolic volume
ESV	End-systolic volume
LVSB	Left ventricular septal bow
P_{ao}	Aortic valve opening pressure (mmHg)
P_{pa}	Pulmonary valve opening pressure (mmHg)
PA	Pulmonary artery
PAH	Pulmonary arterial hypertension
$R_{c,p}$	Pulmonary aortic resistance (kPa ms/mL)
$R_{c,s}$	Systemic aortic resistance (kPa ms/mL)
$R_{per,p}$	Pulmonary peripheral resistance (kPa ms/mL)
$R_{per,s}$	Systemic peripheral resistance (kPa ms/mL)
T_{ref}	Regional myocardial contractility (kPa)
β	RVFW myofiber helix angle (deg)
κ	Regional curvature at the midventricular level (cm^{-1})
κ_n	Normalized septum curvature (ratio of septum curvature to LVFW curvature)
$\kappa_{max,s}$	End-systolic septum curvature (cm^{-1})
$\kappa_{max,d}$	Early-diastolic septum curvature (cm^{-1})

5.1 Introduction

Pulmonary arterial hypertension (PAH) is a disease associated with vasoconstriction of the pulmonary arterial vessels, resulting in an elevated pulmonary arterial pressure. The clinical diagnosis for PAH is an elevated mean pulmonary artery (PA) pressure greater than 25 mmHg with normal wedge pressure [1]. Without treatment, PAH can quickly lead to decompensated right heart failure and death. The current prognosis of PAH remains poor, with about 15% mortality within 1 year on modern therapy [2] and a low 3-year survival rate of 67% [3].

High afterload in the right ventricle (RV) caused by PAH can lead to changes in ventricular mechanics [4]. For example, an elevated RV pressure (RVP) can lead to abnormal ventricular deformation in the form of a “left ventricular septal bow” (LVSB), which is a left-ward motion of the septum into the left ventricle (LV) cavity. Moreover, PAH is also associated with long-term functional, structural, and geometrical changes in the RV [5]. These changes and their impacts on ventricular mechanics are currently not well-understood [6]. Although animal models have been used to understand ventricular mechanics associated with RV remodeling in PAH [7, 8], similar studies in humans are lacking and most clinical investigations have been confined to quantifying global ventricular mechanics through pressure–volume (PV) loop measurements [9,10].

Image-based computational models are increasingly used to analyze ventricular mechanics in heart diseases (e.g., myocardial infarction [11], left branch bundle block [12], and mitral valve regurgitation [13, 14]) as well as heart failure treatments [15]. The focus of these computational analyses is, however, on the LV that has historically received more attention than the RV. On the other hand, computational modeling analyses of PAH have

mostly been performed on pulmonary arteries [16, 17]. The RV, whose function is a major determinant of prognosis in PAH [18], has largely been overlooked.

To fill the void in the current research of PAH, here we describe an image-based computational analysis of the ventricular mechanics in a PAH patient. Specifically, we seek to quantify regional ventricular myofiber stress, myofiber strain, contractility, and passive tissue stiffness in a PAH patient, and compare them to those found in an age- and gender-matched normal subject. We also use the developed biventricular computational model of the PAH patient to investigate and quantify the effects of transseptal pressure gradients on the septum curvature.

5.2 Method

5.2.1 Acquisition

A 3-T Philips scanner with electrocardiography gating was used to acquire cine magnetic resonance (MR) images from one PAH patient as well as one gender- and age-matched normal human subject. The patient was a 42-year-old male who had been diagnosed with severe PAH for 2.5 year at the time of MR imaging and right heart catheterization for the study. Left and right ventricular, atria, and arterial pressures were also acquired from the PAH patients by right heart catheterization as part of their clinical care. All data were acquired at the National Heart Center of Singapore, and all enrolled participants gave written informed consent.

5.2.2 Biventricular geometry

Three-dimensional biventricular geometries of the PAH patient and normal subject were reconstructed by manually delineating the contours of the LV endocardium, RV endocardium, and epicardium in different short- and long-axis views of the cine MR images. These contours were then fitted to obtain 3D surfaces of the LV endocardial, RV endocardial, and epicardial surfaces using a medical image analysis software MEVISLAB Finite element (FE) meshes for the two cases were generated in the volume enclosed by these surfaces using GMSH [19]. The meshes consist of approximately 4000 quadratic tetrahedral elements and 7000 nodes.

5.2.3 Pressure–volume loops

Cavity volumes of the LV and RV were measured in the PAH patient and normal subject at different time frames within a cardiac cycle using the biventricular geometries described in Sec.2.2. These measured volumes were paired with the acquired pressure data to reconstruct the LV and RV PV loops of the PAH patient. To synchronize the MR images with the acquired pressure data, we first adjusted for any differences in heart rate by scaling the heartbeat duration in the MR images to that of the pressure data. Thereafter, the pressure data were synchronized with the MR images (which were acquired starting at end-diastole) using the end-diastolic pressure, which corresponds to the pressure at the beginning of a steep pressure rise. For the normal subject, normal RVP waveform from a previous study [20] and a scaled normal left ventricular pressure (LVP) waveform (with end-systolic pressure equal to 0.9 of the measured cuff pressure [21]) were paired with the cavity volume measurements to reconstruct the PV loops.

5.2.4 Strain analysis of magnetic resonance images

Regional circumferential strain E_{cc} was estimated from the PAH patient and the normal subject using a hyperelastic warping method that is implemented by a plugin (FEWarp) in FEBio [22]. Briefly, in the hyperelastic warping method, an FE model of the biventricular geometry from the template image was deformed into alignment with the corresponding object in the target image via a computed image-based local body force term that depends on (1) the difference in image intensity between the template and target images, (2) the target image intensity gradient, and (3) a prescribed penalty factor [23]. Because previous studies [23, 24] have shown that strain predictions from hyperelastic warping method are insensitive to changes in material coefficients, a compressible neo-Hookean strain energy function with unit material constant was used in both cases, and the penalty factor was increased incrementally until the strain field converged. Spatially averaged E_{cc} was computed in the LV and RV free wall (RVFW) at different cardiac time points using end-diastole as the reference configuration. Circumferential direction was prescribed using the Laplace–Dirichlet rule-based (LDRB) algorithm [25] with myofiber angle set to zero.

5.2.5 Biventricular finite element model

Biventricular geometries reconstructed from MR images corresponding to the time point at which LVP and RVP were at their lowest (in early diastole) were used as the reference state for the FE models of the PAH patient and normal subject (**Figure 5.1(a)**). Myocardial fiber orientation was prescribed in the models using an LDRB algorithm [25]. Based on the previous experimental measurements [26], myofiber helix angle was prescribed in the LV with a linear transmural variation from 60 deg at the endocardium to

- 60 deg at the epicardium (i.e., 60 deg/-60 deg) (**Figure 5.1(b)**). Given the lack of human RV myofiber data, myofiber orientation in the RVFW was described similarly using a linear transmural variation β deg/ $-\beta$ deg, with β as a model parameter that is fitted to the measurements.

5.2.5.1 Cardiac mechanics.

A cellular-based cardiac electro-mechanics model [27, 28] was used to model the mechanical behavior of the biventricular unit over a cardiac cycle. Because the focus here is on biventricular mechanics, we have simplified the model by prescribing a stimulus current I_s everywhere in the model to describe homogeneous activation of the biventricular unit. The resultant model can therefore be described by the following system of ordinary differential equations and partial differential equations:

$$\frac{\partial s}{\partial t} = f(v, s, \lambda) \tag{5.1a}$$

$$\frac{\partial v}{\partial t} + I_{ion}(v, s, \lambda) = I_s \tag{5.1b}$$

$$\nabla \cdot \sigma = 0 \tag{5.1c}$$

Briefly, Eqs. (5.1a) and (5.1b) consist of a system of ordinary differential equations that describe the local coupling between cellular electrophysiology [29] and cross-bridge cycling process [30]. Here, s, I_{ion}, v and λ denote a vector of state variables consisting of various membrane channels and intracellular ionic concentration, the total ionic current that is scaled with the membrane capacitance, the transmembrane potential, and the myofiber stretch, respectively.

Eqs. (5.1c) describes the quasi-static mechanical equilibrium of the cardiac tissue with $\boldsymbol{\sigma}$

denoting the Cauchy stress tensor. As shown previously [31], the inertia effect on stresses is not significant in a beating heart. An active stress formulation was used to model contraction of the tissue. In this formulation, $\boldsymbol{\sigma}$ was decomposed into a passive component $\boldsymbol{\sigma}_p$ and an active component $\boldsymbol{\sigma}_a$ that accounts for the stiffening of the tissue in the myofiber direction during cross-bridge cycling, i.e.,

$$\boldsymbol{\sigma} = \boldsymbol{\sigma}_p + \boldsymbol{\sigma}_a(\boldsymbol{s}, \lambda, \dot{\lambda}; T_{ref}) \tag{5.2}$$

The active stress tensor $\boldsymbol{\sigma}_a$ depends on the time evolution of the state variables $\boldsymbol{s}$, myofiber stretch λ and rate of elastic myofiber stretch $\dot{\lambda}$. The contractile stress was scaled by a reference tension T_{ref}, a model parameter that is associated with the tissue contractility. Although previous studies have suggested the presence of a secondary active stress acting transversely to the muscle fiber [32], we did not include this feature in our model for simplicity. The passive stress $\boldsymbol{\sigma}_p$ was described by a Fung-type transversely isotropic hyperelastic constitutive model with the following strain energy function:

$$\Psi = \frac{1}{2}C(e^Q - 1) + C_{compr}\,(JlnJ - J + 1) \tag{5.3a}$$

where

$$Q = b_{ff}{E_{ff}}^2 + b_{xx}\left({E_{ss}}^2 + {E_{nn}}^2 + {E_{sn}}^2 + {E_{ns}}^2\right) + b_{fx}\left({E_{fn}}^2 + {E_{nf}}^2 + {E_{fs}}^2 + {E_{sf}}^2\right) \tag{5.3b}$$

In the above equation, $\boldsymbol{E} = \frac{1}{2}(\boldsymbol{F}^T\boldsymbol{F} - \boldsymbol{I})$ is the Green-Lagrange strain tensor, J is the Jacobian of the deformation gradient tensor $\boldsymbol{F}$, and E_{ij} with $i, j \in (f, s, n)$ are the strain components with f, s and n, respectively, denoting the fiber, sheet, and sheet normal

directions. The passive material parameters are C_{compr}, C, b_{ff}, b_{xx} and b_{fx}. The passive stress $\boldsymbol{\sigma}_p$ is related to the strain energy function as follows:

$$\boldsymbol{\sigma}_p = \frac{1}{J}\boldsymbol{F}\frac{\partial \Psi}{\partial \boldsymbol{E}}\boldsymbol{F}^T \tag{5.4}$$

5.2.5.2 Simulation of a cardiac cycle.

A full cardiac cycle was simulated based on an open-loop circulatory model. Specifically, passive filling was simulated by incrementally applying pressure to the LV and RV endocardial surfaces until the prescribed end-diastolic pressures (EDP) were reached. The biventricular model was then stimulated, and the LV and RV cavity volumes were constrained to remain constant during the isovolumic contraction phase. The ejection phase was simulated by coupling the LV and RV cavity volumes each to a three-element Windkessel model when the LVP and RVP exceeded the aortic and pulmonary valve opening pressures, respectively (**Figure 1(c)**). The isovolumic relaxation phase was simulated by constraining the cavity volumes and began when outflows from the LV and RV became negative. The base of the biventricular model was constrained from moving out of the plane, and the epicardial surface was imposed with a spring boundary condition (with a distributed spring constant of 0.5 kPa/cm) to simulate the presence of pericardial fluid surrounding the biventricular unit.

5.2.5.3 Model parameterization.

Biventricular FE models of the PAH patient and normal subject were each divided into two material regions, namely, the LV and the RVFW with different passive stiffness C and contractility T_{ref} (**Figure 1(a)**). Together with the peripheral resistance of the Windkessel models (i.e.,$R_{per,s}, R_{per,p}$) and the RVFW myofiber helix angle (i.e., β), these material parameters were manually adjusted to fit the (1) experimentally measured LV

and RV PV loops, and (2) the regional circumferential strain measurements from hyperelastic warping in each case. Specifically, the passive stiffness parameter C in both LV and RV was first adjusted to fit the corresponding measured end-diastolic volumes and pressures. Thereafter, regional myocardial contractility, peripheral resistance (i.e., $R_{per,s}, R_{per,p}$), and RVFW myofiber helix angle (i.e., β) were adjusted to fit the systolic portion of PV loop and the circumferential strain in both LV and RV. All other material parameters were prescribed with the same values in both cases. The model parameters are summarized in **Table 5.1**.

Table 5.1. Model parameters. References from which the parameter values were obtained are denoted by square bracket

	Fitted	**Prescribed**
Passive stress model	C_{LV}, C_{RV}	$C_{compr} = 50kpa;$ $b_{ff} = 14.4,\ b_{fx} = 10.08, b_{xx} = 5.76;$ [30]
Active stress model	$T_{ref,LV}, T_{ref,RV}$	Other parameters [29]
Windkessel model	$R_{per,s}\ R_{per,p}$	$P_{per,s} = 4.5mmHg, R_{per,p} = 3.0mmHg;$ $R_{c,s} = 1.8\ kpa \cdot ms/mL$ $R_{c,p} = 0.01\ kpa \cdot ms/mL$ $C_s = 15\frac{mL}{kpa}, C_p = 5\frac{mL}{kpa}$
Myofiber orientation	β	LV helix angle 60 deg/ -60 deg [25]

5.2.5.4 Septum curvature.

The fitted PAH model was used to quantify the effects of varying RV afterload and preload on the regional curvature of the LV endocardial surface. Regional curvature κ was calculated at the midventricular level (half-way between the apex and base) from the biventricular FE model at different time points within a cardiac cycle. Specifically, the con-

tour of an LV endocardial slice at the midventricular level was parameterized as $r(\theta)$ in a polar coordinate system (**Figure 1(d)**) and κ was computed at each point in the contour using

$$\kappa(\theta) = \frac{r^2+2r'^2-rr'}{(r^2+r'^2)^{\frac{3}{2}}} \tag{5.5}$$

where $r' \equiv dr/d\theta$. Septum and LV free wall (LVFW) curvature were computed by averaging κ for all the points located in their respective region.

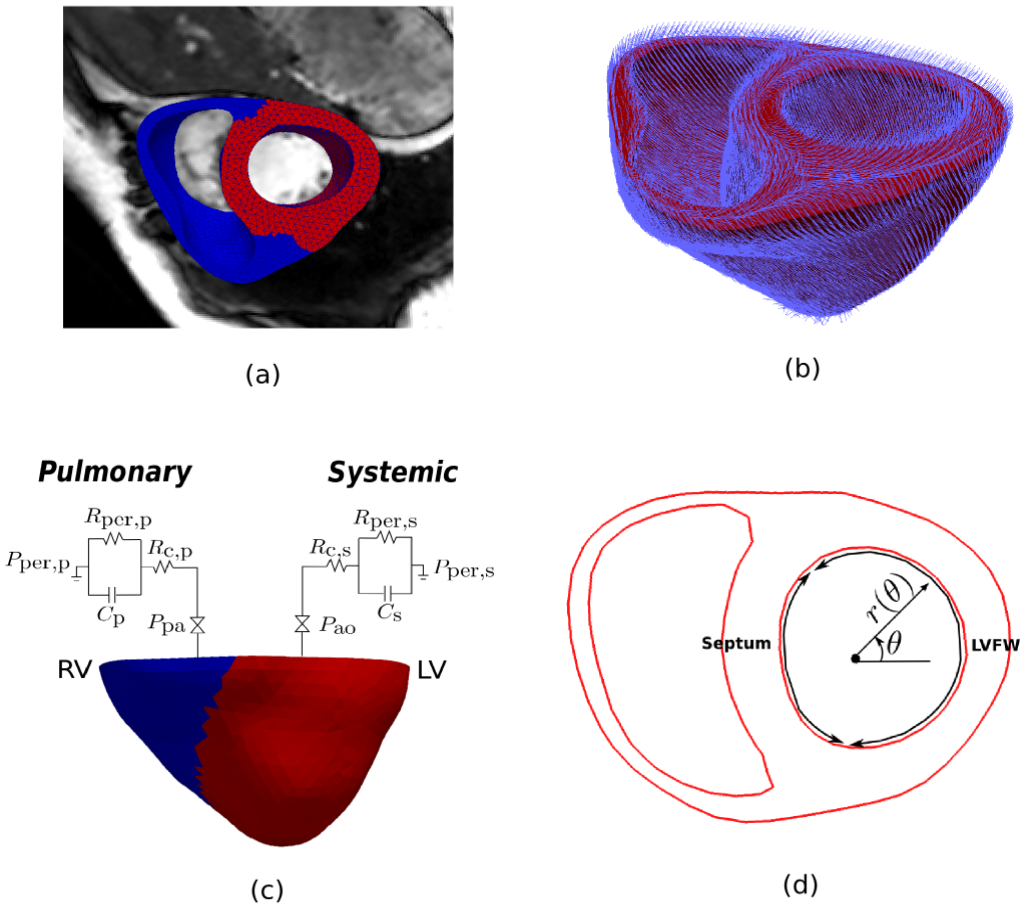

Figure 5.1. (a) Biventricular geometry reconstructed from MR images with LV (right, light region) and RVFW (left, dark region) material regions. (b) Myofiber orientation prescribed using LDRB method [3] with a transmural variation of 60 degree (endo) to -60 degree (epi) for the entire biventricular model. (c) Coupling the biventricular model to three-element Windkessel models. (d) Polar coordinate used to calculate local curvature κ in the LV endocardium.

5.3 Results

5.3.1 Pressure–volume loops

The PV loops of the RV and LV predicted by the model were in agreement with the measurements in both PAH and normal cases (**Figure 5.2**). The average error, which was calculated by averaging the percentage difference of (1) the predicted and measured pressure during the filling and ejection phases, and (2) the predicted and measured volume during the two isovolumic phases, was within 4% for the two cases. The maximum error was 10% and occurred during the LV ejection phase in the PAH case.

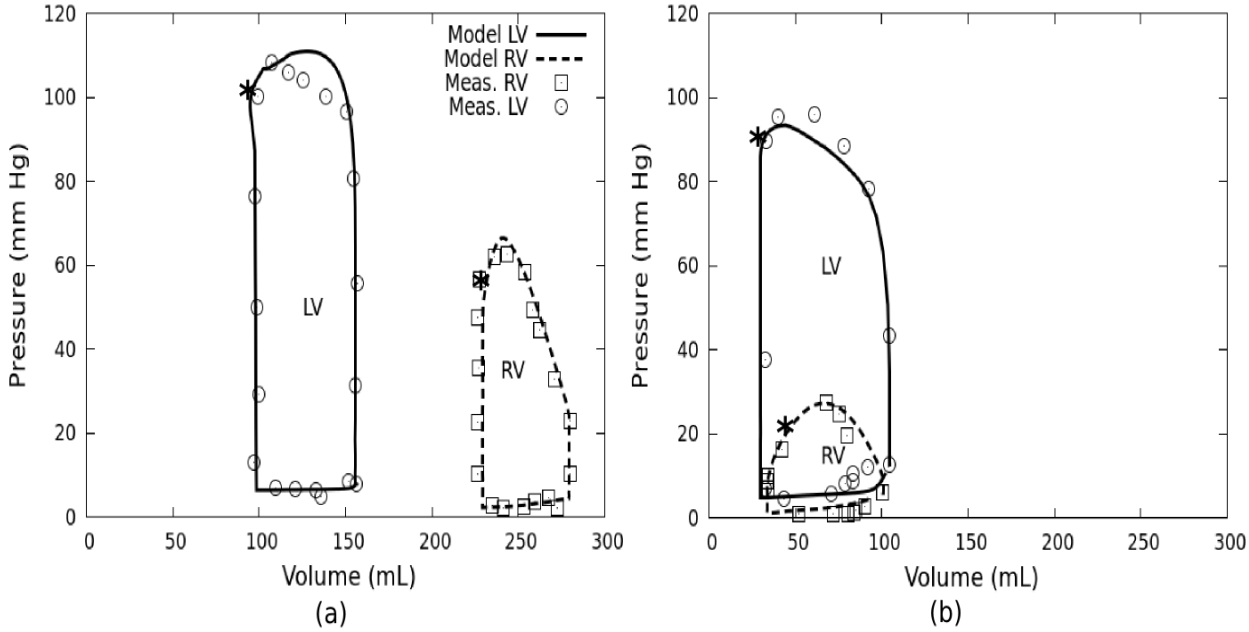

Figure 5.2. Measurements and model predictions of the PV loops for the (a) PAH patient and (b) normal subject (marker "*" denotes end-systole)

Peak RVP was about 3.5 times higher in the PAH patient than that found in the normal subject (65 mmHg vs. 20 mmHg), whereas peak LVP was only slightly higher in the PAH patient (110 mmHg vs. 100 mmHg). End-diastolic volume (EDV) and end-systolic volume (ESV) of the LV and RV were also larger in the PAH patient than in the

normal subject with the largest difference found the RV (RV EDV: 275 ml vs. 100 ml; RV ESV: 225 ml vs. 36 ml). Correspondingly, the ejection fraction (EF) of the PAH patient was substantially lower in both ventricles when compared to that of the normal subject (LV EF: 39% vs. 66% and RV EF: 18% vs. 64%). Work done by the LV and RV was also computed based on the areas enclosed in the PV loops, which show a slightly lower LV work in the PAH patient (5692 mmHg mL vs. 5870 mmHg mL) and a significantly increased RV work in the PAH patient (2438 mmHg mL vs. 1304 mmHg mL).

5.3.2 Regional circumferential strain

Circumferential strain measured using hyperelastic warping was substantially depressed in both LV and RVFW of the PAH patient when compared to the normal subject (**Figure 5.3(a)** and **5.3(b)**). Specifically, spatially averaged peak circumferential strain in a cardiac cycle was 2.1% and 9.4% in the RVFW of the PAH patient and the normal subject, respectively. Left ventricular peak $E_{cc}$was also depressed in the PAH patient when compared to the normal subject (6.8% vs.13.2%). In both cases, peak E_{cc} in the LV was found to be larger than that in the RVFW. The model predictions agreed reasonably well with these strain measurements, with a maximum difference between the model-predicted peak strain and the measurements at about 5% in the LV of the normal subject. We also found that the E_{cc} is very sensitive to the myofiber orientation, and in order to capture differences in E_{cc} between the LV and RVFW, transmural variation of myofiber angle in the RVFW has to be larger than that in the LV.

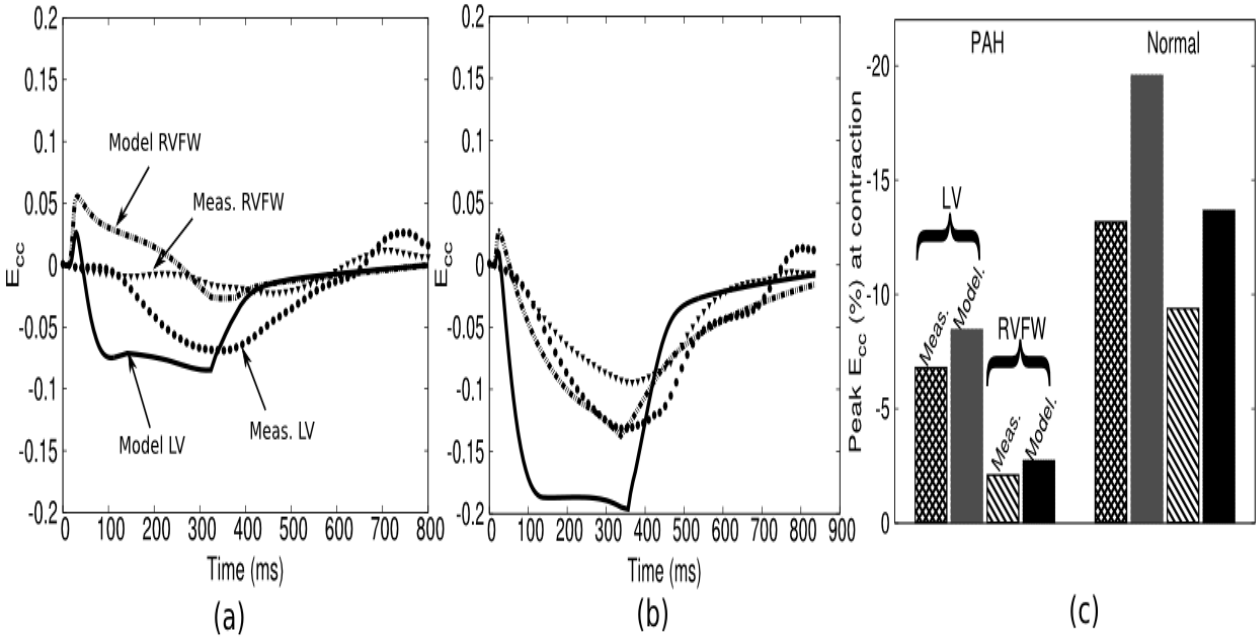

Figure 5.3. Circumferential strain $\boldsymbol{E_{cc}}$ for (a) PAH patient and (b) normal subject. (c) Comparison of regional peak negative $\boldsymbol{E_{cc}}$ between the PAH patient and normal subject.

5.3.3 Myofiber stress

Myofiber stress in the PAH patient was substantially higher in the entire biventricular region compared to the normal subject (Figure 5.4). Specifically, the peak average myofiber stress in the RVFW and LV of the PAH patient was almost twice the values found in the normal subject (LV: 99.7 kPa vs. 51.2 kPa; RVFW: 73.2 kPa vs. 43 kPa). For both PAH patient and normal subject, the myofiber stress in the LV was higher than that in the RVFW. The myofiber stress was also comparatively lower at the thicker RV insertion points than that found in the thinner LVFW and septum in both cases.

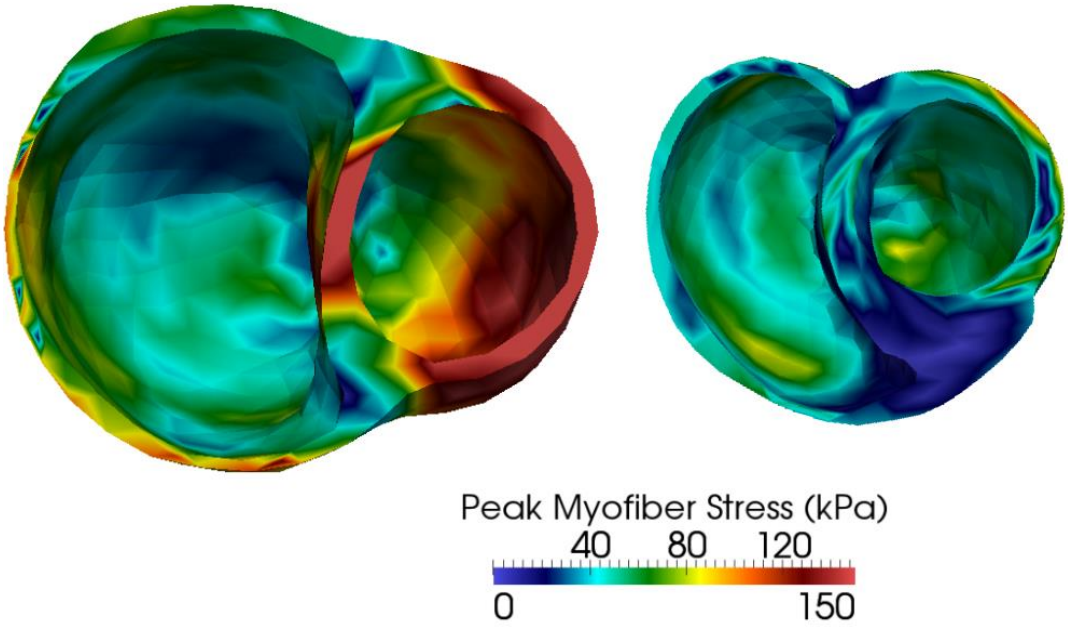

Figure 5.4. Peak myofiber stress in the PAH patient (left) and normal subject (right)

5.3.4 Model parameters

Table 5.2 shows the fitted model parameter values for the PAH patient and normal subject. Model parameters C and T_{ref} reflect the tissue's passive stiffness and contractility, respectively. We found that the tissue's passive stiffness and contractility were both higher in the LV and RVFW of the PAH patient than those in the normal subject. Peripheral resistance in the RV was also substantially higher in the PAH patient than in the normal subject, but was similar in the LV of both. A sensitivity analysis (see **APPENDIX F**) on the parameters C_{RV}, $T_{ref,RV}$ and $R_{per,p}$ shows that the difference in parameter values between the normal and PAH cases cannot be attributed to the uncertainty associated with the measurements of RVP (4 mmHg) [20]. We also found that the transmural variation of myofiber angle was steeper in the RVFW with the fibers oriented more longitudinally than in the LV in both cases. This regional variation was

found necessary to produce a smaller circumferential strain in the RVFW (compared to the LV) as found in the hyperelastic warping measurements (**Figure 5.3**).

Table 5.2. Regional model parameters—units: C *and* T_{ref} in kPa; $R_{per,s}$, $R_{per,p}$ in kPa·ms/mL

Case	LV			RVFW			
	C	T_{ref}	$R_{per,s}$	C	T_{ref}	β(deg)	$R_{per,p}$
PAH	1.68	262.5	40	1.96	160	80	26
Normal	0.035	123	40	0.12	73.8	75	5

5.3.5 Septum curvature

Two-dimensional curvature κ calculated from Eq. (5) on the LV endocardial surface at the midventricular short-axis slice revealed a substantially lower κ in the septum of the PAH patient (**Figure 5(a)** and **5(b)**). Compared to the normal subject, who has a more homogeneous curvature in the LV, the septum curvature in the PAH patient was substantially lower than that found in the LVFW. To eliminate the effects of LV diameter on κ, the septum curvature was normalized against the average LV curvature to give a normalized curvature κ_n. We found that the normalized curvature κ_n was lower in the septum of the PAH patient than that in the normal subject (**Figure 5(c)**).

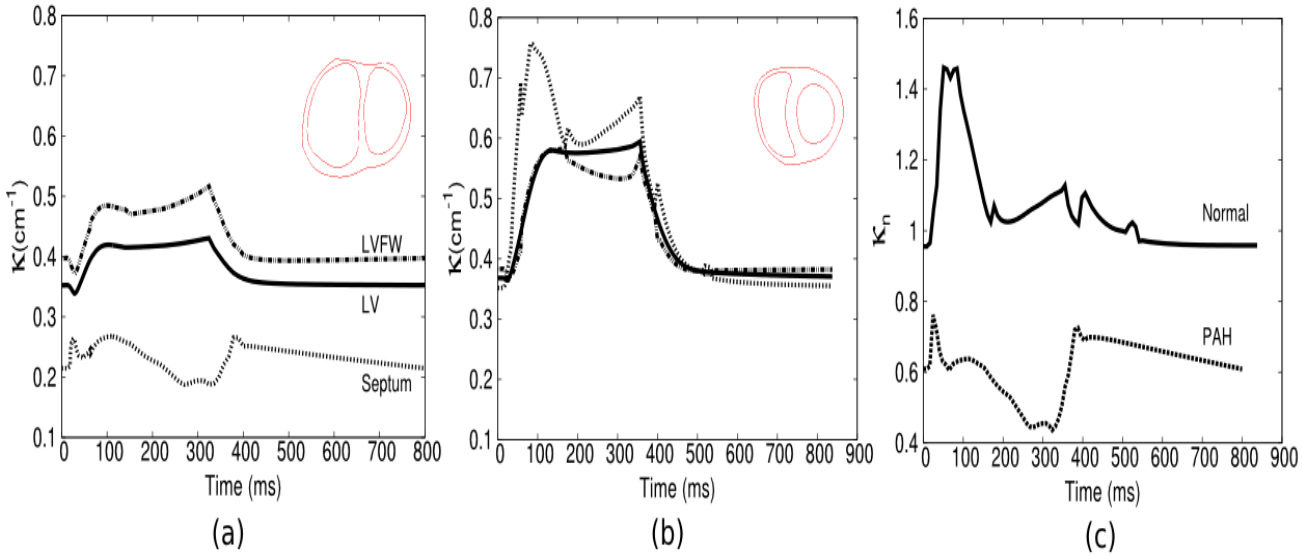

Figure 5.5. Regional curvature κ in the LV endocardial surface of (a) PAH patient and (b) normal subject. (c) Comparison of normalized septum curvature $\boldsymbol{\kappa_n}$ between PAH patient and normal subject.

5.3.5.1 Effects of afterload

The septum curvature decreased with increasing RV afterload (**Figure 5.6(a)**), which was adjusted in the PAH model by simultaneously increasing the pulmonary peripheral resistance $R_{per,p}$ and decreasing the RVFW contractility T_{ref} so that the stroke volume was relatively unchanged (**Figure 5.6(c)**). The largest variation of septum κ with RV afterload occurred during systole, with maximum curvature $\kappa_{max,s}$ varying almost linearly ($R = 0.984$) with the end-systolic transseptal pressure gradient between the LV and RV (i.e., LVP–RVP) (**Figure 5.6(b)**). On the other hand, septum curvature was less than the normal case (**Figure 5.5(b)**) even after reducing the afterload to a value close to the normal physiological RVP of 30 mmHg.

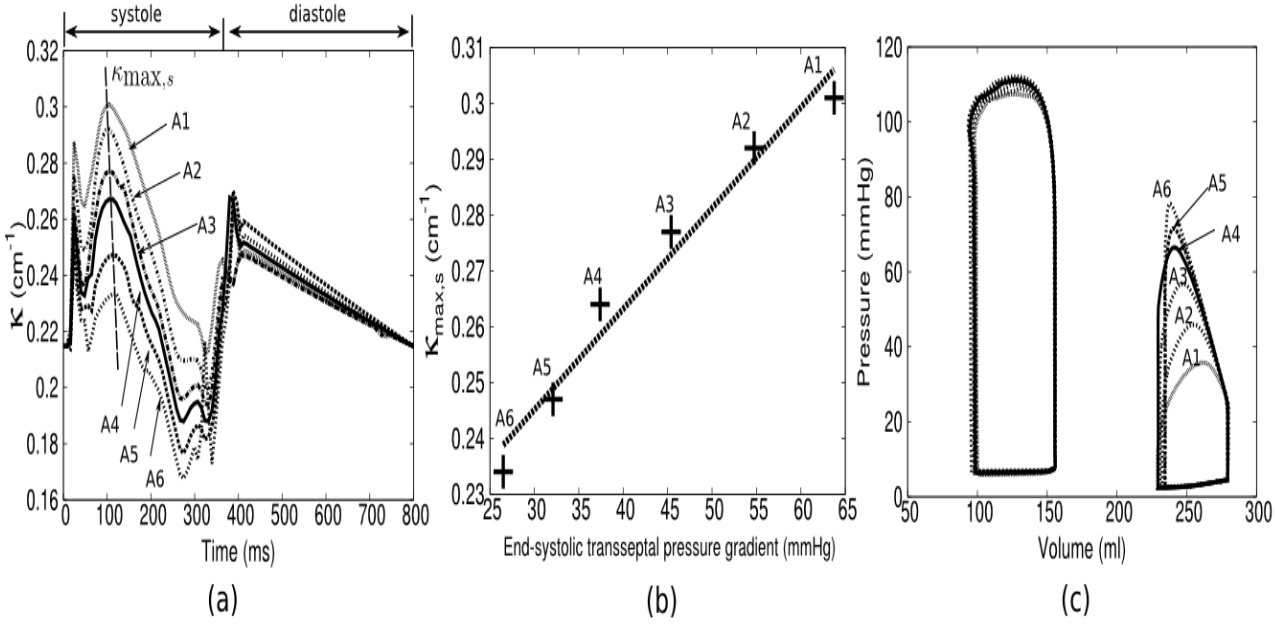

Figure 5.6. Effects of afterload on septum curvature within a cardiac cycle. (a) Time course of κ with different RV afterload. (b) End-systolic curvature $\boldsymbol{\kappa_{max,s}}$ versus end-systolic transseptal pressure gradient. (c) Corresponding PV loops.

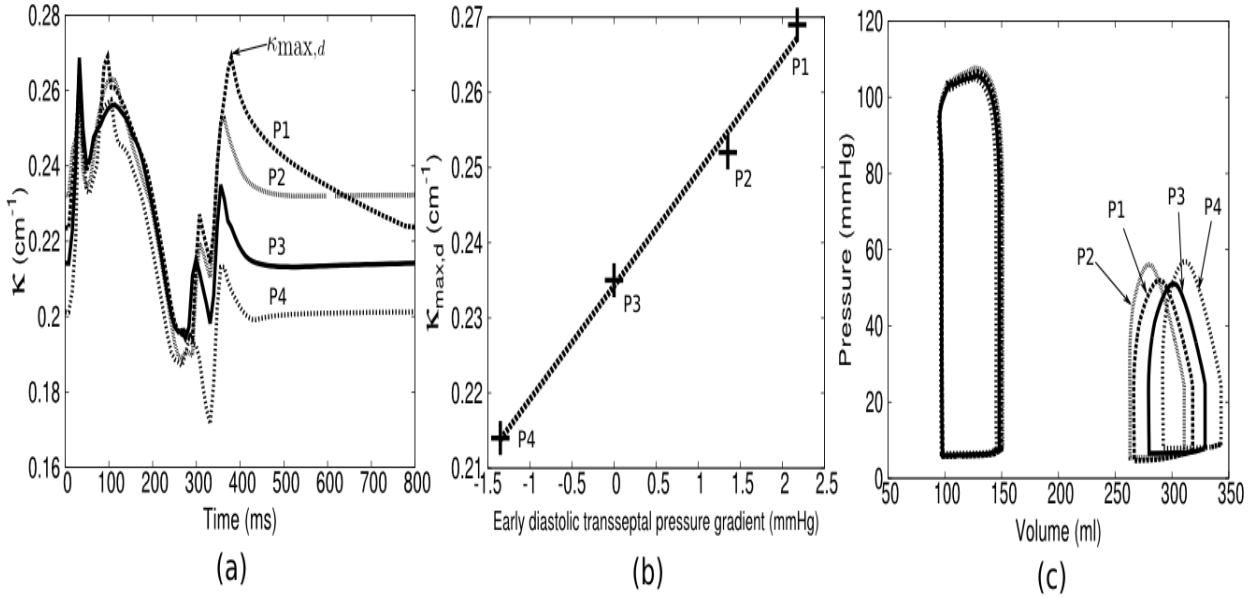

Figure 5.7. Effects of preload on septum curvature within a cardiac cycle. (a) Time course of κ with different RV preload. (b) Early-diastolic curvature $\boldsymbol{\kappa_{max,d}}$ versus early-diastolic transseptal pressure gradient. (c) Corresponding PV loops.

5.3.5.2 Effects of preload

The septum curvature also decreased with increasing RV preload (**Figure 5.7(a)**), which was simulated by increasing the prescribed EDP. Because of the length-dependent effects of the contraction model, RVFW contractility T_{ref} was also simultaneously adjusted to maintain a constant stroke volume in each of the preload cases with respect to the baseline PAH case (**Figure 5.7(c)**). In contrast to the effects of afterload, the largest variation of septum curvature occurred during early diastole, whereas the curvature was little changed in systole. The maximum diastolic curvature $\kappa_{max,d}$ also varied linearly ($R = 0.997$) with the transseptal pressure gradient between LV and RV at early diastole. Specifically, we found that an increase in transseptal gradient by 1 mmHg produces an average increase in by 0.0156 cm^{-1}.

5.4 Discussion

We have described the development of patient-specific biventricular computational models using pressure measurements and MR data from a PAH patient and a normal human subject. In each case, we have reconstructed the LV and RV PV loops using pressure data, and cavity volumes quantified from the MR images. A hyperelastic warping method was also used to compute the LV and RVFW circumferential strains from cine MR images. These strain measurements and PV loops were used to individually parameterize the biventricular computational models.

Using these patient-specific models, we have compared the in vivo regional ventricular mechanics between the PAH patient and normal subject, which includes regional myofiber stress distribution, mechanical properties, and regional curvature.

Additionally, we have also quantified the effects of RV preload and afterload on the septal curvature using the PAH model. As most previous computational studies of PAH have focused on the arteries [16, 17], this study, to the best of our knowledge, is the first patient-specific computational analysis of ventricular mechanics associated with PAH, even though the results and conclusions presented here are based on one PAH patient and normal subject that is clearly insufficient to represent a statistically sufficient sample size.

5.4.1 Circumferential strain

Compared to the LV, quantification of RV strain is significantly more challenging because of its complex geometry and thin wall. Nevertheless, RV strain analysis has been performed on PAH patients using echocardiographic images with speckle tracking [33], as well as strain-encoded MR imaging [34]. In these analyses, RVFW E_{cc} of PAH patients was found to be significantly depressed compared to normal subjects. Our results, which were obtained using a hyperelastic warping method [23] on cine MR images, agree with these studies. Besides a reduction in RVFW E_{cc}, we also found that the LV E_{cc} was reduced in the PAH patient compared to the normal subject (6.8% in PAH versus 13.2% in normal). This feature was also found in another echocardiography study [35] in which LV lateral wall and septum circumferential strains were all found to be significantly reduced in pulmonary hypertensive patients.

5.4.2 Myofiber stress

The use of Laplace's law to estimate RV wall stress is complicated by its irregular geometry [36]. We have overcome this complication in our computational analysis and have found that myofiber stress in the RVFW of the PAH patient was about twice as high as that in the normal subject. The larger RVFW myofiber stress can be attributed to the

combination of a higher afterload (3 X of normal) and a substantially larger RV (2 X of normal) in the PAH patient. Additionally, we found that LV myofiber stress was also about twice as high as that in the normal subject despite having a normal afterload. The higher LV myofiber stress could be attributed to the larger LV cavity (1.5 X of normal). Given that elevated myofiber stress is a feature that is associated with ventricular remodeling [37], this result suggests that remodeling associated with PAH may not only be confined to the RV but could also be found in the LV.

5.4.3 Fitted model parameters

5.4.3.1 Ventricular properties.

Fitted model parameters associated with regional biventricular mechanical properties also suggest significant remodeling in the PAH patient. Specifically, we found that the diastolic passive stiffness C and contractility T_{ref} of the PAH patient were larger than that of the normal subject in both LV and RVFW. These findings were consistent with the previous experimental studies. By comparing the passive tension found in RV tissue of PAH patients undergoing heart/lung transplantation with that from donors having non-failing heart, Rain et al. [38] found that RV diastolic stiffness is increased in PAH patients and is closely associated with the disease severity measured using stroke volume and a 6-min walk test. They attributed this increase to RV fibrosis and the intrinsic stiffening of RV myocytes. A similar finding was also reported in rats subjected to pulmonary artery banding [7]. Interestingly, the study by Rain et al. [38] also found an increase in the RV end-systolic elastance and the force-generating capacity in isolated RV cardiomyocytes from PAH patients. An increase in RV end-systolic elastance was found in rats induced with PH via monocrotaline injection compared to the controls [39].

As suggested in these studies, the increase in RV contractility associated with PAH is most likely a compensatory mechanism attempting to cope with the increased afterload in the RV. As with our findings for E_{cc} and myofiber stress, the substantially higher LV diastolic passive stiffness and contractility found here suggests the presence of remodeling in the LV of the PAH patient. Although we did not find any studies that measure LV mechanical properties that are directly associated with PAH, it was observed that patients with right heart failure often have relaxation abnormalities that may affect the mechanical properties of the LV [40]. Moreover, recent studies have also found evidence of electrophysiological remodeling in the LV of PAH patients [41].

5.4.3.2 Myofiber orientation.

Histological studies have found that compared to the LV that has muscle fiber running obliquely toward the apex, the deep muscle fibers of the RV are longitudinally aligned from base to apex [42]. Our result also suggests that the myofiber orientation is more longitudinal in the RV than in the LV in both cases, an outcome that is in part due to the smaller circumferential strain found in the RVFW in both cases. On the other hand, studies on rats [7] have found that both myofiber and collagen fiber orientations in the RVFW became more longitudinal as a result of RV remodeling in PAH. We, however, did not find this feature in our study.

5.4.4 Septum curvature

The fact that abnormal septal geometry and motion is a well-recognized feature in PAH patients [43] has motivated us to quantify this feature and investigate its sensitivity to RV preload and afterload. Our results show that septum curvature from the short-axis view at midventricular level was substantially lower in the PAH patient compared to that

in the normal subject. Physically, this implies that the septum is more “flattened” in the PAH patient. With varying preload (and constant afterload in the RV), we found that septum curvature at early-diastole increased linearly with increasing diastolic transseptal pressure gradient (LVP–RVP) ($R = 0.997$). Septum curvature in systole is, however, not highly affected by changes in the preload. Similar findings were also reported in other studies [44, 45], which found that the septum shape and motion at early-diastole are sensitive to the transseptal pressure gradient between the LV and RV. Specifically, Tanaka et al. [44] found that diastolic “bowing” of septum toward the LV (negative curvature) in PAH patients resulted from a negative transseptal pressure gradient, whereas Beyar et al. [45] reported that the bowing occurs only at a transseptal pressure gradient lower than 5 mmHg. Although we did not observe any bowing for the range of transseptal pressure gradient between 1.5 and 2.5 mmHg, our finding of a linear variation between the pressure gradient and septum curvature is consistent with these studies. Similarly, we found that the end-systolic septum curvature increased almost linearly with increasing systolic transseptal pressure gradient ($R = 0.984$), and the curvature at diastole was insensitive to this variation. Our result is quantitatively in good agreement with an echocardiographic study on children with pulmonary hypertension [46], which found a highly linear correlation ($R = 0.86$) between septum curvature and RV end-systolic pressure. This direct relationship between septum curvature and end-systolic pressure would suggest that the curvature can potentially be used as a noninvasive marker for quantifying RV pressure in PAH patient. Also, we note that the septal shape was quantified here using 2D curvature, which does not consider the extent of surface bending. The 3D surface curvedness has been used in ischemic cardiomyopathy [47],

heart failure [48], and repaired tetralogy of fallot [49]. Septal 3D curvedness may also be potentially useful in predicting pressure gradient in PAH patients.

5.5 Model limitations.

Overall, the predictions of the biventricular computational models are generally consistent with the results from clinical and experimental studies of PAH. Our results have also suggest that PAH may produce significant LV remodeling though caution must be exercised in extrapolating these results, which are based from only one constructed patient model and control. Additionally, there are also some limitations associated with our models. First, we have used the biventricular geometry that corresponds to the lowest pressure at the filling phase as the zero-stress state, and the values of the fitted mechanical properties may be affected by this assumption. Of course, this is an approximation as the zero-stress state does not exist in vivo. Other investigators have used the end-systole [50] or mid-systole [51] as the zero-stress state, or have estimated the zero-stress state from the end-diastole geometry using prescribed mechanical properties [12]. To the best of our knowledge, there appears to be no consensus on the best approach to address this issue. Second, we have not sampled the entire parameter space in fitting our model. Specifically, we have kept the passive tissue anisotropy fixed based on values obtained in normal humans [52] and the LV myofiber orientation fixed at 60 deg/60 deg. Because of the sensitivity of mechanical models, the use of a rule-based algorithm instead of actual fiber data is also a simplification that could introduce error. However, we have chosen to focus on the key features found in the RV that are

associated with PAH. Although further study is needed, we do not expect these limitations and simplifications to highly impact the results.

CHAPTER 6

EFFICIENT ESTIMATION OF PERSONALIZED BIVENTRICULAR MECHANICAL FUNCTION EMPLOYING GRADIENT-BASED OPTIMIZATION

Abstract

Individually personalized computational models of heart mechanics can be used to estimate important physiological and clinically-relevant quantities that are difficult, if not impossible, to directly measure in the beating heart. Here we present a novel and efficient framework for creating patient-specific biventricular models using a gradient-based data assimilation method for evaluating regional myocardial contractility and estimating myofiber stress. These simulations can be performed on a regular laptop in less than two hours and produce excellent fit between measured and simulated volume and strain data through the entire cardiac cycle. By applying the framework using data obtained from three healthy human biventricles, we extracted clinically important quantities as well as explored the role of fiber angles on heart function. Our results show that steep fiber angles at the endocardium and epicardium are required to produce simulated motion compatible with measured strain and volume data. We also find that the contraction and subsequent systolic stresses in the right ventricle are significantly lower than in the left ventricle. Variability of the estimated quantities with respect to both patient data and modeling choices are also found to be low. Because of its high efficiency, this framework may be applicable to modeling of patient-specific cardiac mechanics for diagnostic purposes.

6.1 Introduction

Cardiac computational modeling has emerged as both a powerful method to provide basic insight into cardiac function / dysfunction, and as a support tool to improve current clinical practice. Its development is in part driven by significant advancements in medical imaging techniques [203]–[205], which now provide a wealth of information about cardiac structure and kinematics. Merging this information with biophysical descriptions of cardiac behavior allows for the creation of powerful patient specific models of the heart [11], [206], [207]. Such models can be used to predict the outcome of different treatment strategies [208] or to extract useful indicators of mechanical function, such as myocardial contractility [209], [210] and myofiber stress [188], [211], potential biomarkers which are currently difficult, if not impossible, to measure directly using imaging techniques [212].

Of particular importance is ventricular myofiber stress [107], which is hypothesized to be a key driver of pathological remodeling processes in cardiac diseases [213]. Correspondingly, quantifying stress and determining how cardiac interventions may reduce abnormal stress is considered a useful avenue in developing treatments for heart failure [214]. However, while measurements of heart motion are possible using an array of imaging techniques, no direct measurements of the load experienced by myocytes are currently possible in vivo and estimates are used instead. One widely used method is the law of Laplace, a simplified model that takes into account pressure, wall thickness and curvature, and can be used to evaluate stress in idealized geometries. However, despite its wide use, it has been shown that this law severely underestimates myofiber stress in largely irregular

patient-specific ventricular geometries [215]. Furthermore, regional stresses also cannot be accurately estimated using this idealized law.

In order to overcome these limitations, patient specific simulation using finite element modeling is widely accepted as a viable way to accurately estimate myofiber stresses in the complex geometry of the heart, and has been used in designing heart failure treatments to reduce myocardial stress [214], [216], [217]. However, one of the many challenges faced by researchers developing patient specific models is to efficiently and accurately incorporate individual data into the them, which often requires determining model parameters that best reproduce the observations i.e., data assimilation [218], [219]. Typically, one defines a cost function representing the mismatch between simulated and observed data, and searches for model parameters that minimize this cost function. Several techniques have been employed to solve this minimization problem. Global methods, using parameter sweeps [42], [220], [221] or genetic algorithms [222], [223], are attractive because they can cover the entire parameter space, and are therefore more likely to retrieve the global minimum of the cost function. However, such methods require an extensive number of functional evaluations, which in the case of heart mechanics can be computationally expensive. Local optimization methods, on the other hand, typically start at some given initial guess, and iteratively search the local neighborhood for better candidates in the minimization of the cost function. These methods are typically faster than global methods, but have the drawback that the solution may depend on the initial guess. One example of a local method is the reduced order unscented Kalman filtering (ruKF) approach [224], which has been applied to personalize cardiac

electromechanical models from cine MRI [225].

Another class of local optimization methods are the gradient-based methods, which successively reduce the cost functional by searching along the gradient descent direction. While these methods may substantially improve the convergence towards the minimum, estimating the gradient in these methods, however, introduces significant additional computational costs. Specifically, estimating the gradient by standard finite differences typically requires as many functional evaluations as the number of control parameters (N + 1 evaluations for N parameters). Gradient-based methods are therefore impractical if the number of control parameters is large. Nevertheless, gradient based approaches have been applied to personalize cardiac mechanics models in several studies [218], [226]–[228]. For example in [227] a sequential quadratic programming (SQP) optimization technique was utilized to estimate passive material parameters, while in [229] a Levenberg–Marquardt method was used to estimate material parameters from shear data. In [228] the minimization was performed using a quasi-Newton BFGS-B method, where the gradient was computed using the adjoint method. In this study, however, the adjoint equation was derived analytically, which may be challenging in more complex problems of cardiac mechanics. More recently, a new approach based on automated derivation of functional gradients via solving the corresponding adjoint system have emerged [230]. Overcoming the issue that gradient-based methods face in dealing with a large number of parameters, this approach enables one to compute the functional gradient at a computational expense that does not depend on the number of control parameters [226].

Here, we apply such a gradient-based data assimilation framework in order to fuse clinical imaging data from a cohort of healthy subjects to a biventricular mechanics model accurately and efficiently. By relating physical processes to the kinematics observed in medical images, we extracted clinically important quantities from these subject-fitted models and evaluated the sensitivity of these quantities to modeling choices such as fiber architecture and model for active contraction.

The paper is organized as follows. In section 6.2 we present the pipeline for data assimilation that includes an outline of the underlying ventricular mechanics model and solution methods. Section 6.3 presents the results of applying the framework to imaging data acquired from three healthy subjects, including a comparison of model prediction with the observed data, analysis of mechanical parameters extracted from the model, and a sensitivity analysis of model parameters to the input data. Finally, in sections 6.4 and 6.5 we discuss the performance of the framework and draw conclusions about its applicability in clinical settings.

6.2 Methods

6.2.1 Data acquisition and pre-processing

Cine magnetic resonance (MR) images of 3 healthy subjects, referred here as CASE1, CASE2 and CASE3, were acquired at the National Heart Center of Singapore and written informed consent was obtained from all participants. Three-dimensional biventricular geometries of each subject were manually segmented from the MR images at multiple cardiac time points using the medical image analysis software MeVisLab (http://www.mevislab.de).

Cavity volumes of the left ventricle (LV) and right ventricle (RV) were computed from the segmented geometries at different time points in a cardiac cycle in each subject. Using a method described in [188], these volumes were paired with normal left and right ventricular pressure wave forms from previous studies [231] to construct pressure-volume loops of the LV and RV. Based on a previous empirical study [232], LV pressure for each subject was also scaled so that the end-systolic pressure is 90% of the measured cuff pressure.

The observed regional circumferential and longitudinal Green-Lagrange strains in the LV free wall (LVFW), septum and RV free wall (RVFW) were estimated from the MR images in each subject using an hyperelastic warping technique [40], [181]. The output of this pre-processing step is used to calculate the estimated regional strain-time data. Briefly, a biventricular finite element model reconstructed from the end-systolic (template) image was registered to all other cine (target) images acquired in the cardiac cycle by minimizing the squared difference between the target and template image intensities. This ill-posed correlation problem is regularized by also minimizing a prescribed strain energy function over the mesh. We note that other regularization approaches have also been proposed, such as regularization based on incompressibility [182] or on equilibrium [184], [233]. Hyperelastic warping offers a good balance between regularization and strain estimation [181]. The implementation of the image correlation procedure is based on FEniCS [129], and is freely available.

Three-dimensional biventricular meshes of the three normal subjects were created using Gmsh with the number of elements ranging from 4000 - 8000

tetrahedral elements. The chosen reference geometries were reconstructed from MR images in late diastole, and all meshes were uniformly refined in order to perform a convergence analysis.

Rule based fibers were assigned using the Laplace Dirichlet Rule-Based (LDRB) algorithm [3]. Although previous histological studies [234] suggest that myofiber fiber helix angle varies transmurally from +60° at the endocardium to −60° at the epicardium, variability in fiber angle, nevertheless, exists between individuals. Therefore, we seek to also test how different fiber angle gradient alters the parameter estimation and the extracted outputs. More specifically, an angle $+\alpha/-\alpha$ is prescribed on the endo-/epicardium for α ranging from 30° to 80° at increments of 10°. If not otherwise specified, an angle of +60° and −60° on the endo- and epicardium respectively is prescribed. In **Figure 6.1**, we show this range of fiber fields for one of the subjects.

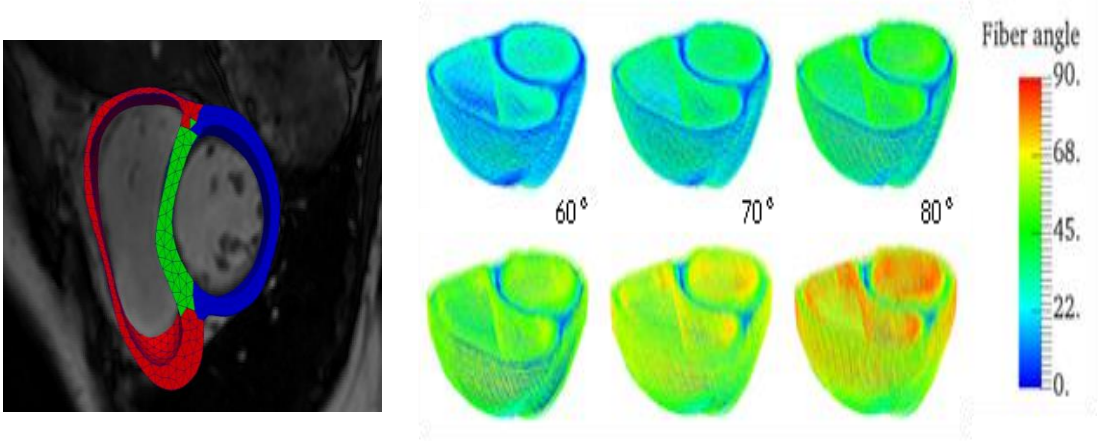

Figure 6.1. Left: finite element mesh of a biventricular geometry reconstructed from MR images separated into 3 material regions, namely, LVFW (blue), septum (green) and RVFW (right). Right: myocardial fiber orientation are assigned using the LDRB algorithm [4] with an angle $+\alpha$ and $-\alpha$ prescribed on the endocardium and epicardium, respectively. Here showing the fiber architecture for α ranging from 30° to 80° with increments of 10°, where the absolute value of the fiber angle is used as color-map.

6.2.2 Mechanical modeling

We consider a configuration of a biventricular continuum body and denote the reference and current configurations by Ω_0 and Ω, respectively. Letting X and x be the coordinates of a given material point in the reference and current configuration, respectively, we have the corresponding displacement field $U = x - X$, and the deformation gradient is given by:

$$\boldsymbol{F} = \frac{\partial \boldsymbol{U}}{\partial \boldsymbol{X}} + \boldsymbol{I} \tag{6.1}$$

Mechanics of the heart wall was described using an active strain formulation ([235]) that assumes a multiplicative decomposition of the deformation gradient,

$$\boldsymbol{F} = \boldsymbol{F}_e \boldsymbol{F}_a \tag{6.2}$$

Here, $\boldsymbol{F}_a$ is associated with an inelastic deformation resulting from the actively contracting muscle fibers, whereas $\boldsymbol{F}_e$ is associated with the elastic deformation that preserves compatibility in the tissue, and passively carrying the mechanical load. We choose $\boldsymbol{F}_a$ to have the specific form as follows:

$$\boldsymbol{F}_a = (1-\gamma)\boldsymbol{f_0} \otimes \boldsymbol{f_0} + \frac{1}{\sqrt{1-\gamma}}(\boldsymbol{I} - \boldsymbol{f_0} \otimes \boldsymbol{f_0}) \tag{6.3}$$

Where the parameter γ is associated with the relative active shortening along the muscle fibers. The same form of the active deformation gradient has previously been applied in e.g. [226], [236].

We consider the transversely Holzapfel and Ogden hyperelastic material [16] model that has the strain energy density function

$$\Psi(\boldsymbol{F}) = \frac{a}{2b}\left(e^{b(I_1-3)} - 1\right) + \frac{a_f}{2b_f}(e^{b_f(I_{4f_0}-1)^2} - 1) \tag{6.4}$$

Where the invariants are given by

$$I_1 = tr\boldsymbol{C},\ I_{4f_0} = \boldsymbol{f_0} \cdot (\boldsymbol{C}\boldsymbol{f_0}) \tag{6.5}$$

Here $\boldsymbol{C} = \boldsymbol{F}^T\boldsymbol{F}$ is the right Cauchy Green tensor, and $\boldsymbol{f_0}$ denotes the unit fiber vector field in the reference configuration. Within the active strain formulation, the strain energy depends only on the elastic deformations, and so the modified strain energy function $\Psi = \Psi(\boldsymbol{F}_e)$ was used instead。

For comparison, we also test the more frequently used active stress formulation [237]. In this formulation, the total Cauchy stress tensor is additively decomposed into a passive and an active component i.e.,

$$\boldsymbol{\sigma} = \boldsymbol{\sigma_p} + \boldsymbol{\sigma_a} \tag{6.6}$$

Where the passive stress tensor is given by

$$\boldsymbol{\sigma_p} = \frac{1}{J}\frac{\partial \Psi}{\partial \boldsymbol{F}}\boldsymbol{F}^T \tag{6.7}$$

And the active stress tensor is given by

$$\boldsymbol{\sigma_a} = T_a[\boldsymbol{f} \otimes \boldsymbol{f} + \eta(\boldsymbol{I} - \boldsymbol{f} \otimes \boldsymbol{f}] \tag{6.8}$$

Here T_a is the magnitude of the active stress and η controls the amount of transverse active stresses. Although active stresses, in principle, develop along the fiber direction, studies have shown [238] that active stresses in the transverse direction are non-negligible due to imperfect alignment of the muscle fibers. We therefore set $\eta = 0.2$ [239], and note that transverse active stresses are naturally embedded in the active strain formulation by requiring $\det(\boldsymbol{F}_a) = 1$.

Myocardium was assumed to be incompressible. The incompressibility was enforced in the model using a two-field variational approach, in which the term $-p(J-1)$ was added to the total strain energy with p denoting a Lagrange multiplier that represents the hydrostatic pressure. The deviatoric and volumetric mechanical responses were

also uncoupled by multiplicatively decomposing the deformation gradient [240]:

$$\mathrm{F} = F_{iso}F_{vol} \tag{6.9}$$

and letting the strain-energy be a function of only isochoric deformations, namely, $\Psi = \Psi(\boldsymbol{F}_{iso})$.

Ventricular base was fixed in the longitudinal direction and the biventricular geometry was anchored by constraining the epicardial surface using a Robin-type boundary condition with a linear spring of stiffness $\mathrm{k} = 0.5\mathrm{kPa/cm}^2$ [188]. Measured cavity pressure in the LV (p_{lv}) and RV (p_{rv}) were applied as a Neumann condition at the endocardial surfaces. The Euler-Lagrange equations in the Lagrangian form reads: Find $(\boldsymbol{U}, p)\epsilon\, V \times Q$ such that for all $(\delta\boldsymbol{U}, \delta p)$ and $U \cdot N)|_{\partial\Omega_{0base}} = 0$,

$$\delta\prod(\boldsymbol{U}, p) = \int_{\Omega_0}[\boldsymbol{P}\colon\nabla\delta\boldsymbol{U} - \delta p(J-1) - pJ\boldsymbol{F}^{-T}\colon\nabla\delta\boldsymbol{U}]dV + \delta\prod_{ext} = 0 \tag{6.10}$$

with

$$\delta\prod{}_{ext} = \int_{\partial\Omega_{0endo,LV}} p_{lv}J\boldsymbol{F}^{-T}\boldsymbol{N}\cdot\delta\boldsymbol{U}dS + \int_{\partial\Omega_{0endo,RV}} p_{rv}J\boldsymbol{F}^{-T}\boldsymbol{N}\cdot\delta\boldsymbol{U}dS + \int_{\partial\Omega_{0epi}} k\boldsymbol{U}\cdot\delta\boldsymbol{U}dS \tag{6.11}$$

Here $V = H^1(\Omega_0)$, completed with homogeneous Dirichlet boundary data, $Q = L^2(\Omega_0)$, $\boldsymbol{N}$ is the outward pointing unit normal and $\boldsymbol{P}$ is the first Piola-Kirchhoff stress tensor.

For an incompressible, hyperelastic, continuum body, the total Cauchy stress tensor is given by

$$\boldsymbol{\sigma} = \frac{1}{J}\frac{\partial\Psi(\boldsymbol{F})}{\partial\boldsymbol{F}}F^T - p\boldsymbol{I} \tag{6.12}$$

With the decoupling of the isochoric and volumetric deformation according to (6.9), the first term in Eq. (6.12) represents the deviatoric stresses and p is the hydrostatic

pressure. Myofiber stress was computed by first a push forward of the fiber field to the current configuration,$\boldsymbol{f} = \boldsymbol{F}\boldsymbol{f_0}$, and then an inner product with the stress tensor $\boldsymbol{\sigma_f} = \boldsymbol{f} \cdot \boldsymbol{\sigma}\boldsymbol{f}$. The average fiber stress in a given region Ω_j was computed by integrating the fiber stress over that region and dividing by the volume, i.e., $\overline{\sigma_f} = \frac{1}{|\Omega_j|}\int_{\Omega_j} \sigma_f dV$.

6.2.3 PDE-constrained optimization

The ventricular mechanics model outlined in Section 6.2.2 contains model parameters that may vary from individual to individual. Calibration of these model (or control) parameters was achieved by solving a PDE-constrained optimization problem, where we minimized a cost functional representing the mismatch between the simulated and observed data, subject to the constraint of satisfying Eqs. (6.10)-(6.11). The minimization problem can be formally stated as

$$\text{minimize } \mathcal{J}((\boldsymbol{U}, p), m) \text{ subject to } \delta\prod(\boldsymbol{U}, p) = 0 \tag{6.13}$$

Here $\mathcal{J}$ is the objective functional that we want to minimize, which depends on the state variable $(\boldsymbol{U}, p)$ and the control parameter(s) m. The state variables may also depend on the control parameters $(\boldsymbol{U}, p) = (U(m), p(m))$. To ease notation, this dependency is not explicitly stated here.

Minimization of the cost functional $\mathcal{J}$ should bring the simulated results closer to the clinical observations. Therefore, $\mathcal{J}$ should reflect a distance between the simulated results and the observed data. Given a measurement point i, let $(\boldsymbol{U}^i, p^i)$ be the simulated state variables at that point, and let m^i represents any generic model parameter, that we want to estimate. The cost functional is then given by

$$\mathcal{J}\left((\boldsymbol{U}^i, p^i), m^i\right) = \alpha\mathcal{J}_{volume}\left((\boldsymbol{U}^i, p^i), m^i\right) + \beta\mathcal{J}_{strain}\left((\boldsymbol{U}^i, p^i), m^i\right) + \lambda\mathcal{J}_{reg}(m^i) \quad (6.14)$$

The first two terms represent the mismatch between simulated and observed volumes and strains, respectively, whereas $\mathcal{J}_{reg}$ is a regularization term that penalizes non-smooth values of the control parameter m^i for numerical stability. The weights α, β and λ control what terms is favored in the optimization.

The simulated cavity volume was given by

$$V = -\frac{1}{3}\int_{\partial\Omega_{0endo}}(\boldsymbol{X} + \boldsymbol{U})J\boldsymbol{F}^{-\boldsymbol{T}}\boldsymbol{N}dS \quad (6.15)$$

This equation holds as long as the base remains flat and is located at the $x = 0$ plane. We let J_{volume} be the sum of the squared relative volume error in each chamber:

$$\mathcal{J}_{volume}\left((\boldsymbol{U}^i, p^i), m^i\right) = \left(\frac{{V_{LV}}^i - \widetilde{V_{LV}}^i}{{V_{LV}}^i}\right)^2 + \left(\frac{{V_{RV}}^i - \widetilde{V_{RV}}^i}{{V_{RV}}^i}\right)^2 \quad (6.16)$$

Here $(\widetilde{V_{LV}}^i, \widetilde{V_{RV}}^i)$ and $({V_{LV}}^i, {V_{RV}}^i)$ are the simulated and measured cavity volumes, respectively.

Volumetric averaged strains were computed in each material region (i.e., LVFW, RVFW and septum) using end-diastolic (ED) as a reference. Letting F_{ED} be the deformation gradient tensor associated with ED, the Green-Lagrange strain tensor with ED as reference was given by $\tilde{E} = \frac{1}{2}(\boldsymbol{F}^{\boldsymbol{T}}{\boldsymbol{F}_{\boldsymbol{ED}}}^{-\boldsymbol{T}}\boldsymbol{F}{\boldsymbol{F}_{\boldsymbol{ED}}}^{-1} - \boldsymbol{I})$. Averaged normal strains along the circumferential direction $\boldsymbol{e_{circ}}$ in material region Ω_j was defined by

$$\widetilde{\varepsilon_j} = \frac{1}{|\Omega_j|}\int_{\Omega_j}\boldsymbol{e_{circ}}\cdot\widetilde{\boldsymbol{E}}\boldsymbol{e_{circ}}dV \quad (6.17)$$

Correspondingly, the strain mismatch functional was given by the total squared error between the simulated circumferential strain $\widetilde{\varepsilon_j}^i$ and the measured circumferential

strain ${\varepsilon_j}^i$ over all material regions:

$$\mathcal{J}_{strain}\left(\left(\boldsymbol{U}^i, p^i\right), m^i\right) = \sum_{j=1}^{N} \left({\varepsilon_j}^i - \tilde{\varepsilon}_j^{\,i}\right)^2 \tag{6.18}$$

Finally, the regularization term was defined as the total squared distance from the mean value, that is if $m^i = (m_1, \cdots, m_N)$, then

$$\mathcal{J}_{reg}\left(m^i\right) = \sum_{j=1}^{N} \left({m_j}^i - \bar{m}^i\right)^2 \quad \text{with } \bar{m}^i = \frac{1}{N}\sum_{j=1}^{N} {m_j}^i \tag{6.19}$$

As noted above, the purpose of this term is to avoid numerical instabilities by penalizing large variations in the control parameters.

The functional gradient

$$\frac{d\mathcal{J}}{dm} = \frac{\partial \mathcal{J}}{\partial m} + \frac{d\mathcal{J}}{dw}\frac{\partial w}{\partial m} \qquad w = (\boldsymbol{U}, p) \tag{6.20}$$

Points in the direction of steepest descent and is required in gradient-based optimization methods. While the terms $\frac{\partial \mathcal{J}}{\partial m}$ and $\frac{d\mathcal{J}}{dw}$ are typically straightforward to compute, the term $\frac{\partial w}{\partial m}$ cannot be computed easily, since the state variable w can only be determined by solving the force-balance equation Eq. (6.10). Specifically, estimating this term with N control parameters using a finite difference approach will require one to solve the (typically computational expensive) force-balance equation N+1 times, becoming impractical when N is large. Instead, it is possible to transform the system of equations into its adjoint system, where the gradient is given by

$$\frac{d\mathcal{J}}{dm} = \frac{\partial \mathcal{J}}{\partial m} - z^* \frac{\partial(\delta \prod\ )}{\partial m} \tag{6.21}$$

With $(.)^*$ referring to the adjoint (for Hermitian transpose) and z is the solution of

$$\left(\frac{\partial(\delta \prod)}{\partial \boldsymbol{w}}\right)^* z = \left(\frac{\partial \mathcal{J}}{\partial m}\right)^* \tag{6.22}$$

We can therefore solve the adjoint equation first Eq. (6.22), and then compute the

functional gradient by plugging the solution into Eq. (6.21). Hence, computing the functional gradient using the adjoint approach requires only one additional solve of a linearized system that is independent of the number of control parameters.

6.2.4 Parameter estimation

The pipeline for fitting the model to patient data was divided into two sequential phases; a passive phase where we estimated the material parameters that define the passive behavior of the myocardium, and an active phase where we estimated the amount of active contraction. In both cases, the control parameters were spatially resolved. During the passive phase the control parameter was allowed to vary spatially on the LV (LVFW + septum) and RV segments, while in the active phase the LV was separated into LV free wall and septal segments, which provided additional degrees of freedom to allow for non-homogeneous LV contraction.

Geometries used in the simulation were reconstructed from medical images. These geometries are, in principle, not load-free. Hence, we need to estimate the unloaded (zero pressure) geometries, which will revert back to the original reconstructed geometries when loaded with the measured pressure. Several methods exists for estimating the unloaded geometry [241], [242]. Among the most simplest ones is the backward displacement method [243], [244] that can also be used to incorporate residual stresses into the finite element models by simulating tissue growth [245]. Nevertheless, this inverse problem (of finding the unloaded geometry) has been shown to produce non-unique solutions, especially when buckling is present [241], although relaxation techniques can be used to improve convergence and stability [246]. For the case of a biventricular geometry, buckling

may occur due to the thin RVFW and a high RV pressure. For this reason, we choose a simpler approach to estimate the unloaded configuration. As shown in the left of **Figure 6.2**, we start by applying one iteration of the backward displacement method with initial values prescribed for the material parameters followed by the material parameter estimation as outlined below. This will result in a deflated geometry as shown in the right of **Figure 6.2**.

Four material parameters, i.e., a, a_f, b and b_f from Eq. (6.4) have to be estimated in the passive phase. Due to the sparsity of passive data used for the optimization, if we let all these parameters vary freely, we may end up in a situation where multiple parameter sets will equally minimize the cost functional, and the optimal control will depend heavily on the initial guess of the optimization.

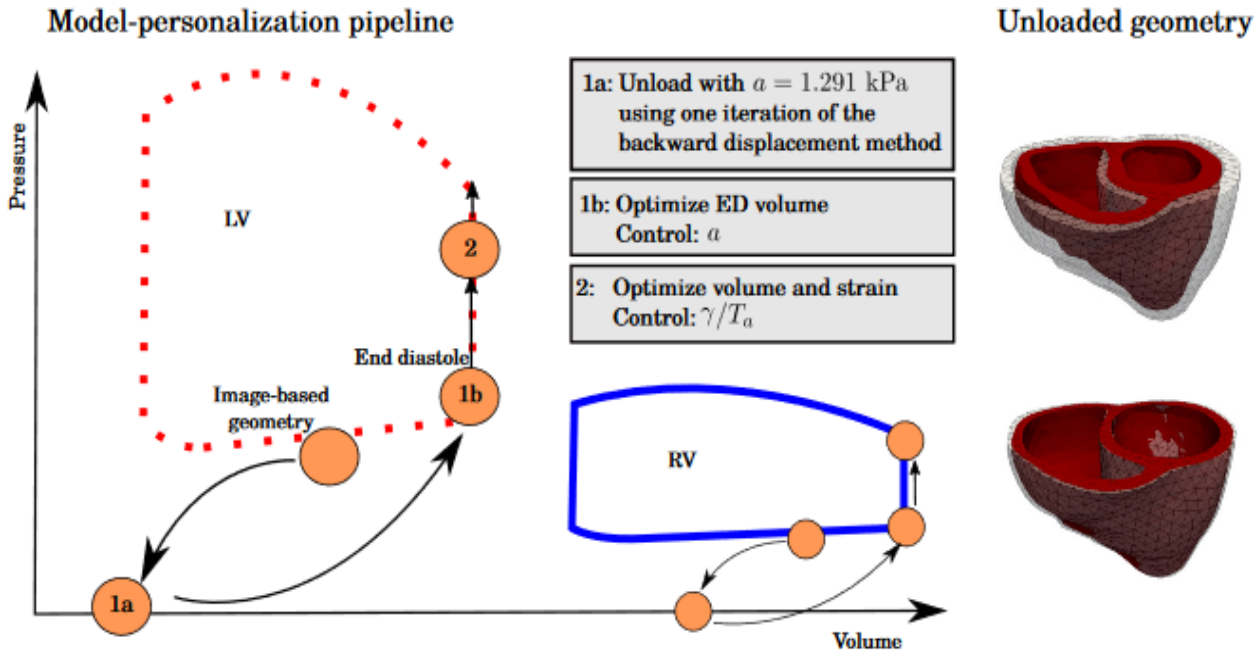

Figure 6.2. To the left we see the model-personalization pipeline. To the right we show a comparison of the unloaded geometry for CASE3. The upper figure shows the resulting unloaded, zero pressure geometry in red and the original image-based geometry in transparent, while the bottom figure shows the unloaded geometry, inflated to the target pressure in the image-based geometry, and the original image-based geometry in transparent for comparison.

We therefore restricted our control parameter to be only the linear isotropic parameter with an initial guess $a = 1.291kPa$, and have the remaining parameters fixed according to [220]. The weights were set to $\alpha = 1.0, \beta = 0.0$ and $\lambda = 10^{-6}$ in Eq. (6.14) so that only ED volumes were used for fitting. Since fitting the left and right ventricular end-diastolic volumes might require different material properties of the left and right ventricular wall, the parameter a was spatially resolved with one parameter associated with the LV (LVFW + septum) and one parameter associated with the RVFW.

In the active phase. The optimized passive material parameters were fixed and the relative active fiber shortening γ in Eq. (6.3) was chosen as control parameter. For this phase, the weights in Eq. (6.14) were set to $\alpha = 0.1, \beta = 1.0$ and $\lambda = 10^{-4}$, so that both strain and volume are considered in the optimization. This choice of weighting was made ad hoc, reflecting the relative size of the different terms in the cost functional. It should also be noted that the volume functional in Eq. (6.16) is a relative error while the strain functional in Eq. (6.18) represents a total error. The cost function parameter values were taken from [226], where they were chosen based on an L-curve type analysis.

For each time point, we estimated γ locally in the LVFW, RVFW and septum. The initial guesses for the optimization were set to zero in the first iteration. In subsequent iterations, the initial guesses were set to the optimized values found in the previous iteration. Note that in the case when active stress formulation was used instead, the parameter T_a in Eq. (6.8) was used as the control parameter and estimated in a similar fashion. A schematic illustration of the full optimization pipeline

is provided to the left in **Figure 6.2**. The control parameter in the active phase represents an index of contractility ([247]), meaning that the higher the value of the control parameter, the more forcefully the myocardium is trying to contract against the external loads. To separate between the LV and RV contractility, we extracted the average value of this control parameter in these two segments.

6.2.5 Implementation details

The force-balance equations of this incompressible nonlinear elasticity problem were solved using the finite element method with Lagrange elements. More specifically, the displacement and hydrostatic pressure fields were interpolated using piecewise quadratic and linear Lagrange basis functions, respectively. These mixed elements, known as the Taylor-Hood finite elements [248], are known to satisfy the discrete inf-sup condition [249] and leads to a stable discretization. The solver was implemented in FEniCS, which is an open-source platform for solving PDEs using the finite element method. Nonlinear systems of equations were solved using Newton's method, and a distributed memory parallel LU solver [250] was used to solve the linear systems. To solve the optimization problem Eq. (6.13) we applied a sequential quadratic programming algorithm (SQP) [251]. This gradient-based optimization algorithm requires the functional gradient Eq. (6.20). This gradient was computed by solving an automatically derived adjoint equation using dolfin-adjoint [230]. The full source code is publicly available.

6.3 Results

In this section we present the results from the model personalization process. Results of the data matching are presented in section 6.3.1, together with a validation of the model and analysis of the solver performance. To validate the model we compare the simulated and measured longitudinal strain which was not used in the optimization. In section 6.3.2 we present the results of the extracted mechanical features such as indices of contractility and fiber stress. We also investigated the efficiency of the algorithm and the effect of mesh refinement, and found that the chosen refinement level was sufficient to yield convergent solutions.

6.3.1 Data assimilation, validation and solver performance

The simulated and measured pressure-volume (PV) loops of the RV and LV, as well as circumferential strain in the LV, septum and RV are shown in **Figure 6.3**. We found that the fit of the data was highly dependent on the choice of fiber angles, which affects both volume change and circumferential shortening. Plotting the average value of the volume cost functional (as defined in Eq. (6.16)) for each choice of fiber angles (see the upper right panel in **Figure 6.3**) revealed that the optimal value of α lies in the range $70^\circ - 80^\circ$ for all 3 cases.

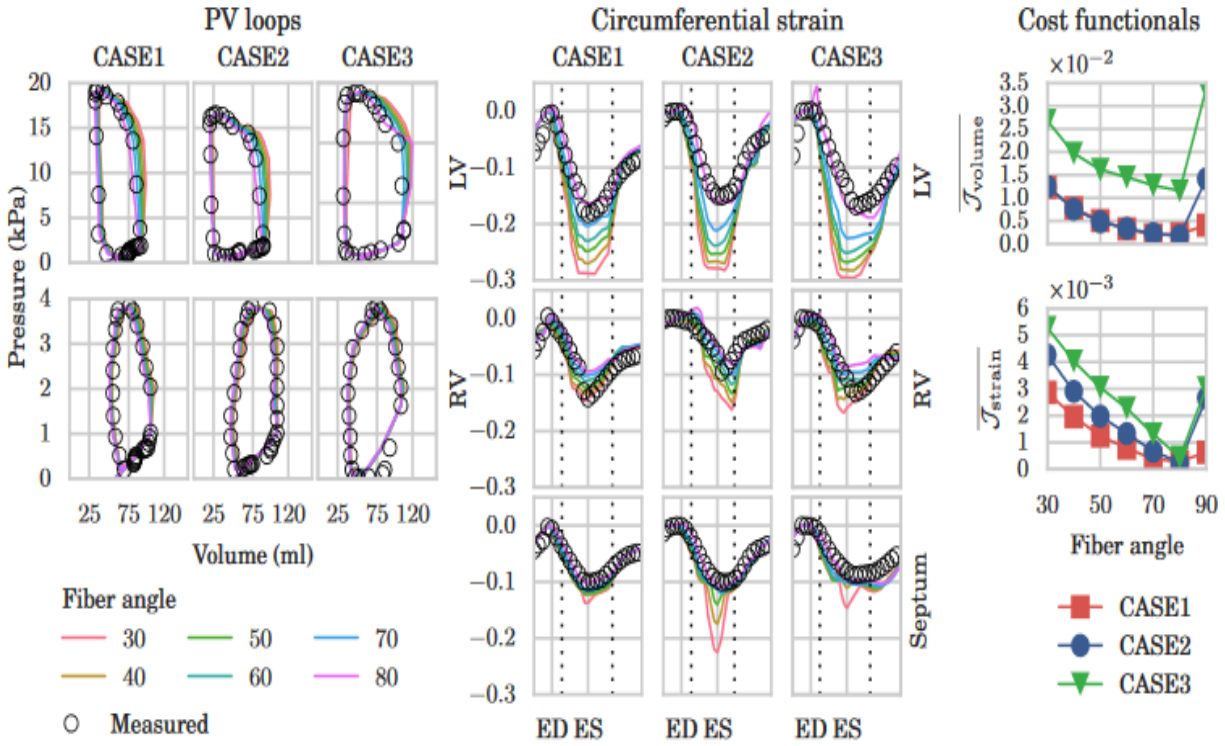

Figure 6.3. Results of the gradient-based minimization of model-data mismatch for different choice of fiber angles. Left: simulated (color lines) and measured (black circles) PV loops in the LV (top row) and RV (bottom row). Center: simulated (color lines) and measured (black circles) circumferential strain in the LV (top row), RV (middle row) and septum (bottom row). Right: average values of cost functional for the volume (top row) and strain (bottom row), for each choice of fiber angle.

Although available, we chose not to use longitudinal strain data in the optimization. Therefore, the comparison of model-predicted longitudinal strain with the measurements serves as a validation of the model-personalization process. The simulated and measured LV longitudinal strain curves are shown in **Figure 6.4**. We note that the fit in all regions was again highly sensitive to the choice of fiber angle. Choosing $\alpha = 70^{\circ}$ produced the best fit for the LV longitudinal strain for CASE1 and CASE3, while an angle 60° gave the best fit for CASE2. The Septal and RV longitudinal strain was best fitted with $\alpha = 80^{\circ}$.

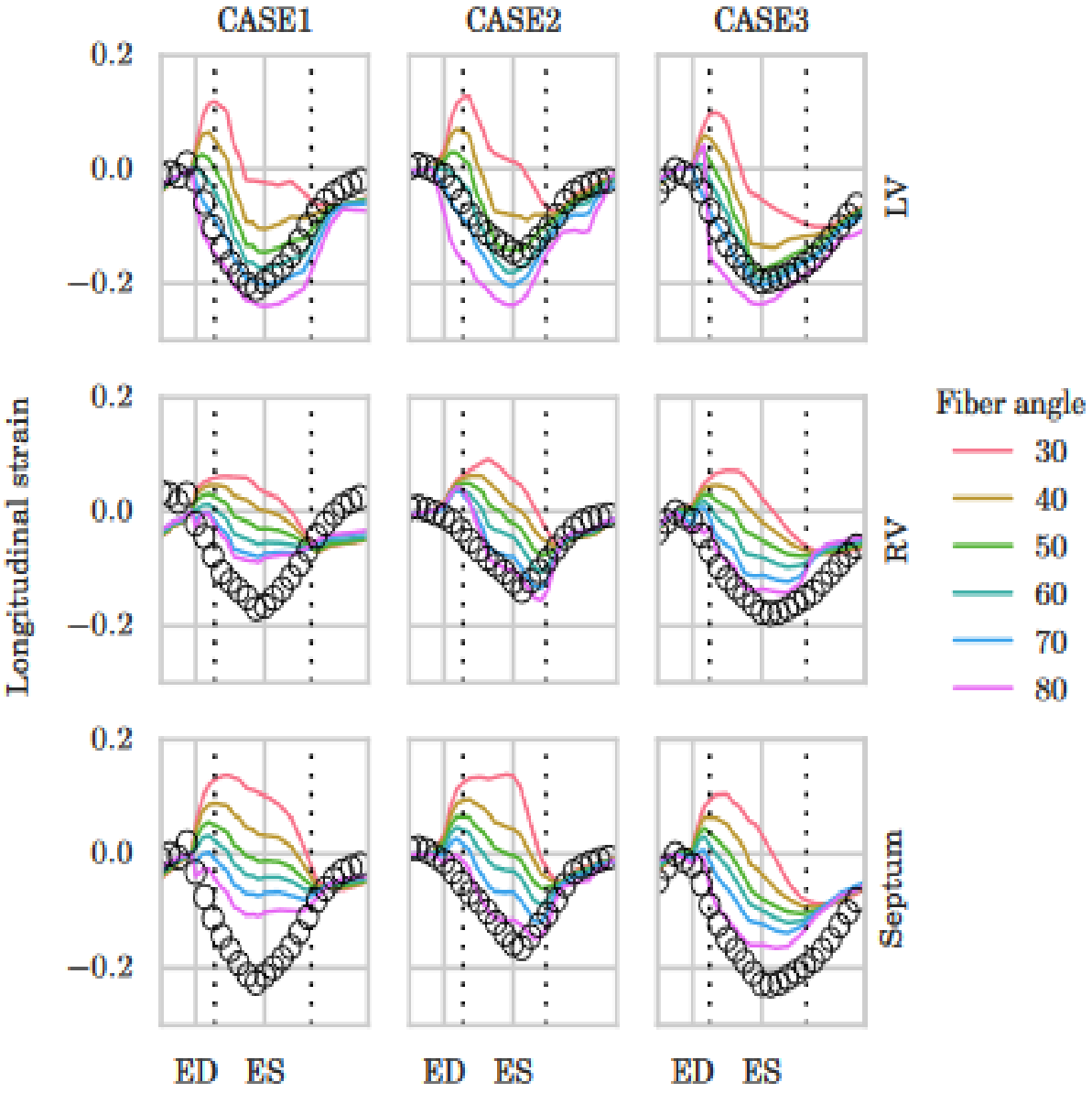

Figure 6.4. Validation of the model-personalization process using simulated and measured longitudinal strain which was not used in the optimization. Upper, middle and lower panel show the longitudinal strain curves for different choice of fiber angles in the LV, RV and septum respectively.

6.3.2 Mechanical analysis

6.3.2.1 Cardiac contraction

The estimated active strain parameter γ in Eq. (6.3), which served as the control parameter during the optimization in the active phase, is plotted for various fiber angles to the left in **Figure 6.5**. This parameter varies regionally in the LVFW, septum and RVFW, but is shown here as an average in the LV containing LVFW + septum (top) and RV containing only RVFW (bottom). As shown in the figure, time-variation and magnitude of γ were similar in the 3 cases and insensitive to the prescribed fiber angles. Time traces of the active strain parameter γ found in the LV and RV are plotted together for the 60° fiber angle case in the left of Figure 6.6 in order better compare their differences. A similar plot of the active stress parameter T_a in logarithmic scale is also shown in the same figure. As shown in the figure, the time-variations of T_a and γ, which are indices of cardiac contractility, were largely similar between the LV and RV with peak values located approximately at end-systole. Peak values found in the RV were, however, lower than those found in the LV. These findings were consistent across all the 3 cases.

6.3.2.2 Fiber stress

Time traces of the average Cauchy fiber stress are shown on the right of **Figure 6.5** for different fiber angle variations. Only very small variations in the average fiber stress were found with respect to the choice of fiber angle in the optimization process. Snap shots of the fiber stress distribution at ED and ES are plotted in **Figure 6.7** for the 60° fiber angle case. Regional variation of fiber stress was largely consistent between the 3

cases with pockets of high and low stresses found, respectively, at the apex-epicardial and endocardial regions at ES. In **Figure 6.6**, we compare the average fiber stress time variation found using the two different active contraction formulations, either active strain or active stress. As shown in the figure, fiber stress in the RV computed using active stress and active strain formulations behaved similarly with time. Similar regional variation was also found where both formulations predicted higher fiber stress in the LV than the RV. Peak fiber stress predicted in the LV, however, was different in the two formulations with higher stress occurring at isovolumic relaxation in the active stress formulation. The specific average value of the end-diastolic and end systolic fiber stress for the case of a 60° fiber angle are displayed in **Table 6.1**, showing small variability between patients, despite differences in individual PV loops.

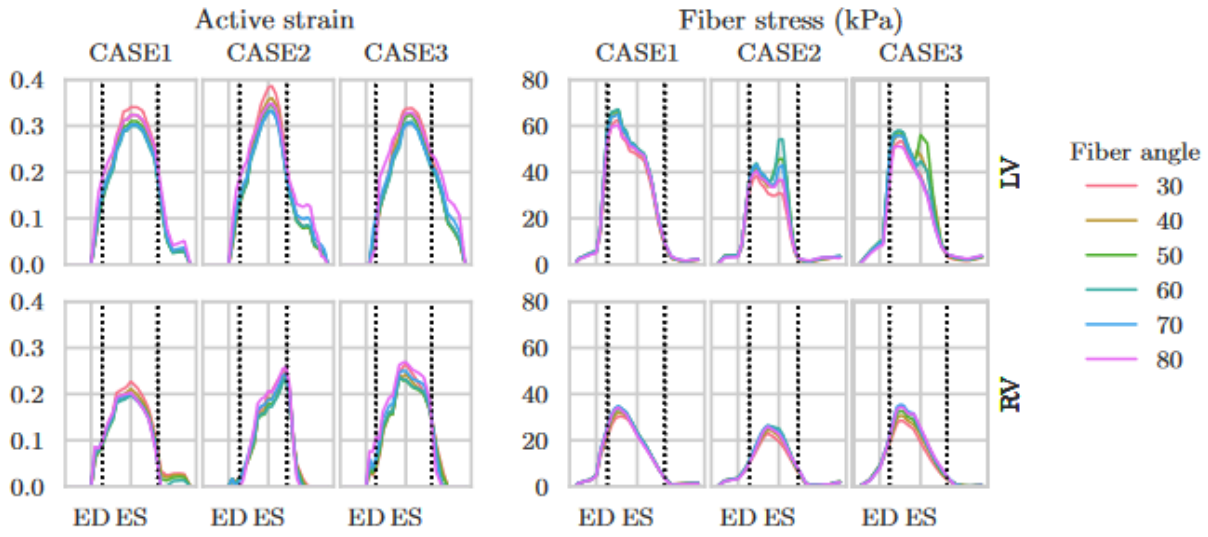

Figure 6.5. To the left, average traces of the active strain parameter γ in Eq. (6.3) in the LV (top) and RV (bottom) for different choice of fiber angle. To the right average traces of Cauchy fiber stress in the LV (top) and RV (bottom) for different choice of fiber angle. The fiber angles were defined symmetrically across the wall with a negative angle on the epicardium and a positive angle on the endocardium ranging from $30^\circ - 80^\circ$ with increments of 10°. On the $x-$axis we plot the normalized time with respect to end-diastole (ED) and end-systole (ES). Horizontal dotted lines indicate timings of opening of the aortic and mitral valve.

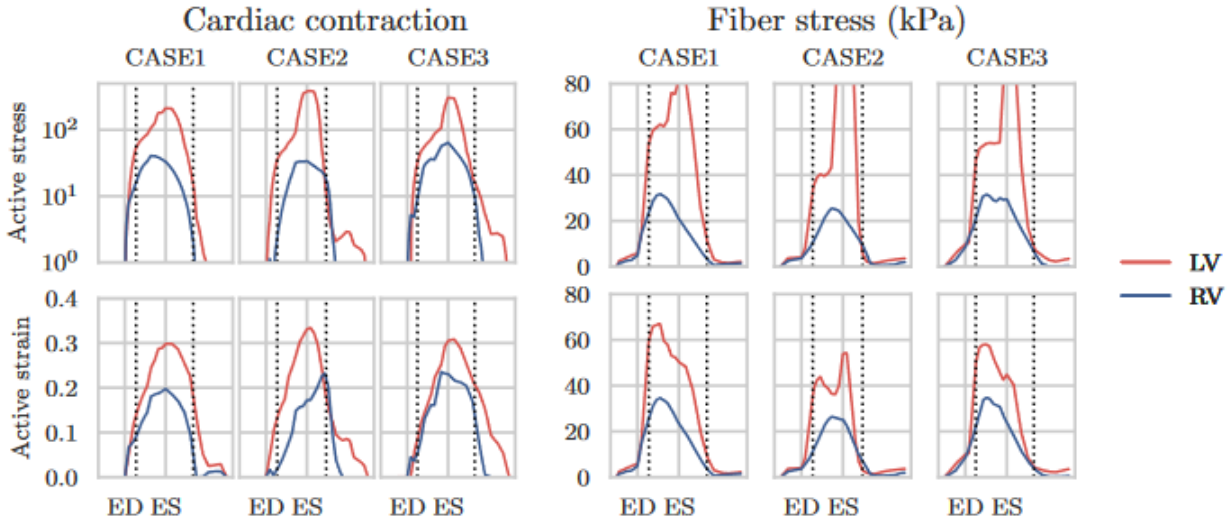

Figure 6.6. Comparison of fiber stress and cardiac contraction using the active strain and active stress approach using 60° fiber angle. To the left, average traces of the active stress (top) parameter $\boldsymbol{T_a}$ in Eq. (6.8), and the active strain (bottom) parameter in 3. The active stress parameter, with unit kPa, is plotted on a logarithmic scale for easier comparison with the active strain parameter. To the right, estimated Cauchy fiber stress using the active stress (top) and active strain formulation (bottom). On the $x-$axis we plot the normalized time with respect to end-diastole (ED) and end-systole (ES). Horizontal dotted lines indicate timings of opening and closing of the aortic valve.

Table 6.1. Average LV and RV fiber stress (kPa) at end-diastole and end-systole

Case ID	LV (ED)	RV(ED)	LV(ES)	RV(ES)
Case1	5.76	4.87	48.3	19.2
Case2	4.04	3.57	54.4	22.7
Case3	9.94	8.34	40.3	18.2
Average ± std	6.58 ± 2.48	5.59 ± 2.01	47.65 ± 5.74	20.03 ± 1.91

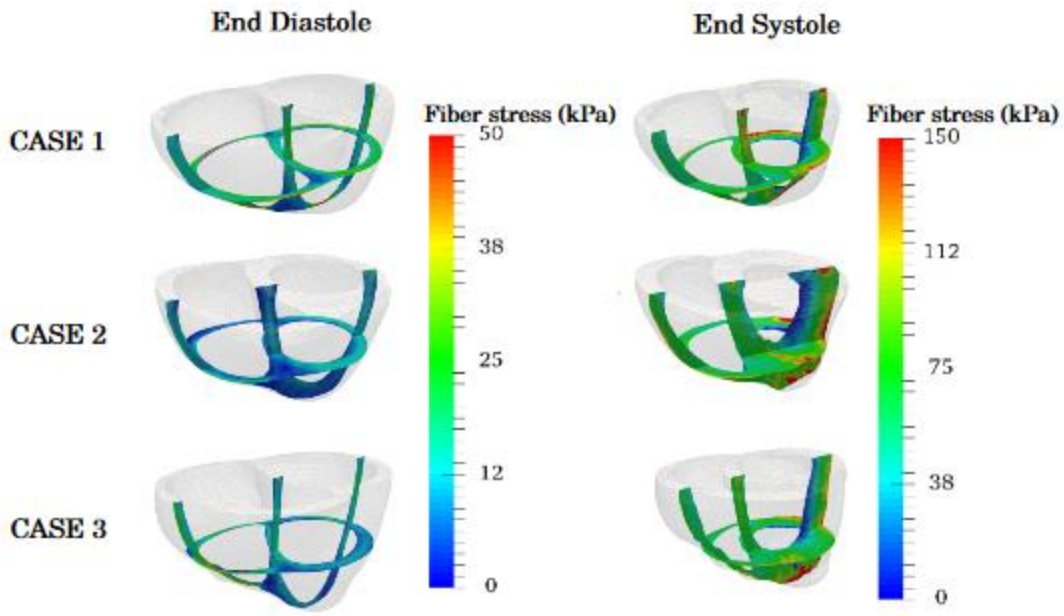

Figure 6.7. Snap shots of the end-diastolic and end-systolic configuration and the estimated fiber stresses shown as color-map

6.4 Discussion

In this study, we have presented a novel and highly efficient method for non-invasive personalization of an image-based biventricular mechanics model based on regional measurements of circumferential strain, as well as global measurements of volumes and pressures in the LV and RV. A gradient based optimization method was used to minimize the model-data mismatch by solving a PDE-constrained optimization problem for each measurement point in order to calibrate model parameters. Passive material parameters and an unloaded (zero-pressure) geometry were estimated using the biventricular geometry that was reconstructed from MR images acquired at late diastole. Time variation of an active contraction parameter was estimated throughout the cardiac cycle starting from ED. This framework was applied using measurements from three

normal subjects to extract estimates of regional fiber stress as well as indices of myocardial contractility. Sensitivity analysis of the model outputs with respect to the choice of fiber angle distribution and active formulation were also conducted. The described framework is effective and efficient in capturing cardiac mechanical behavior throughout the cardiac cycle, and gave low patient-to-patient variability in the extracted mechanical features. As such, it has potential clinical utility in the quantification of contractile function and myocardial stress *in vivo* and the potential differentiation of pathological states.

6.4.1 Data compatibility and multi-objective optimization

The objective functional in problem Eq. (6.13) consists of a weighted sum of different objective functionals. Such problems are referred to as multi-objective optimization problems [252]. While it is possible to perfectly match the strain or volume data individually with the chosen control parameters (data not shown), there is expected to be a trade-off when fitting both the volume and strain data in a combined objective functional. In such cases, a single, unique optimum does not always exist, but rather a family of so called Pareto optimal solutions can be found [252]. The particular solution found will depend on the chosen weights of each objective. In a previous study [226], the weights in the total functional given in Eq. (6.14) were determined by performing an exhaustive search, testing several combinations of weights of the strain and volume functionals, and choosing the corner-point of strain versus volume error curve. However, the weights will depend on the data source, and in our case choosing the weights proposed in [226], resulted in an excellent fit of the volume, while a relatively poor fit of the strain, and hence a higher weight was chosen for the strain. Nevertheless, neither

was captured exactly, and which data source is more important for model utility remains to be determined. In addition, other general methods for solving multi-objective optimization problems [252] may be superior to the weighted sum method used here, and will be considered in future studies.

6.4.2 Contractility

Higher value of the active strain parameter γ or the active stress parameter T_a indicates that the myocardium is contracting more forcefully and our results also suggest that the LV generates a higher contractile force per myocardial volume than the RV. One of the underlying mechanisms that modulate the contractile forces is calcium dynamics [237], [235], and while T_a and γ cannot be directly compared to the calcium concentration because of the difference in units, their time traces have similar shapes when compared to the calcium transient. Further investigation of these estimates is needed, but we hypothesize that these measurements may provide useful biomarkers. Due to the observed consistent results in normal patients, even for wide ranging PV loops, these estimates of contractility could therefore potentially serve as important diagnostic estimates in cases where disease alters myocardial contractility.

6.4.3 Fiber stress

As there is no direct way to measure myocardial fiber stresses, we have compared our results with other patient specific modeling studies. The range of reported values for humans are broad, and are mostly confined to the LV. For example, [211] reported fiber stress computed at ED (2.21 ± 0.58kPa) and ES (16.64 ± 4.73kPa) in normal humans, whereas [253] conducted a stress analysis on healthy biventricles and found that wall stress at ES was 65.7 ± 12.3 kPa in the LV and 23.6 ± 14.2 in the RV.

Our estimated average fiber stresses (**Table 6.1**) are well within the range of values reported in these studies. Fiber stress distributions at ED and ES (**Figure 6.7**) are also consistent in the three subjects investigated here. Furthermore, our results also show small variations in fiber stress with respect to the choice of fiber field. Fiber stresses obtained from active strain and stress formulations are also comparable during late diastole and early systole. A large difference in the fiber stress between these two formulations, however, can be found at late systole and during the isovolumic relaxation when the ventricles are in their most compressed state. In particular, the active stress formulation produces elevated stresses during this time interval. We found that the elevated stresses are always accompanied by very high hydrostatic pressure p, suggesting that the enforcement of incompressibility, which does not hold in vivo due to blood perfusion in the myocardial wall, is causing this artifact. Future studies are needed to examine the effect of compressibility to our results.

6.4.4 Fiber angle sensitivity

In this work, we applied a rule-based algorithm [4] to assign myocardial fiber orientations to the biventricular geometries, and investigated the sensitivity of the data matching and the extracted mechanical features to the choice of fiber field. Different fiber fields, in which the fiber angle varies linearly across the myocardium wall from α at the endocardium to $-\alpha$ at the epicardium were tested, for the range $30^\circ \leq \alpha \leq 80^\circ$. Our results show that α has to be in the upper part of the range i.e., $70 - 80^\circ$, in order to fit the PV loop and circumferential strain measurements simultaneously. The validation study (section 6.3.1), where we compared our model results with the longitudinal strain, confirms this finding.

This highlights a major challenge in building accurate mechanics models of the myocardium. The choice of fiber field is very important, as it controls the amount of longitudinal and radial shortening during contraction. Unless the correct fiber field is used, strain measurements cannot be reproduced simultaneously in the model with the measured pressure volume relationships. Accurate measurements of the underlying ventricular microstructure are lacking, however, and therefore, rule-based methods ([4]) are often the only alternative to prescribe muscle fiber field in subject-specific modeling of cardiac mechanics. Our fundamental knowledge of the myocardial architecture is based largely on early histological studies [234], which found that the muscle fiber orientation varies linearly across the myocardial wall with an angle $\alpha = 60^\circ$ at the endocardium $\alpha = -60^\circ$ at the epicardium. This fiber field is often prescribed in ventricular models without questioning. On the other hand, diffusion tensor MRI (DT-MRI) is now becoming an important tool to measure fiber orientations and could potentially do so *in vivo* [254].

More recent histological studies [255] on the canine left ventricle have shown that the muscle fibers are more longitudinally oriented at the sub-endocardium and sub-epicardium than those obtained using DT-MRI, and such fiber orientation can better reproduce the longitudinal motions observed in the experiments [256]. Our results support this finding.

A few hypotheses on the basis of cardiac muscle fiber orientation in the ventricles have been put forward. For example, it has been hypothesized that myocardial fiber orientations adapts to achieve a minimal fiber-cross fiber shear strain during the cardiac cycle [257]. While our results showed that the active strain parameter γ varied a little with

respect to the different fiber angle α prescribed in the model, they also show that the peak active strain γ is lowest when α lies between 60° and 70° in all 3 cases. This finding suggests that the tight range of α found here is optimal in the sense that the active shortening necessary to produce the same stroke volume is at its minimum.

6.5 Limitations

In this work, we clearly see a variability of model-data fit with respect to choice of the fiber angle, suggesting that the fiber field can be calibrated to better fit the data. Here, we have only prescribed a linear transmural fiber angle variation that has opposite signs at the endo- and epicardium in both LV and RV. Dissection studies, however, generally found that the fibers are more circumferentially oriented at the sub-epicardium and more longitudinally orientated at the sub-endocardium in the RV [258]. This suggests that one should also consider non-symmetric fiber fields across the wall as well as different fiber field in the LV and RV. We seek to investigate these issues in future studies, possibly together with in vivo measures of fiber angles.

As noted above, the constants that balance the terms of the cost functional Eq. (6.14) were adjusted based on a previous study [226] of a single LV, where an L-curve type analysis was performed to estimate an optimal set of weights. Since the present study also considers the RV and the current cost functional form differs from the LV case, it is likely that these differences may affect the optimal choice of weight parameters. Hence, although the chosen parameter values gave good results for our applications here, there may exist even better choices.

While we were able to obtain stress measures across a small cohort of healthy subjects that were both internally consistent as well as in broad agreement with other published studies, the effect of our modelling assumptions remains to be determined. Here we used an incompressible model of the myocardium, even though it is well known that the myocardium is compressible due perfusion of blood. Future studies should investigate the role of compressibility, and in particular how fiber stress is altered when the material is allowed to compress. We clearly see stress effects related to the hydrostatic term in our model, and this will be investigated more closely in future studies. Residual stresses are hypothesized to be important in stress estimation in soft biological tissue [259], and can be incorporated into the finite element model [260],[245]. Because it has been shown in a previous study that residual stresses have little effects on ventricular function [261], they were not considered in the present study. Nevertheless, the effect of including residual stresses in the estimation of fiber stress and contractility remains to be investigated in future studies.

The late diastolic pressure-volume curve is fitted by estimating one material parameter, while fixing the remaining parameters to previously reported values [220]. This is a limitation in our study, and future studies will be geared towards reducing the need for fixing these model parameters by incorporating more clinical data or by revising the constitutive model. In particular, the incorporation of diastolic strains may be useful in more clearly defining material properties.

The simple estimation of unloaded configuration using only one iteration of the backward displacement method can be used with different initial material parameters and still recapitulate the end-diastolic volumes with different optimized material parameters.

Several studies have jointly estimated the unloaded left-ventricular geometry and material parameters [220], [247], [262], but estimation of the unloaded configuration with bi-ventricular geometries is not a well-posed problem, since buckling of the RV free wall might occur. More work on formulating well-posed algorithms for determining the unloaded configuration should be considered in future studies.

Finally, in this study we only considered three normal subjects, and in the future we would like to apply this framework to more individuals and use it to study larger cohorts as well as patients with cardiac pathology.

CHAPTER 7

PATIENT DATA ASSIMILATION ANALYSIS SHOWS AN INVERSE LINEAR RELATIONSHIP BETWEEN RV CONTRACTION AND REMODELING IN PULMONARY ARTERIAL HYPERTENSION

Abstract

Pulmonary arterial hypertension (PAH) causes an increase in the mechanical loading imposed on the right ventricle (RV) that results in progressive changes to its mechanics and function. Here, we quantify the mechanical changes associated with PAH by assimilating clinical data consisting of reconstructed 3D geometry, pressure and volume waveforms as well as regional strains measured in PAH patients (n= 12) and controls (n= 6) within a computational modeling framework of the ventricles. Modeling parameters reflecting regional passive stiffness and load-independent contractility as indexed by the tissue active tension were optimized so that simulation results matched the measurements The optimized parameters were compared with clinical metrics to find usable indicators associated with the underlying mechanical changes. Peak contractility of the RV free wall (RVFW) $\gamma_{RVFW,max}$ was found to be strongly correlated, and had an inverse relationship with the RV and left ventricle (LV) end-diastolic volume ratio (i.e., RVEDV/LVEDV) ($\gamma_{RVFW,max}$ = -0.13(RVEDV/LVEDV) + 0.44, R^2 = 0.77). Correlation with RV ejection fraction (R^2 = 0.50) and end-diastolic volume index (R^2 =0.40) were comparatively weaker. Patients with RVEDV/LVEDV ≥1.5 had 18% higher $\gamma_{RVFW,max}$ (P = 0.09) than that of the control whereas those with RVEDV/LVEDV <1.5 had 25% lower $\gamma_{RVFW,max}$ (P<0.05). On average, RVFW passive stiffness increased progressively with the degree of remodeling as indexed by RVEDV/LVEDV and RVFW myofiber stress was increased by 49% only in patients with RVEDV/LVEDV ≥1.5 (P = 0.14). These results provide the mechanical basis of using RVEDV/LVEDV as a clinical index for delineating disease severity and estimating RVFW contractility in PAH patients.

7.1 Introduction

Pulmonary arterial hypertension (PAH) is a complex disorder caused by an increased vascular resistance in the pulmonary arterial circulatory system. As a consequence, pressure becomes elevated in the pulmonary artery and the right ventricle (RV). Unlike systemic hypertension, PAH is difficult to detect in routine clinical examination; the current gold standard for diagnosing PAH is through invasive right heart catheterization [263]. Because of the difficulty in detecting PAH, the current estimated prevalence of this disease (15 to 50 per million) is most likely underestimated [264]–[266]. Perhaps also because of this difficulty, PAH is arguably less well-studied compared to systemic hypertension, and there are currently no effective treatments for PAH. Existing treatments of PAH have so far been confined to relieving the symptoms and attenuating the disease progression [267]. As the disease progresses, the RV remodels both structurally and geometrically, becomes dysfunctional as a result, and eventually this progression leads to decompensated heart failure and death.

A significant part of our current understanding of the ventricular mechanical alterations due to PAH has been developed using animal models [59], [60], [268]–[270]. Animal models, however, may not fully reproduce the pathologies found in humans [271]. Human studies have so far been largely confined to measuring ventricular function of PAH patients at the global level [62]. Specifically, RV contractility and wall stresses are typically quantified globally using the maximal elastance (Emax) [272], [273] (maximum value of the ratio of ventricular pressure to volume during the cardiac cycle), and Laplace's law [274], respectively. The use of Laplace's law is, however, likely to be inaccurate when applied to the RV because of its irregular geometry [274]; similarly, the

accuracy of Emax estimated using single beat methods (because manipulation of venous return is difficult in practice [272]) has been questioned [275], [276]. On the other hand, while magnetic resonance (MR) and echo imaging can quantify regional (including RV) myocardial strain or motion in vivo [187], [277], [278], strain is a load-dependent quantity and not truly a measure of myocardial contractility. As described by Reichek [279], the popular notion of equating myocardial contractility with strain measures (that are load dependent) is "*off the mark [and] if contractility means anything, it is an expression of the ability of a given piece of myocardium to generate tension and shortening under any loading conditions*".

Mathematical modeling offers an opportunity to overcome this limitation through direct quantification of both passive and active mechanical interactions under varying loading conditions. Such modeling has been heavily used to assess left ventricular dynamics, and a small number of computational modeling studies has been conducted to investigate alterations of the RV mechanics in PAH [188], [280], [281]. These studies are, however, limited either by the use of non-human (rat) PAH data [281], the lack of consideration of patient-specific RV geometry [280], or the failure to take into account of the variability across PAH patients [188]. Consequently, there exists a gap in our current understanding on the changes in RV mechanics during the progression of PAH in humans. Here, we seek to close this gap by using a recently developed gradient-based data assimilation method [282] to evaluate patient-specific regional myocardial contractility and ventricular wall stresses from clinical PAH data. Specifically, we seek to answer the following three questions: First, is myocardial contractility, as indexed by the load-independent active tension generated by the tissue, altered regionally in PAH? Second,

are ventricular wall stresses, particularly in the RV, altered regionally in PAH? Third, how are myocardial contractility and ventricular wall stresses associated with the progression of remodeling in PAH? We believe that answering these questions will help us to better understand the mechanical mechanisms of PAH so that existing treatment strategies can be optimized and new therapies can be developed.

Table 7.1. Demographics of the PAH patient and control groups

Variables	Control (n=6)	PAH (n=12)	P-value
Demographics			
Age, years old	52 ± 14	52 ± 11	0.989
Gender, Male/Female	1/5	2/10	0.755
Weight, kg	63.5 ± 16.9	61.2 ± 12.3	0.739
Height, cm	159 ± 8	161 ± 10	0.68
Clinal Exam			
Body surface area, m2	1.67 ± 0.25	1.65 ± 0.20	0.873
Body mass index, kg/m2	24.9 ± 4.0	23.6 ± 3.8	0.526
6 mins walking test, m	N/A	326 ± 134	N/A
NT-ProBNP, pg/mL	N/A	1188 ± 715	N/A
NYHA functional class I	N/A	1	N/A
NYHA functional class II	N/A	8	N/A
NYHA functional class III	N/A	3	N/A
NYHA functional class IV	N/A	0	N/A
Cardiac magnetic resonance			
LV ejection fraction, %	73 ± 7	58 ± 12	0.014
LVEDV, ml	93 ± 7	86 ± 30	0.574
LVESV, ml	25 ± 6	37 ± 21	0.198
LVSV, ml	68 ± 7	49 ± 14	0.009
LVFW ES wall thickness, mm	10.02 ± 1.25	10.87 ± 1.96	0.353
LVFW ED wall thickness, mm	5.42 ± 0.67	6.43 ± 1.29	0.093
RV ejection fraction, %	54 ± 11	37 ± 14	0.02
RVEDV, ml	103 ± 13	134 ± 72	0.322
RVESV, ml	47 ± 12	91 ± 68	0.148
RVSV, ml	56 ± 14	43 ± 13	0.095
RVFW ES wall thickness, mm	2.77 ± 0.24	6.22 ± 1.88	< 0.001
RVFW ED wall thickness, mm	1.75 ± 0.17	3.83 ± 0.61	< 0.001
Septum ES wall thickness, mm	9.21 ± 2.49	9.09 ± 2.75	0.926
Hemodynamics			
Heart rate, bpm	78 ± 16	88 ± 15	0.216
Diastolic blood pressure, mmHg	81 ± 15	75 ± 14	0.397
Diastolic blood pressure, mmHg	140 ± 19	122 ± 27	0.17
Cardiac output, L/min	4.90 ± 1.16	3.98 ± 1.51	0.211
Cardiac index, L/min/m2	2.94 ± 0.57	2.39 ± 0.84	0.167
Right atrial pressure, mmHg	N/A	9 ± 9	N/A
Mean pulmonary artery pressure, mmHg	N/A	39 ± 9	N/A
Pulmonary capillary wedge pressure, mmH	N/A	11 ± 3	N/A

7.2 Methods

7.2.1 Patient cohort and data processing

Twelve PAH patients were recruited in the study and underwent both cardiac magnetic resonance (CMR) scans and right heart catheterization (RHC) that were performed at rest using standard techniques. Pulmonary arterial hypertension was defined as having a mean pulmonary artery pressure (mPAP) greater than or equal to 25 mmHg with normal pulmonary capillary wedge pressure (≤15 mmHg). Six human subjects who had no known cardiovascular disease or other co-morbidities also underwent CMR scans and served as control in this study. Invasive hemodynamics measurements were not acquired in the control group. Demographics of the two study groups are summarized in **Table 7.1**. The protocol was approved by the Local Institutional Review Board, and informed consents were obtained from all subjects.

Cardiac magnetic resonance imaging was performed using steady-state free precession (SSFP) cine gradient echo sequences. All subjects were imaged in a 3.0T Philips scanner (Philips-Adrglam; Philips Healthcare, Netherlands) with a 12-element body matrix coil. Steady state free precession end-expiratory breath-hold cine images were acquired in multi-planar short- and long-axis views. The typical imaging parameters were: TR/TE 34/1 ms, flip angle 45°, slice thickness 8 mm, echo time 1.404 ms, repetition time 2.808 ms, pixel bandwidth 1796 Hz, percent phase field of view 100 mm, temporal resolution 35 ms, in-plane spatial resolution 1.6 x 1.6 - 1.8 x 1.8 mm, 40 frame/cardiac cycle for the control group and 30 for the PAH group.

Pressure-volume (PV) loops of the LV and RV of the PAH patients were reconstructed by synchronizing the pressure waveforms measured from RHC and volume

waveforms measured from the cardiac magnetic resonance images as described in Xi et al. [188]. Similar to our previous approach [188], the volume waveforms of the control subjects were synchronized with surrogated normal human pressure waveforms from measurements in previous studies as RHC was not performed on these subjects. Specifically, we applied the mean normal RV pressure-waveform acquired from healthy human subjects in a previous study [231] to all the control subjects. On the other hand, we applied a normal LV pressure-waveform in which the end-systolic pressure was scaled to be equal to 0.9 of the control subject's cuff pressure based on a previous empirical study [232].

Regional circumferential strain E_{cc} and longitudinal strain E_{ll} were estimated from the cine CMR images using a hyperelastic warping method as previously described [40], [181], [186], [283]. Briefly, the biventricular unit was reconstructed from the cine CMR images and partitioned into 3 regions consisting of the left ventricular free wall (LVFW), right ventricular free wall (RVFW) and interventricular septum (SEPT) [282]. A hyperelastic warping method was then applied to deform the reconstructed biventricular geometry from the template image into alignment with the corresponding object in the target image [181], [233]. Normal strains in the circumferential and longitudinal directions at the LVFW, SEPT and RVFW regions were computed from the displacement field using end-diastole as the reference configuration. The circumferential and longitudinal directions in the biventricular unit were prescribed using a Laplace-Dirichlet-Rule-Based algorithm [4].

7.2.2 Construction of personalized models

Personalized computational models of biventricular mechanics that fit the corresponding patient's pressure, volume, and regional strain data were created using previously described methods (See details in section 6.2). Briefly, the computational models were formulated based on classical large-deformation solid mechanics, and active contraction of the ventricular wall was incorporated by a multiplicative decomposition of the deformation gradient [235]:

$$\boldsymbol{F} = \boldsymbol{F}_e \boldsymbol{F}_a \tag{7.1}$$

Here, $\boldsymbol{F} = \boldsymbol{I} + \nabla \boldsymbol{U}$ is the total deformation gradient computed from the displacement field $\boldsymbol{U}$, $\boldsymbol{F}_a$ is associated with an inelastic deformation resulting from the actively contracting muscle fibers, and $\boldsymbol{F}_e = \boldsymbol{F}{\boldsymbol{F}_a}^{-1}$ is associated with the elastic deformation that preserves (kinematic) compatibility of the tissue under load. We employ the following form of $\boldsymbol{F}_a$;

$$\boldsymbol{F}_a = (1-\gamma)\boldsymbol{f}_0 \otimes \boldsymbol{f}_0 + \frac{1}{\sqrt{1-\gamma}}(\boldsymbol{I} - \boldsymbol{f}_0 \otimes \boldsymbol{f}_0) \tag{7.2}$$

where $\boldsymbol{f}_0$ is the unit fiber direction in the reference configuration, and γ is a parameter that represents the relative active shortening strain along the muscle fibers i.e., a measure of the local load independent active tension generated by the tissue. Meanwhile, passive mechanics was modeled using a purely incompressible transversely isotropic hyperelastic material low [16] with an isochoric strain energy density given by

$$\Psi(\boldsymbol{C}_e) = \frac{a}{2b}\left(e^{b(I_1-3)} - 1\right) + \frac{a_f}{2b_f}(e^{b_f(I_{4f_0}-1)^2} - 1) \tag{7.3}$$

where a, b, a_f, b_f are material constants and I_1, I_{4f_0} are invariants that are defined as

$$I_1 = tr\overline{\boldsymbol{C}_e}, \quad I_{4f_0} = \boldsymbol{f}_0 \cdot (\overline{\boldsymbol{C}_e}\boldsymbol{f}_0) \tag{7.4}$$

with $\overline{\boldsymbol{C}_e} = {J_e}^{-\frac{2}{3}}$ being the volume preserving contribution of the elastic component to right Cauchy Green strain tensor $\boldsymbol{C}_e = {\boldsymbol{F}_e}^T \boldsymbol{F}_e$ and $J_e = \det(\boldsymbol{F}_e)$ the elastic volumetric deformation.

The ventricular base was fixed in the longitudinal direction and the biventricular geometry was anchored by constraining the epicardial surface using a Robin-type boundary condition with a linear spring of stiffness k= 0.5 kPa/cm [188]. Measured cavity pressure in the LV (p_{lv}) and RV (p_{rv}) were applied as a Neumann condition at the endocardial surfaces. The force-balance equations were solved using the finite element method implemented in FEniCS. A mixed formulation was used to enforce incompressibility of the elastic deformation (J_e=1) [16].

In order to separately determine the active and passive material properties of the computational model for each patient, the clinical measurements were divided into a passive phase and an active phase. Models were then optimized using the active and passive material parameters as controls variables to minimize a weighted cost function based on the differences between model predictions and measurements of pressure, volume and circumferential strain (E_{cc}), data as described previously [247], [282]. Longitudinal strains were not included in the optimization due to the limited number of control parameters in the simulations, but served as an independent measure of the final model fit as in our previous study [282]. To solve the minimization problem, we applied a sequential quadratic programming algorithm (SQP) [251], a gradient-based optimization algorithm where the functional gradient of the cost function with respect to all the control variables was estimated efficiently by solving an automatically derived adjoint equation using dolfin-adjoint [230].

In the passive phase of the optimization, we allowed the isotropic parameter a in Eq. (7.3) to vary while keeping all other parameters fixed. To capture regional differences of this parameter, we allow a associated with the LV (LVFW + SEPT) (a_{LV}) and the RVFW (a_{RVFw}) to vary independently from each other. Similar to Finsberg et al. [282], we first apply one iteration of the backward displacement method [244] to estimate an unloaded, stress-free configuration, thus neglecting residual stresses [245]. The passive parameter was then determined by assimilating the passive phase measurements, starting from an initial guess of a = 1.291kPa in both regions. After fitting the model to the passive phase of the PV-curve and strain data, the parameters a_{LV} and a_{RVFw}were held fixed and the relative active fiber shortening strain γ in Eq. (7.2) was chosen as the control variable for the active phase. We allow γ associated with the LVFW (γ_{LVFW}), SEPT (γ_{SEPT}) and RVFW (γ_{RVFW}) to vary independently from each other. For each time point, we estimated γ_{LVFW}, γ_{SEPT}, and γ_{RVFW}, to obtain their variation with time over a cardiac cycle. The spatially resolved isotropic parameters a and γ-waveforms were estimated with different linear transmural variation of the myofiber helix angles varying from $-\alpha$ at the epicardium to + α at the endocardium, with α ranging from 30° to 80° [282]. The set of parameters yielding the lowest mean square error between the predicted and measured strain and PV data was taken to be the optimal one and used to post-process regional biventricular myofiber wall stresses σ_{ff}.

7.3 Results

7.3.1 Patient data and regional strains

The control and PAH groups have comparable demographic characteristics, with the majority of the patients in the latter group (8/12) classified in NYHA functional class II. In terms of hemodynamics, the PAH group had an mPAP of 39 ± 9 mmHg with a pulmonary capillary wedge pressure (PCWP) 11 ± 3 mmHg. No differences in the systemic hemodynamics measurements (i.e., blood pressure) were detected between the 2 groups.

Evaluation of cardiac magnetic resonance images revealed that the PAH group had significantly (P<0.05) reduced right ventricular ejection fraction (RVEF) (37±14% vs. 54 ±11%), increased RVFW thickness at ED (3.83 ± 0.61mm vs. 1.75 ± 0.17mm) and ES (6.22 ±1.88mm vs. 2.27 ± 0.24mm) compared to the control group. Left ventricular ejection fraction (LVEF) and stroke volume (LVSV) were also significantly reduced in the PAH group compared to the control group (LVEF: 58 ± 12% vs. 73 ± 7%; LVSV: 49 ± 14 ml vs. 68 ± 7 ml). Right ventricular end-diastolic volume (RVEDV) and right ventricular end systolic volume (RVESV) were larger, but not statistically significant, in the PAH group. Absolute peak circumferential strain E_{cc} in the PAH group was significantly lower (one-tailed: P <0.05) than the control group at the LVFW (13 ±4% vs. 17 ± 2%) and RVFW (8±4% vs.11± 2%) (**Figure 7.1**). Similarly, peak longitudinal strain E_{ll} in the PAH group was also significantly lower at the LVFW (13± 5% vs. 17 ± 3%) and RVFW (10 ± 4% vs. 15 ± 3%) compared to the control group. While both E_{cc} and E_{ll} at the septum were lower in the PAH group than the control group, these reductions were not statistically significant (one-tailed P = 0.11 for E_{cc} and 0.05 for E_{ll}).

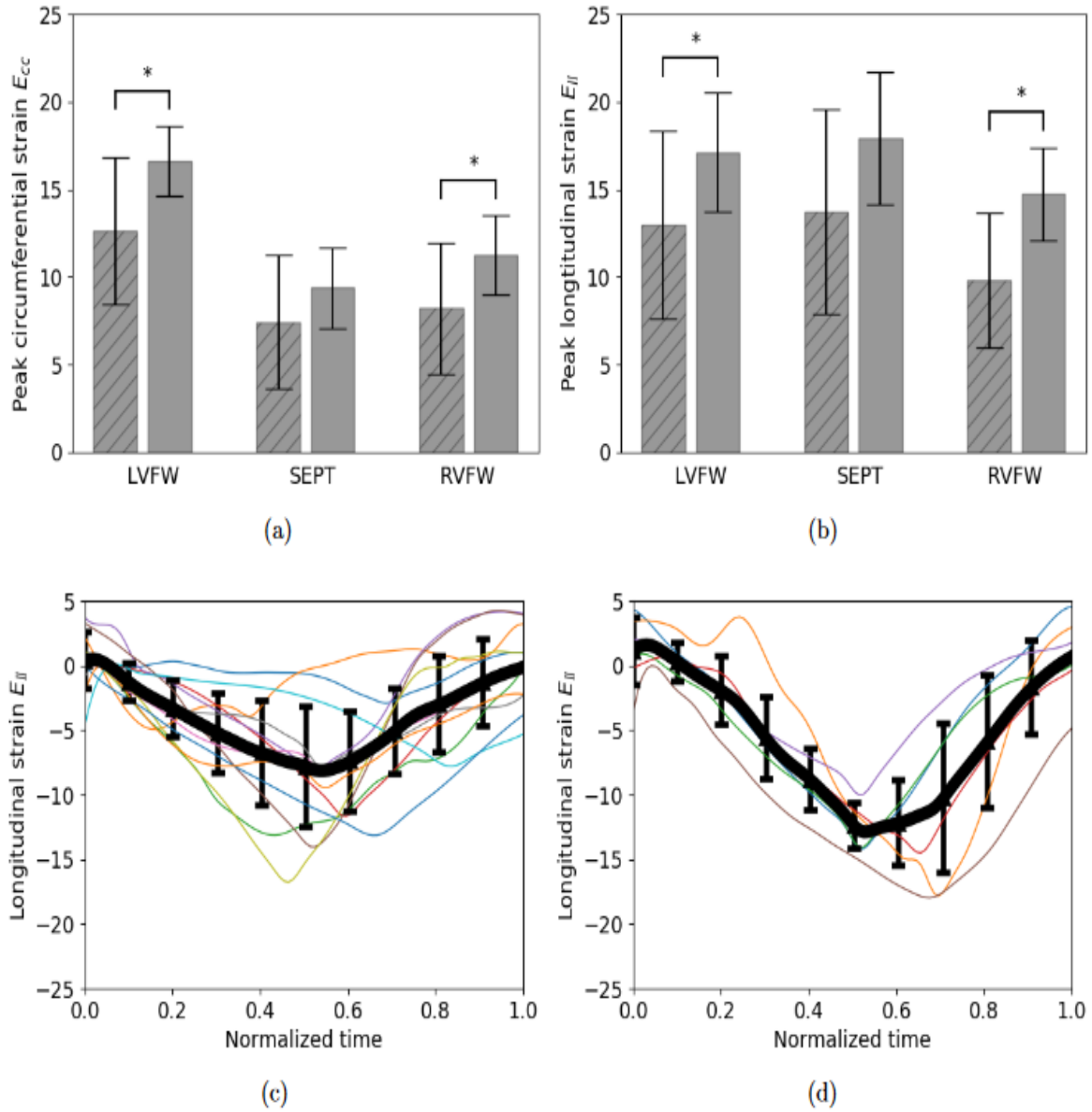

Figure 7.1. Comparison of peak regional (a) circumferential and (b) longitudinal strains between control (unstriped) and PAH (striped) groups with (*) denoting that the latter value is statistically lower (P<0.05) than the former. Time traces of RVFW longitudinal strain of the (c) PAH patients and (d) control subjects. Thick line denotes average and error bar denotes standard deviation.

7.3.2 Model results; contractility, stiffness, and stress

Figure 7.2 shows an example of the patient specific simulations, assimilated with the corresponding measured PV loops as well as estimated regional E_{cc}, from the control and PAH groups. The overall fit of the LV and RV volumes in the patient-specific computational models is very good, with the simulation results agreeing closely with the measurements in the cardiac cycle (**Figure 7.3**). The overall root mean square error (RMSE) of the fit is 3.89 mL for the RV and 6.6 mL for the LV. Compared to the volumes, the fit of the regional strains in the cardiac cycle shows significantly more scatter, especially at lower LV systolic strains. The RMSEs of the regional circumferential strain fit are 4.7% for the LVFW, 1.9% for the SEPT, and 2.6% for the RVFW. Meanwhile, serving as an independent measure of model fit, longitudinal strains, not included in the optimization, had an RMSE of 6.2% for the LVFW, 6.2% for the SEPT, and 5.2% for the RVFW.

Regional contractility for the biventricular units was estimated using fitted values of the corresponding regional active strains during systole. Peak RVFW contractility is not uniformly decreased in the PAH group, but instead presented a pattern with respect to the level of remodeling (**Figure 7.4**). Using the ratio of RVEDV to LVEDV (i.e., RVEDV/LVEDV) as an indicator of remodeling, we found that RVEDV/LVEDV varies substantially in the PAH group (1.55 ± 0.50) but little in the control group (1.11 ± 0.12). Using RVEDV/LVEDV = 1.5 (that is 3 SD from the mean value of the control group) as a threshold to delineate between PAH patients with mild RV remodeling (RVEDV/LVEDV<1.5) and those with severe RV remodeling (RVEDV/LVEDV≥1.5), we

found that in PAH patients with mild RV remodeling, their peak RVFW contractility is larger than that in the control group (P= 0.09). We note that the threshold RVEDV/LVEDV = 1.5

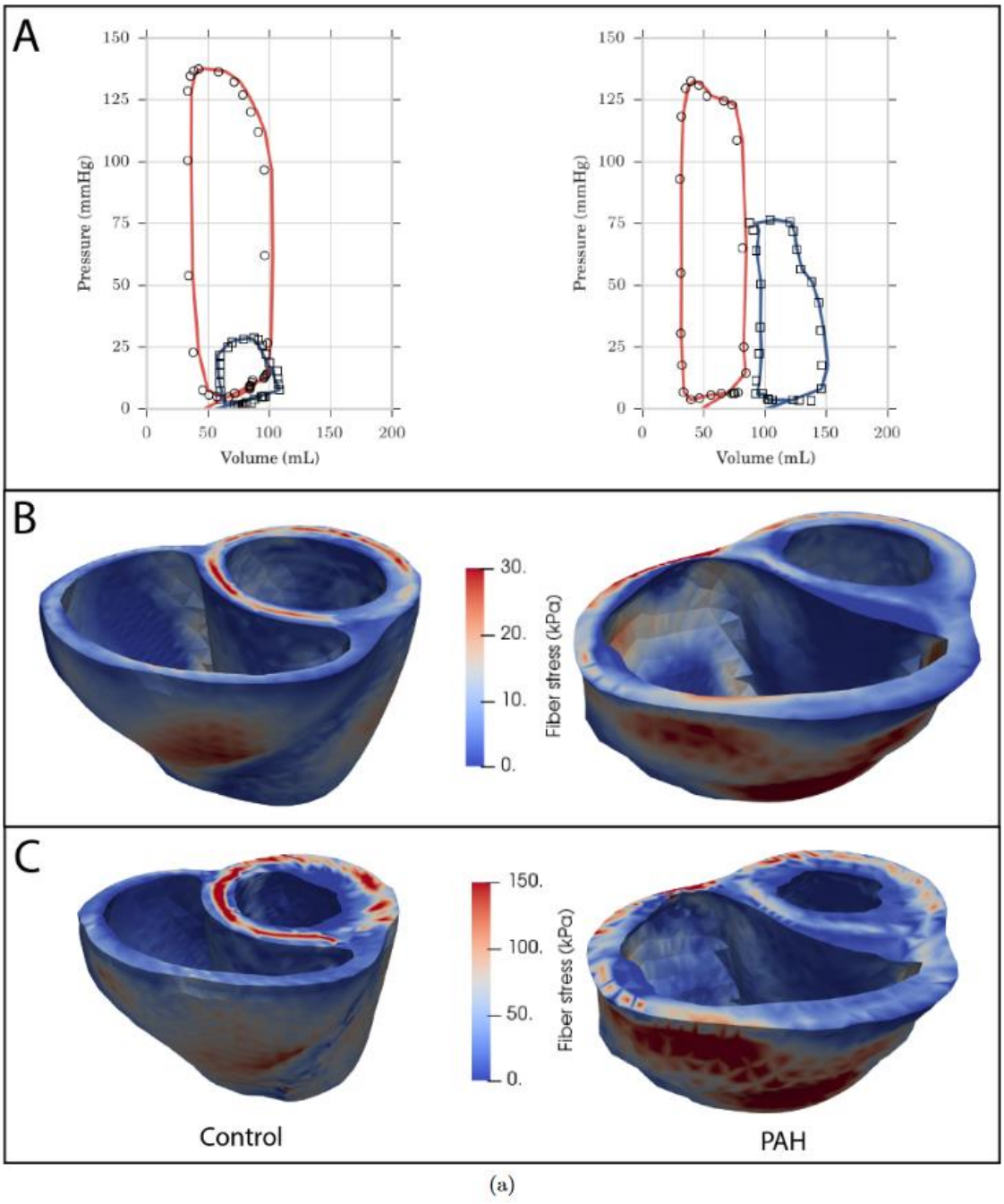

(a)

Figure 7.2. Examples of simulations results from a control (left column) and an extensively remodeled (RVDEV/LVEDV = 1.75) PAH patient (right column). A) PV loop data (open markers) and simulations (solid lines) for the LV (red) and RV (blue). B) Calculated fiber stresses at end diastole, and C) Calculated fiber stresses at end systole.

is approximately the midpoint for the range (1.27 ≤ RVEDV/LVEDV ≤ 1.69) proposed previously [41] to categorize “mild” RV dilation in PAH patients. With increasing RVEDV/LVEDV, however, $\gamma_{RVFW,max}$ decreases linearly so that in PAH patients with RVEDV/LVEDV≥1.5 (severely remodeled PAH) is significantly less than that in the control group. The inverse linear relationship between $\gamma_{RVFW,max}$ and RVEDV/LVEDV is strong and has a coefficient of determination R^2= 0.77. By comparison, $\gamma_{RVFW,max}$ has a weaker linear relationship with RVEF (R^2 = 0.50) and RVEDV index (RVEDVi) (R^2 = 0.40).

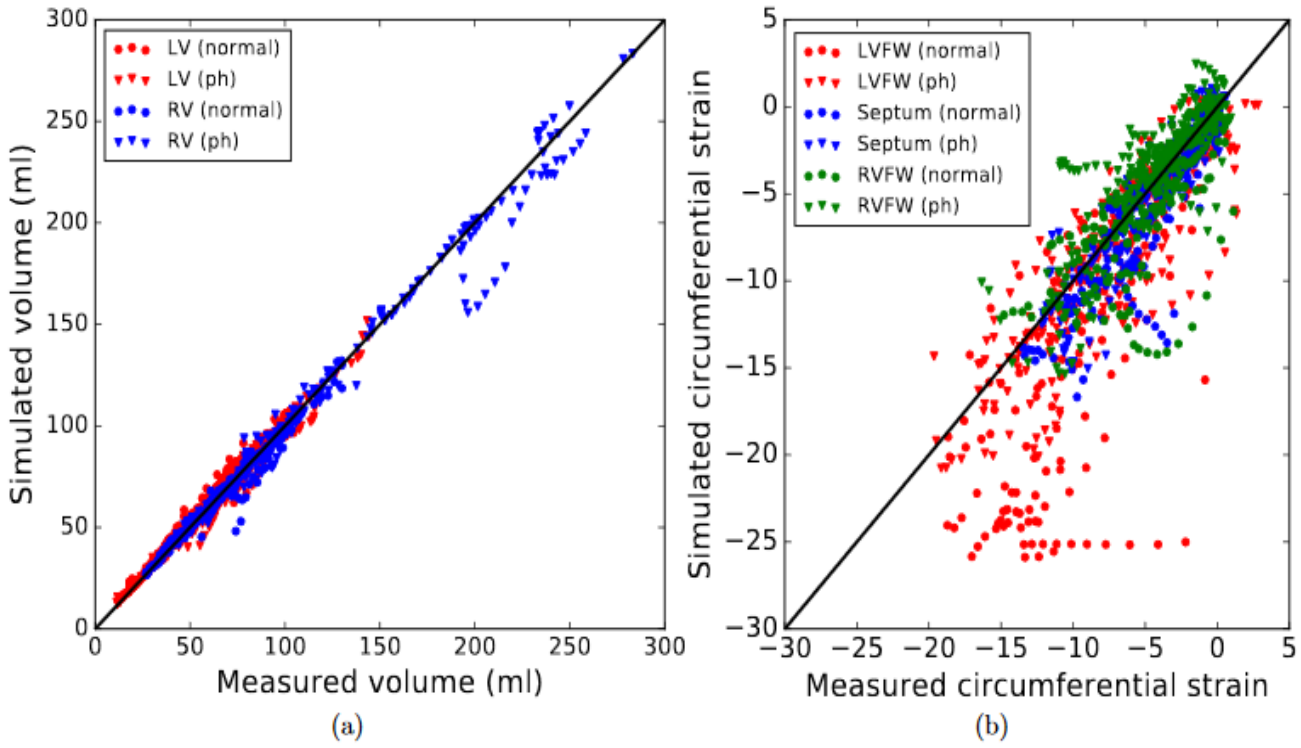

Figure 7.3. Overall data assimilation errors in the control (circle) and PAH patient (diamond) populations. Comparison between measured and simulated (a) volumes for both the RV (blue) and LV (red); (b) $\boldsymbol{E_{cc}}$ for the LVFW (red), SEPT (green), and RVFW (blue) at all cardiac time points. A y = x line is also plotted to show the zero error reference.

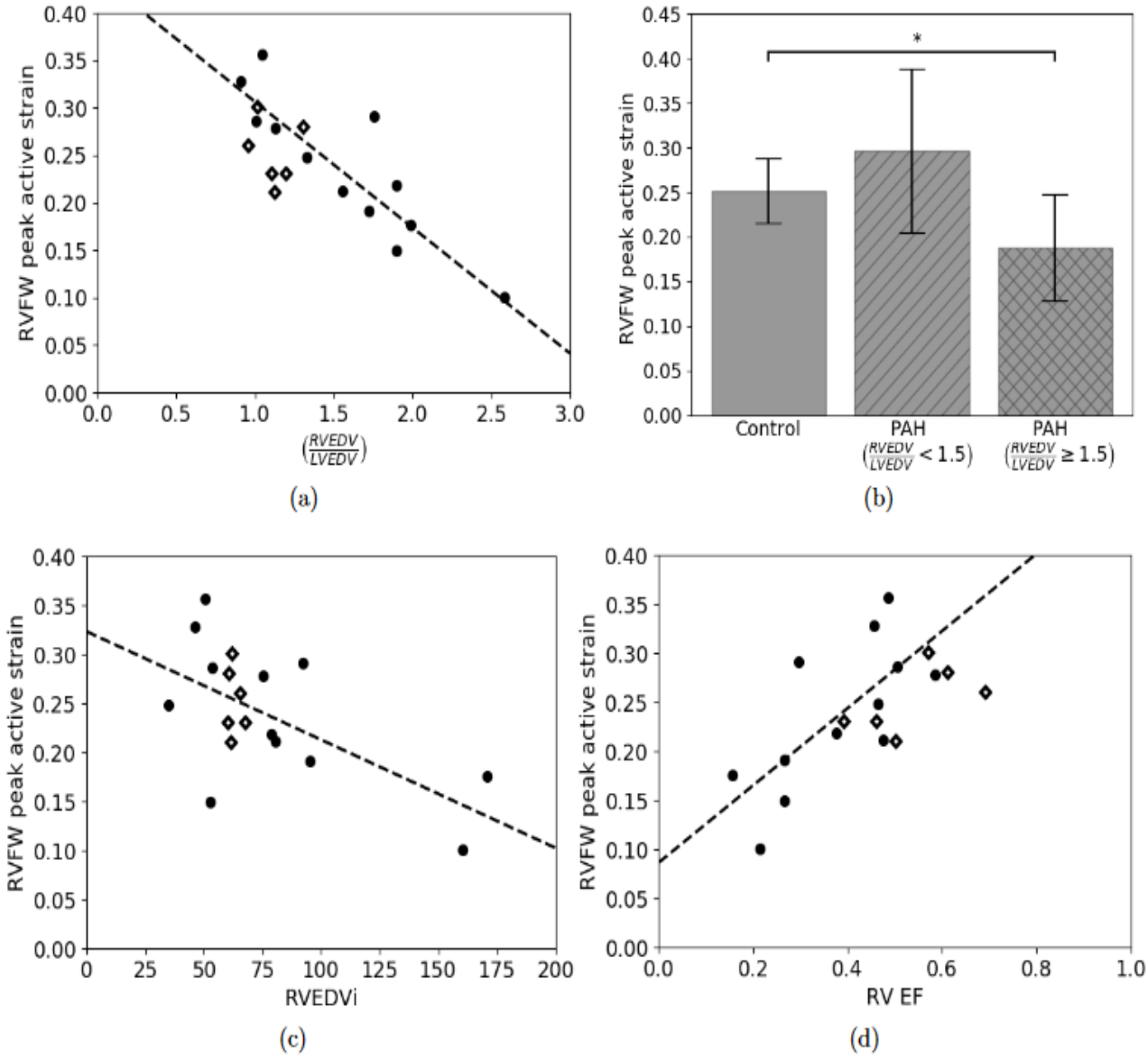

Figure 7.4. Analysis of peak RVFW contractility $\gamma_{RVFW,max}$ for control and PAH patient groups. (a) Graphical depiction of $\gamma_{RVFW,max}$ for both controls (diamonds) and patients (black dots) as a function of the ratio of RVEDV/LVEDV. Dashed line shows a linear fit to the PAH patient group ($\gamma_{RVFW,max}$= -0.13(RVEDV/LVEDV) +0.44, R^2 = 0.77). (b) Average $\gamma_{RVFW,max}$ for controls patients with RVEDV/LVEDV < 1.5 (similar to controls) and patients RVEDV/LVEDV ≥ 1.5. (c) Linear fit of $\gamma_{RVFW,max}$ with RVEDVi ($\gamma_{RVFW,max}$ = -0.001(RVEDVi) +0.32, R^2 = 0.40) (d) Linear fit of $\gamma_{RVFW,max}$ with RVEF ($\gamma_{RVFW,max}$= -0.39(RVEF) +0.09, R^2 = 0.50).

Peak contractility in the LVFW $\gamma_{LVFW,max}$, unlike $\gamma_{RVFW,max}$, did not exhibit any relationship with the level of remodeling as measured by RVEDV/LVEDV (**Figure 7.5**). Specifically, we found that peak contractility in the LVFW is significantly smaller in the mildly remodeled PAH group with RVEDV/LVEDV<1.5 (0.33±0.02) compared to the control (0.38±0.03) (P <0.02). On the other hand, while the average in the severely remodeled PAH group (0.33±0.07) is decreased compared to the control group, that decrease is not statistically significant due to the large standard deviation (P= 0.14).

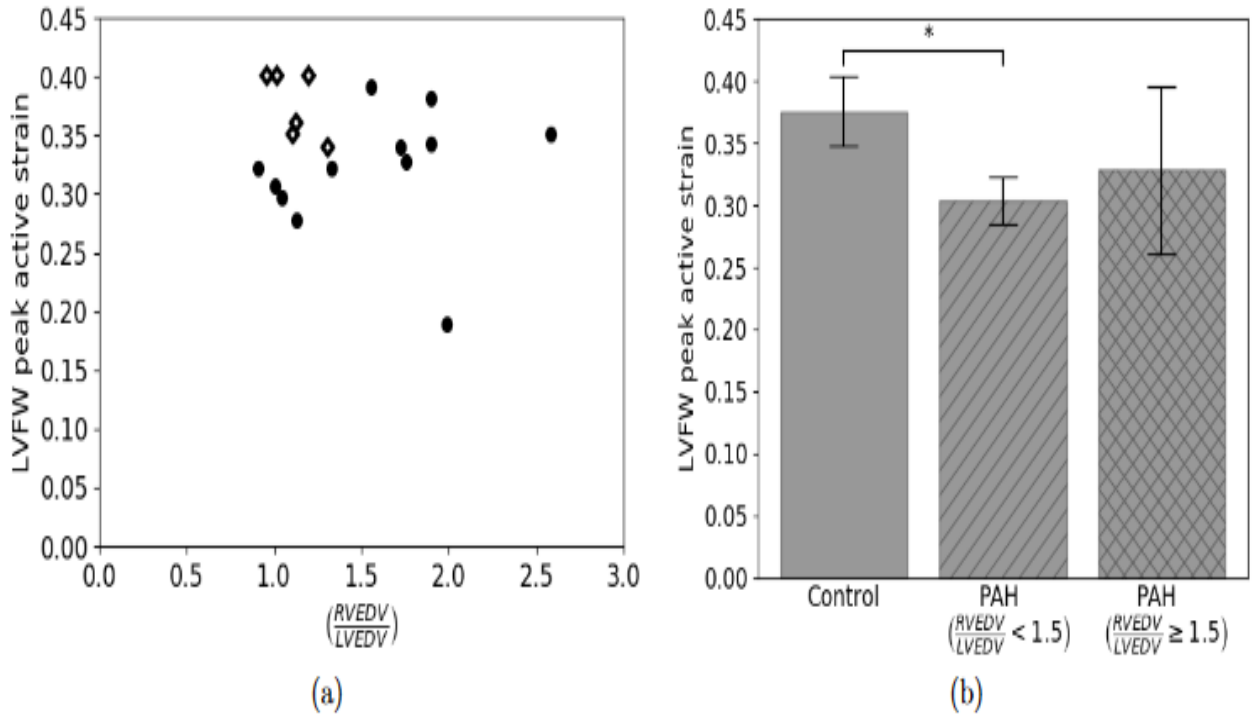

Figure 7.5. Analysis of peak LVFW contractility $\boldsymbol{\gamma_{LVFW,max}}$ for control and PAH patient groups. (a) Graphical depiction of peak LVFW contractility for both controls (diamonds) and patients (black dots) as a function of the ration of RVEDV/LVEDV. (b) Average $\boldsymbol{\gamma_{LVFW,max}}$for controls, patients with RVEDV/LVEDV<1.5 and patients RVEDV/LVEDV ≥ 1.5.

Fitted values of the regional material isotropic parameters a_{LV} and a_{RVFW} are measures of the tissue passive stiffness in the LVFW+SEPT and RVFW of the biventricular unit, respectively. Separating the fitted values in the PAH group based on the degree of remodeling (i.e., RVEDV/LVEDV) revealed a progressive increase in the mean value of a_{LV} and a_{RVFW} with remodeling (**Figure 7.6**). The value of one patient in the severely remodeled PAH group (RVEDV/LVEDV≥1.5) is disregarded as it appears to be an outlier (Z score >2, a = 36.78kPa). In the severely remodeled PAH group, the mean value of (4.3± 3.5 kPa) is 2.4 times higher than that of the control group (1.8± 0.6 kPa) but that increase was not significant due to the large standard deviation in the former group. On the other hand, the mean value of a_{LV} in the severely remodeled PAH group (3.00 ± 2.5 kPa) was significantly higher (P<0.05) than that of the control (0.48 ± 0.12 kPa).

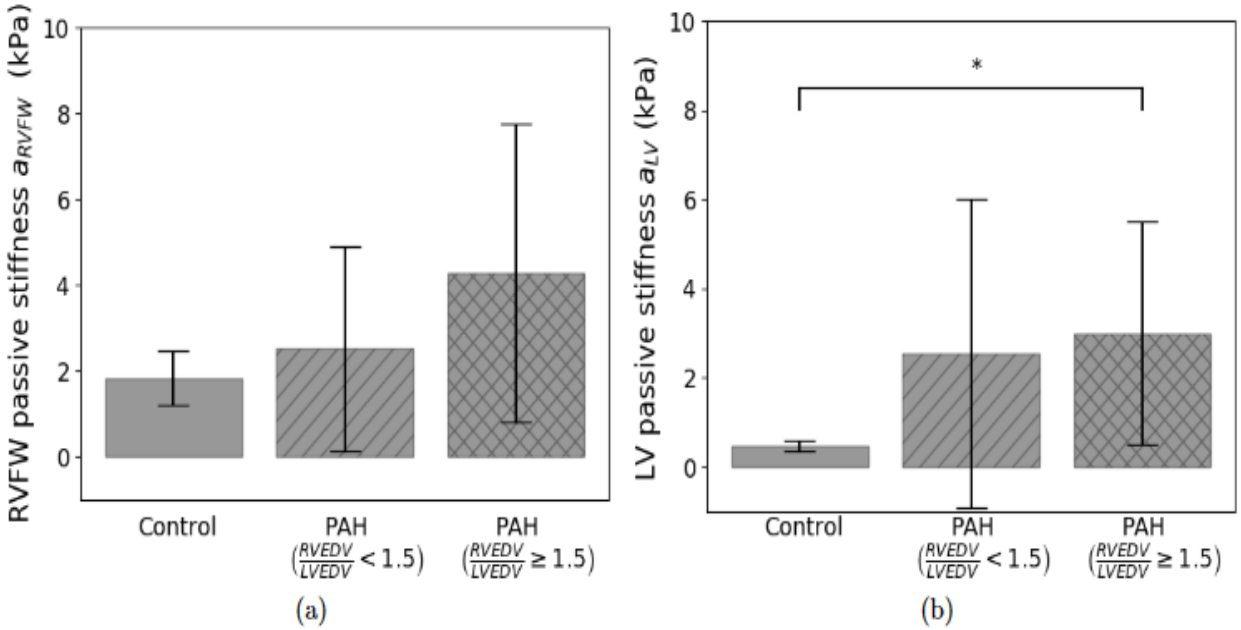

Figure 7.6. Comparison of passive tissue stiffness parameter $\boldsymbol{a}$ between control and the PAH groups in the (a) LVFW + SEPT and (b) RVFW regions

Using the data-assimilated computational models, we computed the peak regional wall stress in the myofiber direction (σ_{ffmax}) (i.e., maximum myofiber load) (**Figure 7.7**). We found that at the RVFW is, on average, the same between the control (36.4 ± 5.7 kPa) and the mildly remodeled PAH (36.5 ± 12 kPa) groups. In the severely remodeled PAH group, however, at the RVFW is on average 1.5 times larger (54.27 ± 25.1 kPa) than these 2 groups but that difference is not significant (P= 0.14) due to its large standard deviation. In comparison, at the LVFW is significantly reduced in the mildly remodeled PAH group (55.4 ± 7.4 kPa) compared to the control group (84±17.6 kPa). In the severely remodeled PAH group, at the LVFW of two patients are disregarded as they appeared to be outliers with substantially large values (Z score>2, = 544.1, 1659.9 kPa), which is due likely to the presence of local stress-concentration in the model. Peak myofiber stress at the LVFW in this group (71.22 ± 7.8 kPa) is significantly larger than the mildly remodeled PAH group but lower (not statistically significant) than the control.

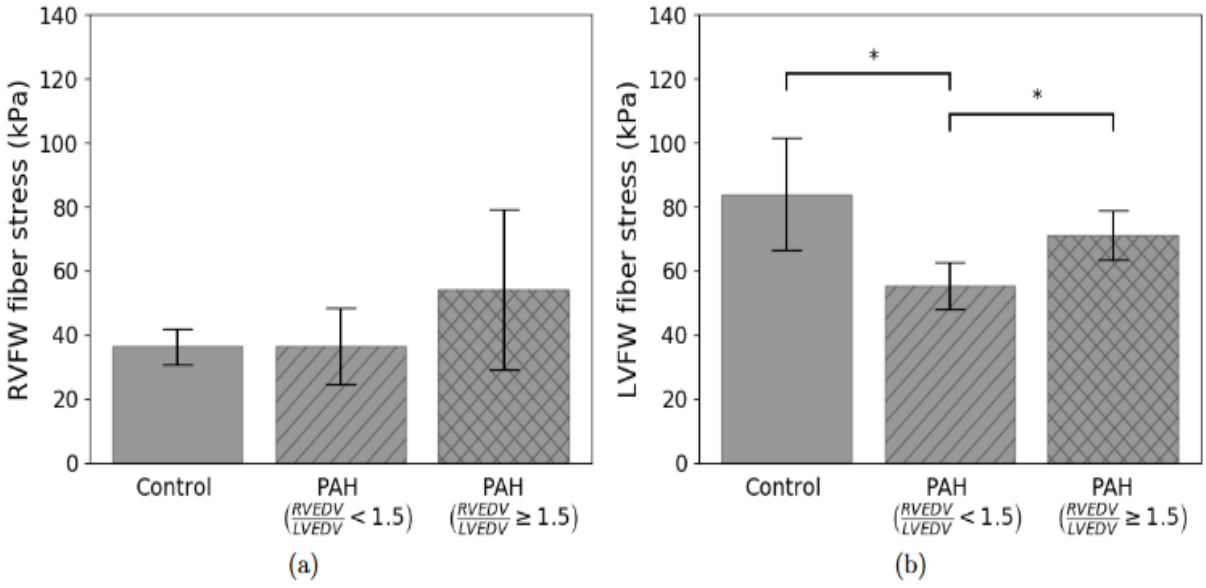

Figure 7.7. Comparison of peak myofiber wall stress $\boldsymbol{\sigma_{ffmax}}$ between control and the PAH groups in the (a) LVFW and (b) RVFW regions.

7.4 Discussion

We have used a previously established data assimilation technique [247], [282] to quantify changes in regional myocardial properties and stresses in PAH based on measurements of PV loops and myocardial strains from patients and a cohort of healthy subjects serving as control. The major finding of this study is a strong inverse linear relationship between RVFW load-independent contractility as indexed by the fitted model's active strain parameter $\gamma_{RVFW,max}$, shown previously to be biomarkers of ventricular failure [247], and the degree of RV remodeling as indexed by the RVEDV/LVEDV in PAH patients. The relationship between RVEDV/LVEDV ($R^2 = 0.77$) is stronger than that between and RVEF ($R^2 = 0.50$) or RVEDVi ($R^2 = 0.40$) in PAH patients. We also found that RVFW contractility is increased by about 20% in the PAH patients when little remodeling is present (i.e., RVEDV/LVEDV<1.5), but decreases linearly with increasing RVEDV/LVEDV.

The strong $\gamma_{RVFW,max}$– RVEDV/LVEDV relationship also provides a mechanistic explanation for recent clinical findings that RVEDV/LVEDV is a better metric (with a higher sensitivity) than RVEDVi for identifying PAH patients based on all-cause mortality [284] as well as for detecting RV enlargement [285]. Besides PAH, this metric is also used for assessing RV dilation and indicating pulmonary valve replacement in patients who have tetralogy of Fallot [286], [287]. There are, however, no other clear mechanistic basis for applying RVEDV/LVEDV to delineate the severity in PAH or electing surgery other than a statistical association of this metric with clinical endpoints [284] or from clinical experience [287]. Our finding therefore provides such basis and suggests that the underlying reason why RVEDV/LVEDV is a better metric in determining PAH severity is

because of its close association with RVFW contractility in PAH. Based on this relationship (**Figure 7.4**), the threshold of RVEDV/LVEDV ~ 2 for distinguishing PAH patients with severe RV dilation as well as electing patients for pulmonary valve replacement is associated with a reduction of RVFW contractility by about 30% from normal.

Fundamentally, our study also provides an insight into the changes in regional contractility during the progression of PAH. Our result suggests there is an increase in the RV contractility in early stages of PAH (RVEDV/LVEDV<1.5), perhaps as a compensatory mechanism to maintain RVEF in response to the increased RV pressure, before decreasing as the disease progresses. The similarity in RVEF in PAH patients with RVEDV/LVEDV<1.5 (49±5%) compared to normal (54±11%) (**Figure 7.4**) support this theory. Because wall thickness is already accounted for geometrically in the computational models, the increase in RVFW contractility indicates that RV cardiomyocytes becomes hypercontractile in an attempt to normalize RVEF in the presence of increased pulmonary afterload at early stages of PAH. This finding is supported by a recent study, which shows that the maximal tension of skinned myocytes of idiopathic PAH patients is 28% higher (than normal) in early stages of disease with RVEF at 46 ± 7% [288], close to that found in PAH patients with RVEDV/LVEDV <1.5 in this study. Other than affecting the RV, we also found that LV contractility γ_{LVFW} in PAH patients is reduced. This reduction is observed even in PAH patients exhibiting little RV remodeling suggesting that there is some early influence on LV function in this disease, a result broadly consistent with findings of reduced myocyte contractility in the LV of PAH patients [289].

Besides contractility, we also found that there is, on average, an increase in the LV and RV passive stiffness (reflected by the increase in values of a_{LV} and a_{RVFW} and that control the general passive isotropic tissue stiffness) with RVEDV/LVEDV in the PAH groups. While this increase is largely not statistically significant due to the large variance of the fitted parameter values, this result is consistent with experimental [290] and clinical [288] findings that PAH is associated with cardiac fibrosis and myocyte passive stiffening. Computation of the peak RV fiber stress using the fitted parameters revealed that it is increased only in PAH patients (P = 0.14) with RVEDV/LVEDV ≥ 1.5 although that increase is not statistically significant (**Figure 7.7**). Because myocardial wall stress is directly correlated with myocardial oxygen consumption (MVO2), this result suggests that MVO2 is increased in the RV of PAH patients with RVEDV/LVEDV ≥ 1.5 but less so in patients without substantial RV remodeling. When taken into account with our finding that RVFW contractility is reduced in PAH patients with RVEDV/LVEDV ≥ 1.5, this result further suggests that coronary flow may not be sufficient to meet the increase in MVO2 due to a higher workload in the RV, and as a result, ischemia sets in this cohort of patients producing a lower contractility. Our finding that RVEDV/LVEDV ≥ 1.5 may represent the threshold at which RV may become ischemic (with reduced contractility) is also consistent with clinical observations that RV ischemia may play a role in later stages in PAH patients [291], [292].

Compared to previous patient data assimilation techniques that have so far been only applied to the LV [42], [43], [247], [293] with a relatively small number of patients (n~6), we have shown that the semi-automatic data assimilation pipeline when applied to the biventricular unit is robust in regards to a sizable patient cohort (n=12) that has

features reflecting those found in the general heterogeneous PAH population. Specifically, PAH patients recruited in this study had mPAP = 39 ± 9 mmHg and PCWP = 11 ± 3 mmHg, which falls within the clinical definition of this disease (mPAP ≥ 25 mmHg and PCWP <15 mmHg) [294]. In terms of geometry and function, the PAH patients had thicker RV wall, higher mean RVEDV, lower RV and LV EF as well as significantly reduced longitudinal and circumferential strains at the RVFW and LVFW that are all consistent with previous clinical observations of this disease[274], [295], [196], [200], [296]–[298]. The data assimilation process produces relatively few data outliers for both the control and patient groups, and is able to fit the patient-specific ventricular volumes and regional strains well, especially considering the fact that only a small number of control variables is used in fitting the data.

7.5 Limitations

Some limitations and challenges still remain in regards to this study. First, the models were fitted using only a small number of control variables so that we do not run into the risk of having non-unique solutions and over-fitting. While we are able to fit the PV loops and regional circumferential strains relatively well in this study, it will be useful to further explore the potential impact of the choice of the computational model and the control variables used to fit the patient data. Second, the cohort size (n = 12) is small although it is still comparatively larger than many other patient-specific computational modeling studies. Nevertheless, we are able to provide a mechanistic explanation as to why some clinical indices are better at characterizing PAH severity as well as features found during the progression of PAH, which are also supported by other clinical studies. A larger cohort

will be considered in future studies. Third, we have applied surrogate pressure waveforms to the control subjects as RHC was not performed on them. Future studies can consider estimating pressures in control healthy subjects using Doppler echocardiography or including human subjects who have had false-positive diagnosis of PAH after undergoing RHC.

7.6 Conclusion

In conclusion, we have shown that RVEDV/LVEDV is strongly associated with the RVFW load-independent contractility estimated from assimilating a computational model of active biventricular mechanics with clinical imaging and hemodynamics data acquired from PAH patients and control subjects. Our study therefore provides a mechanistic basis for using RVEDV/LVEDV as a non-invasive metric for assessing PAH severity as well as a non-invasive approach of estimating RV contractility from measurements of RVEDV/LVEDV.

CHAPTER 8

CONCLUSIONS

The aim of this research was to develop microstructure-based and patient-specific computational models to understand progressive changes in ventricular mechanics associated with HFpEF and PAH.

First, we developed and validated a microstructure-based constitutive model of the passive myocardium in a three-dimensional FE modeling framework. To the best of our knowledge, this is the first FE implementation of a microstructural constitutive model to simulate passive filling of a LV in a representative 3D geometry with experimentally measured transmural muscle fiber orientation. Our results have shown that the LV filling function is sensitive to the collagen ultrastructure and the load taken up by the tissue constituents varies depending on the LV transmural location. These findings underscore the importance of quantifying changes in the collagen fiber network ultrastructure during remodeling, particularly in diseases where fibrosis is a key feature such as HFpEF.

Second, we developed patient-specific computational models to investigate effects of PAH on ventricular mechanics and function. Specifically, we quantified regional ventricular myofiber stress, myofiber strain, contractility, and passive tissue stiffness in PAH patients, and compare them to those found in age- and gender-matched normal controls. Our results showed that RV longitudinal, circumferential and radial strain were depressed in PAH patients compared with controls; RV passive stiffness increased progressively with the degree of remodeling as indexed by the RV and LV end-diastolic volume ratio (RVEDV/LVEDV); Peak contractility of the RV was found to be strongly correlated, and had an inverse relationship with RVEDV/LVEDV. These results provide the mechanical basis of using RVEDV/LVEDV as a clinical index for delineating disease severity and estimating RVFW contractility in PAH patients.

Overall, the presented research benefits the biomechanical community by addressing multiple gaps in the literature and promote the understanding of the effects of HFpEF and PAH on progressive changes in ventricular mechanics through computational modeling.

APPENDICES

APPENDIX A: Plane stress formulation

In the 6 canine specimens found in the experiments, the loading directions ($\boldsymbol{e}_1,\boldsymbol{e}_2,\boldsymbol{e}_3$) coincided with the local material coordinate system i.e., $\boldsymbol{e}_f = \boldsymbol{e}_1,\ \boldsymbol{e}_s = \boldsymbol{e}_2,\ \boldsymbol{e}_n = \boldsymbol{e}_3$. Since the top and bottom of the specimens are traction-free, the normal stress S_{33} in the tissue sheet normal direction $\boldsymbol{e}_3$ can be assumed to be zero. The normal second Piola-Kirchhoff stresses in the muscle fiber, cross-fiber and out-of-plane directions can therefore be derived, respectively, as:

$$S_{11} = S_{g,11} + S_{m,11} + S_{c,11} - p\frac{1}{2E_{11}+1} \tag{A1}$$

$$S_{22} = S_{g,22} + S_{c,22} - p\frac{1}{2E_{22}+1} \tag{A2}$$

$$S_{33} = S_{g,33} + S_{c,33} - p\frac{1}{2E_{33}+1} = 0 \tag{A3}$$

In Eqs. (A1-3), the stress contribution of the non-fibrous ground matrix is given by:

$$S_{g,11} = S_{g,22} = S_{g,33} = \phi_g C_1. \tag{A4}$$

On the other hand, the stress contribution of the muscle fibers can be derived from Eq. (5) in the main text, and is given as:

$$S_{m,11} = 2\phi_m C_2 C_3 \frac{\alpha-1}{\alpha} e^{C_3(\alpha-1)^2}, \tag{A5}$$

where $\alpha = \lambda_1 = \sqrt{2E_{11}+1}$. Finally, the stress contribution of the collagen fiber network can be derived from Eq. (14) in the main text and is given by:

$$S_{c,ii} = \phi_c C_4 \int_0^{2\pi}\int_0^{\pi}\left[\int_0^{\epsilon_c(\theta,\phi)} D(x)\frac{(\epsilon_c(\theta,\phi)-x)}{1+2x}dx\right]R(\theta,\phi)\frac{\partial \epsilon_c}{\partial \boldsymbol{E_{ii}}}d\phi d\theta \tag{A6}$$

$$\epsilon_c(\theta,\phi) = E_{11}cos^2\phi + E_{22}cos^2\theta sin^2\phi + E_{33}sin^2\theta sin^2\phi \tag{A7}$$

Substitution of Eq. (A3) into (A1-2) and invoking the incompressibility constraint (i.e., $\lambda_1{}^2\lambda_2{}^2\lambda_3{}^2 = (2E_{11}+1)(2E_{22}+1)(2E_{33}+1) = 1$) enable one to express S_{11} and S_{22} as a function of the stretch in the muscle fiber direction λ_1 and stretch in the cross-fiber direction λ_2. To compare with the experiments, we transformed the second Piola-Kirchhoff stress components S_{ii} to the Cauchy stress components by:

$$\sigma_{ii} = \lambda_i{}^2 S_{ii}. \tag{A8}$$

APPENDIX B: Results of biaxial tests for other specimens

Specimen 0119

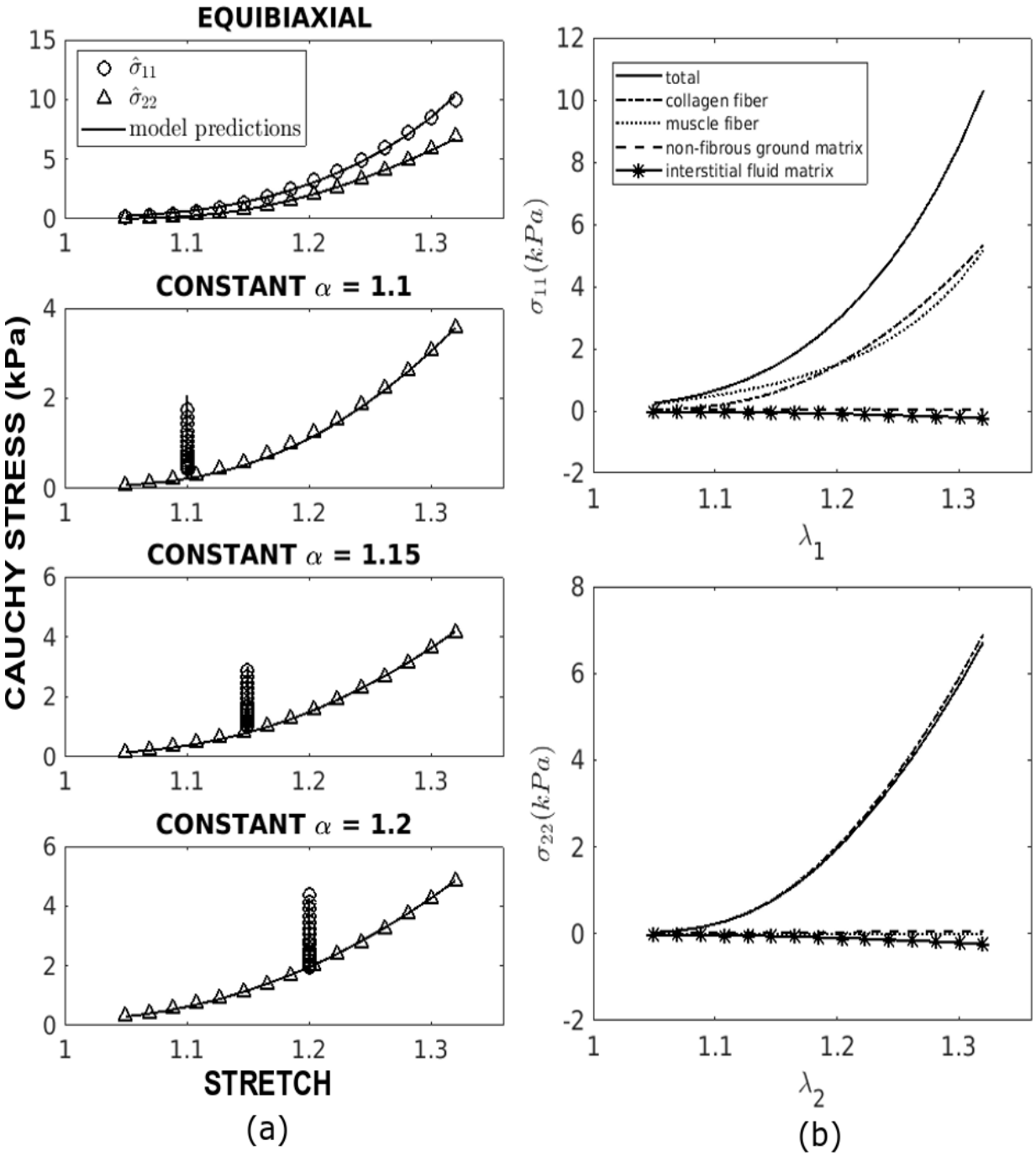

Figure B1. (a) Comparison of the fitted and experimental Cauchy stress-stretch data for equibiaxial and constant **α** = 1.1, 1.15 and 1.2 tests of specimen 0119. (b) Contribution of the collagen fiber network, muscle fibers, non-fibrous ground matrix and interstitial fluid matrix to the total stress in the fiber direction (top) and the cross-fiber (bottom) directions in the equi-biaxial test of specimen 0119

Specimen 0124

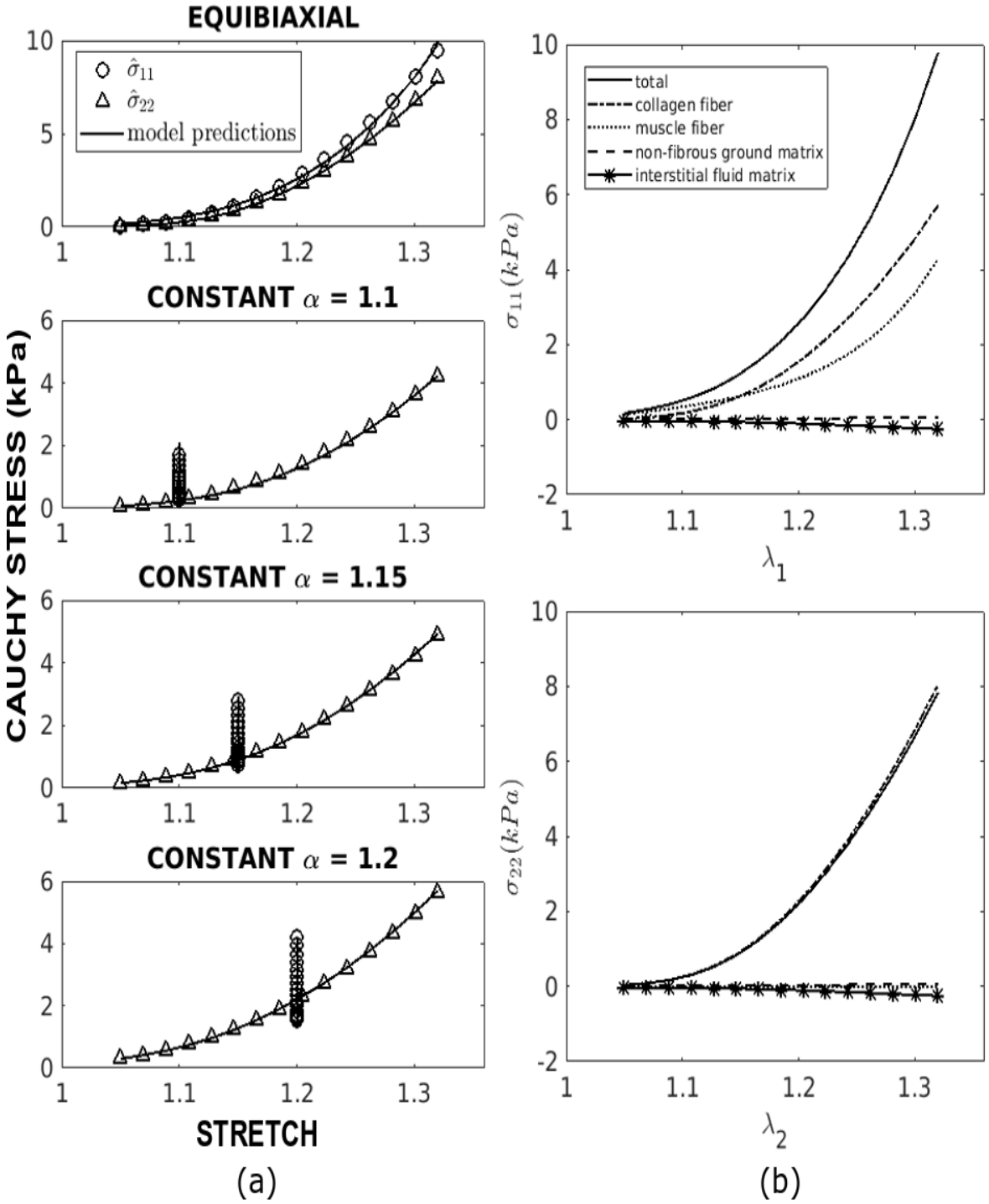

Figure B2. (a) Comparison of the fitted and experimental Cauchy stress-stretch data for equibiaxial and constant **α** = 1.1, 1.15 and 1.2 tests of specimen 0124. (b) Contribution of the collagen fiber network, muscle fibers, non-fibrous ground matrix and interstitial fluid matrix to the total stress in the fiber direction (top) and the cross-fiber (bottom) directions in the equi-biaxial test of specimen 0124

Specimen 0217

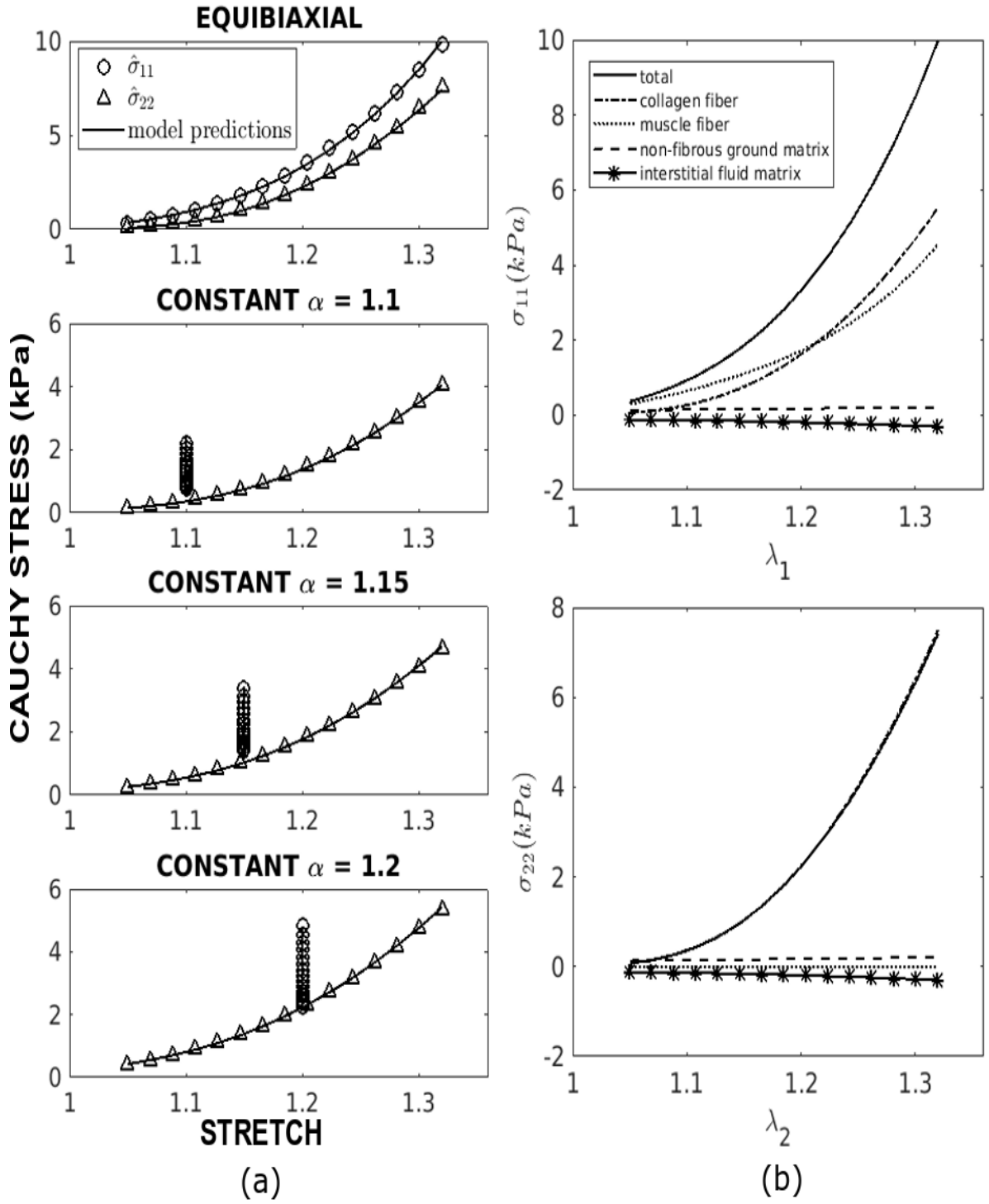

Figure B3. (a) Comparison of the fitted and experimental Cauchy stress-stretch data for equibiaxial and constant **α** = 1.1, 1.15 and 1.2 tests of specimen 0217. (b) Contribution of the collagen fiber network, muscle fibers, non-fibrous ground matrix and interstitial fluid matrix to the total stress in the fiber direction (top) and the cross-fiber (bottom) directions in the equi-biaxial test of specimen 0217

Specimen 0303

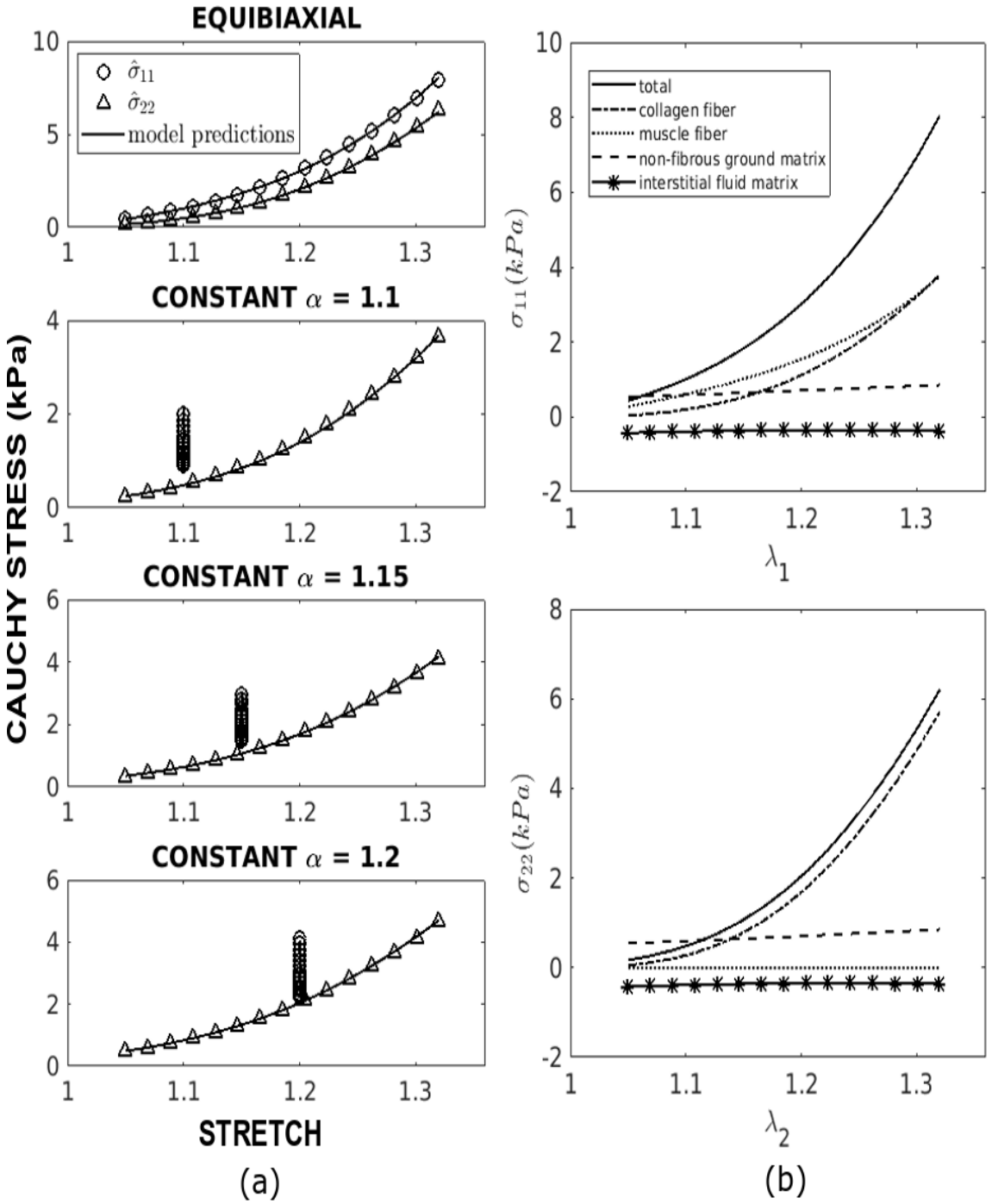

Figure B4. (a) Comparison of the fitted and experimental Cauchy stress-stretch data for equibiaxial and constant **α** = 1.1, 1.15 and 1.2 tests of specimen 0303. (b) Contribution of the collagen fiber network, muscle fibers, non-fibrous ground matrix and interstitial fluid matrix to the total stress in the fiber direction (top) and the cross-fiber (bottom) directions in the equi-biaxial test of specimen 0303

Specimen 0330

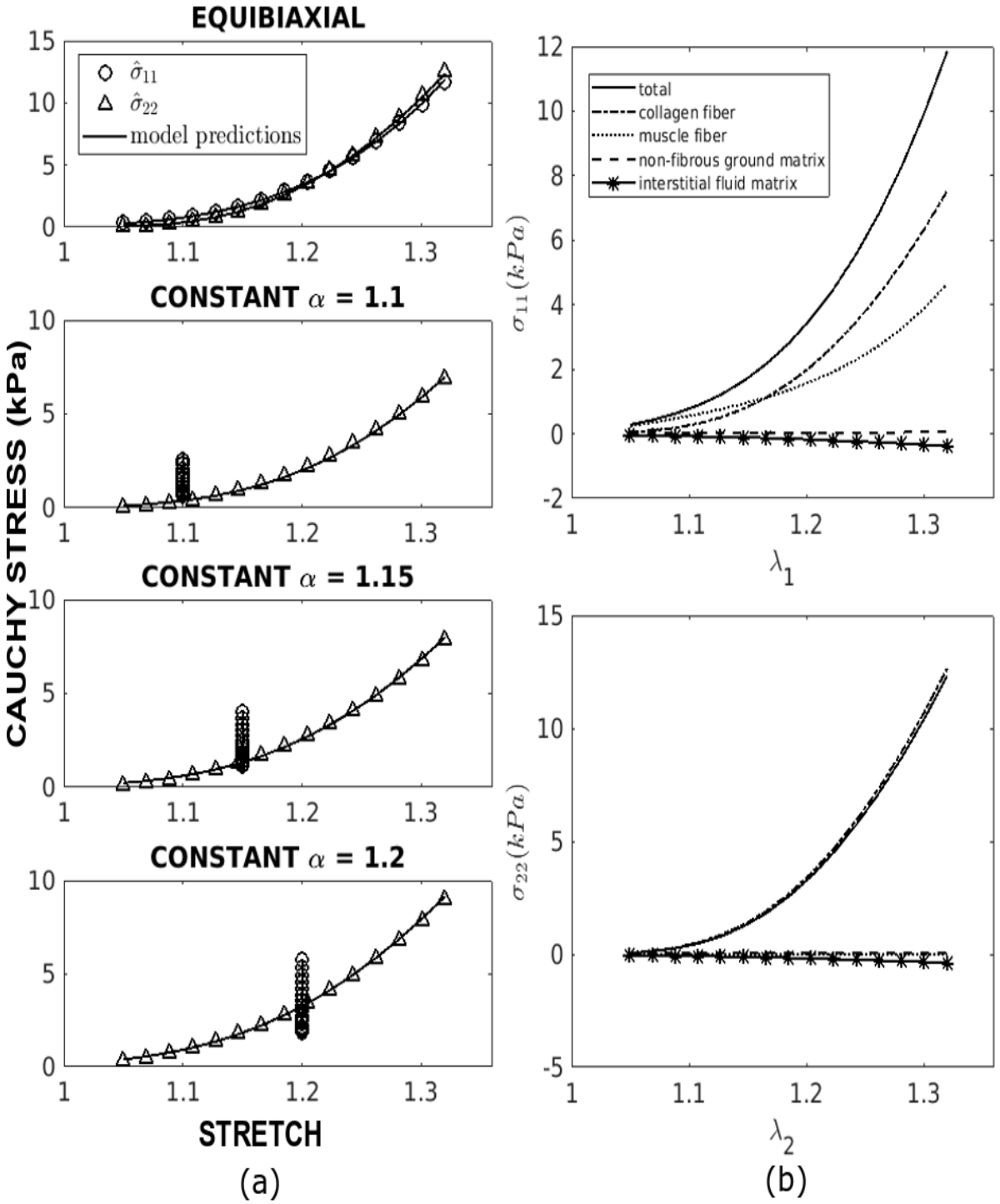

Figure B5. (a) Comparison of the fitted and experimental Cauchy stress-stretch data for equibiaxial and constant **α** = 1.1, 1.15 and 1.2 tests of specimen 0330. (b) Contribution of the collagen fiber network, muscle fibers, non-fibrous ground matrix and interstitial fluid matrix to the total stress in the fiber direction (top) and the cross-fiber (bottom) directions in the equi-biaxial test of specimen 0330

APPENDIX C: Muscle fiber stress and stiffness modulus

From Eq. (3.4) in the main text, the Cauchy stress σ of the muscle fiber with stiffness coefficients of C_2 and C_3 at the given engineering strain ϵ is given by

$$\sigma = 2C_2C_3\epsilon(1+\epsilon)e^{C_3\epsilon^2} \tag{C1}$$

The corresponding stiffness modulus E for the muscle fiber is given by:

$$E = \frac{d\sigma}{d\epsilon} = 2C_2C_3(1+\epsilon)e^{C_3\epsilon^2} + 2C_2C_3\epsilon e^{C_3\epsilon^2} + 4C_2{C_3}^2\epsilon^2(1+\epsilon)e^{C_3\epsilon^2} \tag{C2}$$

APPENDIX D: Strains as a function of volume change ΔV

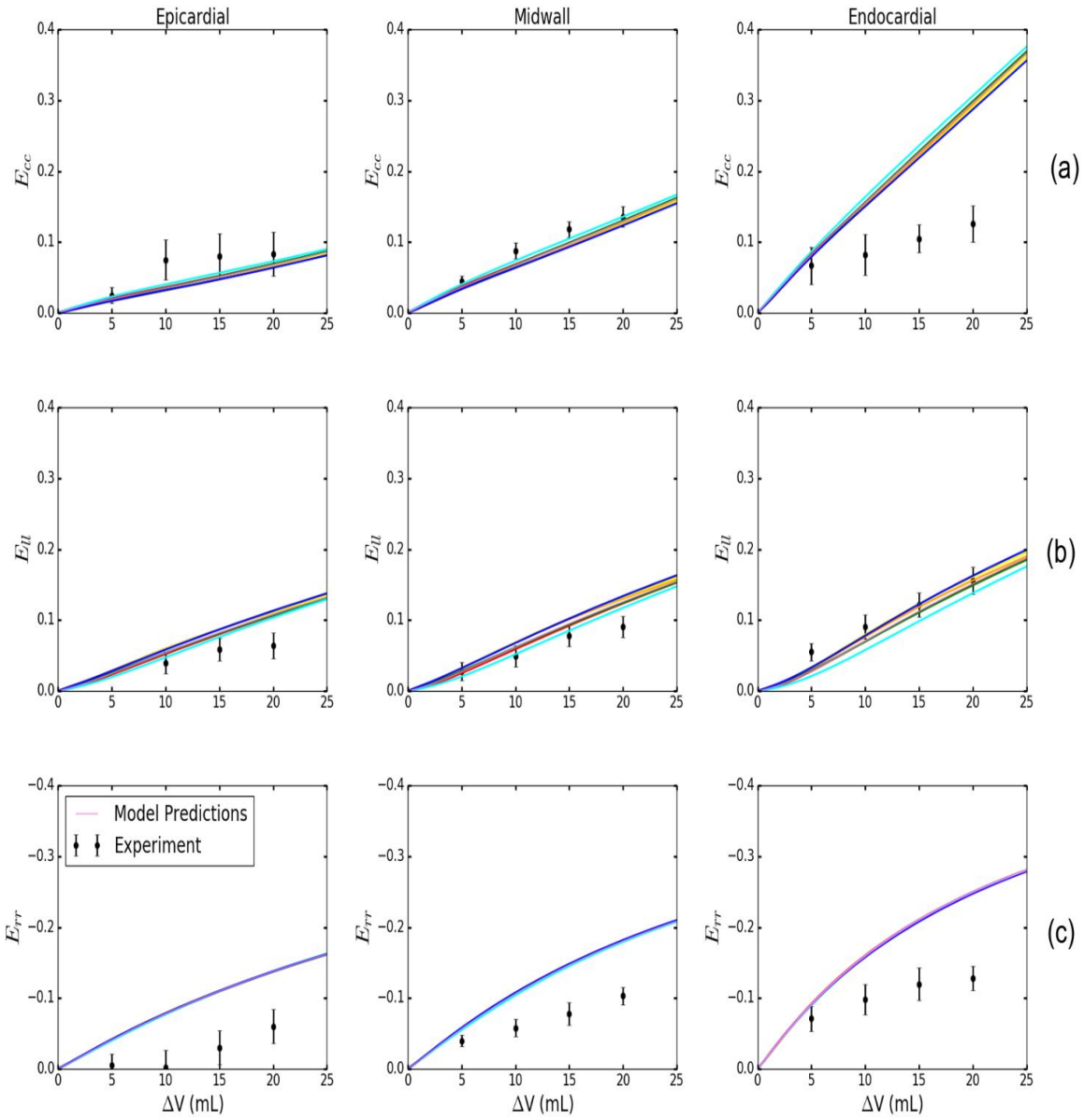

Figure D1. Normal strain components vs. LV cavity volume change ΔV at the sub-endocardial, midwall and sub-epicardial regions. Colored solid lines: model predictions using best-fit parameters and their mean values (Table 3.2 of the main text). Experimental data [2] are plotted as means ± SD. Note: sub-epicardial, midwall and sub-endocardial regions are reported as 2.0 ± 0.3%, 40.6 ± 5.5%, 79.1 ± 10.6% of the total wall thickness with respect to the epicardium in the experiments, which in our case, roughly corresponds to layer 1 (0 -14%), layer 3 (29 - 43%) and layer 6 (71 - 86%) of the LV FE model shown in Figure 3.2 in the main text.

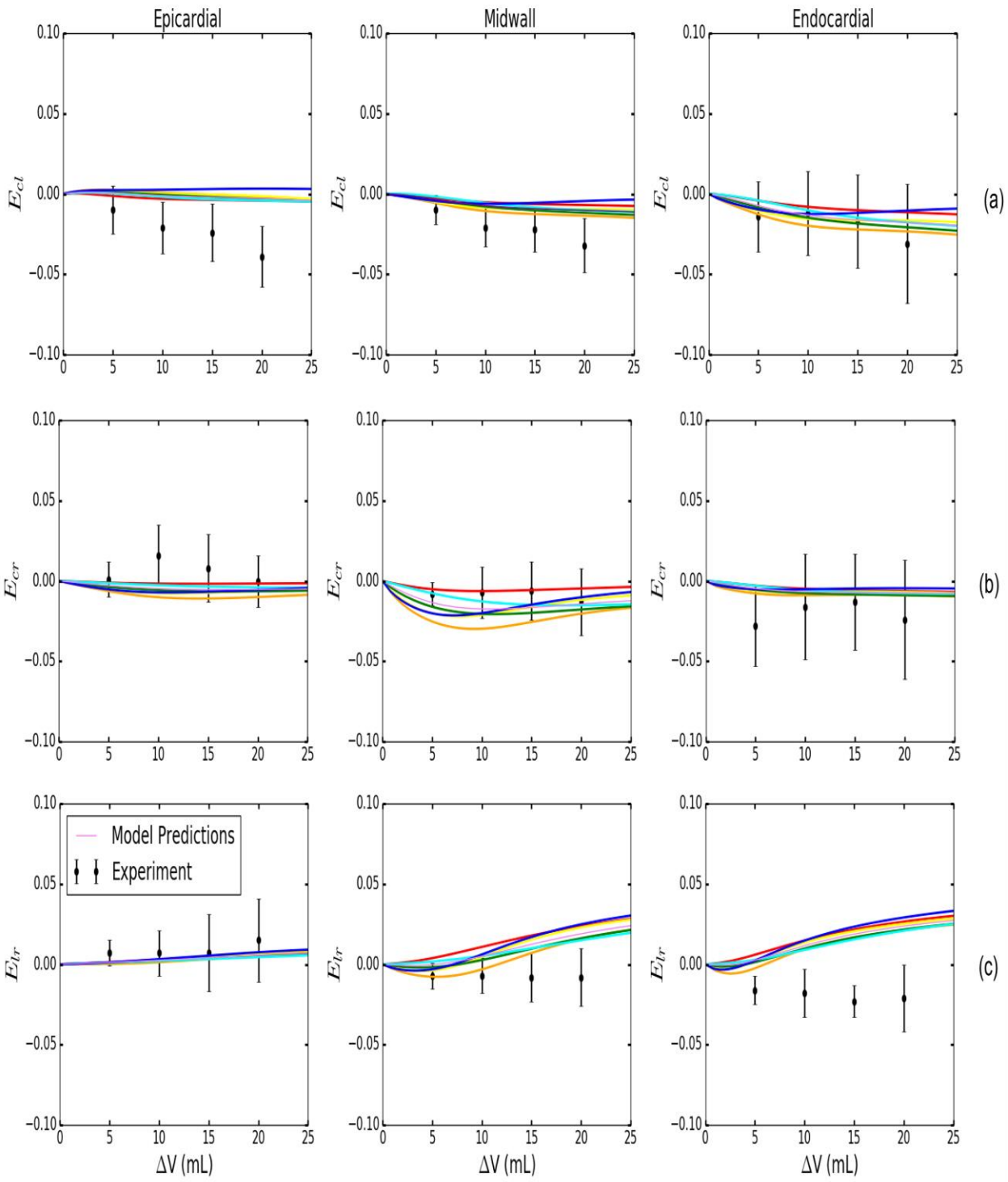

Figure D2. Shear strain components vs. LV cavity volume change ΔV at the sub-endocardial, midwall and sub-epicardial regions. Colored solid lines: model predictions using the best-fit parameters and their mean values in Table 3.2 of the main text. Experimental data [2] are plotted as means ± SD. Refer to Figure D1 for details of the transmural locations.

APPENDIX E: Mesh sensitivity and computational efficiency

Figure E1 shows the passive pressure vs. volume change curves using mean values of the fitted model parameters for the LV FE mesh with the number of finite elements ranging from 3565 to 8780. Our results showed that the difference in the change of LV volume at a pressure of 20 mmHg was about 3% between meshes with 4734 and 6435 elements, suggesting that a FE mesh with around 5000 elements should yield sufficiently accurate passive pressure volume relations.

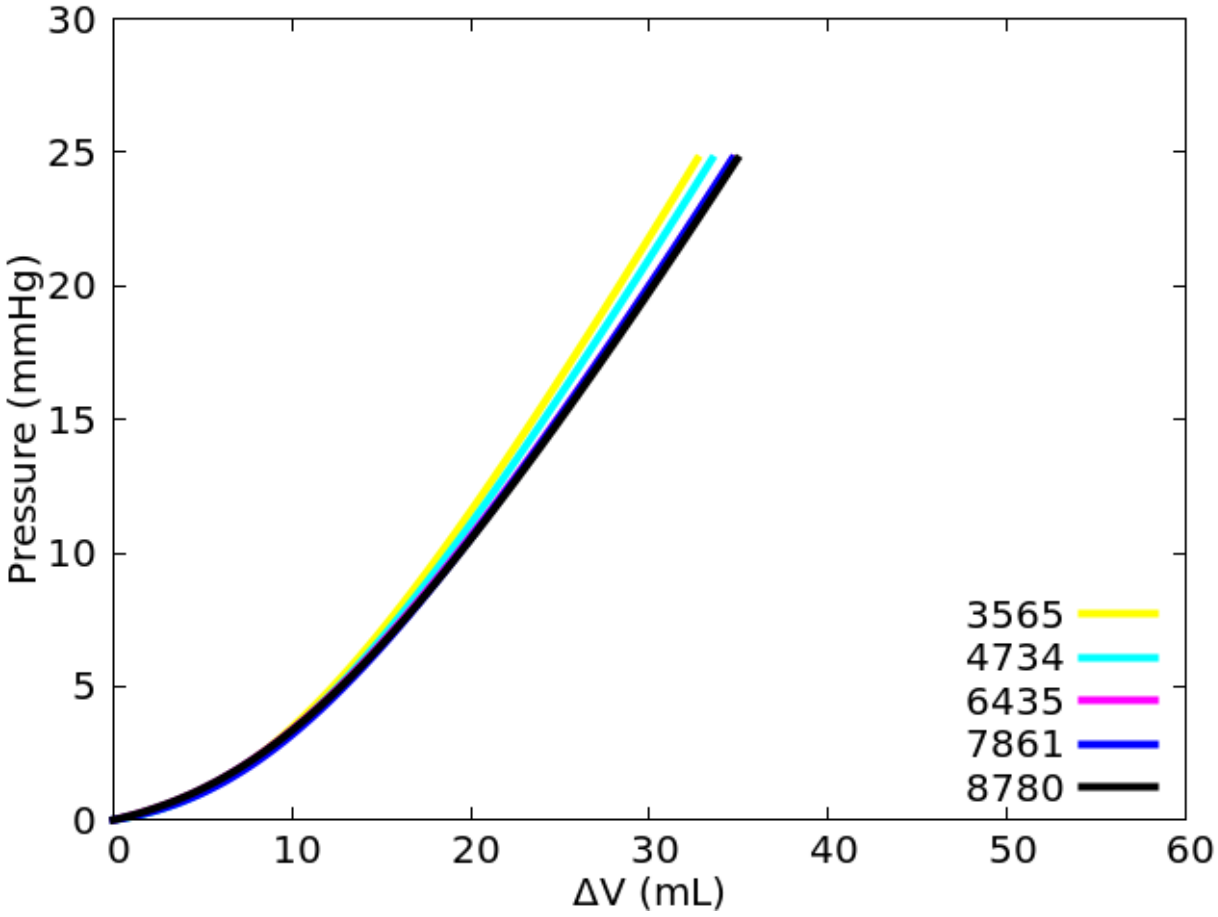

Figure E1. Effects of number of elements on the passive pressure volume relation using the mean fitted model parameters from biaxial tests.

Figure E2 shows the model-predicted transmural distribution of fiber stress using the mean fitted model parameters for the LV FE mesh with the number of finite elements ranging from 6035 to 38985. Our results showed that the difference in transmural fiber stress was less than 2% at each transmural layer between meshes with 17600 and 38985 elements, suggesting that the LV FE mesh with 17600 elements is sufficient to capture the deformation and transmural stress field.

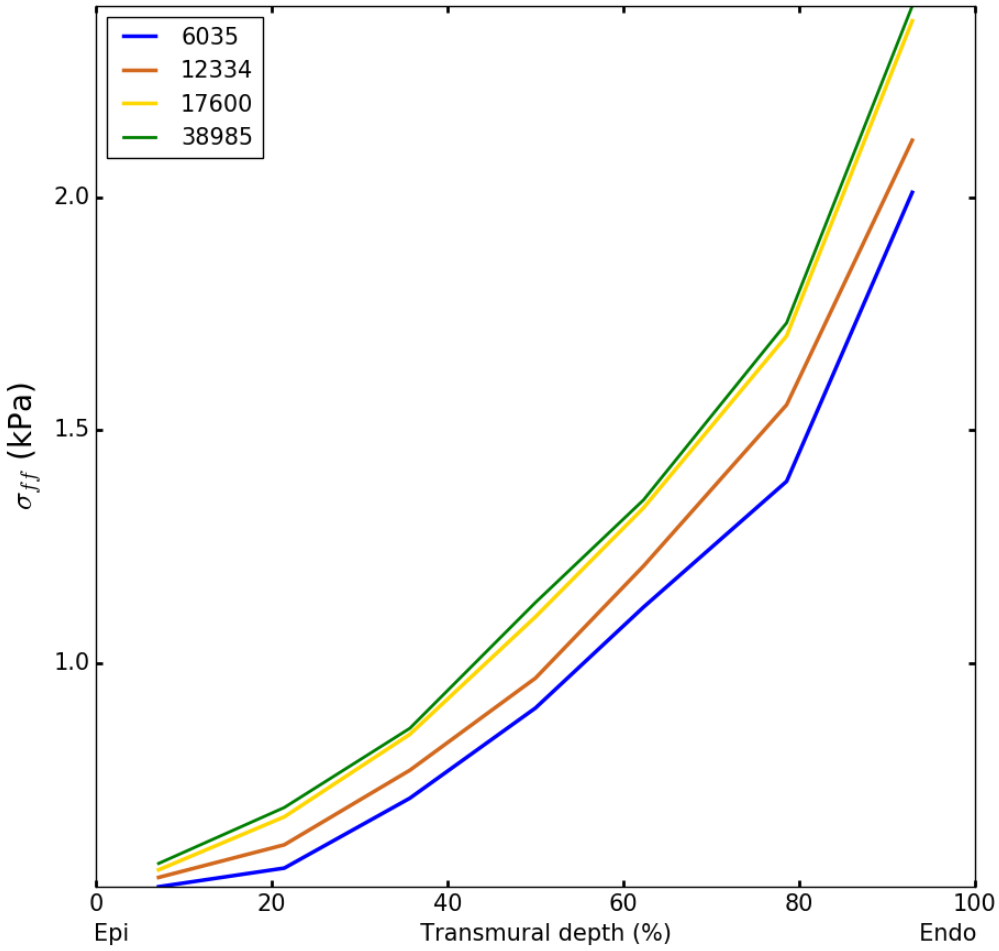

Figure E2. Effects of mesh density (number of cell elements) on the estimated transmural fiber stress at LV pressure of 8mmHg or 1.07kpa using the mean fitted model parameters (Table 3.2) from the biaxial tests.

The FEniCS library uses domain decomposition method that is inherently parallelizable (i.e., partitioning FE problem into sub-problems that can be solved in each processor). Our results showed an approximately linear parallel scalability of the code (**Table E1)**.

Table E1. Running time of passive inflation simulation for a FE mesh of 3565 elements with different number of processors (Intel® Xeon (R) CPU E5-1660 v3@ 3.00GHz x 16)

Number of Processors	Running Time
1	14 h 22 min
2	8 h 12 min
4	5h 30 min
8	3h 6 min
16	1h 37 min

Estimation of running time for simulating active mechanics:

Assuming that we set a time step of 1ms to simulate a cardiac cycle of 1000ms, then we need 1000 time steps, which should take about 39 hours to run for a mesh of 17600 elements with 16 processors (Intel® Xeon (R) CPU E5-1660 v3@ 3.00GHz). Because of the linear scalability exhibited by the code, the computing time can be reduced substantially if we use more processors.

APPENDIX F: Parameter sensitivity analysis

A sensitivity analysis on key parameters associated with the RV function (C_{RV},$T_{ref,RV}$ and $R_{per,p}$) was performed on the normal case by perturbing the parameters from their fitted values. The results of this analysis (**Table A1** and **Figure A1**) show the changes in predicted quantities (e.g., stroke volume and peak pressure) arising from perturbation of the parameter values. Specifically, the results show that these perturbations can produce a change in peak systolic pressure of 4 mmHg, which is the standard deviation of the normal RVP found in the measurements [20]. The results also show that the perturbation is substantially smaller than the fitted parameter values found in the PAH case, suggesting that differences in fitted parameter values between the PAH and normal case cannot be attributed to the uncertainty associated with the measurements of RVP (4 mmHg). To confirm this result, we have also rerun the normal case with parameters found from the PAH case, and the resulting PV loops are substantially different (**Figure A2**).

Table A1. Sensitivity analysis of model parameters in the normal case

		Change in (%)				
Parameters	Perturbation (%)	Peak systolic pressure	Stroke volume	RV work	Myofiber stress	cf. PAH values
$T_{ref,RV}$	+33	+11	+6.5	+19	+12	+117
C_{RV}	-21	+1.7	+3.1	+4.4	+4	+1533
$R_{per,p}$	+20	+4	-5.3	-2.5	+4.2	+420

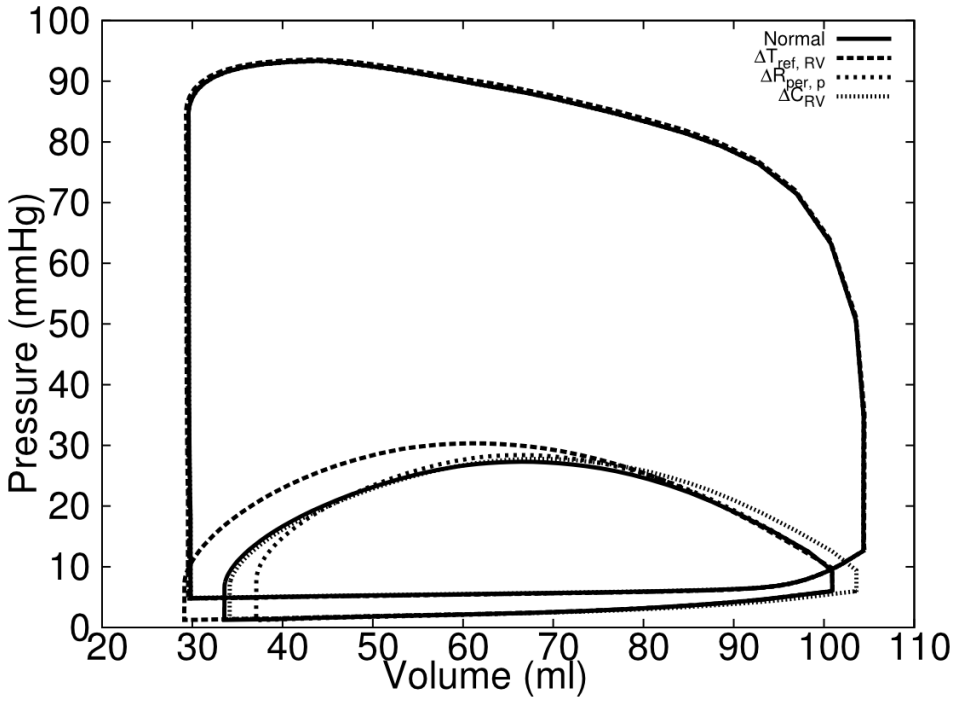

Figure A1. PV loops for perturbation of different model parameters in the normal case

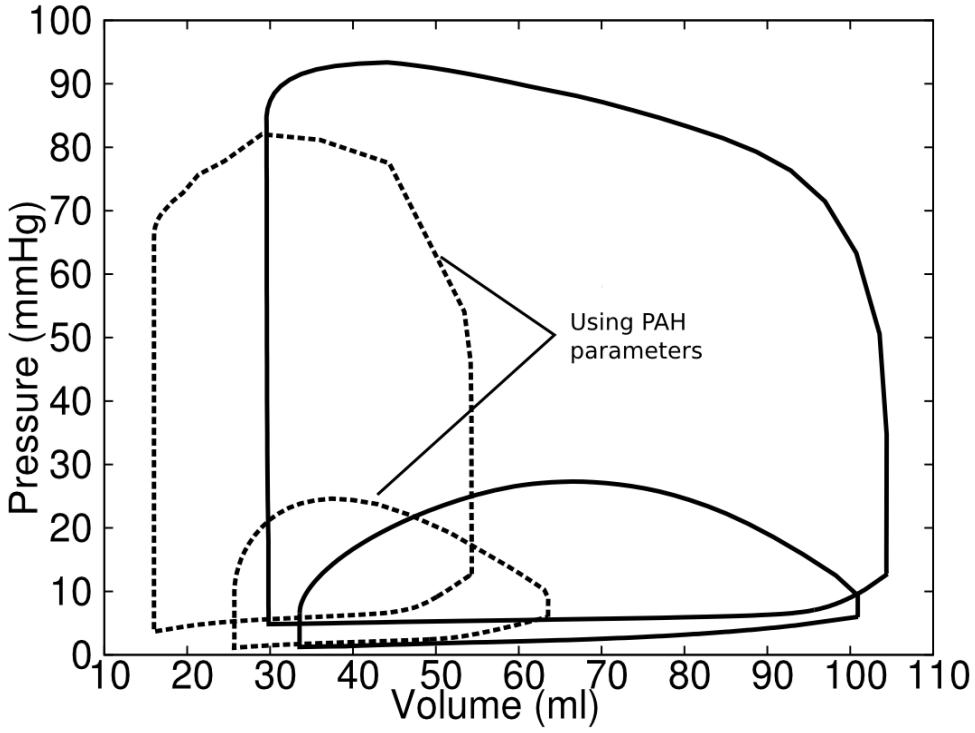

Figure A2. PV loops of the normal case using fitted PAH model parameters

BIBLIOGRAPHY

BIBLIOGRAPHY

[1] K. T. Weber, W. A. Clark, J. S. Janicki, and S. G. Shroff, “Physiologic versus pathologic hypertrophy and the pressure-overloaded myocardium.,” *J. Cardiovasc. Pharmacol.*, vol. 10 Suppl 6, pp. S37-50, 1987.

[2] J. H. Omens, K. D. May, and a D. McCulloch, “Transmural distribution of three-dimensional strain in the isolated arrested canine left ventricle.,” *Am. J. Physiol.*, 1991.

[3] J. D. Bayer, R. C. Blake, G. Plank, and N. A. Trayanova, “A novel rule-based algorithm for assigning myocardial fiber orientation to computational heart models,” *Ann. Biomed. Eng.*, vol. 40, no. 10, pp. 2243–2254, 2012.

[4] J. D. Bayer, R. C. Blake, G. Plank, and N. A. Trayanova, “A novel rule-based algorithm for assigning myocardial fiber orientation to computational heart models,” *Ann. Biomed. Eng.*, vol. 40, no. 10, pp. 2243–2254, 2012.

[5] R. K. Ghanta *et al.*, “Adjustable, Physiological Ventricular Restraint Improves Left Ventricular Mechanics and Reduces Dilatation in an Ovine Model of Chronic Heart Failure,” *Circulation*, vol. 115, no. 10, p. 1201 LP-1210, Mar. 2007.

[6] C.-S. Jhun *et al.*, “Effect of Adjustable Passive Constraint on the Failing Left Ventricle: A Finite-Element Model Study,” *Ann. Thorac. Surg.*, vol. 89, no. 1, pp. 132–137, Mar. 2018.

[7] J. F. Wenk *et al.*, “Biventricular Finite Element Modeling of the Acorn CorCap Cardiac Support Device on a Failing Heart,” *Ann. Thorac. Surg.*, vol. 95, no. 6, pp. 2022–2027, Jun. 2013.

[8] S. J. Sarnoff, E. Braunwald, G. H. Welch, R. B. Case, W. N. Stainsby, and R. Macruz, “Hemodynamic Determinants of Oxygen Consumption of the Heart With Special Reference to the Tension-Time Index,” *Am. J. Physiol. Content*, vol. 192, no. 1, pp. 148–156, Dec. 1957.

[9] B. E. Strauer, K. Beer, K. Heitlinger, and B. Höfling, “Left ventricular systolic wall stress as a primary determinant of myocardial oxygen consumption: Comparative studies in patients with normal left ventricular function, with pressure and volume overload and with coronary heart disease BT - The Hypertrophi,” 1977, pp. 214–221.

[10] W. Grossman, “Cardiac hypertrophy: Useful adaptation or pathologic process?,” *Am. J. Med.*, vol. 69, no. 4, pp. 576–584, Mar. 2018.

[11] L. L. Chuan, G. Martin, D. A. B., G. Liang, G. J. M., and R. M. B., “Applications of Computational Modeling in Cardiac Surgery,” *J. Card. Surg.*, vol. 29, no. 3, pp. 293–302, Apr. 2014.

[12] Y. C. Fung, “Elasticity of soft tissues in simple elongation,” *Am. J. Physiol. Content*, vol. 213, no. 6, pp. 1532–1544, Dec. 1967.

[13] J. D. Humphrey and F. C. P. Yin, “On Constitutive Relations and Finite Deformations of Passive Cardiac Tissue: I. A Pseudostrain-Energy Function,” *J. Biomech. Eng.*, vol. 109, no. 4, pp. 298–304, Nov. 1987.

[14] J. M. Guccione, A. D. McCulloch, and L. K. Waldman, “Passive Material Properties of Intact Ventricular Myocardium Determined From a Cylindrical Model,” *J. Biomech. Eng.*, vol. 113, no. 1, pp. 42–55, Feb. 1991.

[15] K. D. Costa, J. W. Holmes, and A. D. Mcculloch, “Modelling cardiac mechanical properties in three dimensions,” *Philos. Trans. R. Soc. London. Ser. A Math. Phys. Eng. Sci.*, vol. 359, no. 1783, p. 1233 LP-1250, Jun. 2001.

[16] G. A. Holzapfel and R. W. Ogden, “Constitutive modelling of passive myocardium: a structurally based framework for material characterization,” *Philos. Trans. R. Soc. A Math. Phys. Eng. Sci.*, vol. 367, no. 1902, p. 3445 LP-3475, Sep. 2009.

[17] C. J. Chuong and Y. C. Fung, “Three-Dimensional Stress Distribution in Arteries.,” *J. Biomech. Eng.*, vol. 105, no. 3, pp. 268–274, Aug. 1983.

[18] T. C. Gasser, R. W. Ogden, and G. A. Holzapfel, “Hyperelastic modelling of arterial layers with distributed collagen fibre orientations,” *J. R. Soc. interface*, vol. 3, no. 6, pp. 15–35, 2005.

[19] Y. Lanir, “Constitutive equations for fibrous connective tissues,” *J. Biomech.*, vol. 16, no. 1, pp. 1–12, Mar. 2018.

[20] S. M. Mijailovich, D. Stamenovic, and J. J. Fredberg, “Toward a kinetic theory of connective tissue micromechanics,” *J. Appl. Physiol.*, vol. 74, no. 2, pp. 665–681, Feb. 1993.

[21] M. Comninou and I. V Yannas, “Dependence of stress-strain nonlinearity of connective tissues on the geometry of collagen fibres,” *J. Biomech.*, vol. 9, no. 7, pp. 427–433, Mar. 2018.

[22] “On the deformation of slender filaments with planar crimp: theory, numerical solution and applications to tendon collagen and textile materials,” *Proc. R. Soc. London. A. Math. Phys. Sci.*, vol. 372, no. 1748, p. 33 LP-64, Aug. 1980.

[23] T. Farquhar, P. R. Dawson, and P. A. Torzilli, “A Microstructural Model for the Anisotropic Drained Stiffness of Articular Cartilage,” *J. Biomech. Eng.*, vol. 112, no. 4, pp. 414–425, Nov. 1990.

[24] K. L. Billiar and M. S. Sacks, “Biaxial Mechanical Properties of the Natural and Glutaraldehyde Treated Aortic Valve Cusp—Part I: Experimental Results,” *J. Biomech. Eng.*, vol. 122, no. 1, pp. 23–30, Jul. 1999.

[25] S. M. Belkoff and R. C. Haut, “A structural model used to evaluate the changing microstructure of maturing rat skin,” *J. Biomech.*, vol. 24, no. 8, pp. 711–720, Mar. 2018.

[26] Y. Lanir, “A structural theory for the homogeneous biaxial stress-strain relationships in flat collagenous tissues,” *J. Biomech.*, vol. 12, no. 6, pp. 423–436, 1979.

[27] A. Horowitz, Y. Lanir, F. C. P. Yin, M. Perl, I. Sheinman, and R. K. Strumpf, “Structural Three-Dimensional Constitutive Law for the Passive Myocardium,” *J. Biomech. Eng.*, vol. 110, no. 3, pp. 200–207, Aug. 1988.

[28] A. Horowitz, I. Sheinman, Y. Lanir, M. Perl, and S. Sideman, “Nonlinear Incompressible Finite Element for Simulating Loading of Cardiac Tissue—Part I: Two Dimensional Formulation for Thin Myocardial Strips,” *J. Biomech. Eng.*, vol. 110, no. 1, pp. 57–61, Feb. 1988.

[29] A. Horowitz, I. Sheinman, and Y. Lanir, “Nonlinear Incompressible Finite Element for Simulating Loading of Cardiac Tissue—Part II: Three Dimensional Formulation for Thick Ventricular Wall Segments,” *J. Biomech. Eng.*, vol. 110, no. 1, pp. 62–68, Feb. 1988.

[30] N. Oyama-Manabe *et al.*, “The strain-encoded (SENC) MR imaging for detection of global right ventricular dysfunction in pulmonary hypertension,” *Int. J. Cardiovasc. Imaging*, vol. 29, no. 2, pp. 371–378, 2013.

[31] N. Nasim *et al.*, “Utility of Right Ventricular Strain Imaging in Predicting Pulmonary Vascular Resistance in Patients With Pulmonary Hypertension,” *Congest. Hear. Fail.*, vol. 19, no. 3, pp. 116–122, Nov. 2012.

[32] D. Pellerin, R. Sharma, P. Elliott, and C. Veyrat, “Tissue Doppler, strain, and strain rate echocardiography for the assessment of left and right systolic ventricular function,” *Heart*, vol. 89, no. suppl 3, p. iii9 LP-iii17, Nov. 2003.

[33] E. Kraigher-Krainer *et al.*, “Impaired Systolic Function by Strain Imaging in Heart Failure With Preserved Ejection Fraction,” *J. Am. Coll. Cardiol.*, vol. 63, no. 5, pp. 447–456, 2014.

[34] W. Markiewicz, U. Sechtem, and C. B. Higgins, “Evaluation of the right ventricle by magnetic resonance imaging,” *Am. Heart J.*, vol. 113, no. 1, pp. 8–15, Mar. 2018.

[35] U. Sechtem, P. W. Pflugfelder, R. G. Gould, M. M. Cassidy, and C. B. Higgins, “Measurement of right and left ventricular volumes in healthy individuals with cine MR imaging.,” *Radiology*, vol. 163, no. 3, pp. 697–702, Jun. 1987.

[36] P. M. Pattynama, L. N. Willems, A. H. Smit, E. E. van der Wall, and A. de Roos, “Early diagnosis of cor pulmonale with MR imaging of the right ventricle.,” *Radiology*, vol. 182, no. 2, pp. 375–379, Feb. 1992.

[37] S. A. Kleijn *et al.*, “Comparison between three-dimensional speckle-tracking echocardiography and cardiac magnetic resonance imaging for quantification of left ventricular volumes and function,” *Eur. Hear. J. - Cardiovasc. Imaging*, vol. 13, no. 10, pp. 834–839, Oct. 2012.

[38] A. I. Veress, G. Klein, and G. T. Gullberg, “A Comparison of Hyperelastic Warping of PET Images with Tagged MRI for the Analysis of Cardiac Deformation,” *J. Biomed. Imaging*, vol. 2013, p. 9:9--9:9, Jan. 2013.

[39] A. I. Veress, J. A. Weiss, G. J. Klein, and G. T. Gullberg, “Quantification of 3D left ventricular deformation using hyperelastic warping: comparisons between MRI and PET imaging,” in *Computers in Cardiology*, 2002, pp. 709–712.

[40] A. I. Veress, G. T. Gullberg, and J. A. Weiss, “Measurement of strain in the left ventricle during diastole with cine-MRI and deformable image registration.,” *J. Biomech. Eng.*, vol. 127, no. 7, pp. 1195–1207, 2005.

[41] N. S. Phatak, S. A. Maas, A. I. Veress, N. A. Pack, E. V. R. Di Bella, and J. A. Weiss, “Strain measurement in the left ventricle during systole with deformable image registration,” *Med. Image Anal.*, vol. 13, no. 2, pp. 354–361, Mar. 2018.

[42] M. Genet *et al.*, “A Novel Method for Quantifying Smooth Regional Variations in Myocardial Contractility Within an Infarcted Human Left Ventricle Based on Delay-Enhanced Magnetic Resonance Imaging,” *J. Biomech. Eng.*, vol. 137, no. 8, pp. 81008–81009, Aug. 2015.

[43] L. C. Lee *et al.*, “A Novel Method for Quantifying In-Vivo Regional Left Ventricular Myocardial Contractility in the Border Zone of a Myocardial Infarction,” *J. Biomech. Eng.*, vol. 133, no. 9, p. 094506, 2011.

[44] J. Aguado-Sierra *et al.*, “Patient-specific modeling of dyssynchronous heart failure: A case study,” *Prog. Biophys. Mol. Biol.*, vol. 107, no. 1, pp. 147–155, 2011.

[45] B. Baillargeon *et al.*, “Human Cardiac Function Simulator for the Optimal Design of a Novel Annuloplasty Ring with a Sub-valvular Element for Correction of Ischemic Mitral Regurgitation,” *Cardiovasc. Eng. Technol.*, vol. 6, no. 2, pp. 105–116, 2015.

[46] J. F. Wenk *et al.*, “First Finite Element Model of the Left Ventricle With Mitral Valve: Insights Into Ischemic Mitral Regurgitation,” *Ann. Thorac. Surg.*, vol. 89, no. 5, pp. 1546–1553, Mar. 2018.

[47] L. C. Lee, S. T. Wall, M. Genet, A. Hinson, and J. M. Guccione, “Bioinjection treatment: Effects of post-injection residual stress on left ventricular wall stress,” *J. Biomech.*, vol. 47, no. 12, pp. 3115–3119, Mar. 2018.

[48] N. F. Voelkel *et al.*, “Right Ventricular Function and Failure,” *Circulation*, vol. 114, no. 17, p. 1883 LP-1891, Oct. 2006.

[49] D. GE, B. RJ, A. SM, and et al, “Survival in patients with primary pulmonary hypertension: Results from a national prospective registry,” *Ann. Intern. Med.*, vol. 115, no. 5, pp. 343–349, Sep. 1991.

[50] V. V McLaughlin *et al.*, “Survival with first-line bosentan in patients with primary pulmonary hypertension,” *Eur. Respir. J.*, vol. 25, no. 2, p. 244 LP-249, Feb. 2005.

[51] J. Sandoval *et al.*, “Survival in primary pulmonary hypertension. Validation of a prognostic equation.,” *Circulation*, vol. 89, no. 4, p. 1733 LP-1744, Apr. 1994.

[52] K. M. Chin, N. H. S. Kim, and L. J. Rubin, “The right ventricle in pulmonary hypertension,” *Coron. Artery Dis.*, vol. 16, no. 1, 2005.

[53] V. V. McLaughlin *et al.*, “ACCF/AHA 2009 Expert Consensus Document on Pulmonary Hypertension,” *J. Am. Coll. Cardiol.*, vol. 53, no. 17, pp. 1573–1619, 2009.

[54] T. Thenappan, S. J. Shah, S. Rich, and M. Gomberg-Maitland, “A USA-based registry for pulmonary arterial hypertension: 1982-2006,” *Eur. Respir. J.*, vol. 30, no. 6, pp. 1103–1110, 2007.

[55] M. Humbert *et al.*, “Survival in incident and prevalent cohorts of patients with pulmonary arterial hypertension,” *Eur. Respir. J.*, vol. 36, no. 3, pp. 549–555, 2010.

[56] a Vonk Noordegraaf and N. Galiè, “The role of the right ventricle in pulmonary arterial hypertension.,” *Eur. Respir. Rev.*, vol. 20, no. 122, pp. 243–53, 2011.

[57] M. Jessup, M. S. J. Sutton, K. T. Weber, and J. S. Janicki, “The effect of chronic pulmonary hypertension on left ventricular size, function, and interventricular septal motion,” *Am. Heart J.*, vol. 113, no. 5, pp. 1114–1122, Mar. 2018.

[58] M. A. J. Borgdorff, M. G. Dickinson, R. M. F. Berger, and B. Bartelds, “Right ventricular failure due to chronic pressure load: What have we learned in animal models since the NIH working group statement?,” *Heart Fail. Rev.*, vol. 20, no. 4, pp. 475–491, 2015.

[59] M. R. Hill, M. A. Simon, D. Valdez-Jasso, W. Zhang, H. C. Champion, and M. S. Sacks, “Structural and Mechanical Adaptations of Right Ventricle Free Wall Myocardium to Pressure Overload,” *Ann. Biomed. Eng.*, vol. 42, no. 12, pp. 2451–2465, 2014.

[60] W. Zhijie, S. D. A., H. T. A., and C. N. C., “Progressive right ventricular functional and structural changes in a mouse model of pulmonary arterial hypertension,” *Physiol. Rep.*, vol. 1, no. 7, p. e00184, Dec. 2013.

[61] C. McCabe *et al.*, “Right ventricular dysfunction in chronic thromboembolic obstruction of the pulmonary artery: a pressure-volume study using the conductance catheter,” *J. Appl. Physiol.*, vol. 116, no. 4, pp. 355–363, Dec. 2013.

[62] P. Trip *et al.*, “Clinical relevance of right ventricular diastolic stiffness in pulmonary hypertension,” *Eur Respir J*, vol. 45, pp. 1603–1612, 2015.

[63] W. P. Santamore and L. J. Dell’Italia, “Ventricular interdependence: Significant left ventricular contributions to right ventricular systolic function,” *Prog. Cardiovasc. Dis.*, vol. 40, no. 4, pp. 289–308, Mar. 2018.

[64] E. K. Louie, S. S. Lin, S. I. Reynertson, B. H. Brundage, S. Levitsky, and S. Rich, “Pressure and Volume Loading of the Right Ventricle Have Opposite Effects on Left Ventricular Ejection Fraction,” *Circulation*, vol. 92, no. 4, p. 819 LP-824, Aug. 1995.

[65] A. M. Katz, *Physiology of the Heart*. Lippincott Williams & Wilkins, 2010.

[66] B. co. staff and B. co. staff, “Medical gallery of Blausen Medical 2014,” *WikiJournal Med.*, vol. 1, no. 2, p. 10, 2014.

[67] J. S. Frank and G. a Langer, “The myocardial interstitium: its structure and its role in ionic exchange.,” *J. Cell Biol.*, vol. 60, no. 3, pp. 586–601, Mar. 1974.

[68] P. G. CASPARI, M. NEWCOMB, K. GIBSON, and P. HARRIS, “Collagen in the normal and hypertrophied human ventricle,” *Cardiovasc. Res.*, vol. 11, no. 6, pp. 554–558, Nov. 1977.

[69] K. T. Weber, “Cardiac interstitium in health and disease: The fibrillar collagen network,” *J. Am. Coll. Cardiol.*, vol. 13, no. 7, pp. 1637–1652, 1989.

[70] S. Mendis, P. Puska, B. Norrving, W. H. Organization, and others, *Global atlas on cardiovascular disease prevention and control*. Geneva: World Health Organization, 2011.

[71] I. I. Abubakar, T. Tillmann, and A. Banerjee, “Global, regional, and national age-sex specific all-cause and cause-specific mortality for 240 causes of death, 1990-2013: a systematic analysis for the Global Burden of Disease Study 2013,” *Lancet*, vol. 385, no. 9963, pp. 117–171, 2015.

[72] S. P. Gaine and L. J. Rubin, “Primary pulmonary hypertension.,” *Lancet (London, England)*, vol. 352, no. 9129, pp. 719–725, Aug. 1998.

[73] M. Humbert *et al.*, “Pulmonary arterial hypertension in France: results from a national registry,” *Am. J. Respir. Crit. Care Med.*, vol. 173, no. 9, pp. 1023–1030, 2006.

[74] K. W. Prins and T. Thenappan, “World Health Organization Group I Pulmonary Hypertension: Epidemiology and Pathophysiology,” *Cardiol. Clin.*, vol. 34, no. 3, pp. 363–374, Aug. 2016.

[75] M. Humbert, O. Sitbon, and G. Simonneau, “Treatment of pulmonary arterial hypertension,” *N. Engl. J. Med.*, vol. 351, no. 14, pp. 1425–1436, 2004.

[76] M. Humbert *et al.*, “Survival in incident and prevalent cohorts of patients with pulmonary arterial hypertension,” *Eur. Respir. J.*, vol. 36, no. 3, pp. 549–555, 2010.

[77] J. F. Wenk *et al.*, “First finite element model of the left ventricle with mitral valve: insights into ischemic mitral regurgitation.,” *Ann. Thorac. Surg.*, vol. 89, no. 5, pp. 1546–1553, 2010.

[78] L. C. Lee, S. T. Wall, M. Genet, A. Hinson, and J. M. Guccione, “Bioinjection treatment: Effects of post-injection residual stress on left ventricular wall stress,” *J. Biomech.*, vol. 47, no. 12, pp. 3115–3119, 2014.

[79] N. F. Voelkel *et al.*, “Right ventricular function and failure: Report of a National Heart, Lung, and Blood Institute working group on cellular and molecular mechanisms of right heart failure,” *Circulation*, vol. 114, no. 17, pp. 1883–1891, 2006.

[80] T. E. Owan, D. O. Hodge, R. M. Herges, S. J. Jacobsen, V. L. Roger, and M. M. Redfield, “Trends in Prevalence and Outcome of Heart Failure with Preserved Ejection Fraction,” *N. Engl. J. Med.*, vol. 355, no. 3, pp. 251–259, Jul. 2006.

[81] R. S. Bhatia *et al.*, “Outcome of Heart Failure with Preserved Ejection Fraction in a Population-Based Study,” *N. Engl. J. Med.*, vol. 355, no. 3, pp. 260–269, Jul. 2006.

[82] B. A. Steinberg *et al.*, “Trends in patients hospitalized with heart failure and preserved left ventricular ejection fraction: prevalence, therapies, and outcomes.,” *Circulation*, vol. 126, no. 1, pp. 65–75, Jul. 2012.

[83] K. Yamamoto, Y. Sakata, T. Ohtani, Y. Takeda, and T. Mano, “Heart failure with preserved ejection fraction,” *Circ. J.*, p. 902020256, 2009.

[84] L. Guo *et al.*, “Prevalence and Risk Factors of Heart Failure with Preserved Ejection Fraction: A Population-Based Study in Northeast China.,” *Int. J. Environ. Res. Public Health*, vol. 13, no. 8, Jul. 2016.

[85] C. W. Yancy *et al.*, “2013 ACCF/AHA guideline for the management of heart failure: a report of the American College of Cardiology Foundation/American Heart Association Task Force on Practice Guidelines.,” *J. Am. Coll. Cardiol.*, vol. 62, no. 16, pp. e147-239, Oct. 2013.

[86] K. Yamamoto *et al.*, “Myocardial stiffness is determined by ventricular fibrosis, but not by compensatory or excessive hypertrophy in hypertensive heart.,” *Cardiovasc. Res.*, vol. 55, no. 1, pp. 76–82, Jul. 2002.

[87] A. Borbély *et al.*, “Cardiomyocyte stiffness in diastolic heart failure,” *Circulation*, vol. 111, no. 6, pp. 774–781, 2005.

[88] B. A. Borlaug and M. M. Redfield, “Diastolic and systolic heart failure are distinct phenotypes within the heart failure spectrum,” *Circulation*, vol. 123, no. 18, pp. 2006–2014, May 2011.

[89] H. Zou *et al.*, “Quantification of Biventricular Strains in Heart Failure With Preserved Ejection Fraction Patient Using Hyperelastic Warping Method,” *Front. Physiol.*, vol. 9, p. 1295, 2018.

[90] A. D. DeVore *et al.*, “Impaired left ventricular global longitudinal strain in patients with heart failure with preserved ejection fraction: insights from the RELAX trial.,” *Eur. J. Heart Fail.*, vol. 19, no. 7, pp. 893–900, Jul. 2017.

[91] Z. Gregorova, J. Meluzin, R. Stepanova, J. Sitar, H. Podrouzkova, and L. Spinarova, “Longitudinal, circumferential and radial systolic left ventricular function in patients with heart failure and preserved ejection fraction.,” *Biomed. Pap. Med. Fac. Univ. Palacky. Olomouc. Czech. Repub.*, vol. 160, no. 3, pp. 385–392, Sep. 2016.

[92] B. A. Borlaug, “The pathophysiology of heart failure with preserved ejection fraction.,” *Nat. Rev. Cardiol.*, vol. 11, no. 9, pp. 507–515, Sep. 2014.

[93] B. A. Borlaug and W. J. Paulus, “Heart failure with preserved ejection fraction: pathophysiology, diagnosis, and treatment,” *Eur. Heart J.*, vol. 32, no. 6, pp. 670–679, Mar. 2011.

[94] D. W. Kitzman *et al.*, “A randomized double-blind trial of enalapril in older patients with heart failure and preserved ejection fraction: effects on exercise tolerance and arterial distensibility.,” *Circ. Heart Fail.*, vol. 3, no. 4, pp. 477–485, Jul. 2010.

[95] D. Westermann *et al.*, “Cardiac inflammation contributes to changes in the extracellular matrix in patients with heart failureand normal ejection fraction.,” *Circ. Heart Fail.*, vol. 4, no. 1, pp. 44–52, Jan. 2011.

[96] K.-P. Rommel *et al.*, “Extracellular Volume Fraction for Characterization of Patients With Heart Failure and Preserved Ejection Fraction.,” *J. Am. Coll. Cardiol.*, vol. 67, no. 15, pp. 1815–1825, Apr. 2016.

[97] C. Franssen and A. González Miqueo, “The role of titin and extracellular matrix remodelling in heart failure with preserved ejection fraction,” *Netherlands Heart Journal*, vol. 24, no. 4. pp. 259–267, 2016.

[98] J. L. Melero-Ferrer *et al.*, “Novel Imaging Techniques for Heart Failure,” *Card. Fail. Rev.*, vol. 2, no. 1, pp. 27–34, May 2016.

[99] J. N. Kirkpatrick, M. A. Vannan, J. Narula, and R. M. Lang, “Echocardiography in heart failure: applications, utility, and new horizons.,” *J. Am. Coll. Cardiol.*, vol. 50, no. 5, pp. 381–396, Jul. 2007.

[100] G. Captur, C. Manisty, and J. C. Moon, “Cardiac MRI evaluation of myocardial disease.,” *Heart*, vol. 102, no. 18, pp. 1429–1435, Sep. 2016.

[101] T. Geva, “Is MRI the preferred method for evaluating right ventricular size and function in patients with congenital heart disease?: MRI is the preferred method for evaluating right ventricular size and function in patients with congenital heart disease,” *Circ. Cardiovasc. Imaging*, vol. 7, no. 1, pp. 190–197, Jan. 2014.

[102] A. Lopez-Perez, R. Sebastian, and J. M. Ferrero, “Three-dimensional cardiac computational modelling: methods, features and applications.,” *Biomed. Eng. Online*, vol. 14, p. 35, Apr. 2015.

[103] S. Sarnoff, E. Braunwald, … G. W. J.-A. J. of, and undefined 1957, “Hemodynamic determinants of oxygen consumption of the heart with special reference to the tension-time index,” *physiology.org*.

[104] W. Grossman, “Cardiac Hypertrophy: Useful Adaptation or Pathologic Process?,” *Am. J. Med.*, vol. 69, no. 4, pp. 576–584, 1980.

[105] F. H. L., M. R. E., G. COLIN, G. D. G., and B. I. L., “Left Ventricular Wall Stress Calculated from One-Plane Cineangiography ,” *Circ. Res.*, vol. 26, no. 1, pp. 71–83, Jan. 1970.

[106] I. Mirsky, “Left Ventricular Stresses in the Intact Human Heart,” *Biophys. J.*, vol. 9, no. 1957, pp. 189–208, 1969.

[107] F. C. Yin, “Ventricular wall stress.,” *Circ. Res.*, vol. 49, no. 4, pp. 829–842, 1981.

[108] J. D. Humphrey, R. K. Strumpf, and F. C. Yin, “Determination of a constitutive relation for passive myocardium: I. A new functional form.,” *J. Biomech. Eng.*, vol. 112, no. 3, pp. 333–339, 1990.

[109] K. D. Costa *et al.*, “A Three-Dimensional Finite Element Method for Large Elastic Deformations of Ventricular Myocardium: {{II}}\textemdash{}{{Prolate}} Spheroidal Coordinates,” *J. Biomech. Eng.*, vol. 118, pp. 464–472, 1996.

[110] R. C. P. Kerckhoffs, P. H. M. Bovendeerd, J. C. S. Kotte, F. W. Prinzen, K. Smits, and T. Arts, “Homogeneity of cardiac contraction despite physiological asynchrony of depolarization: a model study.,” *Ann. Biomed. Eng.*, vol. 31, no. 5, pp. 536–547, May 2003.

[111] S. Dokos, B. H. Smaill, A. A. Young, and I. J. LeGrice, “Shear Properties of Passive Ventricular Myocardium,” *Am. J. Physiol. Hear. Circ. Physiol.*, vol. 283, no. 6, pp. H2650--9, Dec. 2002.

[112] P. J. HUNTER, “Computational electromechanics of the heart,” *Comput. Biol. Hear.*, pp. 345–407, 1997.

[113] H. Schmid, M. P. Nash, A. A. Young, and P. J. Hunter, “Myocardial Material Parameter Estimation—A Comparative Study for Simple Shear,” *J. Biomech. Eng.*, vol. 128, no. 5, pp. 742–750, Mar. 2006.

[114] Y. Lanir, “Constitutive equations for fibrous connective tissues,” *J. Biomech.*, vol. 16, no. 1, pp. 1–12, 1983.

[115] G. Diamond, J. S. Forrester, J. Hargis, W. W. Parmley, R. Danzig, and H. J. C. Swan, “Dlastolic Pressure-Volume Relationship in the Canine Left Ventricle,” *Circ. Res.*, vol. 29, no. 3, pp. 267–275, 1971.

[116] J. C. Gilbert and S. A. Glantz, “Determinants of left ventricular filling and of the diastolic pressure-volume relation.,” *Circ. Res.*, vol. 64, no. 5, pp. 827–852, May 1989.

[117] M. Golman, W. Padovano, L. Shmuylovich, and S. J. Kovács, “Quantifying Diastolic Function: From E-Waves as Triangles to Physiologic Contours via the ‘Geometric Method,’” *Cardiovasc. Eng. Technol.*, 2018.

[118] G. Pedrizzetti *et al.*, “On estimating intraventricular hemodynamic forces from endocardial dynamics: A comparative study with 4D flow MRI,” *J. Biomech.*, 2017.

[119] A. A. Oktay, J. D. Rich, and S. J. Shah, “The emerging epidemic of heart failure with preserved ejection fraction.,” *Curr. Heart Fail. Rep.*, vol. 10, no. 4, pp. 401–410, Dec. 2013.

[120] M.-Y. M. Su *et al.*, “CMR-Verified Diffuse Myocardial Fibrosis Is Associated With Diastolic Dysfunction in HFpEF,” *JACC Cardiovasc. Imaging*, vol. 7, no. 10, pp. 991–997, 2014.

[121] T. Neumann, A. Vollmer, T. Schaffner, O. M. Hess, and G. Heusch, “Diastolic dysfunction and collagen structure in canine pacing-induced heart failure,” *J. Mol. Cell. Cardiol.*, 1999.

[122] P. J. Hunter, P. M. Nielsen, B. H. Smaill, I. J. LeGrice, and I. W. Hunter, “An anatomical heart model with applications to myocardial activation and ventricular mechanics.,” *Crit. Rev. Biomed. Eng.*, vol. 20, no. 5–6, pp. 403–26, Jan. 1992.

[123] Y. Lanir, “A structural theory for the homogeneous biaxial stress-strain relationships in flat collagenous tissues.,” *J. Biomech.*, vol. 12, pp. 423–436, 1979.

[124] J. W. Y. Jor, M. P. Nash, P. M. F. Nielsen, and P. J. Hunter, “Estimating material parameters of a structurally based constitutive relation for skin mechanics,” *Biomech. Model. Mechanobiol.*, vol. 10, no. 5, pp. 767–778, 2011.

[125] K. L. Billiar and M. S. Sacks, “Biaxial Mechanical Properties of the Native and Glutaraldehyde-Treated Aortic Valve Cusp: Part II—A Structural Constitutive Model,” *J. Biomech. Eng.*, vol. 122, no. 4, pp. 327–335, Mar. 2000.

[126] H. Chen, T. Luo, X. Zhao, X. Lu, Y. Huo, and G. S. Kassab, “Microstructural constitutive model of active coronary media,” *Biomaterials*, vol. 34, no. 31, pp. 7575–7583, 2013.

[127] E. Nevo and Y. Lanir, “The effect of residual strain on the diastolic function of the left ventricle as predicted by a structural model,” *J. Biomech.*, vol. 27, no. 12, pp. 1433–1446, 1994.

[128] R. Fan and M. S. Sacks, “Simulation of planar soft tissues using a structural constitutive model: Finite element implementation and validation,” *J. Biomech.*, vol. 47, no. 9, pp. 2043–2054, 2014.

[129] M. Alnæs *et al.*, “The FEniCS Project Version 1.5,” *Arch. Numer. Softw.*, vol. 3, no. 100, Dec. 2015.

[130] J. B. Caulfield and T. K. Borg, “The collagen network of the heart.,” *Lab. Invest.*, vol. 40, pp. 364–372, 1979.

[131] T. F. Robinson, L. Cohen-Gould, and S. M. Factor, “Skeletal framework of mammalian heart muscle. Arrangement of inter- and pericellular connective tissue structures,” *Lab. Invest.*, vol. 49, no. 4, pp. 482–498, 1983.

[132] Y. Fung, *Biomechanics: mechanical properties of living tissues*. Springer Science & Business Media, 2013.

[133] R. Fan and M. S. Sacks, “Simulation of planar soft tissues using a structural constitutive model: Finite element implementation and validation,” *J. Biomech.*, vol. 47, no. 9, pp. 2043–2054, 2014.

[134] R. M. Buchanan and M. S. Sacks, “Interlayer micromechanics of the aortic heart valve leaflet.,” *Biomech. Model. Mechanobiol.*, vol. 13, no. 4, pp. 813–826, Aug. 2014.

[135] D. Fish, J. Orenstein, and S. Bloom, “Passive stiffness of isolated cardiac and skeletal myocytes in the hamster.,” *Circ. Res.*, vol. 54, no. 3, pp. 267–276, Mar. 1984.

[136] Z. L. Shen, M. R. Dodge, H. Kahn, R. Ballarini, and S. J. Eppell, “Stress-Strain Experiments on Individual Collagen Fibrils,” *Biophys. J.*, vol. 95, no. 8, pp. 3956–3963, 2008.

[137] G. A. Holzapfel, J. A. Niestrawska, R. W. Ogden, A. J. Reinisch, and A. J. Schriefl, “Modelling non-symmetric collagen fibre dispersion in arterial walls,” *J. R. Soc. Interface*, 2015.

[138] G. A. Holzapfel and R. W. Ogden, “Comparison of two model frameworks for fiber dispersion in the elasticity of soft biological tissues,” *Eur. J. Mech. A/Solids*, 2017.

[139] J. D. Humphrey, R. K. Strumpf, and F. C. Yin, “Determination of a constitutive relation for passive myocardium: II. Parameter estimation.,” *J. Biomech. Eng.*, vol. 112, no. 3, pp. 340–346, Aug. 1990.

[140] R. I. Bashey, A. Martinez-Hernandez, and S. A. Jimenez, “Isolation, characterization, and localization of cardiac collagen type VI. Associations with other extracellular matrix components.,” *Circ. Res.*, vol. 70, no. 5, pp. 1006–1017, May 1992.

[141] J. D. Humphrey, “Cardiovascular Solid Mechanics: Cells, Tissues and Organs. 35 Springer-Verlag,” *New York*, 2002.

[142] R. Avazmohammadi, M. R. Hill, M. A. Simon, W. Zhang, and M. S. Sacks, “A novel constitutive model for passive right ventricular myocardium: evidence for myofiber--collagen fiber mechanical coupling,” *Biomech. Model. Mechanobiol.*, vol. 16, no. 2, pp. 561–581, 2017.

[143] S. A. Glantz and R. S. Kernoff, “Muscle stiffness determined from canine left ventricular pressure-volume curves.,” *Circ. Res.*, vol. 37, no. 6, pp. 787–794, 1975.

[144] H. F. Choi, J. D’hooge, F. E. Rademakers, and P. Claus, “Influence of left-ventricular shape on passive filling properties and end-diastolic fiber stress and strain.,” *J. Biomech.*, vol. 43, no. 9, pp. 1745–53, Jun. 2010.

[145] A. J. Brady, “Length dependence of passive stiffness in single cardiac myocytes,” *Am. J. Physiol. Circ. Physiol.*, vol. 260, no. 4, pp. H1062–H1071, Apr. 1991.

[146] W. Yang *et al.*, “On the tear resistance of skin.,” *Nat. Commun.*, vol. 6, p. 6649, Mar. 2015.

[147] D. A. MacKenna, S. M. Vaplon, and A. D. McCulloch, “Microstructural model of perimysial collagen fibers for resting myocardial mechanics during ventricular filling.,” *Am. J. Physiol.*, vol. 273, no. 3 Pt 2, pp. H1576-86, Sep. 1997.

[148] A. D. McCulloch, B. H. Smaill, and P. J. Hunter, “Left ventricular epicardial deformation in isolated arrested dog heart.,” *Am. J. Physiol.*, vol. 252, no. 1 Pt 2, pp. H233-41, Jan. 1987.

[149] D. A. MacKenna, J. H. Omens, and J. W. Covell, “Left ventricular perimysial collagen fibers uncoil rather than stretch during diastolic filling,” *Basic Res. Cardiol.*, vol. 91, no. 2, pp. 111–122, 1996.

[150] J. H. Omens, T. R. Miller, and J. W. Covell, “Relationship between passive tissue strain and collagen uncoiling during healing of infarcted myocardium,” *Cardiovasc. Res.*, vol. 33, no. 2, pp. 351–358, Feb. 1997.

[151] W. A. Linke, V. I. Popov, and G. H. Pollack, “Passive and active tension in single cardiac myofibrils.,” *Biophys. J.*, vol. 67, no. 2, pp. 782–792, Aug. 1994.

[152] F. A. Zouein, L. E. De Castro Brás, D. V. Da Costa, M. L. Lindsey, M. Kurdi, and G. W. Booz, “Heart failure with preserved ejection fraction: Emerging drug strategies,” *J. Cardiovasc. Pharmacol.*, vol. 62, no. 1, pp. 13–21, 2013.

[153] M. Krüger *et al.*, “Protein kinase G modulates human myocardial passive stiffness by phosphorylation of the titin springs,” *Circ. Res.*, vol. 104, no. 1, pp. 87–94, 2009.

[154] C. Dal Lin, F. Tona, and E. Osto, “The heart as a psychoneuroendocrine and immunoregulatory organ,” in *Advances in Experimental Medicine and Biology*, 2018.

[155] S. F. Mohammed, S. Hussain, S. A. Mirzoyev, W. D. Edwards, J. J. Maleszewski, and M. M. Redfield, “Coronary microvascular rarefaction and myocardial fibrosis in heart failure with preserved ejection fraction.,” *Circulation*, vol. 131, no. 6, pp. 550–559, Feb. 2015.

[156] M. R. Grobbel, S. M. Shavik, E. Darios, S. W. Watts, L. C. Lee, and S. Roccabianca, “Contribution of left ventricular residual stress by myocytes and collagen: existence of inter-constituent mechanical interaction,” *Biomech. Model. Mechanobiol.*, vol. 17, no. 4, pp. 985–999, 2018.

[157] N. Wang *et al.*, “A systematic review of the diagnostic accuracy of cardiovascular magnetic resonance for pulmonary hypertension.,” *Can. J. Cardiol.*, vol. 30, no. 4, pp. 455–463, Apr. 2014.

[158] K. Alassas *et al.*, “Cardiac MRI as a diagnostic tool in pulmonary hypertension,” *Futur. Cardiol*, vol. 10, no. 1, pp. 117–130, 2014.

[159] A. J. Swift *et al.*, “Quantitative MR imaging of pulmonary hypertension: A practical approach to the current state of the art Andrew,” *J Thorac Imaging*, vol. 29, no. 2, pp. 68–79, 2014.

[160] E. H. Ibrahim, A. A. Bajwa, and R. D. White, “Assessment of Pulmonary Arterial Hypertension by Magnetic Resonance Imaging,” *Tomography*, vol. 1, no. 1, 2015.

[161] H. B. Van Der Zwaan *et al.*, “Right ventricular quantification in clinical practice: Two-dimensional vs. three-dimensional echocardiography compared with cardiac magnetic resonance imaging,” *Eur. J. Echocardiogr.*, vol. 12, no. 9, pp. 656–664, 2011.

[162] R. Benza, R. Biederman, S. Murali, and H. Gupta, “Role of Cardiac Magnetic Resonance Imaging in the Management of Patients With Pulmonary Arterial Hypertension,” *J. Am. Coll. Cardiol.*, vol. 52, no. 21, pp. 1683–1692, 2008.

[163] H. Shiran *et al.*, “Relationship between Echocardiographic and Magnetic Resonance Derived Measures of Right Ventricular Size and Function in Patients with Pulmonary Hypertension,” *J Am Soc Echocardiogr*, vol. 46, no. 1, pp. 850–857, 2015.

[164] I. Lopez-Costa, S. Bhalla, and C. Raptis, “Magnetic Resonance Imaging for Pulmonary Hypertension,” *Top. Magn. Reson. Imaging*, vol. 23, no. 1, pp. 43–50, 2014.

[165] C. Carre, D. Messika-zeitoun, and E. Schouman-claeys, “Accuracy of contrast-enhanced cine-MR sequences in the assessment of left ventricular function : comparison with precontrast cine-MR sequences . Results of a bicentric study,” *Eur Radiol*, pp. 2838–2844, 2007.

[166] J. T. Kowallick *et al.*, “Inter-study Reproducibility of Left Ventricular Torsion and Torsion Rate Quantification Using MR Myocardial Feature Tracking,” *J. Magn. Reson. imaging*, 2015.

[167] P. P. Swoboda, A. Kidambi, J. Gierula, K. K. Witte, J. P. Greenwood, and S. Plein, “The prognostic value of cardiovascular magnetic resonance in aborted sudden cardiac death,” *Europace*, vol. 16, no. Suppl 1, p. iii30, 2014.

[168] L. Zhong *et al.*, “Impact of surgical ventricular restoration on ventricular shape, wall stress, and function in heart failure patients.,” *Am. J. Physiol. Heart Circ. Physiol.*, vol. 300, no. 5, pp. H1653–H1660, 2011.

[169] L. Zhong *et al.*, “Right ventricular regional wall curvedness and area strain in patients with repaired tetralogy of Fallot,” *AJP Hear. Circ. Physiol.*, vol. 302, no. 6, pp. H1306–H1316, 2012.

[170] L. Zhong, Y. Su, S.-Y. Yeo, R.-S. Tan, D. N. Ghista, and G. Kassab, “Left ventricular regional wall curvedness and wall stress in patients with ischemic dilated cardiomyopathy.,” *Am. J. Physiol. Heart Circ. Physiol.*, vol. 296, no. 3, pp. H573–H584, 2009.

[171] P. Lik Chuan Lee *et al.*, “Patient-specific finite element modeling of the Cardiokinetix Parachute device: Effects on left ventricular wall stress and function,” *Med Biol Eng Comput*, vol. 52, no. 6, pp. 557–566, 2014.

[172] M. Genet *et al.*, “A Novel Method for Quantifying Smooth Regional Variations in Myocardial Contractility Within an Infarcted Human Left Ventricle Based on Delay-Enhanced Magnetic Resonance Imaging,” *J. Biomech. Eng.*, vol. 137, no. 8, p. 081009, 2015.

[173] J. L. Amini, A.A., Prince, *Measurement of Cardiac Deformations from MRI: Physical and Mathematical Models*. Berlin, Germany: Springer Netherlands, 2001.

[174] H. Wang and A. A. Amini, “Cardiac Motion and Deformation Recovery From MRI : A Review,” *IEEE Trans. Med. Imaging*, vol. 31, no. 2, pp. 487–503, 2012.

[175] Y. Fukuda *et al.*, “Utility of right ventricular free wall speckle-tracking strain for evaluation of right ventricular performance in patients with pulmonary hypertension,” *J. Am. Soc. Echocardiogr.*, vol. 24, no. 10, pp. 1101–1108, 2011.

[176] P. M. Smith *et al.*, “Myocardial strain analysis in patients with Heart Failure with preserved Ejection Fraction using bright blood cine MR images: A comparison with speckle-tracking echocardiography,” *J. Cardiovasc. Magn. Reson.*, vol. 16, no. Suppl 1, p. P71, 2014.

[177] Y. Li, Y. Wang, X. Ye, L. Kong, W. Zhu, and X. Lu, “Clinical study of right ventricular longitudinal strain for assessing right ventricular dysfunction and hemodynamics in pulmonary hypertension.,” *Medicine (Baltimore).*, vol. 95, no. 50, pp. 1–8, 2016.

[178] E. L. Hardegree *et al.*, “Role of Serial Quantitative Assessment of Right Ventricular Function by Strain in Pulmonary Arterial Hypertension,” *Am. J. Cardiol.*, vol. 111, no. 1, pp. 143–148, 2013.

[179] A. Sachdev *et al.*, “Right ventricular strain for prediction of survival in patients with pulmonary arterial hypertension,” *Chest*, vol. 139, no. 6, pp. 1299–1309, 2011.

[180] A. I. Veress, G. T. Gullberg, and J. A. *Weiss, “Measurement of strain in the left ventricle with cine-MRI and deformable image registration,” *J. Biomech. Eng.*, vol. 127, no. 7, pp. 1195–1207, 2005.

[181] M. Genet, C. T. Stoeck, C. von Deuster, L. C. Lee, J. M. Guccione, and S. Kozerke, “Finite Element Digital Image Correlation for Cardiac Strain Analysis from Accelerated 3D Whole-Heart Tagging,” *Proc. 24th ISMRM*, p. 3136, 2016.

[182] T. Mansi, X. Pennec, M. Sermesant, H. Delingette, and N. Ayache, “ILogDemons: A demons-based registration algorithm for tracking incompressible elastic biological tissues,” *Int. J. Comput. Vis.*, vol. 92, no. 1, pp. 92–111, 2011.

[183] M. Genet, L. C. Lee, and S. Kozerke, “A continuum formulation of the finite strain equilibrium gap regula- rizer for finite element image correlation problems Variational formulation,” in *CSMA 2017*, 2017, vol. 2, no. 1, pp. 13–17.

[184] D. Claire, F. Hild, and S. Roux, “A finite element formulation to identify damage fields: The equilibrium gap method,” *Int. J. Numer. Methods Eng.*, vol. 61, no. 2, pp. 189–208, 2004.

[185] A. I. Veress *et al.*, “Measuring Regional Changes in the Diastolic Deformation of the Left Ventricle of SHR Rats Using microPET Technology and Hyperelastic Warping,” *Ann. Biomed. Eng.*, vol. 36, no. 7, pp. 1104–1117, 2008.

[186] N. S. Phatak, S. A. Maas, A. I. Veress, N. A. Pack, E. V. R. Di Bella, and J. A. Weiss, “Strain measurement in the left ventricle during systole with deformable image registration,” *Med. Image Anal.*, vol. 13, no. 2, pp. 354–361, 2009.

[187] H. Zou *et al.*, “Characterization of patient - specific biventricular mechanics in heart failure with preserved ejection fraction : hyperelastic warping *,” in *2016 38th Annual International Conference of the IEEE Engineering in Medicine and Biology Society (EMBC)*, 2016, pp. 4149–4152.

[188] C. Xi *et al.*, “Patient-Specific Computational Analysis of Ventricular Mechanics in Pulmonary Arterial Hypertension,” *J. Biomech. Eng.*, vol. 138, no. 11, p. 111001, 2016.

[189] C. Geuzaine and J. F. Remacle, “Gmsh: A 3-D finite element mesh generator with built-in pre- and post-processing facilities,” *Int. J. Numer. Methods Eng.*, vol. 79, no. 11, pp. 1309–1331, Sep. 2009.

[190] J. Schulz-Menger *et al.*, “Standardized image interpretation and post processing in cardiovascular magnetic resonance: Society for Cardiovascular Magnetic Resonance (SCMR) Board of Trustees Task Force on Standardized Post Processing,” *J. Cardiovasc. Magn. Reson.*, vol. 15, no. 1, p. 35, 2013.

[191] T. M. Gorter, T. P. Willems, and J. P. Van Melle, “Ventricular interdependence in pulmonary arterial hypertension: Providing small pieces of a complex puzzle,” *Eur. J. Heart Fail.*, vol. 17, no. 1, pp. 1–2, 2015.

[192] N. M. Fine *et al.*, “Outcome prediction by quantitative right ventricular function assessment in 575 subjects evaluated for pulmonary hypertension,” *Circ. Cardiovasc. Imaging*, vol. 6, no. 5, pp. 711–721, 2013.

[193] M. L. Shehata *et al.*, “Myocardial Delayed Enhancement in Pulmonary Hypertension: Pulmonary Hemodynamics, Right Ventricular Function, and Remodeling,” *AJR Am J Roentgenol*, vol. 196, no. 1, pp. 87–94, 2011.

[194] Y. Ohyama *et al.*, “Comparison of strain measurement from multimodality tissue tracking with strain-encoding MRI and harmonic phase MRI in pulmonary hypertension,” *Int. J. Cardiol.*, vol. 182, no. Suppl 1, pp. 342–348, 2015.

[195] P. Moceri *et al.*, “Three-dimensional right-ventricular regional deformation and survival in pulmonary hypertension,” *Eur. Hear. J. - Cardiovasc. Imaging*, no. November, pp. 1–9, 2017.

[196] B. C. F. Smith, G. Dobson, D. Dawson, A. Charalampopoulos, J. Grapsa, and P. Nihoyannopoulos, “Three-dimensional speckle tracking of the right ventricle: Toward optimal quantification of right ventricular dysfunction in pulmonary hypertension,” *J. Am. Coll. Cardiol.*, vol. 64, no. 1, pp. 41–51, 2014.

[197] E. J. Cho *et al.*, “Right ventricular free wall circumferential strain reflects graded elevation in acute right ventricular afterload.,” *Am. J. Physiol. Heart Circ. Physiol.*, vol. 296, no. 2, pp. H413-20, 2009.

[198] G. S. Nelson, S.-A. E. Y., H. E. D. J. Ter Keurs, J. V. Tyberg, and N. G. Shrive, “A 2D Finite Element Model of the Interventricular Septum Under Normal and Abnormal Loading,” *Comput. Methods Biomech. Biomed. Engin.*, vol. 4, no. 4, pp. 307–322, 2001.

[199] R. G.Q., C. P., C. B., V. A., Q. D., and S. S.D., “Impact of lowering pulmonary vascular resistance on right and left ventricular deformation in pulmonary arterial hypertension,” *Eur. J. Heart Fail.*, vol. 17, no. 1, pp. 63–73, 2015.

[200] S. Puwanant *et al.*, “Ventricular geometry, strain, and rotational mechanics in pulmonary hypertension,” *Circulation*, vol. 121, no. 2, pp. 259–266, 2010.

[201] G. S. Nelson *et al.*, “Compression of interventricular septum during right ventricular pressure loading.,” *Am. J. Physiol. Heart Circ. Physiol.*, vol. 280, no. 6, pp. H2639–H2648, 2001.

[202] C. a Gibbons Kroeker, S. Adeeb, J. V Tyberg, and N. G. Shrive, “A 2D FE model of the heart demonstrates the role of the pericardium in ventricular deformation.,” *Am. J. Physiol. Heart Circ. Physiol.*, vol. 291, no. 5, pp. H2229–H2236, 2006.

[203] A. J. Pope, G. B. Sands, B. H. Smaill, and I. J. LeGrice, “Three-dimensional transmural organization of perimysial collagen in the heart,” *Am. J. Physiol. Circ. Physiol.*, vol. 295, no. 3, pp. H1243--H1252, 2008.

[204] D. W. Townsend, “Multimodality imaging of structure and function,” *Phys. Med. Biol.*, vol. 53, no. 4, p. R1, 2008.

[205] P. Lamata *et al.*, “Images as drivers of progress in cardiac computational modelling,” *Prog. Biophys. Mol. Biol.*, vol. 115, no. 2, pp. 198–212, 2014.

[206] A. Krishnamurthy *et al.*, “Patient-Specific Models of Cardiac Biomechanics.,” *J. Comput. Phys.*, vol. 244, pp. 4–21, Jul. 2013.

[207] R. Chabiniok *et al.*, “Multiphysics and multiscale modelling, data--model fusion and integration of organ physiology in the clinic: ventricular cardiac mechanics,” *Interface Focus*, vol. 6, no. 2, p. 20150083, 2016.

[208] M. Sermesant *et al.*, “Patient-specific electromechanical models of the heart for the prediction of pacing acute effects in CRT: a preliminary clinical validation,” *Med. Image Anal.*, vol. 16, no. 1, pp. 201–215, 2012.

[209] R. Chabiniok, P. Moireau, P.-F. Lesault, A. Rahmouni, J.-F. Deux, and D. Chapelle, “Estimation of tissue contractility from cardiac cine-MRI using a biomechanical heart model,” *Biomech. Model. Mechanobiol.*, vol. 11, no. 5, pp. 609–630, 2012.

[210] H. Finsberg *et al.*, “Estimating cardiac contraction through high resolution data assimilation of a personalized mechanical model,” *J. Comput. Sci.*, vol. 24, pp. 85–90, 2018.

[211] M. Genet *et al.*, “Distribution of normal human left ventricular myofiber stress at end-diastole and end-systole--a target for in silico studies of cardiac procedures,” *J. Appl. Physiol.*, vol. 117, pp. 142–52, 2014.

[212] R. M. Huisman, G. Elzinga, N. Westerhof, and P. Sipkema, “Measurement of left ventricular wall stress,” *Cardiovasc. Res.*, vol. 14, no. 3, pp. 142–153, 1980.

[213] W. Grossman, D. Jones, and L. P. McLaurin, “Wall stress and patterns of hypertrophy in the human left ventricle.,” *J. Clin. Invest.*, vol. 56, no. 1, p. 56, 1975.

[214] J. M. Guccione, A. Salahieh, S. M. Moonly, J. Kortsmit, A. W. Wallace, and M. B. Ratcliffe, “Myosplint decreases wall stress without depressing function in the failing heart: a finite element model study,” *Ann. Thorac. Surg.*, vol. 76, no. 4, pp. 1171–1180, 2003.

[215] Z. Zhang *et al.*, “Comparison of the Young-Laplace law and finite element based calculation of ventricular wall stress: implications for postinfarct and surgical ventricular remodeling,” *Ann. Thorac. Surg.*, vol. 91, no. 1, pp. 150–156, 2011.

[216] L. C. Lee *et al.*, “Algisyl-{{LVR}}\texttrademark{} with Coronary Artery Bypass Grafting Reduces Left Ventricular Wall Stress and Improves Function in the Failing Human Heart,” *Int. J. Cardiol.*, pp. 1–7, Feb. 2013.

[217] S. T. Wall, J. C. Walker, K. E. Healy, M. B. Ratcliffe, and J. M. Guccione, “Theoretical impact of the injection of material into the myocardium: a finite element model simulation.,” *Circulation*, vol. 114 24, pp. 2627–2635, 2006.

[218] M. Sermesant *et al.*, “Cardiac function estimation from MRI using a heart model and data assimilation: advances and difficulties,” *Med. Image Anal.*, vol. 10, no. 4, pp. 642–656, 2006.

[219] D. Chapelle, M. Fragu, V. Mallet, and P. Moireau, “Fundamental principles of data assimilation underlying the Verdandi library: applications to biophysical model personalization within euHeart,” *Med. Biol. Eng. Comput.*, vol. 51, no. 11, pp. 1221–1233, 2013.

[220] L. Asner *et al.*, “Estimation of passive and active properties in the human heart using 3D tagged MRI,” *Biomech. Model. Mechanobiol.*, pp. 1–19, 2015.

[221] J. Xi *et al.*, “The estimation of patient-specific cardiac diastolic functions from clinical measurements,” *Med. Image Anal.*, vol. 17, no. 2, pp. 133–146, 2013.

[222] A. U. Nair, D. G. Taggart, and F. J. Vetter, “Optimizing cardiac material parameters with a genetic algorithm,” *J. Biomech.*, vol. 40, no. 7, pp. 1646–1650, 2007.

[223] K. Sun *et al.*, “A computationally efficient formal optimization of regional myocardial contractility in a sheep with left ventricular aneurysm,” *J. Biomech. Eng.*, vol. 131, no. 11, p. 111001, 2009.

[224] P. Moireau and D. Chapelle, “Reduced-order Unscented Kalman Filtering with application to parameter identification in large-dimensional systems,” *ESAIM Control. Optim. Calc. Var.*, vol. 17, no. 2, pp. 380–405, 2011.

[225] S. Marchesseau *et al.*, “Personalization of a cardiac electromechanical model using reduced order unscented Kalman filtering from regional volumes,” *Med. Image Anal.*, vol. 17, no. 7, pp. 816–829, 2013.

[226] G. Balaban *et al.*, “High Resolution Data Assimilation of Cardiac Mechanics Applied to a Dyssynchronous Ventricle,” *Int. J. Numer. Methods Eng.*, vol. 79, no. 11, pp. 1309–1331, 2016.

[227] V. Y. Wang, H. I. Lam, D. B. Ennis, B. R. Cowan, A. A. Young, and M. P. Nash, “Modelling passive diastolic mechanics with quantitative MRI of cardiac structure and function,” *Med. Image Anal.*, vol. 13, no. 5, pp. 773–784, 2009.

[228] H. Delingette *et al.*, “Personalization of cardiac motion and contractility from images using variational data assimilation,” *IEEE Trans. Biomed. Eng.*, vol. 59, no. 1, pp. 20–24, 2012.

[229] S. Göktepe, S. N. S. Acharya, J. Wong, and E. Kuhl, “Computational modeling of passive myocardium,” *Int. j. numer. method. biomed. eng.*, vol. 27, no. 1, pp. 1–12, 2011.

[230] P. E. Farrell, D. A. Ham, S. W. Funke, and M. E. Rognes, “Automated derivation of the adjoint of high-level transient finite element programs,” *SIAM J. Sci. Comput.*, vol. 35, no. 4, pp. C369--C393, 2013.

[231] A. N. Redington, H. H. Gray, M. E. Hodson, M. L. Rigby, and P. J. Oldershaw, “Characterisation of the normal right ventricular pressure-volume relation by biplane angiography and simultaneous micromanometer pressure measurements,” *Br Hear. J*, vol. 59, pp. 23–30, 1988.

[232] R. P. Kelly *et al.*, “Effective arterial elastance as index of arterial vascular load in humans.,” *Circulation*, vol. 86, no. 2, pp. 513–521, 1992.

[233] M. Genet, C. T. Stoeck, C. Von Deuster, L. C. Lee, and S. Kozerke, “Equilibrated Warping: {{Finite}} Element Image Correlation with Finite Strain Equilibrium Gap Regularization,” *Submitted*, 2017.

[234] D. D. Streeter, H. M. Spotnitz, D. P. Patel, J. Ross, and E. H. Sonnenblick, “Fiber orientation in the canine left ventricle during diastole and systole.,” *Circ. Res.*, vol. 24, no. 3, pp. 339–347, 1969.

[235] D. Ambrosi, G. Arioli, F. Nobile, and A. Quarteroni, “Electromechanical coupling in cardiac dynamics: the active strain approach,” *SIAM J. Appl. Math.*, vol. 71, no. 2, pp. 605–621, 2011.

[236] S. Gjerald, J. Hake, S. Pezzuto, J. Sundnes, and S. T. Wall, “Patient--Specific Parameter Estimation for a Transversely Isotropic Active Strain Model of Left Ventricular Mechanics,” in *Statistical Atlases and Computational Models of the Heart-Imaging and Modelling Challenges*, Springer, 2014, pp. 93–104.

[237] P. J. Hunter, A. D. McCulloch, and H. Ter Keurs, “Modelling the mechanical properties of cardiac muscle,” *Prog. Biophys. Mol. Biol.*, vol. 69, no. 2, pp. 289–331, 1998.

[238] D. H. Lin and F. C. P. Yin, “A Multiaxial Constitutive Law for Mammalian Left Ventricular Myocardium in Steady-State Barium Contracture or Tetanus.,” *J. Biomech. Eng.*, vol. 120, pp. 504–517, 1998.

[239] J. Sundnes, S. Wall, H. Osnes, T. Thorvaldsen, and A. D. McCulloch, “Improved discretisation and linearisation of active tension in strongly coupled cardiac electro-mechanics simulations,” *Comput. Methods Biomech. Biomed. Engin.*, vol. 17, no. 6, pp. 604–615, Apr. 2014.

[240] J. A. Weiss, B. N. Maker, and S. Govindjee, “Finite element implementation of incompressible, transversely isotropic hyperelasticity,” *Comput. Methods Appl. Mech. Eng.*, vol. 135, no. 1–2, pp. 107–128, 1996.

[241] S. Govindjee and P. A. Mihalic, “Computational methods for inverse finite elastostatics,” *Comput. Methods Appl. Mech. Eng.*, vol. 136, no. 1, pp. 47–57, 1996.

[242] M. W. Gee, C. Förster, and W. A. Wall, “A computational strategy for prestressing patient-specific biomechanical problems under finite deformation,” *Int. j. numer. method. biomed. eng.*, vol. 26, no. 1, pp. 52–72, 2010.

[243] M. Sellier, “An Iterative Method for the Inverse Elasto-Static Problem,” *J. Fluids Struct.*, vol. 27, no. 8, pp. 1461–1470, Nov. 2011.

[244] J. Bols, J. Degroote, B. Trachet, B. Verhegghe, P. Segers, and J. Vierendeels, “A computational method to assess the in vivo stresses and unloaded configuration of patient-specific blood vessels,” *J. Comput. Appl. Math.*, vol. 246, pp. 10–17, 2013.

[245] M. Genet *et al.*, “Heterogeneous Growth-Induced Prestrain in the Heart,” *J. Biomech.*, vol. 48, no. 10, pp. 2080–2089, 2015.

[246] M. K. Rausch, M. Genet, and J. D. Humphrey, “An Augmented Iterative Method for Identifying a Stress-Free Reference Configuration in Image-Based Biomechanical Modeling,” *J. Biomech.*, vol. 58, pp. 227–231, Jun. 2017.

[247] H. Finsberg *et al.*, “Estimating cardiac contraction through high resolution data assimilation of a personalized mechanical model,” *J. Comput. Sci.*, 2017.

[248] P. Hood and C. Taylor, “Navier-Stokes equations using mixed interpolation,” *Finite Elem. methods flow Probl.*, pp. 121–132, 1974.

[249] D. Chapelle and K.-J. Bathe, “The inf-sup test,” *Comput. Struct.*, vol. 47, no. 4–5, pp. 537–545, 1993.

[250] X. S. Li and J. W. Demmel, “SuperLU_DIST: A scalable distributed-memory sparse direct solver for unsymmetric linear systems,” *ACM Trans. Math. Softw.*, vol. 29, no. 2, pp. 110–140, 2003.

[251] D. Kraft and others, *A software package for sequential quadratic programming*. DFVLR Obersfaffeuhofen, Germany, 1988.

[252] R. T. Marler and J. S. Arora, “Survey of multi-objective optimization methods for engineering,” *Struct. Multidiscip. Optim.*, vol. 26, no. 6, pp. 369–395, 2004.

[253] F. Scardulla, A. Rinaudo, S. Pasta, and C. Scardulla, “Evaluation of ventricular wall stress and cardiac function in patients with dilated cardiomyopathy,” *Proc. Inst. Mech. Eng. Part H J. Eng. Med.*, vol. 230, no. 1, pp. 71–74, 2016.

[254] N. Toussaint, C. T. Stoeck, T. Schaeffter, S. Kozerke, M. Sermesant, and P. G. Batchelor, “In vivo human cardiac fibre architecture estimation using shape-based diffusion tensor processing,” *Med. Image Anal.*, vol. 17, no. 8, pp. 1243–1255, 2013.

[255] I. J. LeGrice, B. H. Smaill, L. Z. Chai, S. G. Edgar, J. B. Gavin, and P. J. Hunter, “Laminar structure of the heart: ventricular myocyte arrangement and connective tissue architecture in the dog,” *Am. J. Physiol. Circ. Physiol.*, vol. 269, no. 2, pp. H571--H582, 1995.

[256] V. Y. Wang, P. M. F. Nielsen, and M. P. Nash, “Image-based predictive modeling of heart mechanics,” *Annu. Rev. Biomed. Eng.*, vol. 17, pp. 351–383, 2015.

[257] W. Kroon, T. Delhaas, P. Bovendeerd, and T. Arts, “Computational analysis of the myocardial structure: Adaptation of cardiac myofiber orientations through deformation,” *Med. Image Anal.*, vol. 13, no. 2, pp. 346–353, 2009.

[258] S. Y. Ho and P. Nihoyannopoulos, “Anatomy, echocardiography, and normal right ventricular dimensions,” *Heart*, vol. 92, no. suppl_1, pp. i2–i13, 2006.

[259] C.-J. Chuong and Y.-C. Fung, “Residual stress in arteries,” in *Frontiers in biomechanics*, Springer, 1986, pp. 117–129.

[260] H. M. Wang *et al.*, “A modified Holzapfel-Ogden law for a residually stressed finite strain model of the human left ventricle in diastole,” *Biomech. Model. Mechanobiol.*, vol. 13, no. 1, pp. 99–113, 2014.

[261] J. M. Guccione, S. M. Moonly, A. W. Wallace, and M. B. Ratcliffe, “Residual stress produced by ventricular volume reduction surgery has little effect on ventricular function and mechanics: a finite element model study,” *J. Thorac. Cardiovasc. Surg.*, vol. 122, no. 3, pp. 592–599, 2001.

[262] A. Nikou *et al.*, “Effects of using the unloaded configuration in predicting the in vivo diastolic properties of the heart,” *Comput. Methods Biomech. Biomed. Engin.*, vol. 19, no. 16, pp. 1714–1720, 2016.

[263] H. C. Champion, E. D. Michelakis, and P. M. Hassoun, “Comprehensive invasive and noninvasive approach to the right ventricle--pulmonary circulation unit: state of the art and clinical and research implications,” *Circulation*, vol. 120, no. 11, pp. 992–1007, 2009.

[264] A. J. Peacock, N. F. Murphy, J. J. V McMurray, L. Caballero, and S. Stewart, “An epidemiological study of pulmonary arterial hypertension in Scotland,” *Eur. Respir. J.*, 2007.

[265] V. V McLaughlin and M. D. McGoon, “Pulmonary arterial hypertension,” *Circulation*, vol. 114, no. 13, pp. 1417–1431, 2006.

[266] A. O. Mocumbi, F. Thienemann, and K. Sliwa, “A global perspective on the epidemiology of pulmonary hypertension,” *Can. J. Cardiol.*, vol. 31, no. 4, pp. 375–381, 2015.

[267] X. Jais and D. Bonnet, “Treatment of pulmonary arterial hypertension,” *Press. medicale (Paris, Fr. 1983)*, vol. 39, p. 1S22--32, 2010.

[268] M. J. Faber *et al.*, “Right and left ventricular function after chronic pulmonary artery banding in rats assessed with biventricular pressure-volume loops,” *Am. J. Physiol. Circ. Physiol.*, vol. 291, no. 4, pp. H1580--H1586, 2006.

[269] M. A. J. Borgdorff, B. Bartelds, M. G. Dickinson, P. Steendijk, M. de Vroomen, and R. M. F. Berger, “Distinct loading conditions reveal various patterns of right ventricular adaptation,” *Am. J. Physiol. Circ. Physiol.*, vol. 305, no. 3, pp. H354--H364, 2013.

[270] J. Aguero *et al.*, “Characterization of right ventricular remodeling and failure in a chronic pulmonary hypertension model,” *Am. J. Physiol. Circ. Physiol.*, vol. 307, no. 8, pp. H1204--H1215, 2014.

[271] K. R. Stenmark, B. Meyrick, N. Galie, W. J. Mooi, and I. F. McMurtry, “Animal models of pulmonary arterial hypertension: the hope for etiological discovery and pharmacological cure,” *Am. J. Physiol. Cell. Mol. Physiol.*, vol. 297, no. 6, pp. L1013--L1032, 2009.

[272] R. Naeije, S. Brimioulle, and L. Dewachter, “Biomechanics of the right ventricle in health and disease (2013 Grover Conference series),” *Pulm. Circ.*, vol. 4, no. 3, pp. 395–406, 2014.

[273] K. A. Brown and R. V Ditchey, “Human right ventricular end-systolic pressure-volume relation defined by maximal elastance.,” *Circulation*, vol. 78, no. 1, pp. 81–91, 1988.

[274] R. A. Quaife *et al.*, “Importance of right ventricular end-systolic regional wall stress in idiopathic pulmonary arterial hypertension: a new method for estimation of right ventricular wall stress,” *Eur. J. Med. Res.*, vol. 11, no. 5, p. 214, 2006.

[275] B. Lambermont *et al.*, “Comparison between single-beat and multiple-beat methods for estimation of right ventricular contractility,” *Crit. Care Med.*, vol. 32, no. 9, pp. 1886–1890, 2004.

[276] K. E. Kjørstad, C. Korvald, and T. Myrmel, “Pressure-volume-based single-beat estimations cannot predict left ventricular contractility in vivo,” *Am. J. Physiol. Circ. Physiol.*, vol. 282, no. 5, pp. H1739--H1750, 2002.

[277] E. Bossone *et al.*, “Echocardiography in pulmonary arterial hypertension: from diagnosis to prognosis,” *J. Am. Soc. Echocardiogr.*, vol. 26, no. 1, pp. 1–14, 2013.

[278] S. Leng *et al.*, “Three-dimensional tricuspid annular motion analysis from cardiac magnetic resonance feature-tracking,” *Ann. Biomed. Eng.*, vol. 44, no. 12, pp. 3522–3538, 2016.

[279] N. Reichek, “Right ventricular strain in pulmonary hypertension: flavor du jour or enduring prognostic index?,” *Circ. Cardiovasc. Imaging*, vol. 6, no. 5, p. 609, 2013.

[280] S. Acosta, C. Puelz, B. Rivière, D. J. Penny, K. M. Brady, and C. G. Rusin, “Cardiovascular mechanics in the early stages of pulmonary hypertension: a computational study,” *Biomech. Model. Mechanobiol.*, vol. 16, no. 6, pp. 2093–2112, 2017.

[281] R. Avazmohammadi *et al.*, “A Computational Cardiac Model for the Adaptation to Pulmonary Arterial Hypertension in the Rat,” *Ann. Biomed. Eng.*, pp. 1–16, 2018.

[282] H. Finsberg *et al.*, “Efficient estimation of personalized biventricular mechanical function employing gradient-based optimization,” *Int. j. numer. method. biomed. eng.*, p. e2982, 2018.

[283] M. Genet, C. T. Stoeck, C. Von Deuster, L. C. Lee, and S. Kozerke, “Equilibrated warping: Finite element image registration with finite strain equilibrium gap regularization,” *Med. Image Anal.*, vol. 50, pp. 1–22, 2018.

[284] S. P. L. Altmayer, Q. J. Han, K. Addetia, A. R. Patel, P. R. Forfia, and Y. Han, “Using all-cause mortality to define severe RV dilation with RV/LV volume ratio,” *Sci. Rep.*, vol. 8, no. 1, p. 7200, 2018.

[285] S. P. L. Altmayer, A. R. Patel, K. Addetia, M. Gomberg-Maitland, P. R. Forfia, and Y. Han, “Cardiac MRI right ventricle/left ventricle (RV/LV) volume ratio improves detection of RV enlargement,” *J. Magn. Reson. Imaging*, vol. 43, no. 6, pp. 1379–1385, 2016.

[286] A. Frigiola *et al.*, “Biventricular response after pulmonary valve replacement for right ventricular outflow tract dysfunction: is age a predictor of outcome?,” *Circulation*, vol. 118, no. 14 suppl 1, pp. S182--S190, 2008.

[287] C. W. Lindsey, W. J. Parks, B. E. Kogon, D. Sallee III, and W. T. Mahle, “Pulmonary valve replacement after tetralogy of Fallot repair in preadolescent patients,” *Ann. Thorac. Surg.*, vol. 89, no. 1, pp. 147–151, 2010.

[288] S. Hsu *et al.*, “Right Ventricular Myofilament Functional Differences in Humans With Systemic Sclerosis--Associated Versus Idiopathic Pulmonary Arterial Hypertension,” *Circulation*, vol. 137, no. 22, pp. 2360–2370, 2018.

[289] E. Manders *et al.*, “Contractile dysfunction of left ventricular cardiomyocytes in patients with pulmonary arterial hypertension,” *J. Am. Coll. Cardiol.*, vol. 64, no. 1, pp. 28–37, 2014.

[290] S. Rain *et al.*, “Right ventricular myocardial stiffness in experimental pulmonary arterial hypertension: relative contribution of fibrosis and myofibril stiffness,” *Circ. Hear. Fail.*, vol. 9, no. 7, p. e002636, 2016.

[291] A. Gómez *et al.*, “Right ventricular ischemia in patients with primary pulmonary hypertension,” *J. Am. Coll. Cardiol.*, vol. 38, no. 4, pp. 1137–1142, 2001.

[292] R. Naeije and A. Manes, “The right ventricle in pulmonary arterial hypertension,” *Eur. Respir. Rev.*, vol. 23, no. 134, pp. 476–487, 2014.

[293] J. Xi *et al.*, “An automatic data assimilation framework for patient-specific myocardial mechanical parameter estimation,” in *International Conference on Functional Imaging and Modeling of the Heart*, 2011, pp. 392–400.

[294] V. V McLaughlin *et al.*, “A report of the american college of cardiology foundation task force on expert consensus documents and the american heart association,” *Circulation*, vol. 119, no. 16, pp. 2250–2294, 2009.

[295] S. P. Altmayer *et al.*, “CMR RV size assessment should include RV to LV volume ratio,” *J. Cardiovasc. Magn. Reson.*, vol. 17, no. 1, p. P394, 2015.

[296] S. Rajagopal *et al.*, “Comprehensive assessment of right ventricular function in patients with pulmonary hypertension with global longitudinal peak systolic strain derived from multiple right ventricular views,” *J. Am. Soc. Echocardiogr.*, vol. 27, no. 6, pp. 657–665, 2014.

[297] M. L. Shehata *et al.*, “Regional and global biventricular function in pulmonary arterial hypertension: a cardiac MR imaging study,” *Radiology*, vol. 266, no. 1, pp. 114–122, 2013.

[298] R. de Amorim Corrêa *et al.*, “Left Ventricular Function in Patients with Pulmonary Arterial Hypertension: The Role of Two-Dimensional Speckle Tracking Strain,” *Echocardiography*, vol. 33, no. 9, pp. 1326–1334, 2016.